UNIVERSITÀ CA' FOSCARI - VENEZIA

Scuola Dottorale di Ateneo - Graduate School

DOTTORATO DI RICERCA IN
SCIENZA E GESTIONE DEI CAMBIAMENTI CLIMATICI
Stream in Climatologia Dinamica

CICLO XXVIII
Anno 2016

Simulation of Greenland mass balance evolution until 2100

Settore Scientifico-disciplinare di afferenza: FIS/06

Tesi di dottorato di **Daniele Peano**, matricola 955987

Coordinatore del dottorato
Prof. Carlo Barbante

Tutor del dottorando
Dr. Florence Colleoni

Co-Tutor del dottorando
Dr. Simona Masina

To Virginia

Contents

Abstract

The evolution of the Greenland ice sheet mass balance has a potential impact on the regional and global climate. Moreover, the runoff from the Greenland ice sheet into the nearby ocean and its evolution are not well known, despite their potential impacts on ocean circulation. For this reason, this study investigates the evolution of Greenland mass balance and runoff during the 20th and 21st century by means of two thermo-mechanical ice sheet-ice shelves models: GRISLI and SICOPOLIS. Transient simulations forced with the climate simulated from seven CMIP5 models, are performed, and the evolution of surface mass balance and runoff for the entire ice sheet and for seven drainage basins are analyzed. The ability of one of the two thermo-mechanical ice sheet-ice shelves models in simulating basal melting and calving is investigated, in order to close the Greenland ice sheet mass balance. The simulated surface mass balance exhibits values in a wide range in the 20th century (362 Gt/yr to -131 Gt/yr). The simulated surface mass balance decreases in time reaching values ranging from 59 Gt/yr to -436 Gt/yr for the RCP 4.5 simulations, and from -591 Gt/yr to -1857 Gt/yr for the RCP 8.5 simulations by 2100. This decrease is characterized by an acceleration after the 2030s, more evident for the RCP 8.5 scenario, and the strongest reductions are simulated in the northern regions under both scenarios. The simulated present-day (1980–1999) runoff ranges from 0.78 $mm\,SLE\ yr^{-1}$ to 0.86 $mm\,SLE\ yr^{-1}$, and at the end of the 21st century (2081–2100) the runoff is projected to increase to 1.25 $mm\,SLE\ yr^{-1}$ to 1.51 $mm\,SLE\ yr^{-1}$ (2.36 $mm\,SLE\ yr^{-1}$ to 2.94 $mm\,SLE\ yr^{-1}$) under a RCP 4.5 (RCP 8.5) scenario. On regional scale, the highest amount of runoff is found in the northern and western basins, and the north-western one presents the largest values by the end of the 21st century, up to 0.68 $mm\,SLE\ yr^{-1}$ under a RCP 8.5 scenario. Finally, the simulated basal melting produced by one of the two thermo-mechanical ice sheet-ice shelves models exhibits small values compared to the surface meltwater values. Consequently, the basal melting can be neglected in the mass balance computation. The calving, in Greenland, occurs in small embayments along the Greenland margins, which are not properly reproduced in the ice sheet model due to the too low resolution. Consequently, calving has not been accounted for in mass balance calculation due to the technical limitations of the ice sheet models used in this study.

Sommario

L'evoluzione del bilancio di massa superficiale della Groenlandia ha un forte impatto sul clima locale e globale. Inoltre, il flusso di *runoff* in uscita dall'*ice sheet* in Groenlandia nel vicino oceano e le sue variazioni nel tempo non sono propriamente conosciute e studiate, nonostante il loro possibile impatto sulla circolazione oceanica. Di conseguenza, questa tesi si focalizza sullo studio dell'evoluzione del bilancio di massa superficiale e del *runoff* in uscita dalla Groenlandia durante il ventesimo e ventunesimo secolo grazie all'uso di due modelli termo-meccanici di *ice sheet-ice shelves*: GRISLI e SICOPOLIS. Pertanto, vengono effettuate delle simulazioni transienti forzate dagli scenari climatici simulati da sette modelli del CMIP5, e viene analizzata l'evoluzione del bilancio di massa superficiale e della produzione di *runoff* sia su scala di *ice sheet* sia a scala di bacini di drenaggio. Inoltre, viene investigata l'abilità di uno dei due modelli termo-meccanici di *ice sheet* nel simulare la fusione basale ed il *calving* in modo da chiudere il bilancio di massa totale dell'*ice sheet* in Groenlandia. Il bilancio di massa superficiale mostra valori in un ampio raggio a partire dal ventesimo secolo (da 362 Gt/yr a -131 Gt/yr) e diminuisce nel tempo raggiungendo entro il 2100 valori tra 59 Gt/yr e -436 Gt/yr nelle simulazioni forzate da uno scenario futuro di tipo RCP 4.5, e tra -591 Gt/yr e -1857 Gt/yr in uno scenario futuro di tipo RCP 8.5. Questa diminuzione è caratterizzata da una accelerazione dopo la decade 2031–2040, variazione più evidente in uno scenario di tipo RCP 8.5, ed inoltre le maggiori variazioni sono localizzate nei bacini di drenaggio nella zona a nord della Groenlandia per entrambi gli scenari futuri. Il *runoff* in uscita dalla Groenlandia simulato dai modelli presenta valori tra 0.78 $mm\,SLE\ yr^{-1}$ e 0.86 $mm\,SLE\ yr^{-1}$, in media nel periodo 1980–1999, mentre alla fine del ventunesimo secolo (2081–2100) il *runoff* cresce fino a raggiungere valori nell'intervallo tra 1.25 $mm\,SLE\ yr^{-1}$ e 1.51 $mm\,SLE\ yr^{-1}$ (2.36 $mm\,SLE\ yr^{-1}$ e 2.94 $mm\,SLE\ yr^{-1}$) nel caso di uno scenario futuro di tipo RCP 4.5 (RCP 8.5). Sulla scala dei bacini di drenaggio, invece, i valori maggiori di *runoff* in uscita dalla Groenlandia si localizzano nei bacini a nord ed a ovest di quest'ultima, con i valori più alti nel bacino a nord-ovest della Groenlandia, dove vengono simulati 0.68 $mm\,SLE\ yr^{-1}$ di *runoff* in uscita dalla Groenlandia alla fine del ventunesimo secolo in uno scenario RCP 8.5. Infine, la fusione alla base della calotta glaciale simulata da uno dei modelli termo-meccanici di *ice sheet* risulta essere inferiore a quanto prodotto alla superficie della calotta glaciale stessa. Pertanto, la fusione alla base può essere trascurata nel calcolo del bilancio di massa totale. Il *calving*, in Groenlandia, avviene in piccole insenature lungo i margini della Groenlandia, che non vengono simulate correttamente con i modelli di *ice sheet* per via della loro bassa risoluzione. Di conseguenza, il *calving* non viene considerato nel calcolo del bilancio di massa totale a causa delle limitazioni tecniche dei modelli di *ice sheet* usati in questo studio.

Acknowledgements

I want to thank Florence Colleoni, Simona Masina and Aurélien Quiquet and the people of CMCC that helped me during my PhD with their advices. I want to thank Nina Kirchner who helped me in using SICOPOLIS and during my period at the Stockholm University.
I want to thank the reviewers who gave me many suggestions in order to improve my work.
Many thanks to Catherine Ritz, who provided the GRISLI ice-sheet model code, to Louise Sandberg Sørensen, who shared the ICESat data, and to Jonathan Bamber, who shared the freshwater fluxes data obtained in his study.

On a personal point of view, I want to thanks my colleagues and friends who shared the PhD experience with me. A special thanks goes to my wife, who supported me during these three years and in particular during the PhD thesis writing.

Thanks!

Thesis motivation and structure

Motivation and objectives

The cryosphere is an important component of the Earth climate system. Among all the cryosphere components, the Greenland ice sheet (GIS) has an important impact on both regional and global climate. In particular, the Greenland ice sheet changes cause a polar amplification of surface temperature in the Arctic region, (warming of $\sim$1.36 °C century^{-1} over the period 1875–2008, about two times larger than warming in the Northern Hemisphere, Bekryaev et al. 2010) and the GIS acts as source of freshwater to the nearby ocean. Its melting would potentially cause irreversible changes to the mean global climate state (e.g. Hansen and Lebedeff 1987; Bindoff et al. 2013). Consequently, the Greenland ice sheet is one of the climate system component that can reach a tipping point if the ongoing climate change does not stop. The term tipping point refers to "a critical threshold at which a tiny perturbation can qualitatively alter the state or development of a system" (Lenton et al. 2008). The threshold, in the Greenland case, is represented by a long-term negative condition in the mass balance which would lead to a reduction of the ice volume. This change could be triggered by a warming of the temperature in the Arctic region (e.g. Lenton et al. 2008; Ridley et al. 2010; Robinson et al. 2012). In addition, the melting of the Greenland ice sheet would have a direct impact on the ocean circulation, and, in particular, on the meridional overturning circulation (e.g. Fichefet et al. 2003; Rahmstorf et al. 2005; Driesschaert et al. 2007), because Greenland is close to the main North Atlantic ocean convection sites. For these reasons, most of the community efforts aim to study the present-day and the near-future changes in Greenland ice sheet (e.g. Bamber et al. 2012; Nowicki et al. 2013; Edwards et al. 2014). In particular, SeaRISE project (Bindschadler et al. 2013) and ICE2SEA project (Edwards et al. 2014) investigate the present-day and near-future volume changes of GIS with a set of ice sheet models of different complexity and under a set of possible future conditions. However, their analysis focuses only on the overall reduction of the Greenland ice sheet volume. Furthermore, only few works analyze the spatial distribution of freshwater flowing out of Greenland (e.g. Large and Yeager 2008; Bamber et al. 2012). These latter works base their assessment on reanalysis and regional climate model simulations, and focus only on the present-day freshwater distribution. For these reasons, this work tries to better assess the present-day conditions and future evolution of the Greenland ice sheet. In particular, this thesis focuses on:

- evaluating the performance of two state-of-the-art ice sheet models (ISMs) in simulating the 20th and 21st centuries evolution of the GIS surface mass balance (SMB) and its components, i.e. accumulation (Acc) and ablation (Abl), at ice sheet and regional scales under many climatic forcing;

- simulating the 20th and 21st centuries variations in the runoff produced by the GIS melting and its distribution along the Greenland coasts in order to link ice sheet to ocean;
- investigating the influence of all the components of the mass balance, i.e. dynamical discharge, basal melting and surface melting, on the future evolution of the GIS by means of a state-of-the-art ice sheet model.

Structure of the thesis

This work focuses on the Greenland ice sheet, which is introduced with a short summary of the state-of-the-art knowledge on the GIS in Chapter 1, and, in particular, it analyzes the present-day and near-future evolution of Greenland mass balance and freshwater runoff distribution along the Greenland margins. This analysis is performed by using two different three-dimensional thermo-mechanical ice sheet-ice shelves models: GRenoble Ice Shelf and Land Ice model (GRISLI, Ritz et al. 2001) and SImulation COde for POLythermal Ice Sheet model (SICOPOLIS, Greve 1997a). The physics described by both models is summarized in Chapter 2. To perform the present-day and near-future simulations, the ice sheet models require climate forcing, namely air surface temperature and precipitation, which are retrieved from (1) one reanalysis (ERA Interim, Dee et al. 2011), (2) one regional climate model (Modèle Atmosphérique Régional, MAR, version 3.5 Fettweis et al. 2013) and (3) a set of seven atmosphere-ocean general coupled model coming from the fifth phase of the Coupled Model Intercomparison Project (CMIP5, Taylor et al. 2012). These sets of climate forcing fields are presented and analyzed in Chapter 3.

The Greenland ice sheet mass balance evolution over the 20th and 21st centuries is considered and analyzed in its main components: surface mass balance, dynamical discharge and basal melting. In particular, the impact of climate forcing, ice sheet models and resolution on the surface mass balance is analyzed at both ice sheet and regional scales in Chapter 4. The ability of the ice sheet models in reproducing calving is analyzed in Chapter 6. The production of basal melting is also analyzed in Chapter 6. In Chapter 5, the flow of the surface meltwater and the runoff production and distribution along the Greenland coasts are studied by means of a routing scheme at both ice sheet and regional scales. Finally, the limitations and implications of this work are discussed in Chapter 7, while the main conclusions are summarized in Chapter 8.

Chapter 1

Introduction

1.1 Impact of cryosphere on current climate changes

The cryosphere is a component of the Earth system that includes snow, sea ice, glaciers, ice shelves, ice sheets, and frozen ground (Figure 1.1 and Table 1.1).

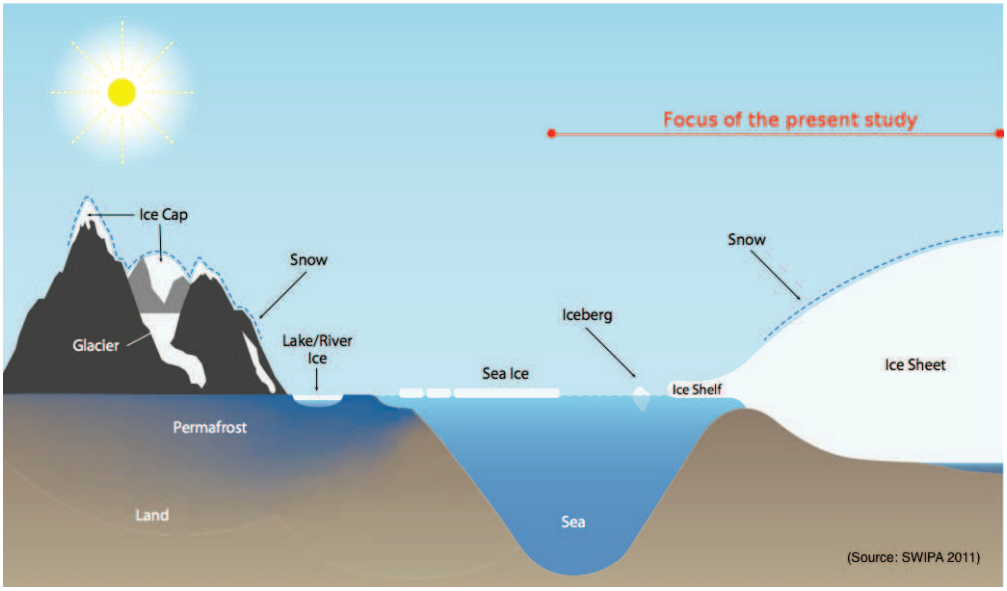

Figure 1.1: The cryosphere components. Figure after AMAP (2011).

The cryosphere interacts with the Earth's climate through many major cycles and budgets such as the surface energy budget (albedo), the water cycle, the surface gas exchanges and the sea level. Thus, the cryosphere has a fundamental control on physical, biological and social environments over a large part of the Earth's surface (Vaughan et al. 2013). Furthermore, as feedback effect, the cryosphere components are sensitive to the climate changes, thus the cryosphere is often considered as a "natural thermometer" of the Earth climate system (Vaughan et al. 2013).

The last Intergovernmental Panel on Climate Change (IPCC) assessment report (AR5, Vaughan et al. 2013) highlights a continuous mass loss during the last decades from the cryosphere as a results of the ongoing climate changes, although there are differences among components and regions. For example the Arctic sea ice extent decreased

Table 1.1: Representative statistics for the Earth's cryosphere components from the Fifth Assessment Report of the IPCC (Vaughan et al. 2013).

Ice on land	**Percent of global land surface**	**Sea level equivalent (m)**
Antarctic ice sheet	8.3	58.3
Greenland ice sheet	1.2	7.36
Glaciers	0.5	0.41
Ice in the ocean	**Percent of global ocean area**	**Volume (10^3 Km^3)**
Arctic sea ice (boreal autumn/spring)	1.7/3.9	13.0/16.5
Antarctic sea ice (austral autumn/spring)	0.8/5.2	3.4/11.1

over the period 1979–2012 with a rate of about 3.5–4.1% per decade (e.g. Comiso et al. 2008; Comiso 2012; Vaughan et al. 2013). Similarly, the worldwide glaciers are shrinking as revealed by the time series of measured glacier length (e.g. WGMS 2008). Those data show that glaciers are loosing mass at a rate of about 0.76 mm/yr of sea level equivalent (SLE) in average over the period 1993–2009 (e.g. Vaughan et al. 2013). Similarly studies show that the Greenland and Antarctic ice sheets are loosing mass during the last decades. In particular, the mass loss from the Greenland ice sheet increased from 0.09 $mm\,SLE/yr$, over the period 1992–2001, to 0.59 $mm\,SLE/yr$, over the period 2002–2011, while the Antarctic ice sheet mass loss increased from 0.08 $mm\,SLE/yr$ to 0.40 $mm\,SLE/yr$ during the same time frames (Vaughan et al. 2013).

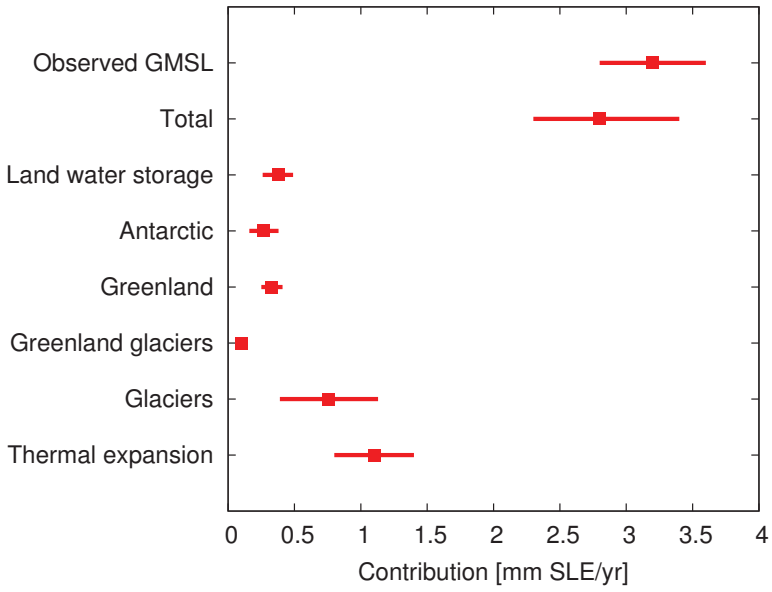

Figure 1.2: Observed global mean sea level budget in $mm\,SLE/yr$ in the period 1993–2010. Values from Church et al. (2013).

Consequently, the cryosphere is one of the main source of sea level changes. The observations from tide gauges and satellite altimeter allow to monitor the ongoing changes in mean global sea level (e.g. Fu and Cazenave 2001; Nerem et al. 2006; Cazenave and Llovel 2010; Holgate et al. 2013). Many efforts has been done in identifying and in quantifying all the sources of present-day sea level changes (e.g. Milne et al. 2009; Cazenave and Llovel 2010). The IPCC AR5 identifies the ocean thermal expansion and mountain glaciers melting as the dominant contributors to the 20th century global mean sea level rise (Figure 1.2, Church et al. 2013). According to Rignot et al. (2011) and given the observed acceleration in mass loss coming from both surface mass balance and dynamical discharge during the last decades, the impact of the ice sheets, especially of Greenland, on sea level changes is expected to increase during the next century (Church et al. 2013). For this reason, it is important to assess the ongoing mass loss from the GIS and to simulate its future evolution.

1.2 Interaction between Greenland ice sheet and climate system

Greenland is located between 60 °N and 83 °N in the North Atlantic area (Figure 1.3).

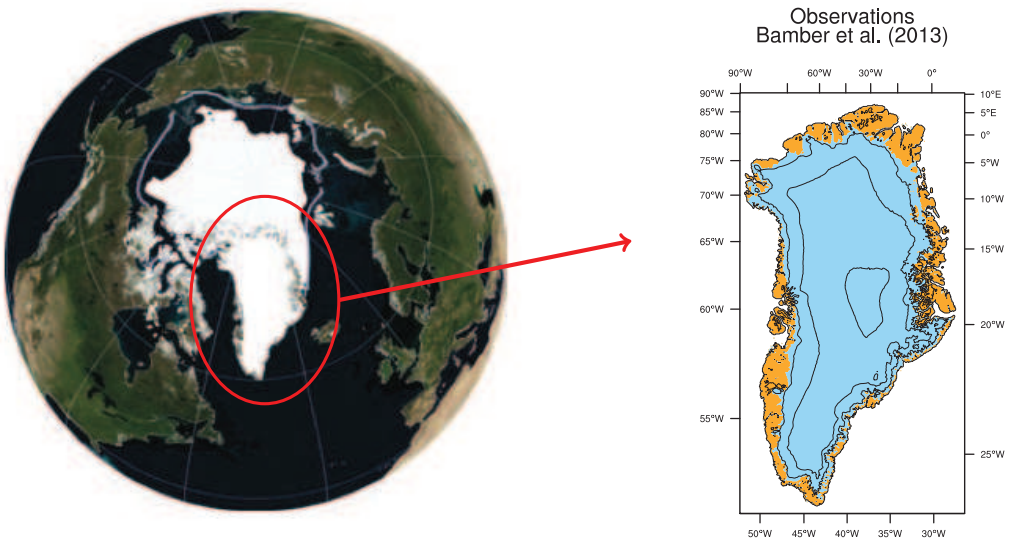

Figure 1.3: Greenland location and observed Greenland topography (cyan area is the ice covered region, brown area is the region without ice, Bamber et al. 2013). Figures after AMAP (2011).

The ocean currents around Greenland are part of the cyclonic sub-polar gyre circulation of the North Atlantic and the Arctic region (AMAP 2011). The surface waters in the southern part of Greenland are dominated by the warm and saline Irminger water, which is part of the North Atlantic current (Figure 1.4). The eastern and western currents along the Greenland coasts are characterized by the cold and low-saline Arctic outflow currents: the East Greenland Current, along the eastern side of Greenland, and the outflow from the Canadian Arctic archipelago, along the western side of Greenland (Figure 1.4). Furthermore, the Greenland ice sheet is close to the main North Atlantic

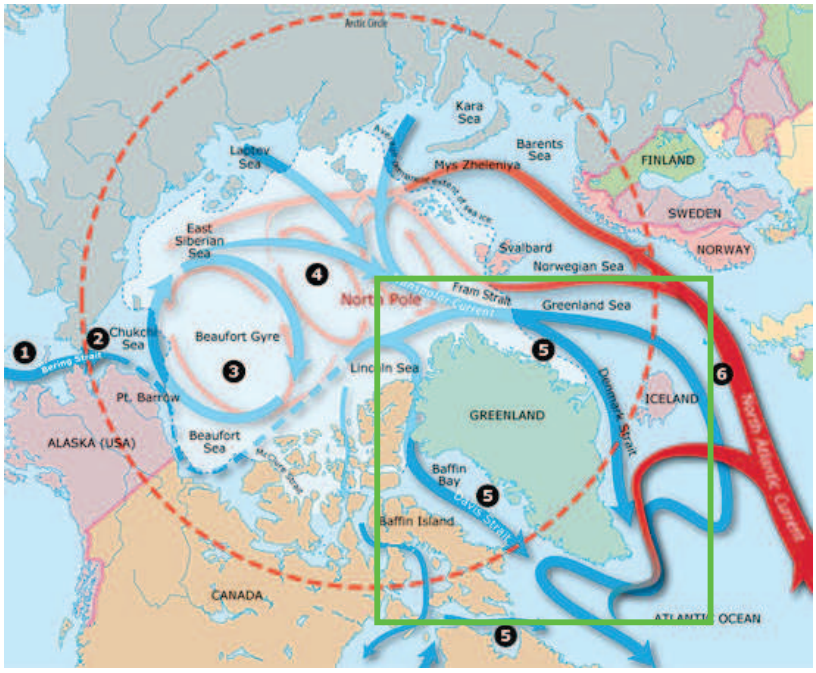

Figure 1.4: Summary of the ocean circulation in the Arctic and around Greenland (green box). Figure after Comiso (2010)

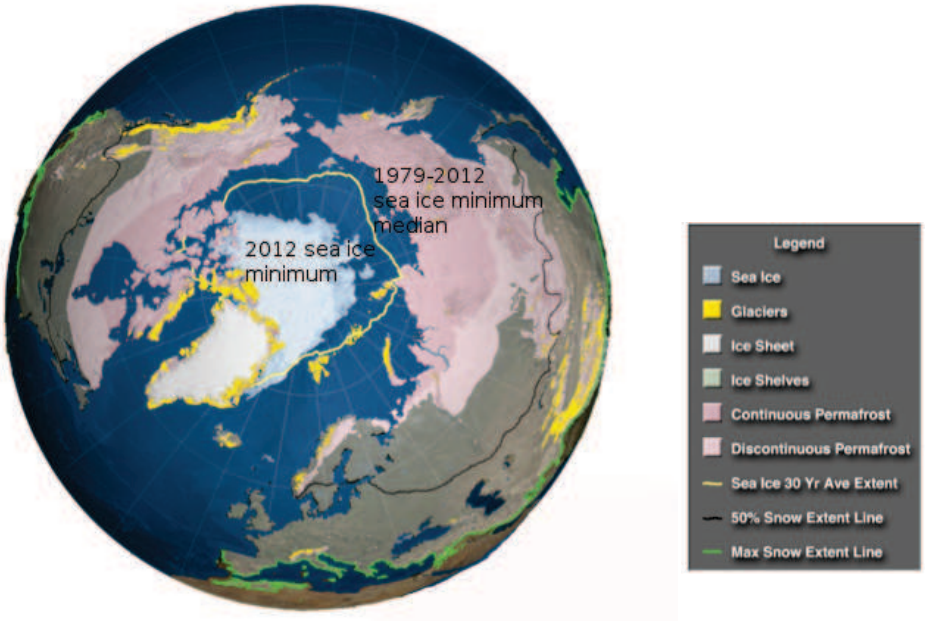

Figure 1.5: Minimum Arctic sea-ice extent comparison between 1979–2012 median (yellow line) and 2012 minimum (white region). Figure after Vaughan et al. (2013).

ocean convection site, located in the Labrador sea. Finally, the northern side is influenced by the transpolar current in the Arctic ocean. The main currents are summarized in Figure 1.4. Note that along the southeastern coasts of Greenland the Irminger water and the East Greenland Current flow side by side. However, the polar water flows on the continental shelf, while the Irminger water flows over the continental slope.

Moreover, the Arctic sea-ice extent decreased during the last decade (Figure 1.5). This retreat is expected to impact on the GIS, as well. For example, Day et al. (2013) simulate the impact of an ice-free Arctic ocean on the Greenland SMB. Under this condition, they simulate a 23% increase in winter SMB linked to higher evaporation from the nearby ocean. On the contrary, the summer SMB is simulated to reduce by about 65% leading to an overall reduction in the GIS surface mass balance.

The atmospheric circulation over Greenland is characterized by the presence of the polar jet stream. However, the atmospheric circulation over Greenland is strongly influenced by the phase of the North Atlantic Oscillation (NAO, Figure 1.6).

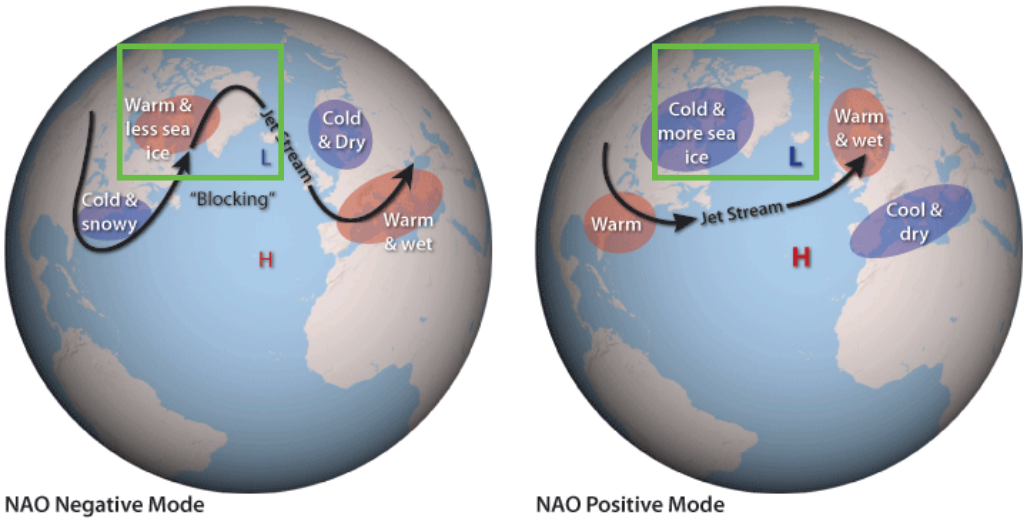

Figure 1.6: Summary of the main climatic conditions related to the NAO phases. Green boxes highlight the Greenland location. Figure adapted from NOAA

The NAO is characterized by two phases: a positive phase and a negative phase. Strong positive phases of the NAO are associated with warm temperatures in the eastern United States and across northern Europe and cold temperatures in Greenland and across southern Europe and the Middle East. High precipitation occurs over northern Europe and Scandinavia in winter, while low precipitation occur over southern and central Europe. The negative phase of the NAO exhibits opposite patterns of temperature and precipitation. Furthermore, a NAO positive phase leads to stronger than average westerlies over the middle latitudes (Figure 1.6, and Hurrell 1996).

Given its position, it has been shown that the Greenland natural climate variability is influenced by three main teleconnections (summarized in Figure 1.7):

1. North Atlantic Oscillation (NAO), which is defined as the difference of normalized pressure between Portugal (Lisbon) and Iceland (Stykkisholmur) which are near to

the center of the teleconnection during winter;

2. Greenland Blocking Index (GBI), which is defined as the mean 500-hPa geopotential height over the Greenland area 60–80° N, 20–80° W emphasizing the northern center of the NAO dipole pattern;

3. Atlantic Multi-decadal Oscillation (AMO), which is indexed by the time-filtered mean SST of the Atlantic Ocean between the equator and 60° N.

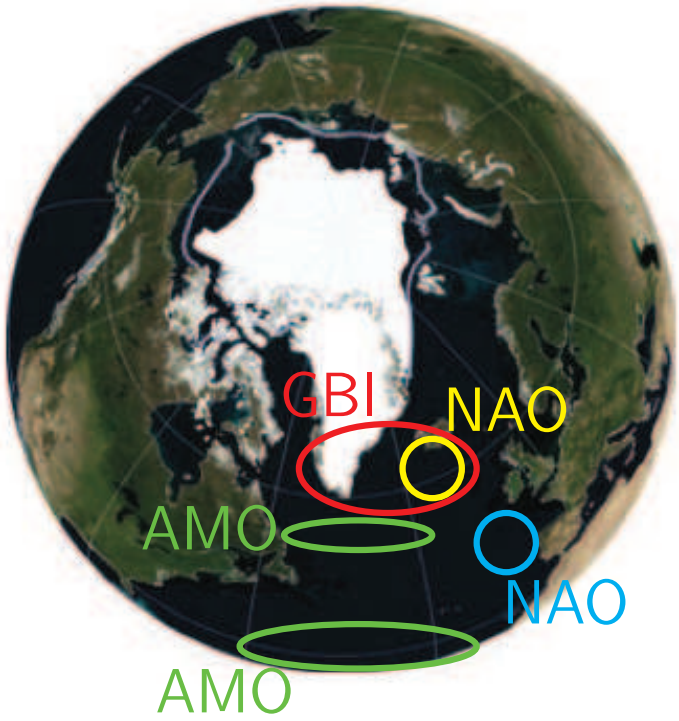

Figure 1.7: Summary of the main teleconnections which impact on the Greenland climate. Figure after AMAP (2011).

In particular, Hurrell (1996), using a regression analysis, showed that the NAO index accounts for 31% of the north hemisphere extratropical surface temperature variance. Subsequently, Chylek et al. (2004) show that there is a high anti-correlations between the NAO index and the Greenland temperature records, especially in the western and southern Greenland. For example, the recent negative shift of the NAO correlates with 1990s warming in Greenland. However, the correlation between Greenland temperature and NAO reveals temporal variations over the last 100 years, with specific periods characterized by high correlations, such as in the early 20th century and during the last decades, and periods with lower correlations (i.e. Arguez et al. 2009; Hanna et al. 2013).

Recently, the current melt and retreat of the Greenland ice sheet along the margins, and, in particular, of the Greenland outlet glaciers has been linked to a warming of the surrounding ocean (e.g. Holland et al. 2008; Straneo et al. 2010). In the North Atlantic the natural oscillations of sea surface temperature (SST) are described by the AMO. During warm phases of the AMO, high SSTs off the southeast Greenland coast are more likely to occur. The warm phase of the AMO, then, may drive cyclic variations

in temperature along the Greenland margins impacting on the outlet-glacier flow (i.e. Howat et al. 2008; Arguez et al. 2009).

The recent work by Hanna et al. (2013) exhibits a stronger correlation between GBI and Greenland temperature with respect to the correlations obtained between Greenland air surface temperature and NAO and AMO indexes. This blocking component of the NAO pattern is introduced by Woollings et al. (2010), who argue that the NAO is a two-state regime, corresponding to (1) blocked or (2) zonal atmospheric flow over Greenland. They also suggest that, among these two regimes, the frequency of Greenland blocking occurrence has a major influence in determining the NAO phase.

Previous studies (i.e. Francis and Vavrus 2012; Overland et al. 2012) already suggest that a regional atmospheric blocking mechanism is responsible for the presence of a persistent Arctic wind pattern that leads to a possible increase in Arctic-subarctic weather linkages through higher-amplitude upper-level flow. Furthermore, this persistent pattern is in agreement with the increased sea ice loss in summer, long-lived positive temperature anomalies and ice sheet loss in Greenland.

In general, the temperature over Greenland is related to changes in atmospheric circulation (NAO and GBI correlation). The Greenland runoff, instead, is also influenced by the oceanic temperature forcing as gauged through the AMO. These works, then, suggest that the same atmospheric and oceanic processes that are responsible for the NAO and AMO are also affecting Greenland's climate. Moreover, recent studies highlight the GBI as a potentially useful predictor of ice-sheet mass balance changes.

Moreover, the Greenland ice sheet interacts with the other components of the Earth climate system (Figure 1.8).

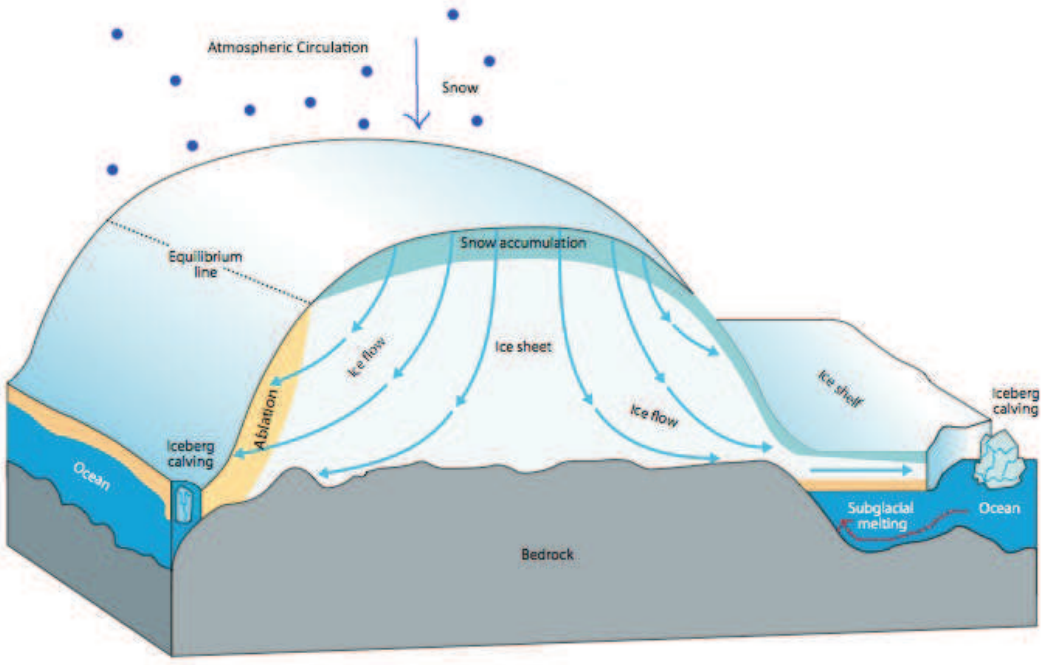

Figure 1.8: Summary of the interactions between ice sheet and Earth system components. Figure after AMAP (2011).

The interactions between atmosphere and ice sheet occur at the surface of the ice sheet

through the processes of accumulation and ablation. The accumulation is represented by the solid fraction of the precipitation (e.g. Marsiat 1994; Bales et al. 2009). The ablation depends on the energy exchanges between ice and atmosphere. The parameterizations of these exchanges can be related only to the air surface temperature variable (e.g. Reeh 1991; Calov and Greve 2005), or to a set of atmospheric variables, such as radiation, latent heat, sensible heat, heat conduction between inner snow layers and the surface layer, and the heat exchanged with the surface due to the fall of precipitation (e.g. Vizcaíno et al. 2010). On the other hand, the ice sheet influences the surface energy exchanges. For example, the albedo of the ice sheet has a strong impact on the energy exchanges between surface and atmosphere (e.g. Kuipers Munneke et al. 2011).

The interactions between the ice sheet and the bedrock are influenced by the geothermal heat flux and by the nature of the bedrock (soft sediment, hard rocks, etc.). A map of the surface heat flux distribution has been inferred by means of a global tomographic model by Shapiro and Ritzwoller (2004) (Figure 1.9), it produces basal melting which is responsible for the surge behavior of the outlet glaciers in most GIS (Straneo et al. 2010). On the contrary, the weight of the ice sheet deforms the Earth crust below the ice sheet leading to long term isostatic response of the bedrock to changes in the ice volume (e.g. Huybrechts 2002; Mitrovica and Milne 2003; Bassett et al. 2005). This directly impacts on the surface climate by changing the topography and thus temperature and precipitation (e.g. Peltier 1998).

The interactions between Greenland ice sheet and ocean occur mainly from the release of freshwater from the melting of ice. This freshwater input from Greenland can also impact on the regional oceanic circulation, and, consequently on the climate system. Many studies focus on the response of the ocean circulation and the climate system to a increase of freshwater coming from Greenland ice sheet (e.g. Rahmstorf et al. 2005; Stouffer et al. 2006; Driesschaert et al. 2007; Stammer et al. 2011; Swingedouw et al. 2013). Usually, these experiments are idealized and account for a large release of freshwater from Greenland (from 0.1 to 1 Sv per year, where 1 $Sv = 10^6\ m^3\ s^{-1}$). Furthermore, the freshwater input is considered either equally distributed along the Greenland coasts (e.g. Driesschaert et al. 2007; Swingedouw et al. 2013; Agarwal et al. 2015) or following a spatial distribution close to the observed one (e.g. Stammer et al. 2011). This category of experiments is known as hosing experiments. The experiments by Rahmstorf et al. (2005) show that enough freshwater input from Greenland (range from 0.1 Sv to 0.5 Sv) can lead to an interruption of the deep water formation in the North Atlantic. Stammer et al. (2011) analyze the response of ocean sea surface height to the freshwater input at global scale. Their analysis exhibits an initial regional response after about 10 years, but the impact of the freshwater input reaches a global scale after 45 years. Furthermore, the use of a coupled ocean-atmosphere model leads to a faster influence with respect to the only ocean simulations, since the coupled model keeps into account possible teleconnections driven by the atmosphere circulation. Finally, the more recent work by Agarwal et al. (2015) evaluates the ocean response to the simulated freshwater fluxes from the GIS during the 21st century. The freshwater fluxes from the GIS lead to an increase of about 1 $cm\,SLE$ on mean global sea level change during the 21st century. However, most of the signal produced by accounting for the GIS simulated freshwater fluxes is below the decadal variability described by a control run.

On the other hand, the ocean circulation impacts on the evolution of ice shelf and outlet glaciers. In fact, the acceleration of melting of many Greenland outlet glaciers is

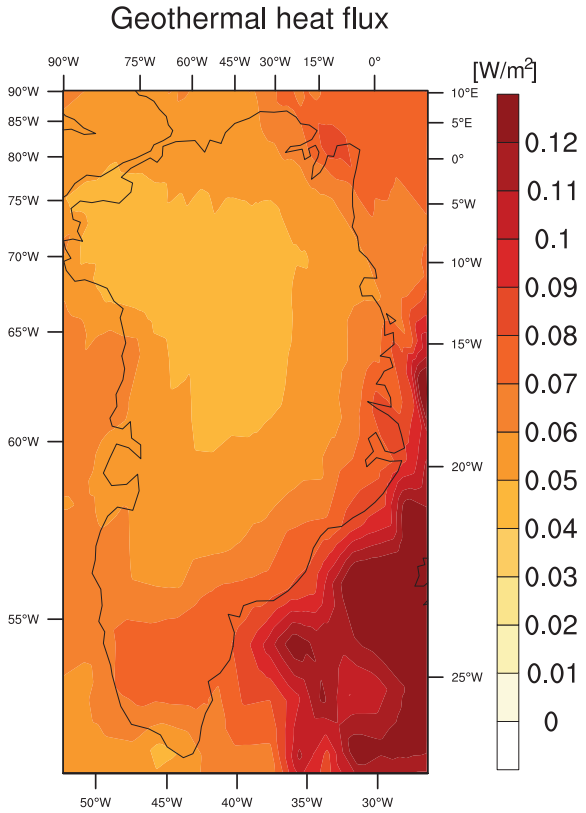

Figure 1.9: Geothermal heat flux in the Greenland region by Shapiro and Ritzwoller (2004). Value are in W/m^2.

triggered by a warming of the ocean water (e.g. Holland et al. 2008; Straneo et al. 2010), which lead to an increase of the melting at the submerged face of the ice shelf or outlet glacier (e.g. Rignot et al. 2010; Motyka et al. 2011). For example, Motyka et al. (2011) found a strong submarine melt fluxes that varies from 9.1±1.0 to 16.8±1.3 m/day during the late summer 2012 at LeConte Glacier, Alaska. Rignot et al. (2010) found submarine melt fluxes of about 0.7±0.2 m/day for the Eqip Sermia, 2.6±0.5 m/day for the Kangilerngata Sermia and 3.9±0.8 m/day for the Sermeq Kujatdleq and Avangnardleqin glaciers in central West Greenland during summer 2008.

Furthermore, the Greenland ice sheet impact on atmospheric and oceanic circulations through its orography. In fact, an idealized experiment developed with the removal of the Greenland ice sheet impacts on the regional atmospheric circulation as well as on the oceanic circulation leading to a weakening of the Atlantic Meridional Overturning Circulation by about 12%, also without accounting for the freshwater input from the Greenland ice sheet melt (Davini et al. 2015).

1.3 Greenland ice sheet

1.3.1 Past history

The past evolution of the Greenland ice sheet is studied by means of proxy data such as marine records and ice core.

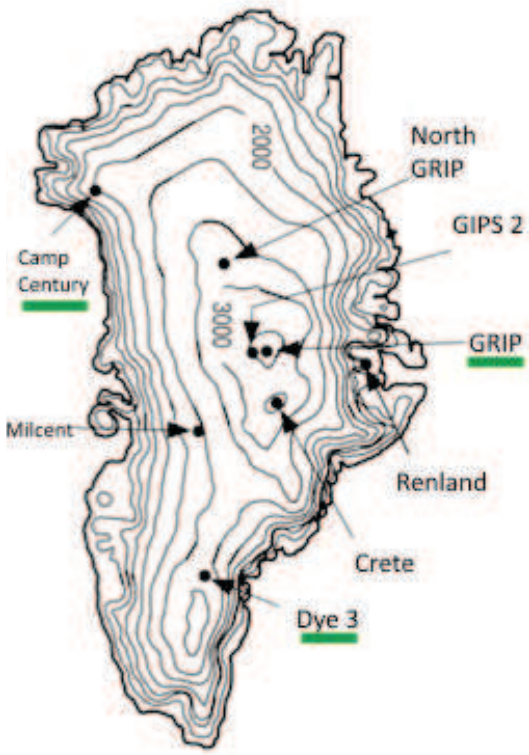

Figure 1.10: Greenland ice core drilling sites. Figure after Rapp (2012).

Past marine records suggest that Greenland glacial inception started at the end of the Pliocene period towards 3.3 Myr BP (Jansen et al. 2000). In that period the climate was about 2 $^{\circ}C$ warmer than during pre-industrial and atmospheric CO_2 concentration slightly higher than today (Pagani et al. 2010). Many mechanisms have been indicated as possible sources of the Greenland ice sheet inception: (1) decrease in atmospheric CO_2 in late Pliocene (e.g. Lunt et al. 2008), (2) closure of the Panama seaway (e.g. Haug and Tiedemann 1998), (3) termination of permanent El Niño state (e.g. Wara et al. 2005) and (4) tectonic uplift (e.g. Ruddiman and Kutzbach 1989). However, the modeling study by Lunt et al. (2008) point at the decrease in atmospheric CO_2 in late Pliocene as the main controlling mechanism on the Greenland glaciation.

Over the past three million years, GIS is believed to have increased and decreased following the glacial and interglacial periods found in the marine sediment data. For example, during the last 500 kyrs glacial/interglacial cycles with period of about 100 kyrs are found in many marine sediment data (e.g. Rohling et al. 1998; Rabineau et al. 2006).

The Greenland ice core data, instead, give information only on the last glacial cycle (e.g. Lambeck and Chappell 2001; Bonelli et al. 2009; Quiquet et al. 2013b), since ice core data older than the last interglacial as been found only at the base of the DYE 3 core site in South Greenland (Figure 1.10, North Greenland Ice Core Project members 2004; Alley et al. 2010). The ice core data give many information on the last glacial cycle climate, such as temperature variations, which are retrieved from the changes in $\delta^{18}O$, or information on the ice sheet temperature structure. For example, these variable, along with many other, have been retrieved from the GRIP ice core data (Figure 1.11, Dansgaard et al. 1993; Johnsen et al. 1997, 1995).

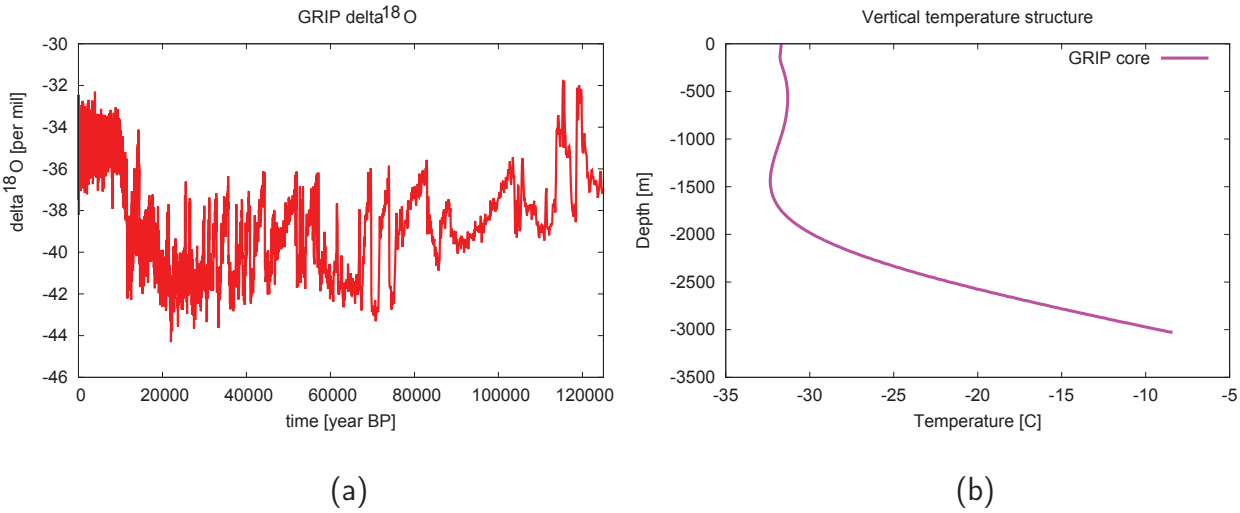

Figure 1.11: (a) $\delta^{18}O$ series retrieved from the GRIP ice core (Dansgaard et al. 1993; Johnsen et al. 1997). (b) Vertical temperature structure measured at the GRIP ice core site (Johnsen et al. 1995).

The ice core data exhibit that throughout the last glacial period the climate was very unstable and 25 rapid climate changes events occurred in that period. These events are named "Dansgaard-Oeschger events" and are characterized by increase in temperature up to 15 $°C$ and sea level increase up to 20 m (e.g. Siddall et al. 2003; Steffensen et al. 2008). These rapid changes are believed to have been caused by large release of freshwater into ocean from the Laurentide ice sheet over North America, which impacted on the North Atlantic ocean circulation (e.g. Flückiger et al. 2006). Consequently, these rapid events can be considered as analogue for possible future release of freshwater from the GIS. For this reason, much effort have been done in order to understand the GIS answer to rapid climate changes.

Similarly, the last interglacial period, the Eemian (Marine Isotope Stage 5e, MIS5e), is of particular interest for future evolution of the GIS. In fact, the Eeemian is considered as an analogue for the future GIS conditions, since in that period the air temperature is believed to have been up to 5 $°C$ warmer than during the pre-industrial condition (e.g. North Greenland Ice Core Project members 2004). Many model reconstruction of the GIS have been developed (e.g. Otto-Bliesner et al. 2006; Cuffey and Marshall 2000; Robinson et al. 2011; Born and Nisancioglu 2012; Quiquet et al. 2013b) showing a melting contribution from the GIS ranging from 2.7 m to 5.5 m. The GIS is simulated to reduce along its marginal areas, especially along the northern margins (e.g. Robinson et al.

2011; Born and Nisancioglu 2012; Quiquet et al. 2013b). Note that evidences about the extent and volume of the Greenland ice sheet during the Eemian period are still relatively limited.

Finally, many studies and models have been developed in order to evaluate the global ice volume during the last glacial maximum (21 kyrs BP, e.g. Huybrechts 2002; Tushingham and Peltier 1991; Peltier 2004; Argus et al. 2014; Peltier et al. 2015). For example, the ICE6G model by Argus et al. (2014) and Peltier et al. (2015) uses information from proxy data from paleo beaches, isostasy model, atmosphere model to reconstruct the distribution of ice over land at the last glacial maximum. The Greenland ice sheet is simulated to release into ocean about 2.5 $m\,SLE$ during the last 21 kyrs.

1.3.2 Current ice evolution

The present-day condition of the Greenland ice sheet are largely studied by means of both observations (e.g. Oerlemans and Vugts 1993; Bamber 2001; Hanna et al. 2005; Joughin et al. 2010; Rignot et al. 2011; Sasgen et al. 2012; Bamber et al. 2013; Velicogna et al. 2014) and models (e.g. Fettweis 2007; Ettema et al. 2009; Bamber et al. 2012; Franco et al. 2012; Quiquet et al. 2012; Rae et al. 2012; Fettweis et al. 2013; Vernon et al. 2013; Edwards et al. 2014).

First of all, the work by Bamber et al. (2013) gives the Greenland bedrock and surface topographies (Figure 1.12). These information are fundamental in the ice sheet models simulations.

Most of the community efforts aim at evaluating the present-day ice sheet mass balance conditions. The observed mass balance values are retrieved from satellite data since 1992 (launch of Gravity Recovery and Climate Experiment, GRACE), and show an acceleration in mass loss from 0.09 $mm\,SLE/yr$ over 1992–2001 to 0.59 $mm\,SLE/yr$ over 2002–2011 (Church et al. 2013; Vaughan et al. 2013). More specifically, the observed mass loss ranges between 101 $\pm$ 16 Gt/yr for the period 2003–2005 (gravimetry measurements, GRACE, Luthcke et al. 2006) and 171 $\pm$ 4 Gt/yr for the period 2003–2007 (altimetry measurements, Ice Cloud and land Elevation Satellite, ICESat, Zwally et al. 2011). Furthermore, the Greenland mass loss has increased during the last years from about 166 Gt/yr over the period 2000–2008 to about 273 Gt/yr over the period 2006–2008 (van den Broeke et al. 2009). The mass loss acceleration during the first decade of the 21st century is estimated around -17 Gt/yr^2 (e.g. Rignot et al. 2011; Svendsen et al. 2013). However, more recent data show a mass loss from Greenland up to 280 $\pm$ 58 Gt/yr over the period 2003–2013, characterized by an acceleration of about 25.4 $\pm$ 1.2 Gt/yr^2 (Velicogna et al. 2014). On regional scale, the southeast and northwest regions of Greenland generate about the 70% of the total Greenland mass loss, while the southwest region accounts for about 54% of the total acceleration in Greenland mass loss (Velicogna et al. 2014).

Motivated by the need to understand sea-level changes and the economical impact on coastal areas, and to predict the long-term impact on the climate system, the changes in Greenland surface mass balance have been studied also by means of numerical models. Some studies use regional atmospheric climate models (e.g. Box et al. 2006; Fettweis 2007; Ettema et al. 2009; Rae et al. 2012; Fettweis et al. 2013) to simulate surface mass balance changes by means of snowpack energy balance models. For the 20th century the studies reported above simulate a gain in surface mass balance for the present-day ranging between 170 Gt/yr (Box et al. 2006) and 469 Gt/yr (Ettema et al. 2009). Note that

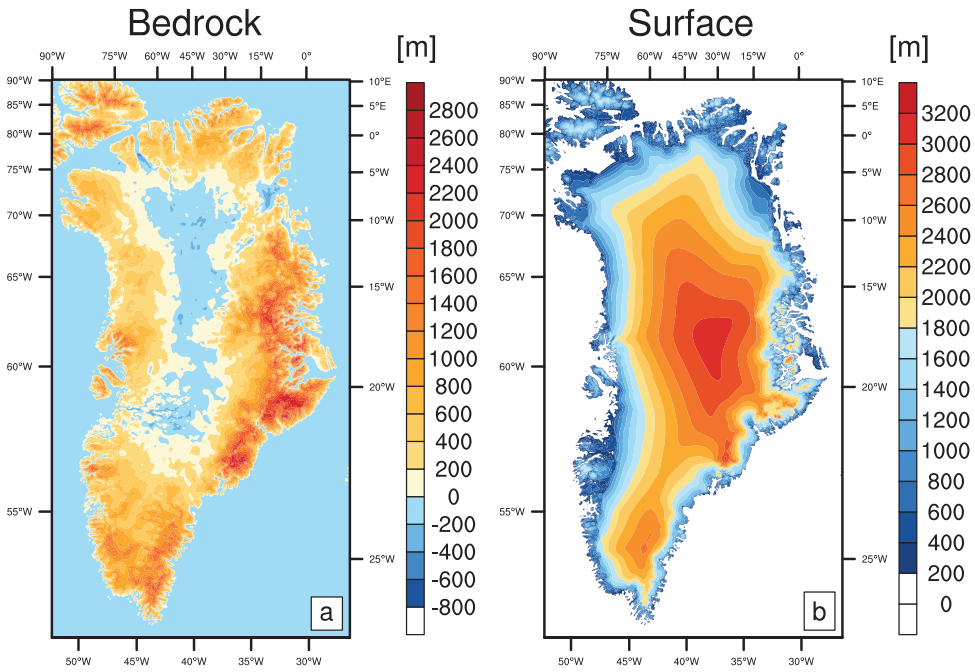

Figure 1.12: (a) Greenland bedrock topography and (b) Greenland surface topography. Value from Bamber et al. (2013)

this wide range in surface mass balance estimates may result in the physical differences of the different regional climate models (Rae et al. 2012) and by the computation of the averages over different periods. Thus, the lower bound of 170 Gt/yr is obtained over the period 1988–2004 with the regional climate model Polar MM5 (Box et al. 2006), while the upper bound of 469 Gt/yr corresponds to the period 1958–2007 with the regional climate model RACMO2/GR (Ettema et al. 2009). Vizcaíno et al. (2013) simulate the GIS surface mass balance by means of the CESM (Community Earth System Model)-Glimmer CISM (Glimmer Community Ice Sheet Model) coupled model obtaining SMB values of about 359±120 Gt/yr over the period 1960–2005, which is in the range of the regional climate model values.

Aside from the response to surface climate changes, the Greenland ice sheet surface mass balance evolution is affected by its own dynamics that induces elevation changes. This process is not accounted for in regional climate models. Previous works have shown the importance of changes in ice dynamics and surface topography on the Greenland surface mass balance estimates (e.g. Gillet-Chaulet et al. 2012; Church et al. 2013; Fettweis et al. 2013; Goelzer et al. 2013; Edwards et al. 2014; Vizcaíno et al. 2015). For example, Edwards et al. (2014) found an increase of about 5% on their runoff values when ice-elevation feedback is accounted for. Similarly, Vizcaíno et al. (2015) found an impact of the elevation feedback in the range 8% to 11% during the 21st century. For this reason, some surface mass balance estimates are calculated by means of thermo-dynamical ice-sheet models (e.g. Greve et al. 2011; Gillet-Chaulet et al. 2012; Helsen et al. 2012; Seddik et al. 2012; Quiquet et al. 2013a; Edwards et al. 2014). In most of these studies, the

ISM is not coupled to climate model. Some discrepancies in modelled surface mass balance arise from model resolution (Franco et al. 2012), surface mass balance formulations (Vernon et al. 2013), and ice-sheet models initialization methods (Yan et al. 2013).

Many literature works present also estimates of the present-day amount of runoff flowing out of Greenland (e.g. Mote 2003; Hanna et al. 2005; Box et al. 2006; Fettweis 2007; Large and Yeager 2008; Ettema et al. 2009; Bamber et al. 2012; Mernild and Liston 2012; Rae et al. 2012), with simulated values in the range between 0.69 $mm\,SLE\ yr^{-1}$ (Ettema et al. 2009) and 0.95 $mm\,SLE\ yr^{-1}$ (Box et al. 2006). However, the freshwater distribution along the Greenland coasts is analyzed only in few works (e.g. Large and Yeager 2008; Bamber et al. 2012), even if the freshwater fluxes from Greenland into the North Atlantic can affect the ocean circulation and in particular the strength of the Atlantic meridional overturning circulation (e.g. Swingedouw et al. 2013; Bamber et al. 2012). Moreover, only few estimates are obtained from observations or reanalysis (Mote 2003; Hanna et al. 2005). In fact, the few available runoff observations are recovered only in few localized regions, such as in the Zackenberg basin (Mernild et al. 2008), or in the Kangerlussuaq region (West Greenland, Hasholt et al. 2012).

Finally, the present-day dynamical discharge from the outlet glaciers along the Greenland coasts is obtained from observations (e.g. Howat et al. 2007; Stearns and Hamilton 2007; Rignot et al. 2011; Shepherd et al. 2012; Khan et al. 2014) or from specific outlet glacier models (e.g. Nick et al. 2010; Bamber et al. 2012; Goelzer et al. 2013; Nick et al. 2013; Calov et al. 2015). For example, Howat et al. (2007) observed a loss of about 47 Gt over the period 2000–2006 for the Kangerdlugssuaq glacier, thanks to an extensive digital elevation model (DEM) coverage at the lower basin of the glacier. Stearns and Hamilton (2007) observed that the coastal portions of Kangerdlugssuaq and Helheim glaciers in the southeast of Greenland lost a volume of about 51±8 $\mathrm{km}^3\ yr^{-1}$ due to thinning and terminus retreat over the period 2001–2006. Furthermore, Khan et al. (2014) observed a change in Greenland mass loss due to dynamical discharge in the last decades, for example the dynamical discharge in the North East Greenland Ice Stream (NEGIS) area passed from about $11.2 \pm 2.0\ Gt/yr$ over the period 2006–2009 to about $13.9 \pm 3.7\ Gt/yr$ over the period 2009–2012. The model experiments by Bamber et al. (2012) simulate a discharge of about 497±50 $km^3\ yr^{-1}$ for the entire GIS.

1.3.3 Future

The use of models in simulating Greenland ice-sheet dynamics is motivated by the ability to provide projections of its short-term and long-term future evolution. However, the surface mass balance computed from regional climate models and ice sheet models have been shown to be model-dependent (e.g. Rae et al. 2012; Bindschadler et al. 2013; Edwards et al. 2014). For this reason, some studies base their calculation on a multi-model approach. For example, Rae et al. (2012) study the uncertainties upon the Greenland ice sheet surface mass balance estimates with different regional climate models. They obtain changes in GIS surface mass balance from a gain of 59 Gt/yr to a loss of 524 Gt/yr by the end of the 21st century (2080–2099) compared to present-day (1980–1999) condition. The SeaRISE project (Sea-level Response to Ice Sheet Evolution, Bindschadler et al. 2013) bases its assessment and estimates of surface mass balance changes on a set of eight thermo-mechanical ice sheet-ice shelves models (Nowicki et al. 2013). They obtain a range of possible projected Greenland ice-sheet contribution to the mean global sea level in the next 100 years amounting to 0.9 to 6.6 $cm\,SLE$ (Bindschadler et al. 2013)

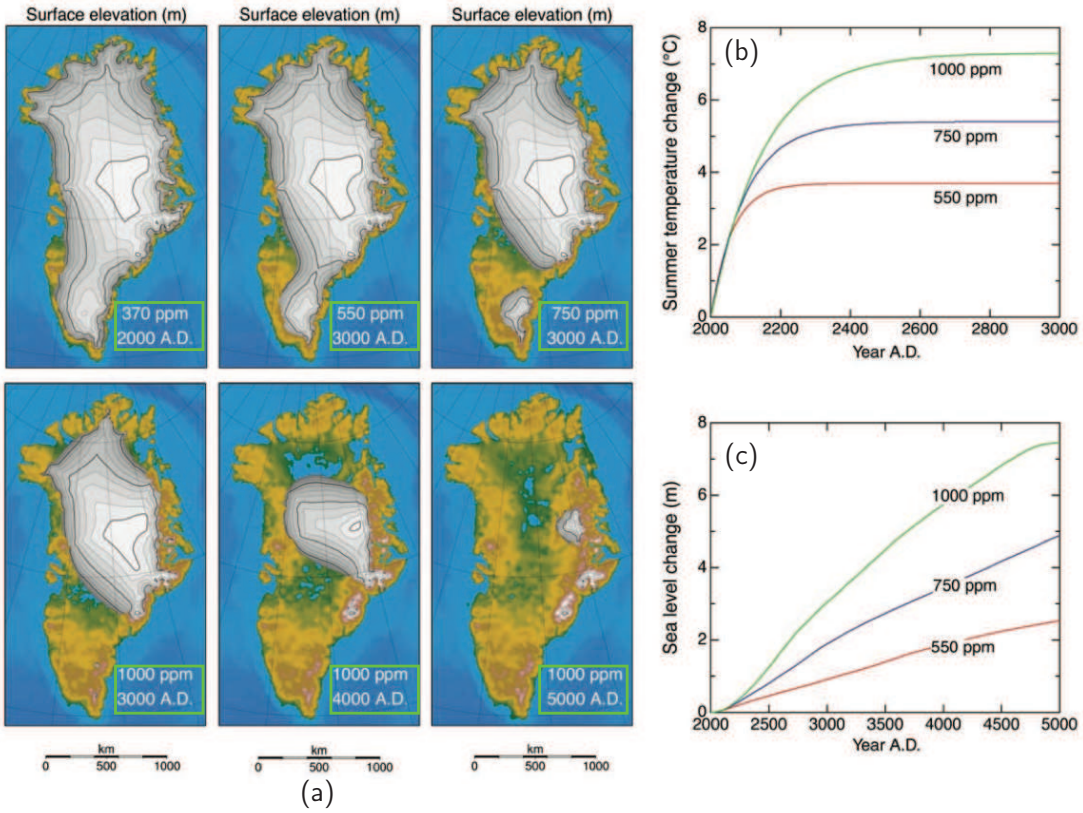

Figure 1.13: Greenland ice sheet projected evolution up to year 5000 AD under a set of three experiments. Simulated (a) surface elevation (b) summer temperature change and (c) sea level changes. Figure from Alley et al. (2005).

under the SRES A1B climate scenario (Special Report on Emissions Scenarios, SRES, Nakićenović et al. 2000). Similarly, the ICE2SEA project (Edwards et al. 2014) uses the simulations from a set of five ice sheet models of different complexity, obtaining a mean Greenland ice sheet sea level contribution spanning from 5.7 $cm\,SLE$ to 6.4 $cm\,SLE$ by the end of the 21st century under the same future scenario. The work by Vizcaíno et al. (2014) bases its estimates on the CESM-Glimmer CISM coupled model and simulates a decrease from 372±100 Gt/yr in 1980–1999 to -78±143 Gt/yr in 2080–2099 in the GIS SMB under a RCP 8.5 scenario. Note that many studies (e.g. Franco et al. 2011; Yan et al. 2014) show that the surface mass balance simulated with ice sheet models are strongly influenced by the climate used to force the ice sheet models, partially explaining the differences obtained in those projects.

The dynamical discharge from the GIS is simulated by means of outlet glacier models (e.g. Nick et al. 2010, 2013). For example, starting from the present-day mass loss ($\sim$ 87 km^3/yr) of four major marine-terminating outlet glaciers, i.e. Helheim, Kangerdlugssuaq, Petermann and Jakobshavn, Nick et al. (2013) projected the mass loss from these outlet glaciers at the end of the 21st century. Their simulations show mass loss ranging from 125 to 147.5 km^3/yr during the 21st century under a RCP 8.5 scenario.

Furthermore, the Greenland ice sheet is also expected to reach a tipping point during the next century. The threshold at which the GIS passes the tipping point is estimated to occur for an increase of about 3.1 $°C$ in mean global temperature, equivalent to a

local increase of about 4.5 $^{\circ}C$ (Gregory and Huybrechts 2006) or for a mean summer temperature increase of about 1.6 $^{\circ}C$ (Robinson et al. 2012). Moreover, a sufficiently warm climate maintained for a few thousand years can lead to an almost complete melting of the GIS, going towards a second threshold, after which the original ice volume can not be regained. Ridley et al. (2010) simulated that the original GIS volume can be regained only if the ice-sheet volume has not fallen below 80 to 90% of the initial ice-sheet volume. This limit represent the threshold of irreversibility for the GIS.

The Greenland ice sheet contribution to sea level rise has been studied also on longer time scale. The SeaRISE project gives estimates of global sea-level increase at 200 and 500 years from present-day, simulating values from 1.2 to 15.5 $cm\,SLE$ by 2200 and from 5.4 to 38.7 $cm\,SLE$ by 2500 under a A1B scenario (Bindschadler et al. 2013). Similarly, ICE2SEA project highlights a possible impact on the sea level from Greenland in the range from 16.4 to 17.6 $cm\,SLE$ by the end of the 22nd century (Edwards et al. 2014). However, some studies evaluate the GIS evolution on even longer time scales (e.g. Huybrechts and De Wolde 1999; Gregory et al. 2004; Alley et al. 2005). Alley et al. (2005) simulate the future behavior of the GIS up to year 3000 AD under a set of three experiments in which the atmospheric carbon dioxide concentration stabilizes at levels (1) 550 ppm, (2) 750 ppm and (3) 1000 ppm after a few centuries (Figure 1.13b). Under the third experiment, the Greenland ice sheet is shown to disappear within year 3000, and by year 5000 AD only some residual ice over the eastern mountains remains (Figure 1.13).

Chapter 2

Ice Sheet Models Physical Formulation

2.1 Introduction

In this chapter I provide a description of the main physical characteristics of the two three-dimensional thermo-mechanical ice sheet-ice shelves models (ISMs) used in this work: GRenoble Ice Shelf and Land Ice model (GRISLI, Ritz et al. 2001) and SImulation COde for POLythermal Ice Sheet model (SICOPOLIS, Greve 1997a,b). I further detail the methods used for the Surface Mass Balance computation (SMB) and the routing scheme implemented in both ISMs. Finally, I describe the initialization spin-up for the two ice sheet models. Note that a summary of the main variables used in this chapter is given in Appendix A.

2.2 Ice-sheet physics

2.2.1 Ice flow areas

The term ice sheet, in general, defines a mass of land ice of continental size which shape is determined by its dynamics. On Earth only two ice sheets are present nowadays: Greenland ice sheet and Antarctic ice sheet. The first one has a volume of about 2.85 10^6 km^3 covering an area of about 1.71 10^6 km^2. The Antarctic ice sheet has a volume of about 25.7 10^6 km^3 with an additional 0.58 10^6 km^3 of attached ice shelves, and covers an area of 12.4 10^6 km^2 and 1.1 10^6 km^2, respectively (Greve and Blatter 2009).

In the ice-sheet models, three different regions of ice flow are considered: ice sheet, ice stream zones and ice shelves (Figure 2.1). The ice sheet and ice stream zones are areas with grounded ice, while ice shelves are regions with floating ice. These three ice flow regions have different features:

- ice sheet, or inland ice, are areas of grounded ice where ice flow results mainly from ice deformation. Sliding, instead, can occur only in areas where the ice base is at the pressure melting point;
- ice streams are regions of fast-flowing ice. These areas are usually located in narrow valleys characterized by thick sediment layers saturated by meltwater or by low effective basal pressure which support the velocity of these regions. For example

the velocity near the front of North East Greenland Ice Stream (NEGIS) reaches values of about 250 m/yr (Joughin et al. 2010);

- ice shelves are areas of floating ice, in contrast to ice sheets and streams which are grounded, and are fed by inland ice. The line where ice begins to float is called grounding line (Figure 2.1). In Greenland, the floating ice is located in small fjords, usually not captured by ice sheet models, and are called outlet glaciers.

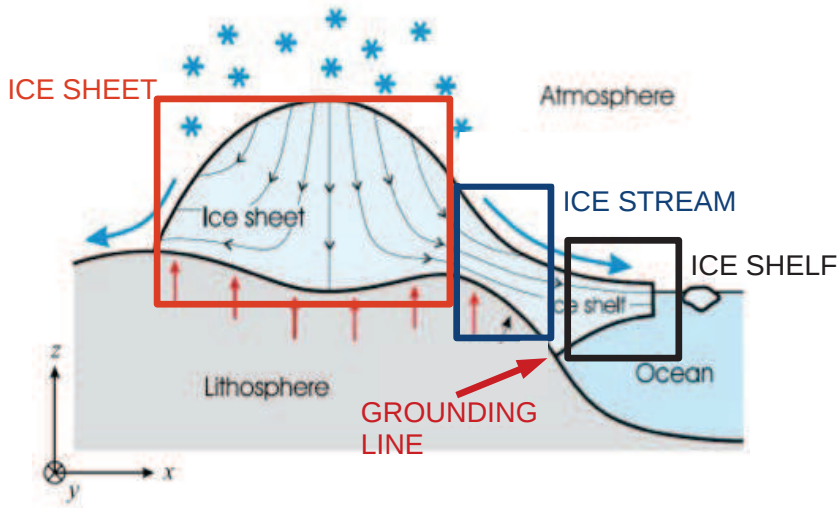

Figure 2.1: Summary of the main flow areas in an ice sheet. Figure after Greve and Blatter (2009).

2.2.2 Fundamental equations and approximations

An ice sheet is described in terms of flow and and in terms of solid deformation. The governing equations of ice sheet dynamics are based on the balance equation of mass, momentum and energy:

$$\frac{\partial \rho}{\partial t} + \nabla \cdot (\rho \mathbf{u}) = 0 \tag{2.1}$$

$$\rho \frac{d\mathbf{u}}{dt} = \nabla \cdot \sigma + \rho \mathbf{g} \tag{2.2}$$

$$\rho c \left(\frac{\partial T}{\partial t} + \mathbf{u} \cdot \nabla T \right) = \nabla (\kappa \nabla T) + Q_i \tag{2.3}$$

where ρ stands for the ice density $[Kg\ m^{-3}]$, $\mathbf{u}$ for the ice velocity vector $[m\ yr^{-1}]$, σ for the stress tensor $[Pa]$, $\mathbf{g}$ for the gravitational acceleration $[m\ yr^{-2}]$, c for the heat capacity of ice $[J\ mol^{-1}\ Kg^{-1}]$, T for the ice temperature $[^{\circ}C]$, κ for the thermal conductivity of

ice [$W\ {}^{\circ}C^{-1}\ m^{-1}$], and Q_i for the deformation heat [$W\ m^{-2}$]. With respect to a given orthonormal basis, the stress tensor σ is

$$\sigma = \begin{pmatrix} \sigma_{xx} & \sigma_{xy} & \sigma_{xz} \\ \sigma_{yx} & \sigma_{yy} & \sigma_{yz} \\ \sigma_{zx} & \sigma_{zy} & \sigma_{zz} \end{pmatrix} \tag{2.4}$$

where the diagonal elements (σ_{xx}, σ_{yy}, σ_{zz}) are referred to as normal stresses, and the six off-diagonal elements are called shear stresses. The positioning of these components is reported in Figure 2.2.

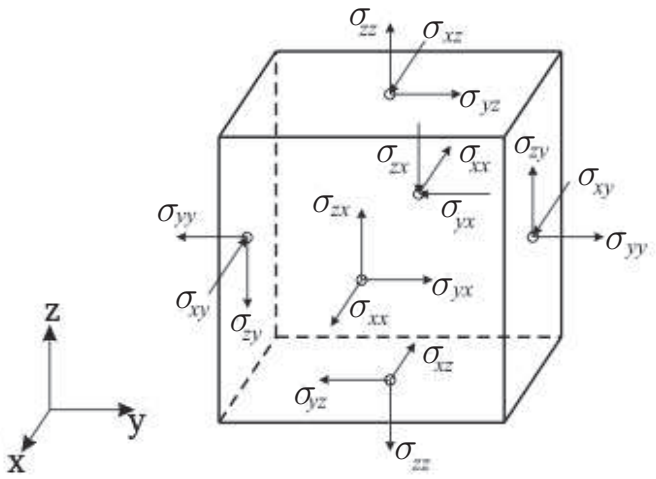

Figure 2.2: Components of the stress tensor σ. Figure after Greve and Blatter (2009).

A first approximation consists in assuming ice as an incompressible fluid with a constant density. Given this assumption, the continuity equation (Eq. 2.1) simplifies to:

$$\nabla \cdot \mathbf{u} = \frac{\partial u}{\partial x} + \frac{\partial v}{\partial y} + \frac{\partial w}{\partial z} = 0 \tag{2.5}$$

where u,v,and w are the x,y and z components of the velocity vector $\mathbf{u}$, respectively. At this point, the vertical integration of Eq. 2.5 from the base of the ice sheet B [m] to the surface elevation S [m] leads to an equation for the ice thickness, where the ice thickness H [m] is defined as the difference between the surface elevation and the base of the ice sheet (S-B):

$$\frac{\partial H}{\partial t} + \frac{\partial (H\,u)}{\partial x} + \frac{\partial (H\,v)}{\partial y} = SMB - F \tag{2.6}$$

where SMB stand for the surface mass balance [$m\ yr^{-1}$], given by the difference between accumulation and ablation (further details in section 2.3.1), and F for the melting at the base [$m\ yr^{-1}$]. The basal melting depends on the pressure melting point below the ice sheet and is generated mainly by friction, by geothermal heat flux (see Figure 1.9), and by ocean heat at the base of the ice shelves. These two terms together with the calving at the front of the ice shelves are the main source/sink of ice for an ice sheet. Equation 2.6, then, represents the time evolution of the ice.

Table 2.1: Typical values for ice sheet geometry and field velocities in an ice sheet. Values taken from Greve and Blatter (2009).

Term	**Description**	**Typical value**
L	Horizontal extent	1000 km
H	Vertical extent	1 km
U	Horizontal velocity	100 $m\ yr^{-1}$
W	Vertical velocity	0.1 $m\ yr^{-1}$
P = ρ g H	Pressure	10 $M\,Pa$
t = L/U = H/W	Time-scale	10^4 yr

The equations of motion are derived from Eq. 2.2. A scale analysis performed using typical values for ice sheet geometry and field velocities (Table 2.1), allows us to assume that the acceleration term in the equation of motion is negligible (i.e Greve and Blatter 2009). Therefore, the left-hand-side of Eq. 2.2 is set to zero (Stokes assumption), and thus can be written as:

$$\begin{aligned} \frac{\partial \sigma_{xx}}{\partial x} + \frac{\partial \sigma_{xy}}{\partial y} + \frac{\partial \sigma_{xz}}{\partial z} &= 0 \\ \frac{\partial \sigma_{yx}}{\partial x} + \frac{\partial \sigma_{yy}}{\partial y} + \frac{\partial \sigma_{yz}}{\partial z} &= 0 \\ \frac{\partial \sigma_{zx}}{\partial x} + \frac{\partial \sigma_{zy}}{\partial y} + \frac{\partial \sigma_{zz}}{\partial z} &= \rho g \end{aligned} \tag{2.7}$$

This formulation is also known as Stokes equation.

On the solid deformation point of view, it is convenient to split the stress tensor into a deviatoric part τ $[Pa]$ and an isotropic pressure p $[Pa]$:

$$\begin{aligned} \sigma_{ij} &= \tau_{ij} - \frac{1}{3}(\sigma_{xx} + \sigma_{yy} + \sigma_{zz})\delta_{ij} \\ &= \tau_{ij} - p \end{aligned} \tag{2.8}$$

In fact, the constitutive equation for polycristalline ice links the deviatoric stresses to the strain rate (Paterson 1994):

$$\begin{aligned} \tau = 2\,\eta\,\dot{\epsilon} &= 2\eta \begin{pmatrix} \dot{\epsilon}_{xx} & \dot{\epsilon}_{xy} & \dot{\epsilon}_{xz} \\ \dot{\epsilon}_{yx} & \dot{\epsilon}_{yy} & \dot{\epsilon}_{yz} \\ \dot{\epsilon}_{zx} & \dot{\epsilon}_{zy} & \dot{\epsilon}_{zz} \end{pmatrix} \\ &= 2\eta \begin{pmatrix} \frac{\partial u}{\partial x} & \frac{1}{2}\left(\frac{\partial u}{\partial y} + \frac{\partial v}{\partial x}\right) & \frac{1}{2}\left(\frac{\partial u}{\partial z} + \frac{\partial w}{\partial x}\right) \\ \frac{1}{2}\left(\frac{\partial u}{\partial y} + \frac{\partial v}{\partial x}\right) & \frac{\partial v}{\partial y} & \frac{1}{2}\left(\frac{\partial v}{\partial z} + \frac{\partial w}{\partial y}\right) \\ \frac{1}{2}\left(\frac{\partial u}{\partial z} + \frac{\partial w}{\partial x}\right) & \frac{1}{2}\left(\frac{\partial v}{\partial z} + \frac{\partial w}{\partial y}\right) & \frac{\partial w}{\partial z} \end{pmatrix} \end{aligned} \tag{2.9}$$

where η is the viscosity $[Pa\ yr^{-1}]$.

At this point, there is a link missing between the Stokes equations and the solid mechanics. These two components can be coupled using a law linking ice temperature

and ice deformations, which has been developed by Glen (1955). The non-linear Glen-type flow law gives (i.e. Greve and Blatter 2009):

$$\dot{\epsilon} = A(T^*)\,\tau_*^{n-1}\,\tau \tag{2.10}$$

where n is the flow law exponent (usually set equal to three), τ_* is the effective shear stress:

$$\tau_* = \sqrt{\frac{1}{2} tr(\tau)^2} \tag{2.11}$$

The flow law coefficient $A(T^*)$ follow an Arrhenius relationship:

$$A(T^*) = A_0\, e^{\frac{E_a}{R}\left(\frac{1}{T^*}-\frac{1}{T}\right)} \tag{2.12}$$

where A_0 is a coefficient $[s^{-1}\ Pa^{-3}]$, E_a is the activation energy $[kJ\ mol^{-1}]$, $R = 8.3145$ $J\ mol^{-1}\ {}^{\circ}C^{-1}$ is the universal gas constant, and T^* is the absolute temperature corrected for the dependence on the melting point on pressure:

$$T^* = T\ + \beta p = T + \beta\rho g(S - z) \tag{2.13}$$

where the Clausius-Clapeyron constant is set equal to: $\beta = 9.76\,10^{-8}\,K\,Pa^{-1}$.

Now combining together Eq. 2.7 and Eq. 2.9, the equation of motion becomes:

$$\begin{aligned}
&\frac{\partial}{\partial x}\left(2\eta\frac{\partial u}{\partial x}\right) + \frac{\partial}{\partial y}\left(\eta\frac{\partial u}{\partial y} + \eta\frac{\partial v}{\partial x}\right) + \frac{\partial}{\partial z}\left(\eta\frac{\partial u}{\partial z} + \eta\frac{\partial w}{\partial x}\right) - \frac{\partial p}{\partial x} = 0 \\
&\frac{\partial}{\partial x}\left(\eta\frac{\partial u}{\partial y} + \eta\frac{\partial v}{\partial x}\right) + \frac{\partial}{\partial y}\left(2\eta\frac{\partial v}{\partial y}\right) + \frac{\partial}{\partial z}\left(\eta\frac{\partial v}{\partial z} + \eta\frac{\partial w}{\partial y}\right) - \frac{\partial p}{\partial y} = 0 \\
&\frac{\partial}{\partial x}\left(\eta\frac{\partial u}{\partial z} + \eta\frac{\partial w}{\partial x}\right) + \frac{\partial}{\partial y}\left(\eta\frac{\partial v}{\partial z} + \eta\frac{\partial w}{\partial y}\right) + \frac{\partial}{\partial z}\left(2\eta\frac{\partial w}{\partial z}\right) - \frac{\partial p}{\partial z} = \rho g
\end{aligned} \tag{2.14}$$

An ice sheet model that resolves this complete set of equation is called Full Stokes model. Further details could be find in literature (e.g. Greve and Blatter 2009; Thoma et al. 2014).

An ice sheet is characterized by different flow regimes. For this reason, different approximations can be applied to the ice motion in each area (Figure 2.3).

Hydrostatic approximation

This approximation is derived from scale analysis and applies on the vertical direction (third equation in Eq. 2.7). The shear stresses σ_{xz} and σ_{yz} are small compared to the vertical normal stress σ_{zz}, which is approximately equal to the pressure p. For this reason, the vertical momentum balance reduce to a balance between the vertical gradient σ_{zz} and the gravity force:

$$\frac{\partial \sigma_{zz}}{\partial z} = \rho g \tag{2.15}$$

This approximation is also known as hydrostatic approximation, and its integration along the vertical direction leads to the hydrostatic pressure equation:

$$p = \rho g(H - z) \tag{2.16}$$

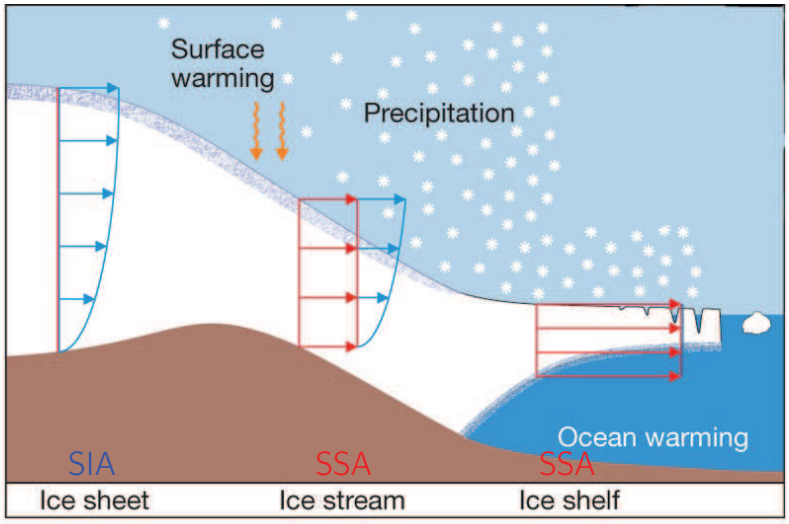

Figure 2.3: Summary of the main flow areas and approximations used in each region. Figure after Winkelmann et al. (2012).

Shallow Ice Approximation

The shallow ice approximation (SIA, Hutter 1983) is a reasonable simplification for large bodies of ice, since it is based on the assumption that the horizontal length scale is much larger than the ice thickness. On this assumption, the flow regime is mainly characterized by bed-parallel shear, and, thus, the relevant component of the deviatoric stress tensor are the shear stresses along the horizontal plane (τ_{xz} and τ_{yz}), which are supported by the basal drag. Note that this approximation applies only to the grounded ice. Given this assumption and the hydrostatic approximation, the equation of motion (Eq. 2.14) simplifies to:

$$\begin{aligned} \frac{\partial}{\partial z}\left(\eta\frac{\partial u}{\partial z}\right) - \frac{\partial p}{\partial x} &= 0 \\ \frac{\partial}{\partial z}\left(\eta\frac{\partial v}{\partial z}\right) - \frac{\partial p}{\partial y} &= 0 \\ -\frac{\partial p}{\partial z} &= \rho g \end{aligned} \tag{2.17}$$

In this specific case the effective shear stress (Eq. 2.11) reduces to:

$$\tau_* = \sqrt{\tau_{xz}^2 + \tau_{yz}^2} \tag{2.18}$$

Combining Eq. 2.18 and Eq. 2.17 with the flow law (Eqs. 2.8 - 2.13) and integrating over the vertical, an equation for the horizontal velocity $\mathbf{u}$ ($\mathbf{u}$=(u,v)) is obtained:

$$\mathbf{u} = -(\rho g)^n (\nabla S \cdot \nabla S)^{\frac{n-1}{2}} \nabla S \, E_f \int_B^z A(T')(S - z')^n dz' + \mathbf{u}_b \tag{2.19}$$

where E_f is the flow enhancement factor, usually set to 3 $J\ mol^{-1}$, S the surface and $\mathbf{u}_b$ is the basal velocity. The computation for the basal velocity and, in general, the basal

processes are described in the next section (Section 2.2.4). More detailed description of the SIA could be found in literature (e.g. Hutter 1983; Ritz et al. 2001; Greve and Blatter 2009; Rutt et al. 2009; Thoma et al. 2014)

Shallow Shelf Approximation

Ice streams and ice shelves are characterized by a fast flow and low surface slope. These regions, then, are treated separately in the model by applying a different approximation: the shallow shelf approximation (SSA MacAyeal 1989). The SSA, similarly to SIA, assumes that the horizontal length scale is larger than the vertical length scale. However, in the SSA the horizontal velocity is independent from depth ($\frac{\partial u}{\partial z} = \frac{\partial v}{\partial z} = 0$). Given these assumption, Eq. 2.7 simplifies to:

$$\begin{aligned} \frac{\partial \tau_{xx}}{\partial x} + \frac{\partial \tau_{xy}}{\partial y} + \frac{\partial \tau_{xz}}{\partial z} &= \frac{\partial p}{\partial x} \\ \frac{\partial \tau_{yx}}{\partial x} + \frac{\partial \tau_{yy}}{\partial y} + \frac{\partial \tau_{yz}}{\partial z} &= \frac{\partial p}{\partial y} \\ \frac{\partial \tau_{zz}}{\partial z} &= \frac{\partial p}{\partial z} + \rho g \end{aligned} \tag{2.20}$$

After linking the deviatoric stresses to the strain rates (Eq. 2.9) and integrating trough the ice from the base B to the surface S, the equation of motion turns into a set of elliptic equation for the vertically averaged horizontal components of the ice velocity (U,V):

$$\begin{aligned} \frac{\partial}{\partial x}\left[2H\bar{\eta}\left(2\frac{\partial U}{\partial x} + \frac{\partial V}{\partial y}\right)\right] + \frac{\partial}{\partial y}\left[H\bar{\eta}\left(\frac{\partial U}{\partial y} + \frac{\partial V}{\partial x}\right)\right] - \tau_{bx} &= \rho g H \frac{\partial S}{\partial x} \\ \frac{\partial}{\partial y}\left[2H\bar{\eta}\left(2\frac{\partial V}{\partial y} + \frac{\partial U}{\partial x}\right)\right] + \frac{\partial}{\partial x}\left[H\bar{\eta}\left(\frac{\partial V}{\partial x} + \frac{\partial U}{\partial y}\right)\right] - \tau_{by} &= \rho g H \frac{\partial S}{\partial y} \end{aligned} \tag{2.21}$$

where $\bar{\eta}$ is the ice viscosity averaged over the ice thickness, and $\tau_{bx/by}$ are the basal shear stresses or basal drag, which are set equal to zero in case of ice shelves (since ice shelves are floating on the water without any resistance). In case of ice streams, the basal drag is defined following the methods presented in Section 2.2.4. More detailed description of the SSA can be found in literature (e.g. MacAyeal 1989; Ritz et al. 2001; Greve and Blatter 2009; Pattyn 2010; Thoma et al. 2014).

2.2.3 Temperature calculation

The ice temperature is required to calculate the flow law coefficient ($A(T^*)$ in Eq. 2.12), the basal melting (F) and the basal velocity $\mathbf{u}_b$, since sliding occurs only in areas where the basal ice temperature is at the melting point.

The thermal evolution of the ice sheet is described by the Eq. 2.3, whose terms can be divided into an advective, a diffusive and a source term:

$$\rho c \left(\frac{\partial T}{\partial t} + \underbrace{\mathbf{u} \cdot \nabla T}_{advection}\right) = \underbrace{\nabla(\kappa \nabla T)}_{diffusion} + \underbrace{Q_i}_{internal\ sources} \tag{2.22}$$

This equation can be simplified by neglecting horizontal diffusion and assuming that the internal heat source results mainly from ice deformation (Paterson 1994). Thus, Eq.

2.22 can be expressed as

$$\frac{\partial T}{\partial t} = \frac{k}{\rho c}\frac{\partial^2 T}{\partial z^2} - u\frac{\partial T}{\partial x} - v\frac{\partial T}{\partial y} - w\frac{\partial T}{\partial z} + \frac{4\eta\dot{\epsilon}^2}{\rho c} \tag{2.23}$$

where the internal sources term, assuming ice deformation as source of internal heat and neglecting the horizontal diffusion, becomes $Q_i = 4\eta\dot{\epsilon}^2$, where $\dot{\epsilon}$ is the strain rate. To solve this equation, boundary conditions are required. The mean air surface temperature is applied at the upper boundary. At the lower boundary, the ice is heated by the geothermal heat flux (G) and by the sliding friction

$$\left.\frac{\partial T}{\partial z}\right|_{z=B} = -\frac{G + \tau_b \cdot \mathbf{u}_b}{k} \tag{2.24}$$

where the basal drag and the basal velocity are computed as described in Section 2.2.4.

Finally, the ice temperatures are held constant if they reach the pressure melting point (T_{pmp})

$$T = T_{pmp} \quad \text{if} \quad T \geq T_{pmp} \tag{2.25}$$

and the excess heat is used for basal melting (F):

$$F = \frac{k}{\rho L}\left(\frac{\partial T^*}{\partial z} - \frac{\partial T}{\partial z}\right) \tag{2.26}$$

where L is the specific latent heat of fusion and T^* is the absolute temperature corrected for the dependence of the melting point on pressure (Eq. 2.13).

The temperature vertical structure measured in the Greenland Ice core Project (GRIP) location is reported in Figure 2.4, as example of the internal vertical temperature structure of the Greenland ice sheet.

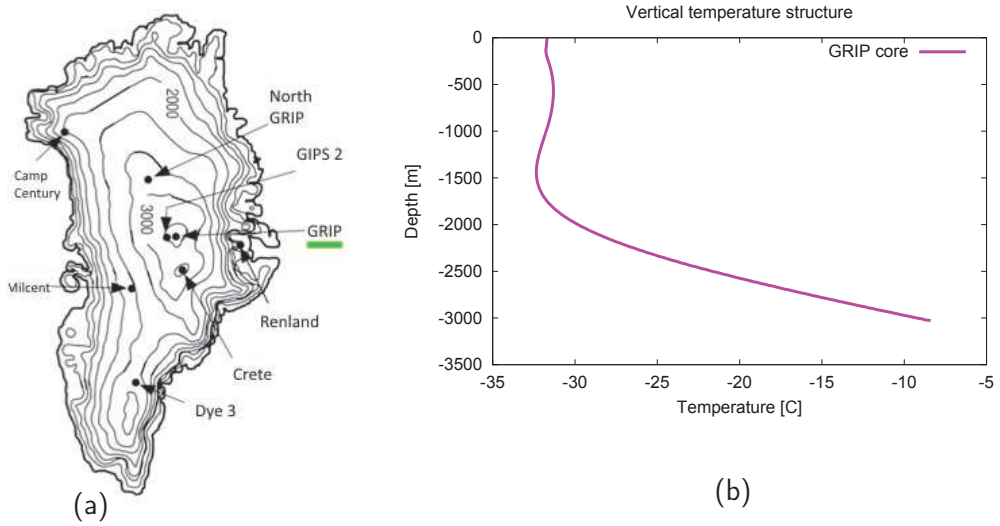

Figure 2.4: (a) Location of the main ice core drilling sites in Greenland (Figure after Rapp (2012)). (b) Vertical temperature structure measured in the GRIP ice core (data from Johnsen et al. 1995).

2.2.4 Basal processes

Basal velocity

The basal velocity is one of the boundary conditions required to solve the equation of motion under the SIA (Eq. 2.19). The horizontal velocity at the base can be solved by different methods:

- no-slip condition;
- basal velocity proportional to basal shear stress;
- Weertman-type sliding law (Weertman 1957).

The basal velocity $\mathbf{u}_b$ can be set equal to zero or proportional to the basal shear stress (Rutt et al. 2009):

$$\mathbf{u}_b = -B_{sl}\,\rho\,g\,H\,\nabla S \tag{2.27}$$

where B_{sl} is the sliding parameter $[m\ s^{-1}\ Pa^{-1}]$ which can be specified in many form: (1) $B_{sl} = 0$ for a no sliding condition; (2) constant sliding parameter, which may vary spatially.

The Weertman-type sliding law links the basal velocity $\mathbf{u}_b$ to the basal shear stress and to the effective pressure N (Weertman 1957):

$$\mathbf{u}_b = k_{sl}(\rho g H)^3(\nabla S \cdot \nabla S)^{1/2}\frac{\nabla S}{N} \tag{2.28}$$

where k_{sl} is an adjustable parameter, set to $0.5\ 10^{-8}\ m\ yr^{-1}\ Pa^{-2}$ in GRISLI (Ritz et al. 2001), and the effective pressure is given by:

$$N = \rho g H - p_w \tag{2.29}$$

where p_w is the sub-glacial water pressure, set to zero or equal to:

$$p_w = \rho_w g B \tag{2.30}$$

where ρ_w is the density of seawater $[kg\ m^{-3}]$.

The same Weertman-type sliding law can be modified following the work by Hindmarsh and Le Meur (2001). This method is applied in SICOPOLIS (Greve 2005), and the basal velocity is given by:

$$\mathbf{u}_b(T_b^*) = -C_b\,e^{\frac{T_b^*}{\gamma}}\,\frac{\tau_b^p}{N_b^q} \tag{2.31}$$

where p and q are sliding exponents (usually set to 3 and 2, respectively), C_b is the sliding coefficient $[m\ yr^{-1}\ Pa^{-1}]$, γ is the sub-melt-sliding parameter $[^\circ C]$, τ_b is the basal drag, N_b is the basal normal stress $[Pa]$, and T_b^* is the basal temperature relative to pressure melting. In the SIA, the basal normal stress is equal to the hydrostatic basal pressure:

$$N_b = \rho g H \tag{2.32}$$

Note that these basal velocities are valid for regions where the basal ice temperature reaches the melting point. If the base is below the melting point, instead, the basal velocity is set to zero. Further details on the basal velocity could be found in literature (e.g. Ritz et al. 2001; Greve 2005; Greve and Blatter 2009; Rutt et al. 2009; Thoma et al. 2014).

Basal drag

The basal shear stress, also called basal drag, can be derived by means of different methods. A first method consists in defining the basal drag as the sum of all basal resistive forces which in the SIA reduces to a relation between basal drag and basal pressure, and surface slope (e.g. Greve and Blatter 2009; Thoma et al. 2014):

$$\tau_b = \rho g H \mid \nabla S \mid \tag{2.33}$$

where ∇S is the gradient operator in the horizontal plane of the surface elevation S. Another method consists in using a solid friction law, which relates basal drag and effective pressure:

$$\tau_b = fN \tag{2.34}$$

where f is a parameter and N is the effective pressure defined in Eq. 2.29.

For the fast flowing areas of the ice sheet, namely ice streams and ice shelves, the basal drag (Eq. 2.21, SSA formulation) take specific formulation. In case of ice streams, the friction law (Eq. 2.34) becomes:

$$\tau_b = -c_f N \mathbf{U} \tag{2.35}$$

where $\mathbf{U}\,(U, V)$ is the vertically averaged velocity, N is the effective pressure and c_f is a different basal drag coefficient. In case of ice shelves, the basal drag is set equal to zero.

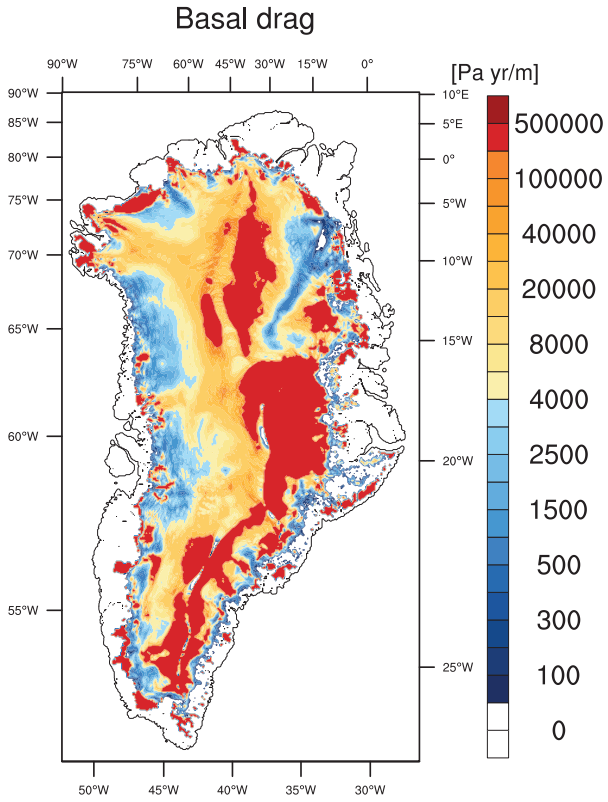

Figure 2.5: Basal drag retrieved using the iterative inverse method by Edwards et al. (2014).

Finally, the basal drag can be inferred from observed surface velocities by means of a control method (e.g. Morlighem et al. 2010) or by means of an iterative inverse method (e.g. Edwards et al. 2014, Figure 2.5).

Basal hydrology

The basal hydrology is characterized by different hydrological features, ranging from drainage through a thin film of water to flow through a network of cavities and rivers. Also percolation of basal water into the porous sub-glacial sediment plays an important role. Nonetheless, due to a lack of observations, the hydrological processes occurring below ice sheets are still not fully understood (Figure 2.6).

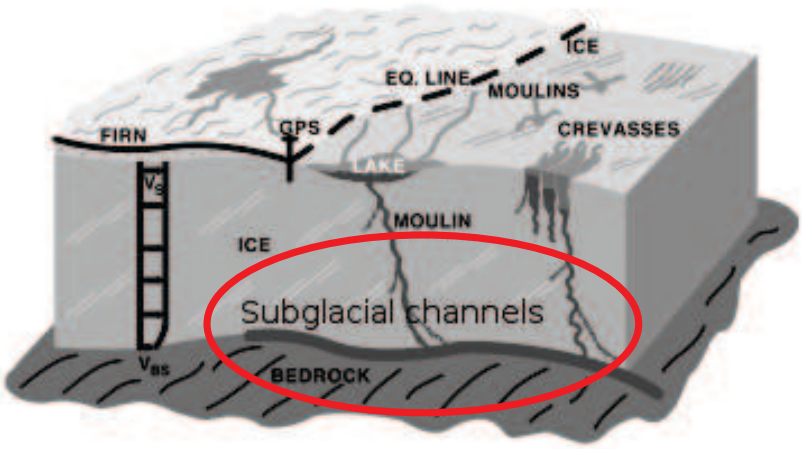

Figure 2.6: Scheme of the basal hydrology of an ice sheet with the internal network of cavities. Figure after Zwally et al. (2002).

A first method used to describe the basal hydrology relies on a local water balance (Rutt et al. 2009), which assumes that the local melt rate F is transported out of the system over a prescribed time scale λ_w. In this way, the basal meltwater (d_w) varies with:

$$\frac{\partial d_w}{\partial t} = F - \frac{d_w}{\lambda_w} \tag{2.36}$$

Another method is based on a Darcy-type flow law (Peyaud 2006). The drainage of sub-glacial water depends on the pressure imposed onto the base. This pressure can be expressed as a potential Φ:

$$\Phi = p_w + \rho_w g B + \rho g H + \Phi_0 \tag{2.37}$$

where p_w is the sub-glacial water pressure, the second term is the influence of the altitude of the base, the third term is the pressure resulting from the weight of the ice, and Φ_0 is a constant. Then the flow of meltwater follows the potential gradient, which can be expressed as:

$$\nabla\Phi = \nabla p_w + \nabla(\rho_w g B + \rho g H) = \nabla p_w + \rho g \left[\left(\frac{\rho_w}{\rho} - 1 \right) \nabla B + \nabla S \right] \tag{2.38}$$

Note that the surface gradient (∇S) is larger than the bedrock one (∇B). Darcy's law relates the flow through a porous medium to a hydraulic gradient. This hydraulic gradient corresponds to the variation of the hydraulic head h_w:

$$h_w = \frac{\Phi}{\rho_w g} \tag{2.39}$$

The flow velocity can be expressed as:

$$V_e = -K\nabla h_w = -\frac{K}{\rho_w g}\nabla\Phi \tag{2.40}$$

where K is the hydraulic conductivity $[m\ s^{-1}]$, which depends on the property of the soil (e.g. clay: $< 10^{-9}\ m/s$, till: 10^{-12} to $10^{-5}\ m/s$, fine sand: 10^{-7} to $10^{-5}\ m/s$).

2.2.5 Ice shelves

As stated before, the ice shelves' motion is described by the shallow shelf approximation in which the basal drag τ_b is set to zero. The spatial extent of ice shelves is controlled by the calving process, which occurs at the front of the ice shelves. Here, we briefly describe the method used in determine the location of the ice shelf front and in describing the calving process.

Location of the ice shelf front

First of all, the position of ice shelves is determined by a flotation criterion, which is based on the Archimede's principle of floating bodies:

$$\rho H = \rho_w(Sl - B) \tag{2.41}$$

where ρ and ρ_w are ice and water density, respectively, Sl is the sea level and B is the ice base.

Subsequently, the ice shelf front is defined as an ice floating point with ice thickness not equal to zero surrounded by point without ice and located in the ocean domain.

Calving

The spatial extent of ice shelves is controlled by the calving process. Calving occurs at the front of the ice shelves and it can be defined as the volume of ice that breaks off at the ice shelves front (Figure 2.7).

The most common and simple parameterization of calving relies on a thickness criterion. This method relies on two conditions (1) the ice thickness must decrease below a thickness threshold (H_{calv}) and (2) the ice coming from the upstream points must fail to maintain the thickness above H_{calv} (Peyaud et al. 2007). The ice-shelf thickness variations are computed by means of a Lagrangian scheme:

$$\frac{dH}{dt} = SMB - b_{melt} - H\left(\frac{\partial u}{\partial x} + \frac{\partial v}{\partial y}\right) \tag{2.42}$$

where b_{melt} is the melting at the base of the ice shelf. b_{melt} is given by a prescribed uniform heat flux from the ocean which varies with the ocean depth (depth criterion,

Ritz et al. 2001). Equation 2.42 is applied to the upstream node of the pixel tested for calving. This upstream node has thickness $H_{upstream}$ ($H_{upstream} > H_{calv}$) and it loses mass towards the front node of the ice shelf, which has a thickness H_{front} given by:

$$H_{front} = H_{upstream} + t_f \frac{dh}{dt} \tag{2.43}$$

where the second term is the change of ice thickness between upstream and front node. If H_{front} is lower than H_{calv}, then calving occurs, otherwise the ice shelf can develop.

Another calving method relies on the link between near front ice thickness, half width and strain rate (e.g. Doake et al. 1998; Alley et al. 2008). The calving rate, then, is computed by means of the eigenvalues ($\dot{\epsilon_{\pm}}$) of the horizontal components of the strain rate ($\dot{\epsilon}$, Eq. 2.9). The corresponding eigen-directions are parallel to and transverse to the flow. On the region where the flow diverges, both eigenvalues are positive, the calving rate is computed using:

$$Calv = K_{calv}\ det(\dot{\epsilon}) = K_{calv}\ \dot{\epsilon_+}\ \dot{\epsilon_-} \tag{2.44}$$

where K_{calv} (> 0) is a proportionality constant, elsewhere the calving rate is set to zero. This calving method is called Eigen Calving Law (Winkelmann et al. 2011).

More complex methods rely on the fact that calving events occur after the propagation of fractures (crevasses) in response to stress (Benn et al. 2007). Some calving model take into account this information in order to obtain a different physically based calving model (i.e. Nick et al. 2010; Pollard et al. 2015).

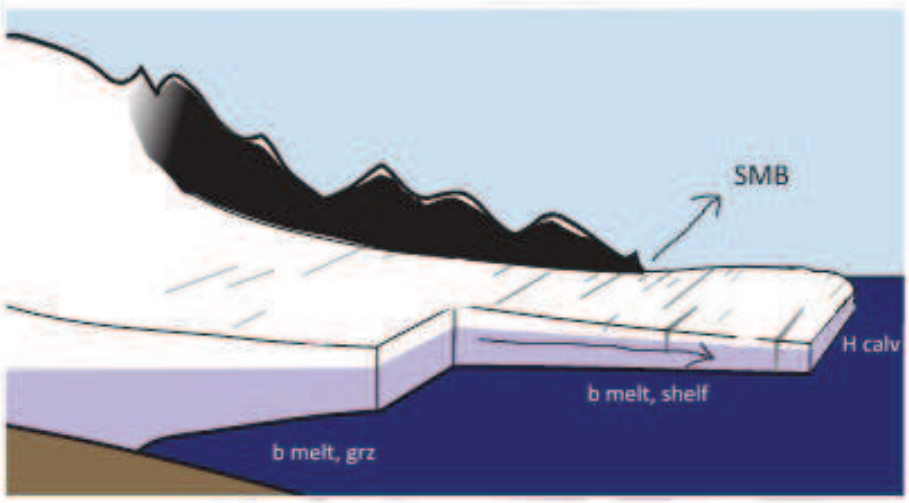

Figure 2.7: Cartoon representing the calving of an ice shelf front with the main term of Eqs. 2.42 and 2.43. Figure after Winkelmann et al. (2011).

2.3 Ice sheet models

2.3.1 Surface mass balance

The surface mass balance is determined by the difference between accumulation and ablation. The accumulation corresponds to the solid fraction of precipitation. In many

ice sheet models, the solid fraction of precipitation is retrieved by using a threshold on temperature, below which the precipitation is considered to occur as solid precipitation (e.g. Bougamont et al. 2005; Rutt et al. 2009; Vizcaíno et al. 2010). Here, both ice sheet models calculate the solid fraction of precipitation using the relation introduced by Marsiat (1994), which relates the solid precipitation to total precipitation and temperature, on a monthly basis:

$$\frac{S_m}{P_m} = \begin{cases} 0 & T_m \geq T_{liq} \\ \frac{T_{liq}-T_m}{T_{liq}-Tsolid} & T_{solid} < T_m < T_{liq} \\ 1 & T_m \leq T_{solid} \end{cases} \tag{2.45}$$

where S_m is the monthly solid precipitation (or snowfall) rate [$m\ yr^{-1}$] and P_m is the monthly total precipitation [$m\ yr^{-1}$]. T_m is the mean air surface temperature, which is calculated from annual mean (T_{ann}) and July mean temperature (T_{July}) using a sinusoidal function as described by Fausto et al. (2009): $T_m(t) = T_{ann} + (T_{July} - T_{ann}) \cos\left(\frac{2\pi t}{A}\right)$ where A is set equal to one year. T_{liq} and T_{solid} are two temperature threshold (7.2 $°C$ and -11.6$°C$, respectively taken from Bales et al. (2009)). In our formulation, the rainfall can run off instantaneously, without contributing to the formation of superimposed ice, or it can contribute to the superimposed ice formation (Janssens and Huybrechts 2000).

The retention scheme of meltwater and rainfall, then, is described by means of two different methods:

1. a constant and uniform fraction of snowmelt is retained by any possible processes (Reeh 1991):

$$p_r = csi \cdot snow \tag{2.46}$$

   where p_r is the potential retention mass, csi represents the retained fraction (csi = 0.6, Reeh 1991), and $snow$ is the solid fraction of the yearly precipitation;

2. a simple thermo-dynamics parameterization that takes into account both the retention by refreezing and by capillary suction effect (Janssens and Huybrechts 2000):

$$p_r = min\left\{\frac{c(T)}{L}T_{ann} \cdot \frac{d}{P_{ann}} + \left(\frac{S_{ann} - M}{P_{ann}}\right) \cdot \left(\frac{\rho_e}{\rho_0} - 1\right); 1\right\} \tag{2.47}$$

   where M is the snow melt, T_{ann} is the annual mean air surface temperature, P_{ann} is the annual mean total precipitation, S_{ann} is the annual mean snow accumulation rate, d is the thickness of the active layer, $c(T)$ is the specific heat capacity [$J\ kg^{-1}\ K^{-1}$], which is a function of the temperature (146.3 + 7.253 $T[K]$), and L is the latent heat of ice (335 $kJ\ kg^{-1}$), finally ρ_0 is the dry snow density while ρ_e is the wet snow density, set to 300 $kg\ m^{-3}$ and 960 $kg\ m^{-3}$, respectively in Janssens and Huybrechts (2000).

The ablation is parameterized by means of many techniques going from the positive degree day method (PDD, e.g. Reeh 1991; Calov and Greve 2005; Fausto et al. 2009) to energy balance methods (e.g. Gallée and Duynkerke 1997; Vizcaíno et al. 2010). Here, both ice sheet models use the PDD semi-empirical method. This method relates linearly the number of positive degree days to the amount of ice and snow melt through the melting factors C_{snow} and C_{ice}, which are derived from observations from present-day Greenland ice sheet.

The number of PDD is calculated using a semi-empirical relation introduced by Reeh (1991)

$$PDD = \int_{t=0}^{A} \int_{T'=0}^{\infty} T' \frac{1}{\sigma_{pdd}\sqrt{2\pi}} exp\left[-\frac{(T' - T_m(t))^2}{(2\sigma_{pdd})^2}\right] dT'dt \tag{2.48}$$

where σ_{pdd} is the standard deviation of the temperature distribution and $T_m(t)$ is the reconstructed sinusoidal annual cycle, and A is 1 year.

The same amount of PDD can be calculated using the semi-analytical solution by Calov and Greve (2005)

$$PDD = \int_{t=0}^{A} dt \left[\frac{\sigma_{pdd}}{\sqrt{2\pi}}\, exp\left(-\frac{T_m(t)^2}{2\sigma_{pdd}^2}\right) + \frac{T_m(t)}{2}\, erfc\left(-\frac{T_m(t)}{\sqrt{2}\sigma_{pdd}}\right)\right] \tag{2.49}$$

where $erfc(x)$ represents the complementary error function:

$$erfc(x) = 1 - erf(x) = \frac{2}{\sqrt{\pi}} \int_{x}^{\infty} exp(-\tilde{x}^2) d\tilde{x} \tag{2.50}$$

The number of positive degree days are used to evaluate ablation in several steps:

1. the PDD are used to melt the snow layer, if it is present, at a C_{snow} rate. Meltwater is supposed to percolate into the snow layer and refreezes as superimposed ice. This process is described using one of the methods presented (Eq. 2.46 or Eq. 2.47);

2. the superimposed ice is melted at C_{ice} rate;

3. the remaining PDD are used to melt the glacier ice at C_{ice} rate.

Depending on the available energy, not all steps or even none of the steps are carried out.

The melting factors are derived from observations and they vary as a function of July temperature following Tarasov and Peltier (2002):

$$\begin{aligned} C_{ice} &= \begin{cases} C_{ice}^{C} & T_{July} \le T_C \\ C_{ice}^{W} + \frac{\beta_{ice}^{C} - \beta_{ice}^{W}}{(T_w - T_C)^3}(T_W - T_{July})^3 & T_C \le T_{July} \le T_W \\ C_{ice}^{W} & T_{July} \ge T_W \end{cases} \\ C_{snow} &= \begin{cases} C_{snow}^{C} & T_{July} \le T_C \\ C_{snow}^{W} + \frac{\beta_{snow}^{C} - \beta_{snow}^{W}}{(T_w - T_C)}(T_{July} - T_C) & T_C \le T_{July} \le T_W \\ C_{snow}^{W} & T_{July} \ge T_W \end{cases} \end{aligned} \tag{2.51}$$

where two temperature thresholds (T_C, cold transition and T_W, warm transition) are used to determine the effective melting factors values for cold ($C_{ice/snow}^{C}$) or warm ($C_{ice/snow}^{W}$) conditions.

2.3.2 New implementation: meltwater routing scheme

Part of snow and ice that melts refreeze as superimposed ice. The remaining fraction of meltwater, instead, flow over the ice sheet surface via supra glacial streams, forming the so called runoff, or percolate through the ice sheet to the ice sheet base trough moulins

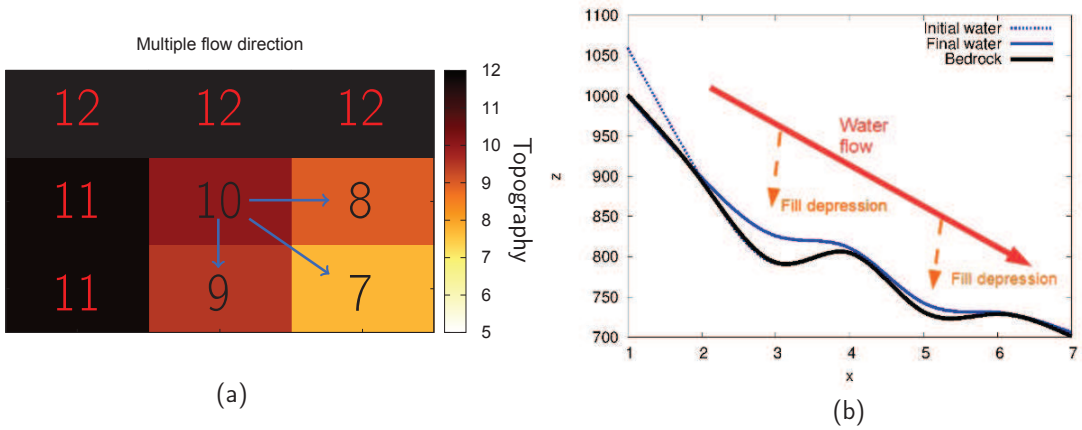

Figure 2.8: (a) Scheme representing the "multiple flow direction" methods by Quinn et al. (1991). The numbers represents an idealized topography, in which the water is placed in the central cell, while the blue arrows represents the downhill directions followed by the meltwater. (b) Scheme representing the mechanisms used in filling possible depressions along the path. The meltwater starts at the top of the slope. The meltwater meets a topographic depression and the amount required to fill the topographic depression stops there, while the remaining extra water is allowed to continue to flow downhill.

or crevasses. Many techniques are used to study the runoff from the melting location towards the final point of its travel, which usually corresponds to a depression or a coastal grid-point. The detection of pathways and drainage basins is based on different form of steepest slopes determined by the gravitational force techniques (e.g. Quinn et al. 1991; Renssen and Knoop 2000; Tarasov and Peltier 2005; Goelzer et al. 2012).

The "multiple flow direction" algorithm introduced by Quinn et al. (1991), allows the meltwater accumulated in the up-slope area to be distributed among all down-slope directions (Figure 2.8a) and not towards the single steepest direction, as done in single flow direction algorithm (e.g. Renssen and Knoop 2000). Furthermore, the amount of meltwater in each down-slope direction is also proportional to the gradient of each downhill flow path. The amount of meltwater passed to the ith downhill cell (ΔA_i) is given by

$$\Delta A_i = \frac{A(tan\,\beta_i L_i)}{\sum_{j=1}^{n}(tan\,\beta_j L_j)} \tag{2.52}$$

where A is the total up-slope meltwater amount, n is the total number of downhill directions, $tan\beta_i$ is the gradient in the ith downhill direction, and L_i is the contour length of the ith direction.

In the example reported in Figure 2.8a, we consider a rectangular Cartesian grid in which three downhill directions are found (up to eight paths can be followed in this grid). As a consequence, the meltwater will flow along these three directions, but a different amount of meltwater will flow in each direction due to the differences in slope.

Finally, the meltwater along its path can pass by some topographic depression. In this case, we retain the minimum amount of water required to fill the depression while the extra water, if exist, continues its flow (Figure 2.8b).

Here, we consider the meltwater produced at the surface of the ice sheet and, subse-

quently, we assume that the meltwater flow on the surface of the ice sheet. This assumption is justified by the absence of any percolation scheme in GRISLI able to describe the structure of channels used by the meltwater to reach the base of the ice sheet.

2.3.3 GRenoble Ice Shelf and Land Ice model

GRISLI (Ritz et al. 2001) is a three-dimensional thermo-mechanical ice-sheet model that belongs to the hybrid category (Kirchner et al. 2011) in which the dynamics of grounded ice is described by the SIA (Section 2.2.2, Hutter 1983), and fast ice streams and ice shelves are described by the SSA (Section 2.2.2, MacAyeal 1989). The basal drag coefficient is inferred with an iterative inverse method based on the observed surface velocities (Edwards et al. 2014). The spatial extent of ice shelves is controlled by the calving and ocean basal melting processes are described in Section 2.2.5.

GRISLI is run on a rectangular regular Cartesian grid using the polar stereographic projection with the standard parallel at 71°N and the central meridian at 39°W at 20 x 20 km and 5 x 5 km horizontal resolution. On the vertical structure, GRISLI consists of 21 layers of cold ice, and 4 layers in the bedrock to propagate the geothermal conditions to the base of the ice-sheet.

The initial present-day bedrock elevation and ice-sheet thickness maps are derived from Bamber (2001) and Bamber et al. (2013) for the simulations at 20 km and 5 km resolution, respectively (Figures 1.12, 2.14a and 2.14d).

GRISLI is forced by air surface temperature and total precipitation. During the simulations, both fields are adjusted from changes in ice sheet elevation. The air surface temperature is corrected by means of an uniform atmospheric lapse rate (λ = 6.309 °C/km, Fausto et al. 2009):

$$T_{cor}(t) = T_0 + \lambda\,(S(t) - S_0) \tag{2.53}$$

where T_{cor} is the corrected air surface temperature, T_0 is the initial temperature, S is the time-varying topography and S_0 is the initial topography. Changes in precipitation are related to changes in temperature corrections, assuming that the saturation pressure of water vapor depends exponentially on temperature Charbit et al. (2002):

$$P_{cor}(t) = P_0\, exp(-\gamma\,(T_{cor}(t) - T_0)) \tag{2.54}$$

where P_{cor} is the corrected precipitation field, P_0 is the initial precipitation, and γ is the precipitation correction factor (0.07, Quiquet et al. 2012).

The surface mass balance is given by the difference between accumulation and ablation. The accumulation corresponds to the solid fraction of total precipitation (Section 2.3.1, Marsiat 1994). The ablation is parameterized using the PDD semi-empirical method by Reeh (1991) (Eq. 2.48).

Finally, the routing of surface meltwater is computed by means of the routing scheme described in Section 2.3.2. The main features of GRISLI are summarized in Table 2.2 and Figure 2.11. Further details on the model physics can be found in Ritz et al. (2001).

2.3.4 SImulation COde for POLythermal Ice Sheet model

SICOPOLIS (version 3.1, publicly available at http://sicopolis.net/ Greve et al. 2011) is a three-dimensional thermo-mechanical ice-sheet model. As GRISLI, it is based on

Table 2.2: Main characteristics of GRISLI and SICOPOLIS.

	GRISLI	**SICOPOLIS**
Inland ice	SIA	SIA
Ice stream	SSA	SIA
Ice shelf	SSA	SSA
Shelf melt	depth criterion	depth criterion
Calving	thickness criterion	thickness criterion
Ablation	PDD	PDD
	Reeh (1991)	Calov and Greve (2005)
Horizontal res.	20 km, 5 km	20 km
Vertical res.	21 layers	81 layers
Vertical ice temperature	cold ice	polythermal ice

the SIA for the grounded ice, while the ice shelves are described by means of the SSA. However, differently from GRISLI, no specific treatment is applied to the ice streams. Basal sliding is described by a Weertman-type sliding law (Eq. 2.31), in which the basal drag is derived from the basal pressure and the surface slope (Eq. 2.33).

The main difference between GRISLI and SICOPOLIS is that SICOPOLIS accounts for a possible polythermal vertical ice temperature mode. Cold ice, i.e. temperature below melting point, and temperate ice, i.e. temperature at the pressure-melting point, are treated differently. The temperate ice is considered as a mixture of cold ice and a small amounts of meltwater, which impacts on the ice-sheet flow.

The temperate ice, then, is described by means of two mass balance equations (one for the mixture and one for the water alone), one momentum equation and one energy balance equation, while the temperature is at the pressure melting point.

For the formulation of the temperate ice field equations, we follow the work by Greve (1997b) and Greve and Blatter (2009) (Figure 2.9).

First, some quantities from mixture theory are introduced. The barycentric velocity ($\mathbf{u}_m$, $[m\ yr^{-1}]$) is defined as:

$$\mathbf{u}_m = \frac{1}{\rho_m}(\rho\mathbf{u} + \rho_w\mathbf{u}_w) \tag{2.55}$$

where ρ_m is the density of the mixture, ρ and $\mathbf{u}$ are density and velocity of ice, respectively, and ρ_w and $\mathbf{u}_w$ are density and velocity of water. The water content W [%] is introduced as the mass fraction of water in the mixture

$$W = \frac{\rho_w}{\rho_m} \tag{2.56}$$

and the diffusive water mass flux ($\mathbf{j}$ $[kg\ m^{-2}\ s^{-1}]$) is defined as:

$$\mathbf{j} = \rho_m W(\mathbf{u}_w - \mathbf{u}_m) \tag{2.57}$$

which describes the water motion with respect to the motion of the barycentre.

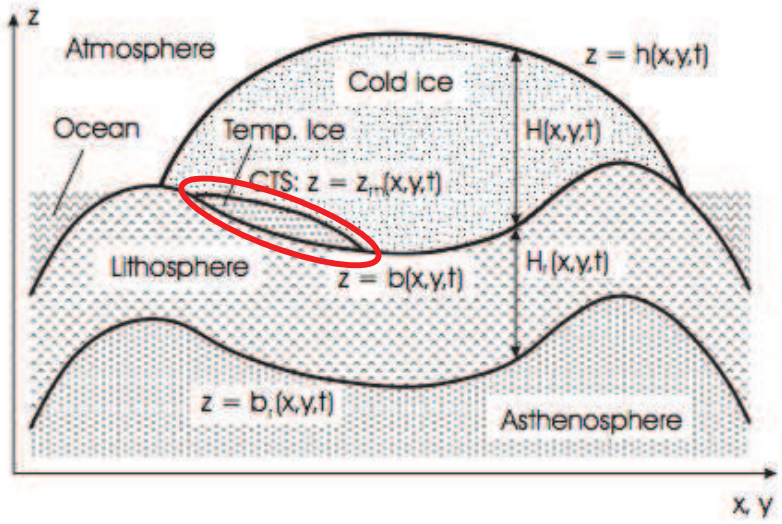

Figure 2.9: Sketch of a polythermal ice sheet. Figure after Greve (1997b).

As for cold ice, the mixture of ice and water is considered incompressible. Since the amount of water is low (usually less than 3% Greve and Blatter 2009), the density of the mixture can be set equal to the ice density $\rho_m \approx \rho \approx 918\ kg\ m^{-3}$.

As a consequence the mixture mass balance and mixture momentum balance have the same form as for the cold ice:

$$\nabla \cdot \mathbf{u}_m = 0 \tag{2.58}$$

$$\nabla \cdot \tau - \nabla p + \rho \mathbf{g} = 0 \tag{2.59}$$

The mass balance for the water component of the mixture, instead, has a non constant density. In fact, the mass of water is not conserved since the mass of water changes due to melting and freezing processes. It is, then, necessary to use the general formulation of the mass balance (Eq. 2.1) in which a production term M is introduced:

$$\frac{\partial \rho_w}{\partial t} + \nabla \cdot (\rho_w \mathbf{u}_w) = M \tag{2.60}$$

which can be also expressed as

$$\rho_m \frac{dW}{dt} = -\nabla \cdot \mathbf{j} + M \tag{2.61}$$

The energy equation in term of water content is defined as:

$$\rho_w L \left(\frac{\partial W}{\partial t} + \mathbf{u} \cdot \nabla W + \nabla \cdot \mathbf{j} \right) = Q_i \tag{2.62}$$

To close the system some constitutive relations are required. In particular, four relation are introduced:

1. a counterpart for the Glen's flow law:

$$\dot{\epsilon} = A(W)\, \tau_*^{n-1}\, \tau \tag{2.63}$$

in which the temperature-dependent rate factor $A(T^*)$ is replaced by a factor depending on the water content:

$$A(W) = A(T_{pmp})(1 + 1.8125W[\%]) \tag{2.64}$$

where T_{pmp} is the temperature at the pressure melting point;

2. a relation between internal energy and changes in water content and melting temperature:
$$\frac{dQ_i}{dt} = L\frac{dW}{dt} + c(T_{pmp})\frac{dT_{pmp}}{dt}; \tag{2.65}$$

3. a Fick's diffusion law for the motion of water:
$$\mathbf{j} = \nu\nabla W \tag{2.66}$$
where ν represent the water diffusivity in ice $[kg\ m^{-2}\ s^{-1}]$;

4. a Fourier's law of heat conduction for the sensible heat flux:
$$q_s = -\kappa(T_{pmp})\nabla T_{pmp} \tag{2.67}$$
the counterpart for cold ice is:
$$q_s = -\kappa(T)\nabla T. \tag{2.68}$$

Introducing these constitutive relation into the water mass balance (Eq. 2.61) and into the mixture energy balance (Eq. 2.62) leads to an equation for the water production rate

$$M = \frac{1}{L}\left(2A_t(W)\tau_*^{n-1} + \nabla\cdot(k\nabla T_{pmp}) - \rho c\frac{dT_{pmp}}{dt}\right) \tag{2.69}$$

the energy available for melting/refreezing has three terms: (1) heat dissipated by stress power; (2) heat conducted to the considered area; (3) heat stored by changes in the melting temperature.

Finally, the interface that separates cold and temperate ice (CTS in Figure 2.9) is tracked through the use of Stefan-type energy-flux and mass-flux matching conditions. The CTS is defined explicitly as: $z = z_m(x, y, t)$ or implicitly by:

$$F_m(\mathbf{x}, t) = z - z_m(x, y, t) = 0 \tag{2.70}$$

Defining a normal unit vector with the positive side in the cold ice and negative side in the temperate ice (Figure 2.10) the kinematic condition for the CTS becomes:

$$\begin{aligned} &\frac{\partial F_m}{\partial t} + \nabla F_m\cdot\mathbf{u} = -N_m a_m \\ &\frac{\partial z_m}{\partial t} + u\frac{\partial z_m}{\partial x} + v\frac{\partial z_m}{\partial y} - w = N_m a_m \end{aligned} \tag{2.71}$$

where a_m is the ice volume flux through the CTS: $a_m = (\mathbf{w} - \mathbf{u})\cdot\mathbf{n}$ and
$N_m = |\nabla F_m| = \left[1 + \left(\frac{\partial z_m}{\partial x}\right)^2 + \left(\frac{\partial z_m}{\partial y}\right)^2\right]^{1/2}$.

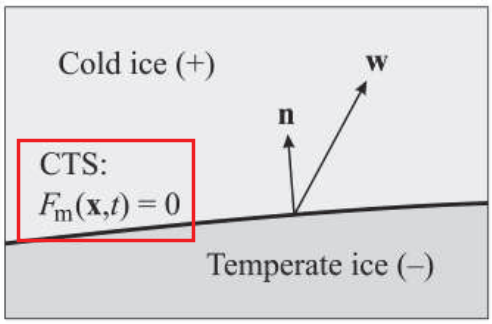

Figure 2.10: Geometry of the CTS. Figure after Greve and Blatter (2009).

More detailed description of the polythermal ice structure could be found in the literature (e.g. Greve 1997b; Greve and Blatter 2009).

Here, to account for the polythermal structure, SICOPOLIS considers 81 layers of cold ice and 11 basal temperate ice layers.

Similarly to GRISLI, SICOPOLIS is run on a polar stereographic rectangular Cartesian grid at 20 x 20 km horizontal resolution using the initial present-day bedrock elevation and ice-sheet thickness from Bamber (2001).

Accumulation is derived from the Marsiat (1994) (Eq. 2.45) empirical relationship, while ablation is parameterized following the semi-analytical solution for the PDD integral of Calov and Greve (2005) (Eq. 2.49).

The routing of surface meltwater is computed by means of the routing scheme described in Section 2.3.2. The main features of SICOPOLIS are summarized in Table 2.2 and Figure 2.11. Further details on SICOPOLIS can be found in Greve (1997a,b).

2.4 Initialization of the ice sheet models

Because of the slow diffusivity of surface temperature within the ice sheet, a spin-up is required in order to obtain proper initial temperature conditions to simulate the present day and future ice-sheet dynamics evolution. Two different types of long-term spin-up can be performed: a steady state spin-up driven by fixed present-day climate conditions (e.g. Payne and Baldwin 1999; Edwards et al. 2014), and a transient spin-up, driven by reconstructed time varying paleo-climatic conditions (e.g. Huybrechts 2002). In the present work, we use transient spin-up to initialize the simulations. Among the transient spin-up methods, the index method is the most common one (e.g. Cuffey and Marshall 2000; Lhomme et al. 2005; Greve et al. 2011; Applegate et al. 2012; Quiquet et al. 2013a). The index method uses a paleo-climate index, most of the time based on $\delta^{18}O$ retrieved from ice core data, to reconstruct the past time evolution of air surface temperature and precipitation departing from present-day climate conditions. The spin-up is usually performed over the entire last glacial cycle from $\sim$ 125 kyrs BP (e.g. Greve et al. 2011; Applegate et al. 2012) or over the last 30 kyrs (e.g. Herzfeld et al. 2012). The index method can also be performed using interpolations between global climate models climate snapshots in order to constrain the spatial evolution of the paleo-climate index, as for instance described by Charbit et al. (2002), Born and Nisancioglu (2012), and Fyke et al. (2014).

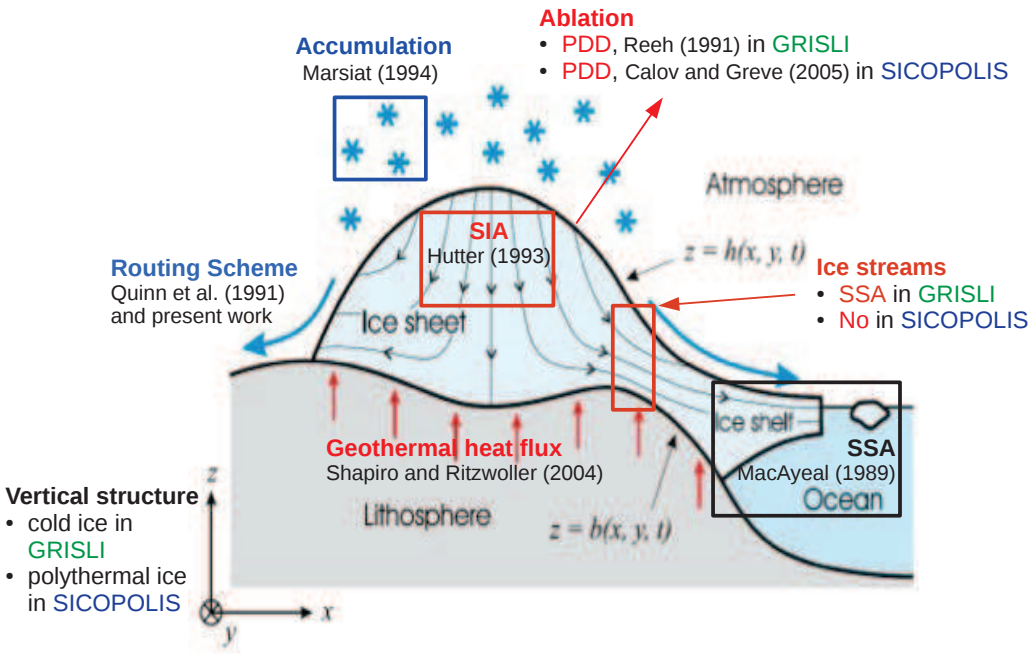

Figure 2.11: Summary of the main features and differences between the two ISMs used in this work. Figure after Greve and Blatter (2009).

Rogozhina et al. (2011) and Yan et al. (2013) point out the importance of the dependence of the simulated present-day GIS conditions to the initialization method. Both papers show that the steady state spin-up leads to an overall warmer ice sheet with respect to those developed using a transient method. Moreover, Yan et al. (2013) show that the simulated elevation variations for the 1993-2010 period are close to observations when transient methods are used. For these reasons, we perform transient long-term spin-up based on the index method used in the SeaRISE experiments (Greve et al. 2011; Bindschadler et al. 2013; Nowicki et al. 2013), and, to balance the initialization time and the computational time, these simulations run over the last 24 kyrs, starting a little before the Last Glacial Maximum (21 kyrs BP), similarly to Herzfeld et al. (2012).

We use the $\delta^{18}O$ variations derived from the GRIP (Johnsen et al. 1997; Dansgaard et al. 1993) as climate index to reconstruct the time-evolution of annual mean air surface temperature (T_{ma}) and annual mean precipitation (P_{ma}) over Greenland for the past 24 kyrs (Figure 2.12).

The spin-up is performed following Greve et al. (2011). The method uses the temperature parameterization from Fausto et al. (2009) and uses the simulated present-day precipitation from Ettema et al. (2009). The temperature parameterization is based on surface elevation (S), latitude (ϕ) and longitude (θ) and has been tuned on present-day observations:

$$\begin{aligned} T_{ma,pd}(\theta,\phi) &= d_{ma} + \lambda_{ma}\, S + c_{ma}\, \phi + k_{ma}\, \theta \\ T_{mj,pd}(\theta,\phi) &= d_{mj} + \lambda_{mj}\, S + c_{mj}\, \phi + k_{mj}\, \theta \end{aligned} \tag{2.72}$$

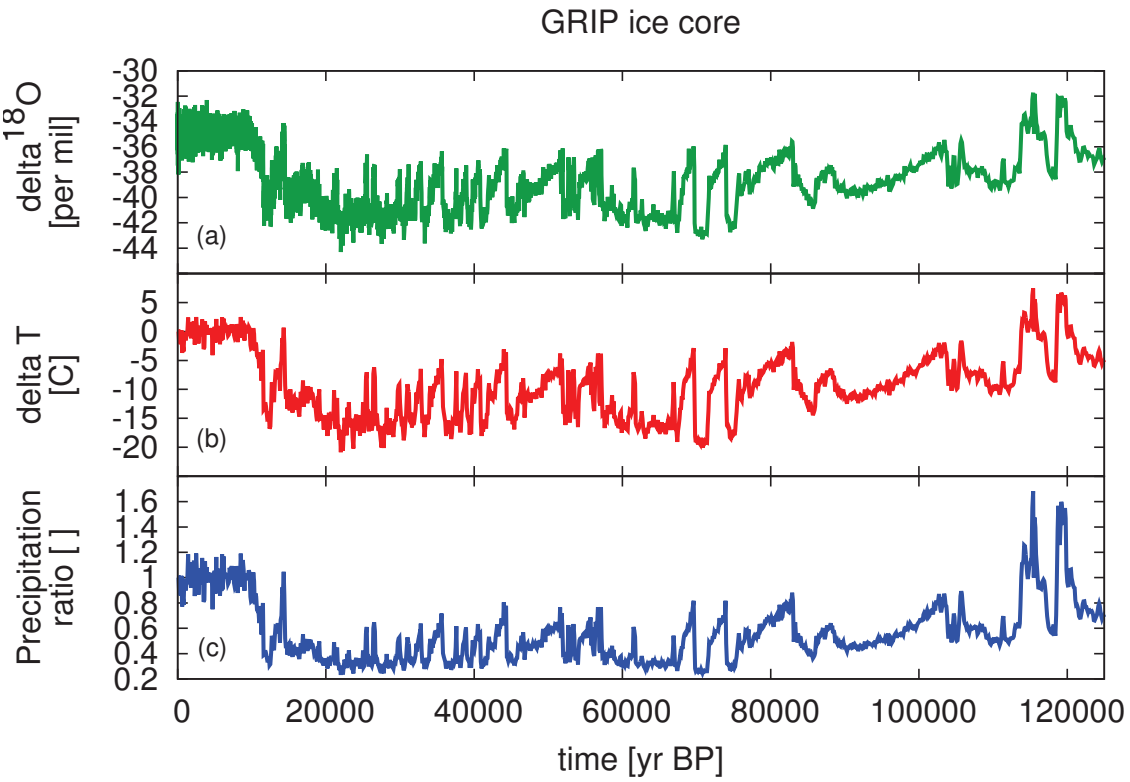

Figure 2.12: Time series of (a) $\delta^{18}O$ [‰] retrieved from GRIP (Dansgaard et al. 1993; Johnsen et al. 1997), (b) computed changes in mean annual temperature [° C] (Eq. 2.73), and (c) computed change in precipitation [ratio] (Eq. 2.73).

where the constant values are $d_{ma} = 41.83°\text{C}$ and $d_{mj} = 14.70°\text{C}$; $\lambda_{ma} = -6.309°\text{C}$ km^{-1} and $\lambda_{mj} = -5.426°\text{C}$ km^{-1}; $c_{ma} = -0.7189°\text{C}$ $°\text{N}^{-1}$ and $c_{mj} = -0.1585°\text{C}$ $°\text{N}^{-1}$; and $k_{ma} = 0.0672°\text{C}$ $°\text{W}^{-1}$ and $k_{mj} = 0.0518°\text{C}$ $°\text{W}^{-1}$.

The time evolution of annual mean temperature and precipitation is obtained using the time-varying index derived by the GRIP ice core data, using the relations:

$$\begin{aligned} T_{ma}(\theta,\phi,t) &= T_{ma,pd}(\theta,\phi) + d_{cf}\,(\delta^{18}O(t) + 34.83) \\ P_{ma}(\theta,\phi,t) &= P_{ma,pd}(\theta,\phi)\; exp[\gamma\,(T_{ma}(\theta,\phi,t) - T_{ma,pd}(\theta,\phi))] \end{aligned} \tag{2.73}$$

where d_{cf} represents the standard $\Delta T/\delta^{18}O$ conversion factor, $d_{cf} = 2.4°\text{C}$ $‰^{-1}$ (Huybrechts 2002).

The ISMs paleo-climatic runs start at 24 kyr BP with a present-day ice distribution. At the end of the simulations, the resulting ice-sheet topography is not in good agreement with present-day one for both ISMs (Figure 2.13). To improve the final ice-sheet geometry, the PDD method was tuned by adding a correction term to the melting factors (Eq. 2.51), following the work by Greve et al. (2011):

$$C^{cor}_{ice/snow}(\theta,\phi) \rightarrow correction(\theta,\phi) \;\times\; C_{ice/snow} \tag{2.74}$$

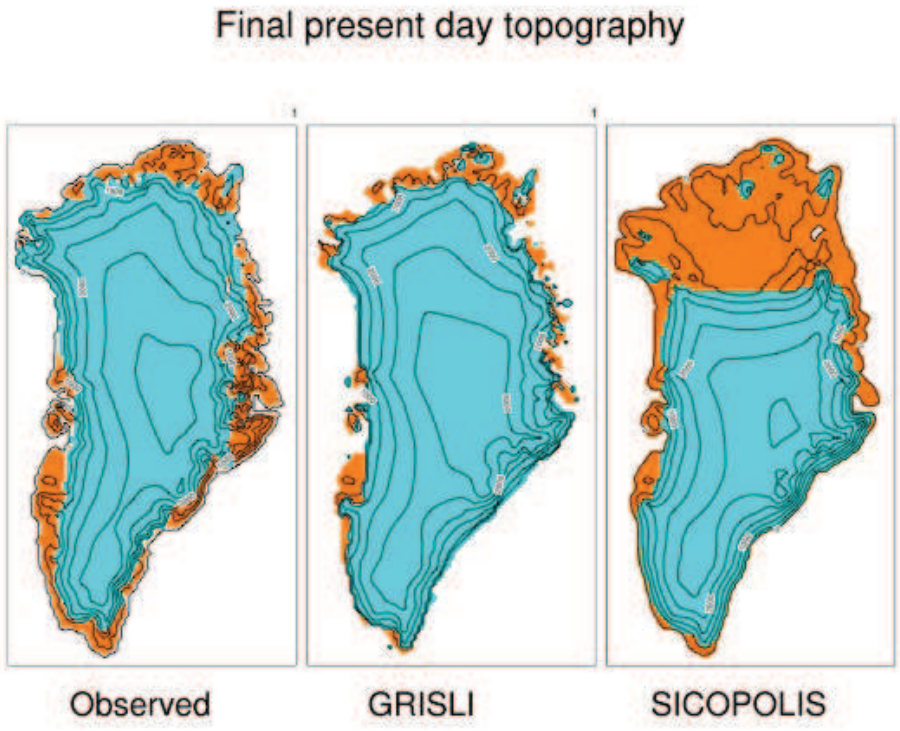

Figure 2.13: Observed Greenland ice topography at 20 km resolution (Bamber 2001) and the ice topography at the end of the spin-up simulation with GRISLI and SICOPOLIS performed at 20 km horizontal resolution without applying the tuning procedure (Eq. 2.74). The cyan areas represent the ice covered region, while the brown areas represent the region without ice. The black lines depict the ice elevation limit from 0 to 3000 m with steps of 500 m.

this correction term varies linearly with latitude and takes a different value for West and East Greenland, where the longitudinal distinction is given at 44 °W (Greve et al. 2011). The correction values are reported in Table 2.3.

After applying the correction, the resulting spin-up topographies show that, in general, ice is thicker along the southeastern coast and thinner in the northern part of the ice sheet compared with present-day observed topography (Figure 2.14). In particular, the ISMs are not simulating ice in the north-western end of the GIS (Figure 2.15). The discrepancies in the northern and north-western areas mainly result from the distribution of precipitation. In fact, the present-day precipitation from Ettema et al. (2009) is drier than the rest of the ice sheet in the central and northern areas of Greenland. This explains why the ice thickness is underestimated in the simulations over those regions. On the contrary, the discrepancies along the southeastern coast mainly derive from the coarse resolution (20km) that was used for the spin-up, which is not enough to properly capture the ablation in such a mountainous region. When accounting for a higher resolution (5 km) the overestimation in ice thickness in those areas reduces (Figure 2.14e).

Note that the spin-up at 5 km horizontal resolution was not performed with SICOPOLIS, because SICOPOLIS at this high horizontal resolution presented numerical instabilities.

Overall, GRISLI simulates a better ice topography with respect to SICOPOLIS at

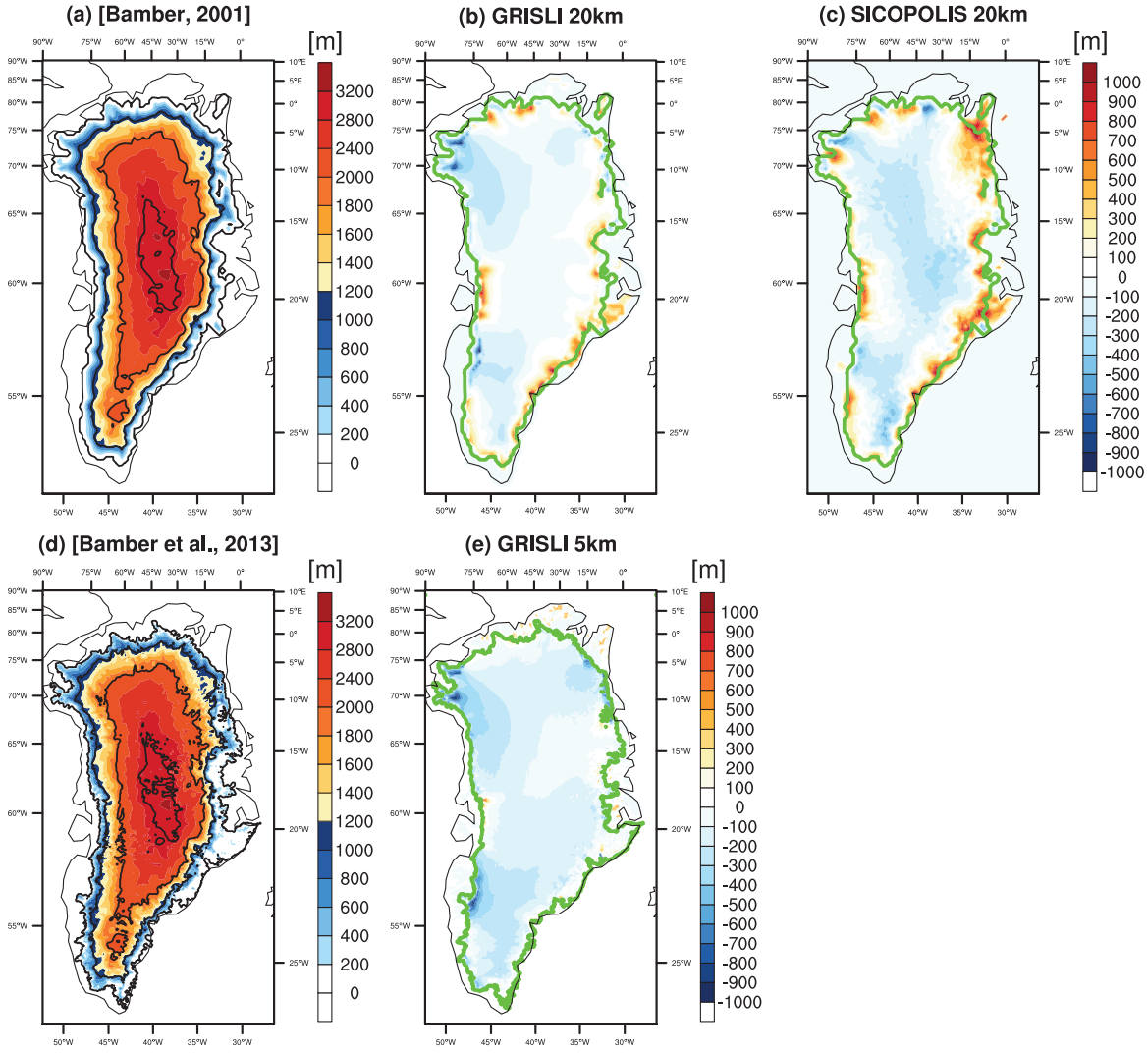

Figure 2.14: (a) Observed Greenland ice topography at 20-km resolution (Bamber 2001). (b) Difference between present-day ice topography at the end of the paleo-climatic run of GRISLI at 20-km resolution and observed topography. (c) As (b) but for SICOPOLIS. (d) Observed topography at 5-km resolution (Bamber et al. 2013). (e) As for (b) but at 5-km resolution. The green line represents the observed Greenland ice extent, while the black lines in (a) and (d) depict the ice elevation limit from 0 m to 3000 m with steps of 1000 m.

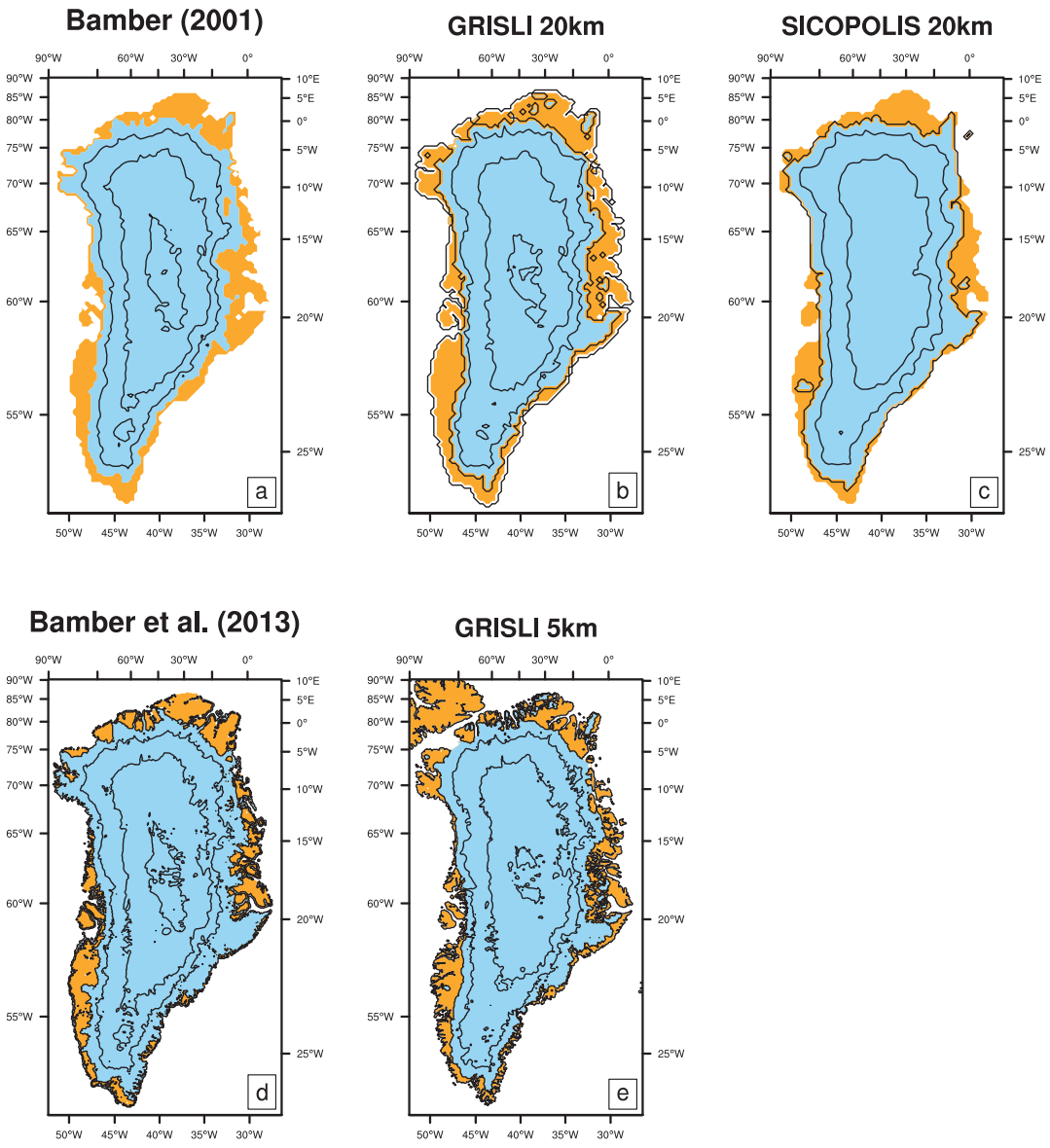

Figure 2.15: (a) Observed Greenland ice topography at 20-km resolution (Bamber 2001). (b) Ice topography at the end of the paleo-climatic run of GRISLI at 20-km resolution. (c) As (b) but for SICOPOLIS. (d) Observed topography at 5-km resolution (Bamber et al. 2013). (e) As for (b) but at 5-km resolution. The cyan areas represent the ice covered region, while the brown areas the region without ice. The black lines depict the ice elevation limit from 0 m to 3000 m with steps of 1000 m.

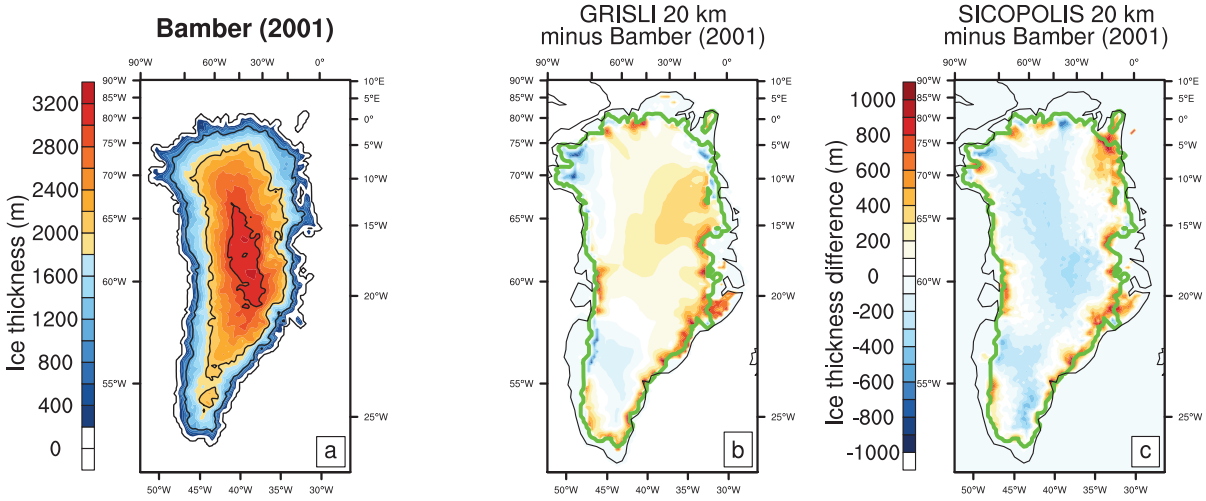

Figure 2.16: (a) Observed Greenland ice topography at 20-km resolution (Bamber 2001). (b) Difference between present-day ice topography at the end of the paleo-climatic run of GRISLI at 20-km resolution, when the ice stream are turned off, and observed topography. (c) Difference between present-day ice topography at the end of the paleo-climatic run of SICOPOLIS at 20-km resolution and observed topography (as Figure 2.14c). The green line represents the observed Greenland ice extent, while the black lines in (a) depict the ice elevation limit from 0 m to 3000 m with steps of 1000 m.

the same grid resolution (20 km), especially in the northeastern part of Greenland (Figures 2.14b and 2.14c) and in the central summit area (Figures 2.15b and 2.15c). This improvement is related to the specific treatment of the ice streams used in GRISLI, in fact when this treatment is turned off, both models display similar results in that area (Figure 2.16). Finally, the increase in resolution in GRISLI from 20 km to 5 km leads to a further improvement of the spun-up ice topography, especially along the Eastern margin (Figure 2.14e). This is due to (1) a better representation of the ice streams and ice shelves dynamics along the ice margins, and (2) to a better calculation of ablation in the marginal areas.

Those spin-up topographies are used as initial conditions for all the subsequent simulations of the 20th and 21st centuries carried out in this work.

Table 2.3: Latitude dependent PDD correction applied to each ISM to improve the spin-up simulations following Greve et al. (2011). The longitudinal distinction between West and East Greenland is set at 44 ° W. In general, values >1 are chosen in regions where the previous ice-sheet simulations produced thicker ice with respect to present-day topography, while values <1 are chosen where the previous ice-sheet simulations show thinner ice with respect to present-day topography. Note that the number of regions considered differs between each ISM, i.e. four regions for GRISLI and ten regions for SICOPOLIS.

Latitude	60 °N	64 °N	65 °N	66 °N	68 °N	70 °N	72 °N	76 °N	77 °N	79 °N	80 °N	82 °N	84 °N
SICOPOLIS													
Corr. East	2.8	-	2.8	2.8	3.5	-	3.5	1.0	1.0	-	0.6	1.2	1.5
Corr. West	1.8	-	1.3	1.2	1.2	-	1.2	1.0	0.6	-	0.4	0.8	1.0
GRISLI 20km													
Corr. East	-	4.0	-	-	-	7.5	-	2.5	-	1.5	-	-	-
Corr. West	-	1.5	-	-	-	1.2	-	1.5	-	0.3	-	-	-
GRISLI 5km													
Corr. East	-	4.0	-	-	-	7.5	-	2.5	-	1.5	-	-	-
Corr. West	-	1.5	-	-	-	0.8	-	1.6	-	0.1	-	-	-

Chapter 3

Climate Forcing

3.1 Introduction

The Greenland ice sheet interacts with the other Earth climate system components and, consequently, it is influenced by the climate variability, as described in Section 1.2. In particular, the ice sheet models used in this work require air surface temperature and precipitation fields as initial conditions for 20th and 21st century simulations. The climatic fields for the 20th century are retrieved from reanalysis and from climate model simulations due to the lack of observations at the scale of the whole ice sheet. The climate model simulations are also used in retrieving the climatic fields for the 21st century under two future emission scenarios: the IPCC's Representative Concentration Pathways (RCP) 4.5 and 8.5. In this chapter, I describe the 20th century reanalysis and the 20th and 21st centuries climate simulations that I use to force the ice sheet models in the present work.

3.2 Greenland climate

To force the ice sheet models over the 20th century, we use the climate simulated by both global and regional climate models. In particular, we use the air surface temperature and precipitation from one reanalysis, one regional climate model (RCM) and a set of coupled atmosphere-ocean general circulation models (AOGCMs). For the 21st century, the climate forcing is retrieved from the CMIP5 AOGCMs projections based on two future emission scenarios. The specific reanalysis and models used in this work are summarized in Table 3.1, and more details on each data sets are given in the following.

The air surface temperature and precipitation fields retrieved from reanalysis, RCM and AOGCMs present different horizontal resolutions, coarser than the ice-sheet models horizontal resolution used in the experiments. For this reason, we need to downscale all the climate fields to the resolutions required for the ice sheet experiments. Numerous downscaling technique exists such as the SMHiL (surface mass balance high-resolution downscaling) method by Agosta et al. (2013) or techniques based on dynamical approach or statistical method (e.g. Fowler et al. 2007). In the present work, all climate forcing fields are downscaled on both ISM grids by means of a simple downscaling method. This method uses an atmospheric lapse rate (λ in $^{\circ}C/km$) and a precipitation factor (γ in %)

Table 3.1: Climate forcing used in this work from ERA Interim reanalysis (Dee et al. 2011), from the regional climate model MAR (Fettweis et al. 2013) and from seven CMIP5 AOGCMs (http://cmip-pcmdi.llnl.gov/cmip5/). The last two columns report the number of realizations for each CMIP5 AOGCM accounted for in the RCP 4.5 and RCP 8.5 future scenarios.

Model	Horizontal resolution	# RCP 4.5 realizations	# RCP 8.5 realizations
ERA Interim	0.7° x 0.7°	-	-
MAR	25 km x 25 km	-	-
CCSM4	1.25° x 0.9375°	6	6
CESM1-CAM5	1.25° x 0.9375°	3	3
CMCC-CM	0.75° x 0.75°	1	1
CNRM-CM5	1.40625° x 1.40625°	1	5
IPSL-CM5A-MR	2.5° x 1.25°	1	1
MIROC5	1.40625° x 1.40625°	3	3
MPI-ESM-MR	1.875° x 1.875°	3	1
Total		**18**	**20**

to account for the difference in elevation between the AOGCMs and the ice sheet models:

$$\begin{aligned} T_{ism} &= T_{model} + \lambda(S_{ism} - S_{model}) \\ P_{ism} &= P_{model}\, exp[-\gamma(T_{ism} - T_{model})] \end{aligned} \tag{3.1}$$

where T_{ism}, P_{ism}, and S_{ism} are air surface temperature, precipitation and topography at the ice-sheet model resolution, respectively. T_{model}, P_{model}, and S_{model} are the same variables at the climate model resolution, where *model* stands for one among reanalysis, RCM or AOGCM (Figure 3.1). The values of λ (6.309 $°C\ km^{-1}$) and γ (0.07) are retrieved from Fausto et al. (2009) and Quiquet et al. (2012), respectively. These downscaled fields are then used in the ice sheet experiments presented in the following chapters.

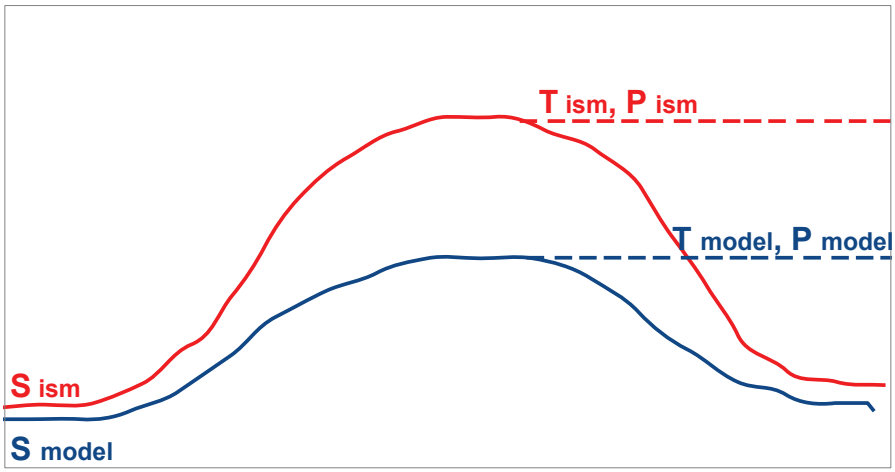

Figure 3.1: Summary of the fields used in the downscaling technique Eq. 3.1.

In the following sections, we provide more details on the reanalysis, RCM, and AOGCMs and on their respective performance compared with the reanalysis.

3.2.1 Atmospheric reanalysis: ERA Interim

The main requirement for reanalysis is that it represents available climate observations on global scale. For this reason, substantial efforts have been made over the past decades in producing global data sets of the basic atmospheric dynamical fields that are consistent with observations.

Many reanalysis products are publicly available, for example the global reanalysis from the National Centers for Environmental Prediction (NCEP, Saha et al. 2010), from the Japanese Meteorological Agency (JMA, Onogi et al. 2007), from the National Aeronautical and Space Administration (NASA, Rienecker et al. 2011) and from the European Centre for Medium-Range Weather Forecasts (ECMWF, Dee et al. 2011).

Models and reanalysis commonly have biases over the glaciated regions (e.g. Bromwich et al. 2007; Walsh et al. 2008) Previous works show that the ECMWF reanalysis is better than the other reanalysis products over Greenland (i.e. Hanna et al. 2005, 2006, 2008; Chen et al. 2011). In particular, Hanna et al. (2006) validate the accumulation provided by the ECMWF reanalysis against 58 ice core accumulation data sets across the ice sheet. They found that the overall simulated accumulation exhibits a good correlation with the observed accumulation. Furthermore, the reanalysis shows significant correlation ($p < 0.05$) in the temporal variability between modeled and observed accumulation in 47 out of 58 sites. However, the central and northern Greenland ice sheet plateaus are drier by $\sim$ 10% to 30% with respect to observations. Similarly, Hanna et al. (2005) compare the reanalysis of air surface temperature against observations. They obtain a good agreement with observations for the stations at altitude lower than 1750 m, while a slight warm model bias ($\sim$ 1.5 °C) remains over the regions above 2000 m.

ERA Interim has the advantage of being available at a higher spatial resolution with respect to the other reanalysis products, i.e. NCEP-1 and NCEP-2 (Chen et al. 2011). For this reason, and given the high performance of this reanalysis product over Greenland, we use the ERA Interim air surface temperature and precipitation to force the ice sheet model experiments. Further details on the ERA Interim reanalysis could be found in Dee et al. (2011).

In the following, the ERA Interim reanalysis fields are considered as 20th century reference climate and compared with the regional climate model and AOGCMs simulated climate (Section 3.2.4).

3.2.2 Regional Climate Model: MAR

The regional climate models focus on a specific region and the interactions with the rest of the climate system occur at the lateral boundaries, where the RCM is forced by climate fields coming from large scale climate models or from global reanalysis. In the present work, we are interested in the RCMs that focus on Greenland. Many RCMs focus on this specific region such as MAR (Fettweis et al. 2013), HIRHAM5 (Lucas-Picher et al. 2012), Polar MM5 (Box et al. 2006) and RACMO2 (Ettema et al. 2009).

For the simulations, we consider the air surface temperature and precipitation fields coming from the RCM Modèle Atmosphérique Régional (MAR, version 3.5, Fettweis et al. 2013). The main components of the snow-ice model used inside MAR are the 1-D surface

vegetation atmosphere transfer scheme SISVAT (Soil Ice Snow Vegetation Atmosphere Transfer, Gallée and Schayes 1994), in which the snow-ice part is based on the CEN (Centre d'Etudes de la Neige) snowpack model called CROCUS (Brun et al. 1992). This snow-ice module is a one-dimensional multi-layered energy balance model and consists of a thermodynamic module (Gallée and Duynkerke 1997), and a snow metamorphism and settling module (Brun et al. 1992). The snow albedo is calculated according to the simulated surface snow grains size, and presence of snow, ice and water at the surface of the snowpack (Gallée et al. 2001). Further details and applications can be found, for example, in Gallée and Schayes (1994); Gallée et al. (2001); Lefebre et al. (2003).

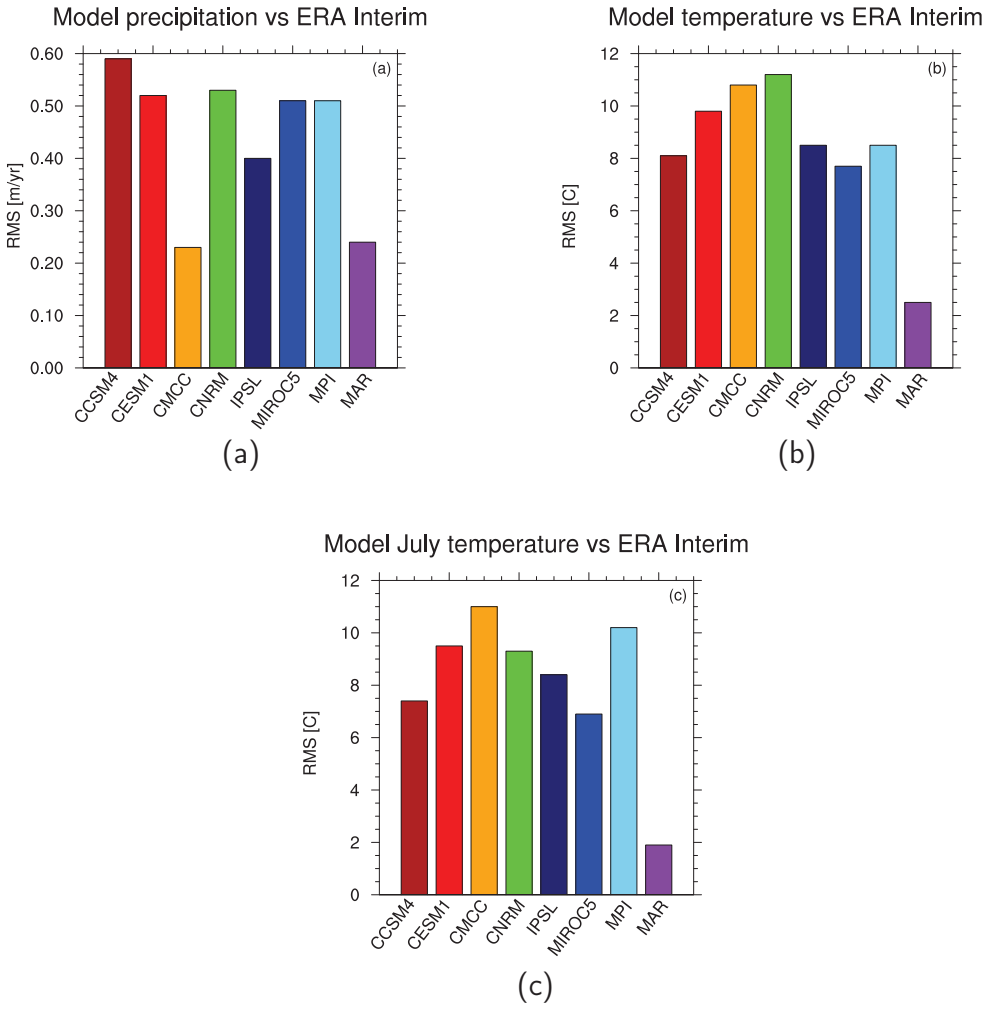

Figure 3.2: Root mean square difference (RMS) of the set of seven CMIP5 models and MAR with respect to ERA Interim for (a) annual precipitation, (b) annual air surface temperature, and (c) July air surface temperature. RMS are calculated over the glaciated area, i.e. Greenland ice sheet.

Here, we use MAR climate forcing over the 20th century since it has been proven to be able to simulate Greenland climate in good agreement with observations (i.e. Fettweis

et al. 2011; Franco et al. 2012; Rae et al. 2012). For example, Fettweis et al. (2011) show that the modeled near-surface melt extent is consistent with the values obtained from spaceborne microwave data. Differences between satellite-derived and model-simulated results still occur and can be attributed to biases in the RCM snow model or to the limitations in the use of passive microwave data for snowmelt detection. However, MAR is able to reproduce the main climatic features over Greenland as required for our purposes.

3.2.3 Atmosphere-Ocean coupled General Circulation Models: CMIP5

Finally, we use a set of climate forcing simulated by means of AOGCMs in the framework of the fifth phase of the Coupled Model Intercomparison Project (CMIP5, Taylor et al. 2012). Data are publicly available from the CMIP5 Earth Science Grid Federation distribution nodes (http://cmip-pcmdi.llnl.gov/cmip5/). The CMIP5 effort was established with the aim of providing a freely available state-of-the-art multi-model data set designed to advance our knowledge of climate variability and climate change. More specifically, we selected seven AOGCMs whose forcing were available from 1850 to the end of the 21st century (Table 3.1). The starts at 1850 was a prerequisite of the selection in order to branch the pre-industrial climate to the end of the spin-up simulation. In particular, we use the historical (1850 + 20th century), the RCP 4.5 and the RCP 8.5 climate forcing of the selected AOGCMs (Taylor et al. 2012).

These models present a wide range of horizontal resolution, spanning from coarser models, such as IPSL (2.5°x1.25°) and MPI (1.875°x1.875°), to intermediate resolution models, such as CMCC (0.75°x0.75°). On top of the discrepancies, this difference in resolution might influence the ability of each AOGCMs in modeling the climate over Greenland. To illustrate this issue, we conduct a brief analysis of the performance of the CMIP5 AOGCMs over Greenland against ERA Interim, which is reported in Section 3.2.4, while a more detailed analysis has been performed by Yan et al. (2014).

The CMIP5 AOGCMs, then, represent the most recent ensemble of coupled global climate models and provide the most recent state-of-the-art knowledge of climate dynamics.

3.2.4 Climate model performance

Extensive evaluations of CMIP5 models against observations at both global scale and over Greenland have been done, for example, in Sillmann et al. (2013) and Yan et al. (2014). The MAR climate fields have been already evaluated in previous work, as well (Rae et al. 2012). Here, we focus on evaluating the performance over Greenland of air surface temperature and precipitation fields coming from each CMIP5 AOGCMs and MAR against the ERA Interim ones. This analysis allow us to highlight the main differences between the set of air surface temperature and precipitation fields used in this work and to relate the potential changes in Greenland ice sheet evolution in the simulations.

The performance of the CMIP5 AOGCMs and MAR models with respect to ERA Interim reanalysis is evaluated calculating the root mean square difference (RMS), following the method used by Walsh et al. (2008). The RMS is calculated as follow:

$$RMS = \sqrt{\frac{\sum(f_{model} - f_{ERAI})^2}{n}} \tag{3.2}$$

in which f_{model} represents the air surface temperature and precipitation fields simulated by the seven CMIP5 AOGCMs and by MAR, while f_{ERAI} corresponds to the ERA Interim reanalysis fields. The values of the RMS are reported in Figure 3.2. The RMS calculations are performed over the glaciated areas, i.e. the ice sheet.

MAR

From all the models considered, MAR presents the smallest RMS with ERA Interim. In particular, the mean annual precipitation differs from the ERA Interim one by 0.24 m/yr in average (Fig. 3.2a), while the air surface temperature show a RMS of 2.5 °C on annual basis (Fig. 3.2b) and of 1.9 °C for mean July temperature (Fig. 3.2c). To better assess the source of those discrepancies, we analyze the spatial differences between ERA Interim and MAR (Figure 3.3).

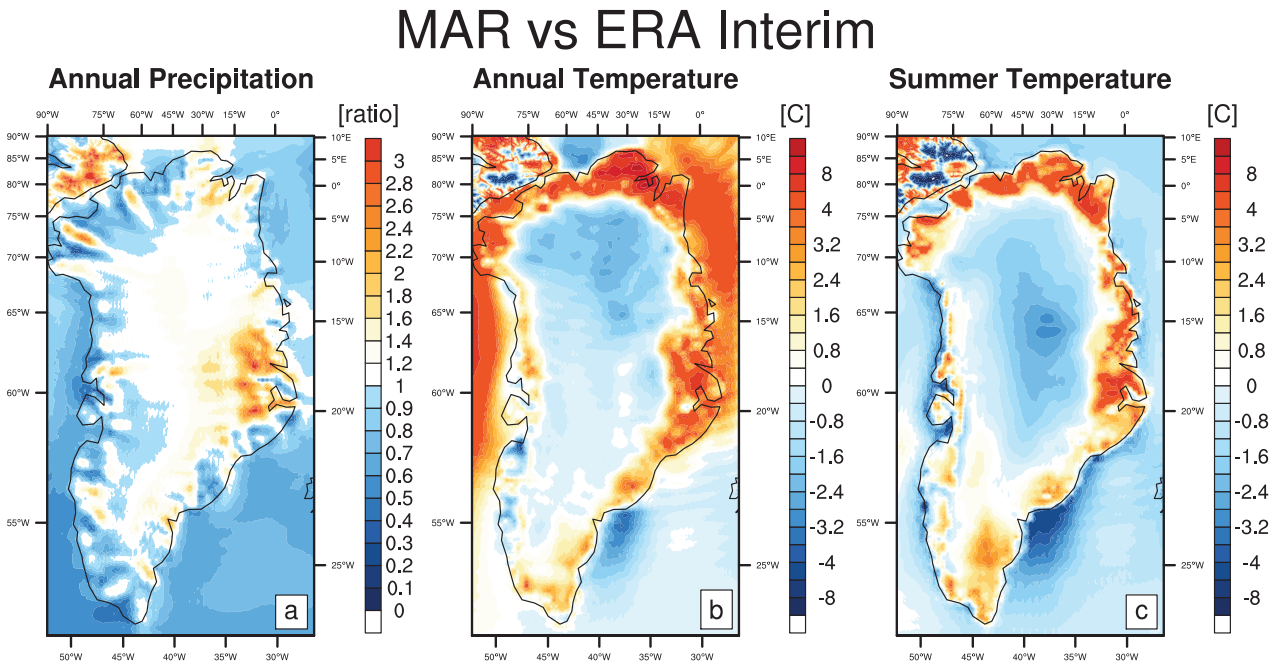

Figure 3.3: Difference of MAR 1980–1999 mean (a) precipitation (ratio), (b) air surface temperature (°C) and (c) July air surface temperature (°C) with respect to ERA Interim ones.

The main discrepancies in the precipitation pattern between MAR and ERA Interim are located along the ice-sheet margins, with MAR precipitation up to 2 times larger than ERA Interim in the eastern coast of the Greenland ice sheet (Figure 3.3a). On the contrary, the differences in air surface temperature are characterized by a colder region in the GIS interior (MAR air surface temperature 2 °C lower in average) and a warmer area along the marginal regions (MAR air surface temperature up to 8 °C higher than ERA Interim ones). Summer differences are smaller in amplitude (about 1°C in average) with respect to annual one, especially along the Greenland margins (Figure 3.3c).

MAR simulations are developed at a resolution of 25 x 25 km which is higher than ERA Interim one (0.7° x 0.7°), and it uses a more complex snow scheme with respect

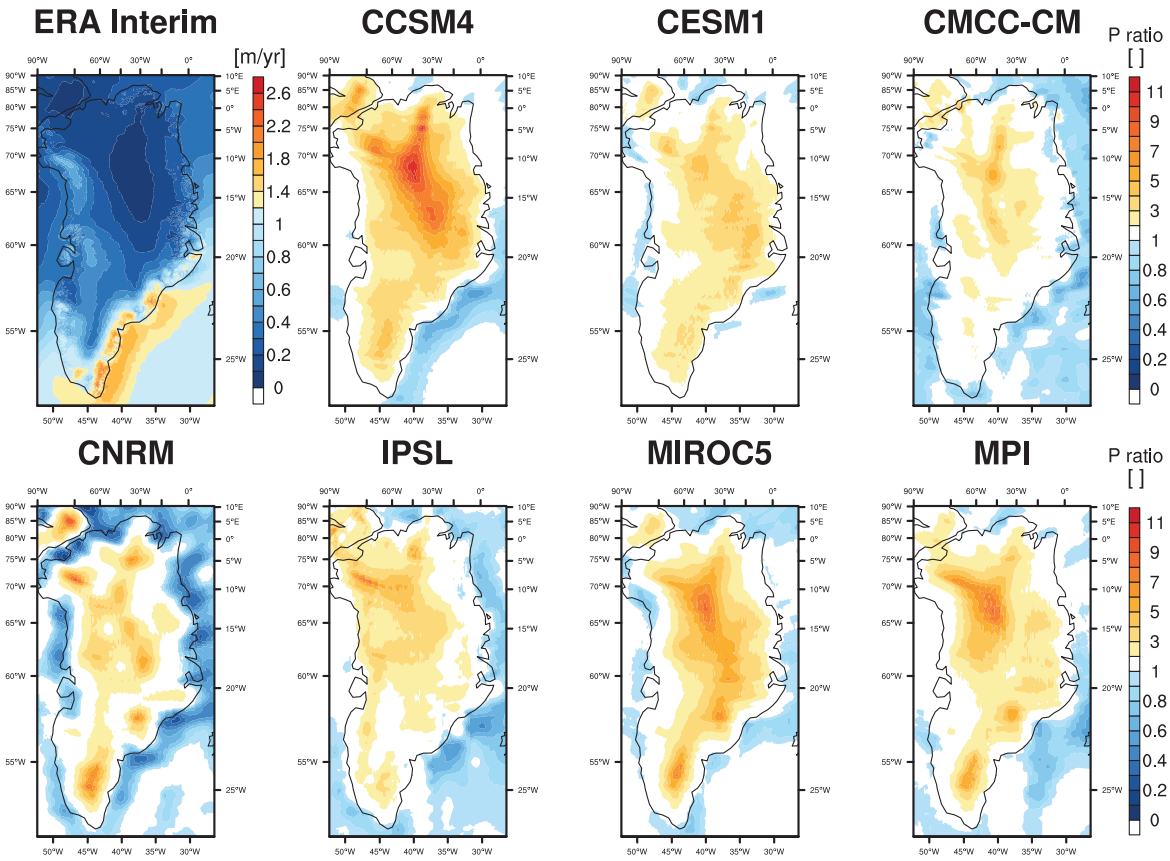

Figure 3.4: ERA Interim mean 1980–1999 precipitation field (m/yr), and the precipitation ratio ($\frac{AOGCM}{ERA\,Interim}$, dimensionless) of the set of seven CMIP5 AOGCMs with respect to the ERA Interim over 1980–1999.

to ERA Interim one. For example, MAR snow scheme accounts for bare ice albedo in ablation zone, whereas ERA-Interim snow scheme accounts only for wet snow albedo at the ablation zone. This difference in resolution and snow scheme can explain the discrepancies in the air surface temperature simulated by MAR with respect to ERA Interim. In fact, the MAR horizontal resolution and snow scheme allow to distinguish between the ice free marginal areas and ablation zone, where MAR simulates a warmer climate with respect to ERA Interim, and the central ice-covered area of Greenland, where colder climate is simulated by MAR with respect to ERA Interim.

Therefore, we also consider MAR climate as a reference climate in the ice sheet experiments developed in the following chapters.

CMIP5

The set of seven CMIP5 AOGCMs considered in this work show RMS values larger than MAR ones. In general, the CMIP5 AOGCMs display a mean increase of 0.47 m/yr in precipitation, ranging between 0.23 m/yr (CMCC-CM) and 0.59 m/yr (CCSM4, Figure 3.2a). The air surface temperature exhibits a mean reduction of 9.2 °C ranging from 7.7 °C (MIROC5) to 11.2 °C (CNRM) on annual basis compared with ERA Interim (Figure 3.2b). During summer (July), the RMS amounts in average to 9 °C, ranging from 6.9

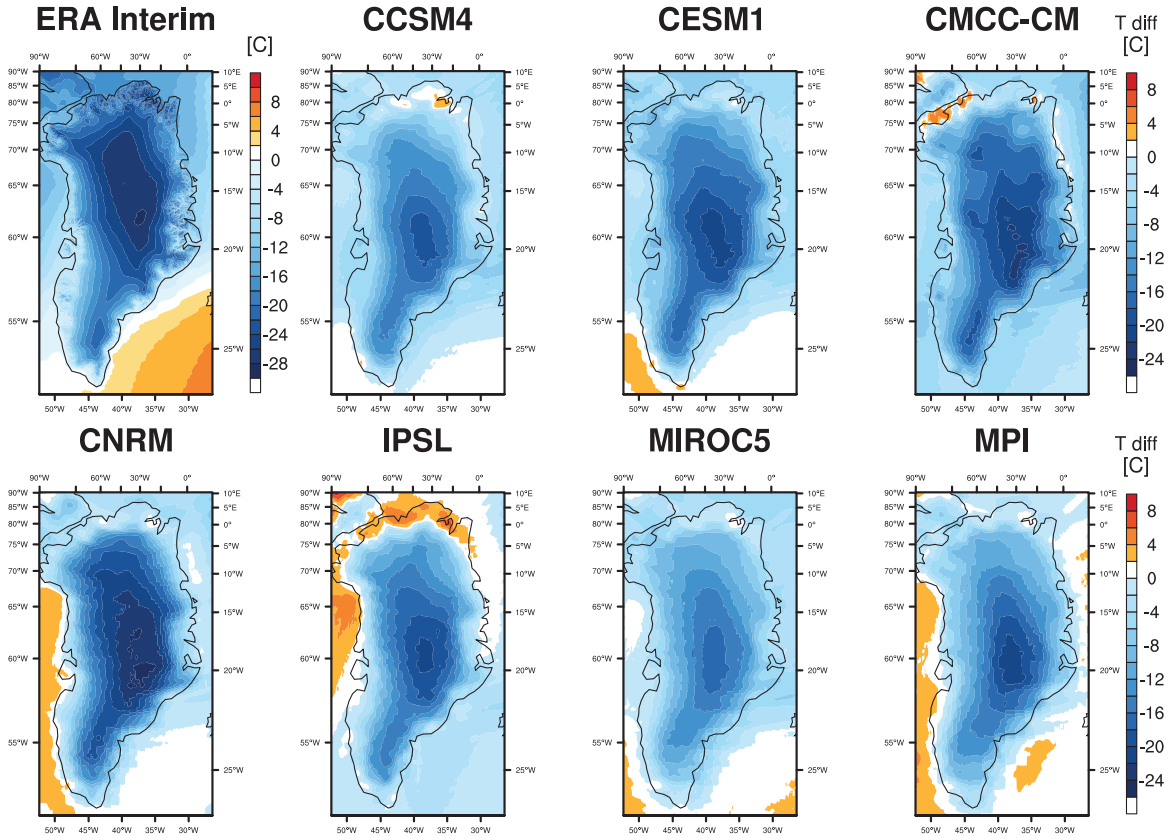

Figure 3.5: ERA Interim mean annual 1980–1999 air surface temperature (°C), and the difference (AOGCM − ERA Interim, °C) of the set of seven CMIP5 AOGCMs mean annual air surface temperature with respect to the ERA Interim over 1980–1999.

°C (MIROC5) to 11 °C (CMCC-CM) compared with ERA Interim (Figure 3.2c).

On a spatial case, the AOGCMs precipitation fields present larger values with respect to ERA Interim in the central-northern part of Greenland, reaching, in the worst case (CCSM4), values about 8 times larger than ERA Interim ones (Figure 3.4). The southern part of Greenland also exhibits higher values of precipitation with respect to ERA Interim in some of the AOGCMs, i.e. CNRM, MIROC5 and MPI (Figure 3.4).

In terms of mean annual temperature, the difference appears to be homogeneous over Greenland with the strongest discrepancies in the central part of the ice sheet, where the AOGCMs present values from 18 °C (MIROC5) to 26 °C (CNRM) lower than ERA Interim ones (Figure 3.5). During summer, the temperature differences are slightly reduced in all AOGCMs, for example in the central part of Greenland the AOGCMs present values from 12 °C to 24 °C lower than ERA Interim ones (Figure 3.6).

Those differences in precipitation and air surface temperature have been related in previous studies to low model skills in reproducing some processes in the high latitudes. For example, Belleflamme et al. (2013) show an increase in negative NAO index values in the atmospheric reanalysis, which leads to an anticyclonic pattern over Greenland, favoring southerly warm air advection. This feature is not captured by all the CMIP5 AOGCMs and seems to derive directly from the diversity of the parameterizations em-

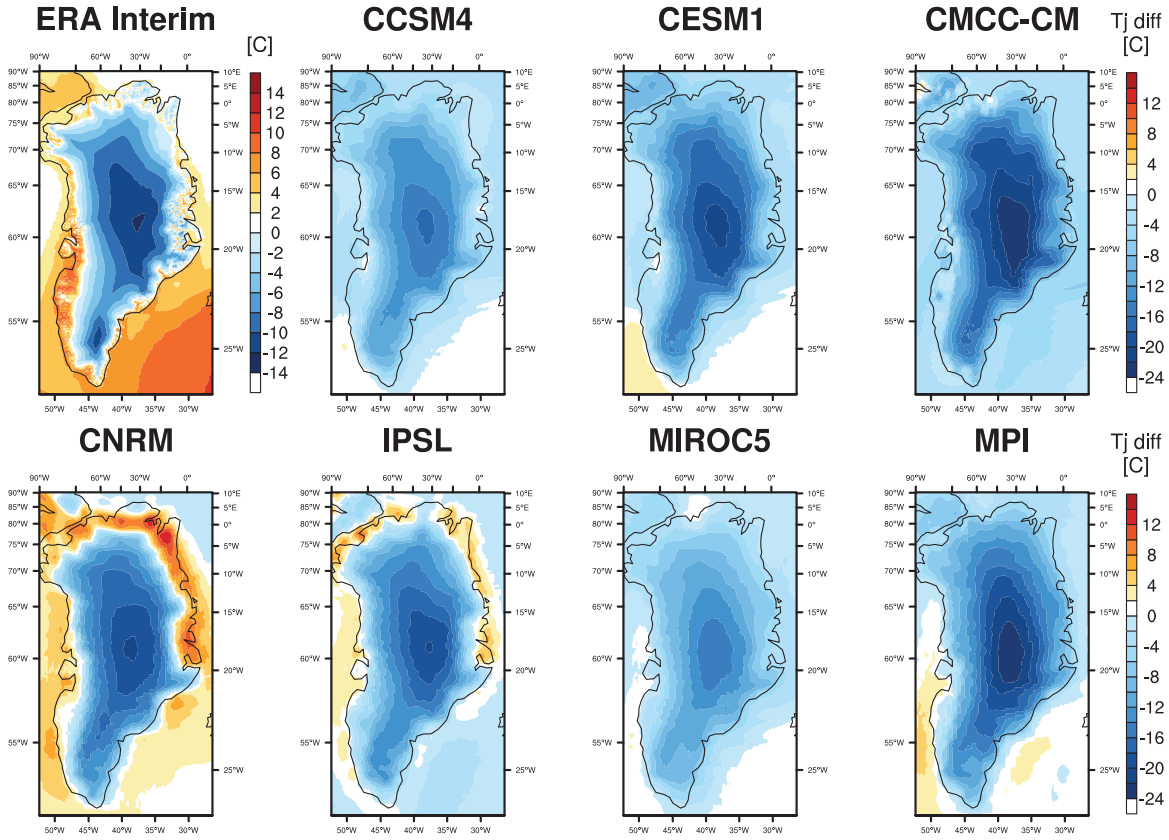

Figure 3.6: As Figure 3.5, but for the mean 1980–1999 July air surface temperature field (° C).

bedded in each model (Belleflamme et al. 2013). On the contrary, the climate of the northern part of Greenland is also influenced by the local warming induced by the recent Arctic sea ice cover reduction (Fettweis et al. 2013), which is well reproduced by the CMIP5 ensemble (Stroeve et al. 2012). The considered set of CMIP5 AOGCMs present a large range of resolution (Table 3.1), which could also impact on the simulated climate. However, Walsh et al. (2008) in their analysis show that horizontal resolution seems not to be a key factor in determining the skill of each AOGCMs over Greenland. In this section, we evaluate the skill of each AOGCM in simulating Greenland climate since, in the present work, we want to investigate the impact of the climate forcing on the simulated Greenland ice sheet surface mass balance and runoff production. For this reason, we use simulated air surface temperature and precipitation from a set of AOGCMs, instead of the multi-model ensemble mean (MME) alone, which, anyway, has been shown to perform better in simulating the climate over Greenland relative to most of the individual CMIP5 models (Yan et al. 2014).

3.3 Climate projections

The climate projections are based on two emission scenarios, the IPCC's Representative Concentration Pathways (RCP) 4.5 and 8.5 (Moss et al. 2010) spanning 2006–2100. We take this two scenarios since the RCP 4.5 represents an intermediate evolution for the

21st century, while the RCP 8.5 represents an extreme case. However, given the seven AOGCMs considered, the total number of realizations differ for each future scenario. In particular, we have 20 realizations with RCP 8.5 future scenario and 18 with RCP 4.5 one (Table 3.1). In this section, we show, as example, the evolution of the MME air surface temperature and of the MME precipitation over the 21st century (Figure 3.7).

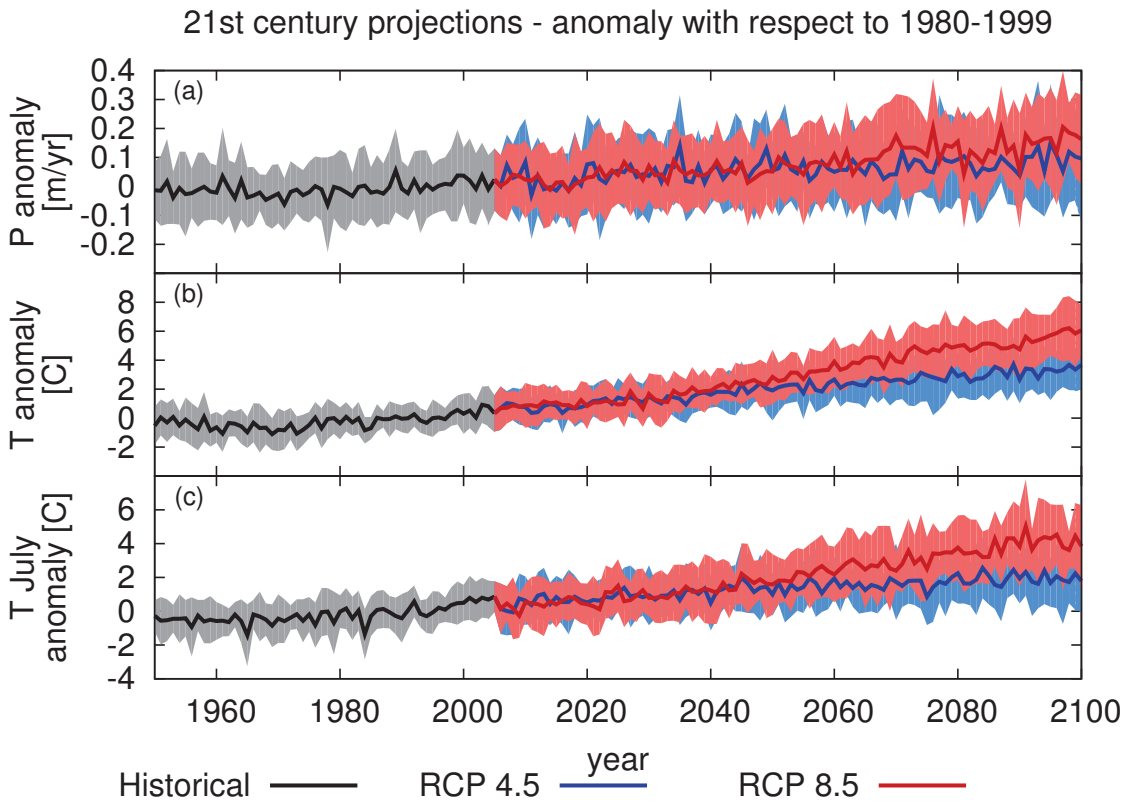

Figure 3.7: Time series of (a) mean annual precipitation (m/yr), (b) mean annual air surface temperature (°C), and (c) mean July air surface temperature (°C) anomalies with respect to the period 1980–1999. The values are averaged over the entire present-day ISMs domain. Shaded regions indicate the ensemble spread, while solid lines represent the multi-model ensemble means.

The MME precipitation in the RCP 4.5 case shows a slight increase of about 0.10 m/yr in average over the 21st century. However, the ensemble spread exhibits a large range of trends, from a decrease in precipitation of about 0.07 m/yr to an increase of 0.32 m/yr by the end of the 21st century simulations (Figure 3.7a). In the RCP 4.5, the MME mean annual air surface temperature increases of about 3.3 °C, with values ranging from 1.8 °C to 4.9 °C, by the end of the 21st century (Figure 3.7b). Similarly, the MME July temperature shows a mean increase of 1.9 °C, ranging from 0.1 °C to 3.7 °C over the 21st century (Figure 3.7c).

Compared with the RCP 4.5, the RCP 8.5 presents only small difference in the MME precipitation until 2100 (mean increase of 0.17 m/yr). On the contrary, the MME air surface temperature reaches values twice as large as in the RCP 4.5 simulations for both annual (5.8 °C, Figure 3.7b) and July averages (4.2 °C, Figure 3.7c) by the end of the

21st century.

Finally, we analyze the spatial change of air surface temperature and precipitation fields during the 21st century. In particular, we show the MME air surface temperature and precipitation anomaly between the period 1980-1999 and the last two decades of the 21st century (2081–2100, Figure 3.8).

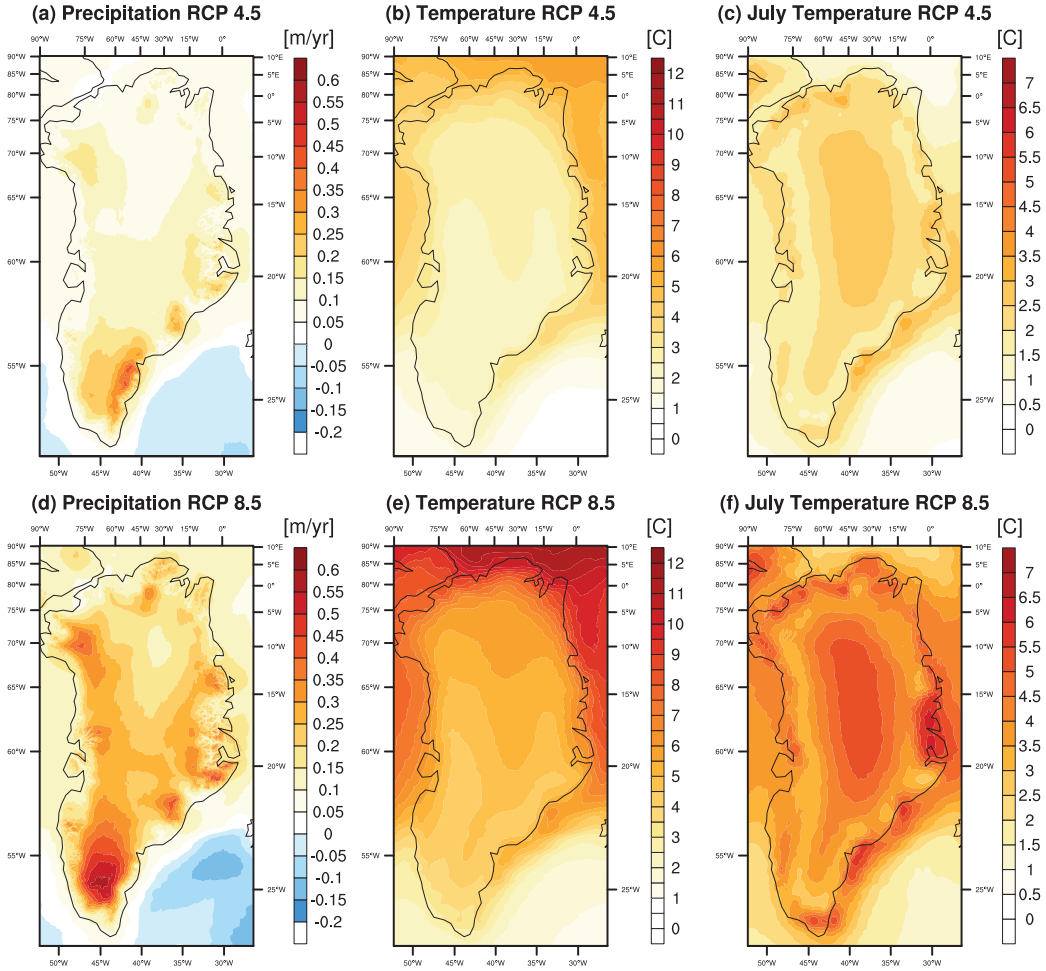

Figure 3.8: Spatial distribution of (a,d) mean annual precipitation (m/yr), (b,e) mean annual air surface temperature (°C) and (c,f) mean July air surface temperature (°C) anomaly fields with respect to 1980–1999 obtained from the multi-model ensemble mean at the end of the 21st century (2081–2100). The first row reports the anomaly fields obtained under a RCP 4.5 scenario, while the second row are obtained under a RCP 8.5 scenario.

At spatial scale, the MME precipitation is projected to increase during the 21st century with the largest increase in the southern part of Greenland in both scenarios. In particular, under a RCP 4.5 scenario the precipitation field shows an homogeneous increase of about 0.1 m/yr over all Greenland with a localized increase up to 0.35 m/yr along the southeastern coast. Under a RCP 8.5 scenario, the precipitation field exhibits a strong increase in the entire southern part of the ice sheet up to 0.6 m/yr. Furthermore, precipitation increase significantly along the western coast compared with RCP 4.5, with

increase up to 0.35 m/yr in the north-western part of Greenland.

The MME air surface temperature field displays a different pattern of anomaly between annually averaged values and July values. The MME mean annual air surface temperature anomaly exhibits an increase in temperature characterized by a gradual northward increasing trend. For example the southern part of Greenland shows larger temperatures of about 2 °C, which increase to about 6 °C in the northern part of the ice sheet in a RCP 4.5 scenario (Figure 3.8b). The MME mean July air surface temperature anomaly, instead, shows the largest increase in the Greenland interior and along the ice-sheet margins (about 4 °C in RCP 4.5). The same pattern is found under RCP 8.5 scenario, but the temperature increase are about twice as large as the temperature changes in a RCP 4.5 scenario (Figures 3.8b and 3.8e).

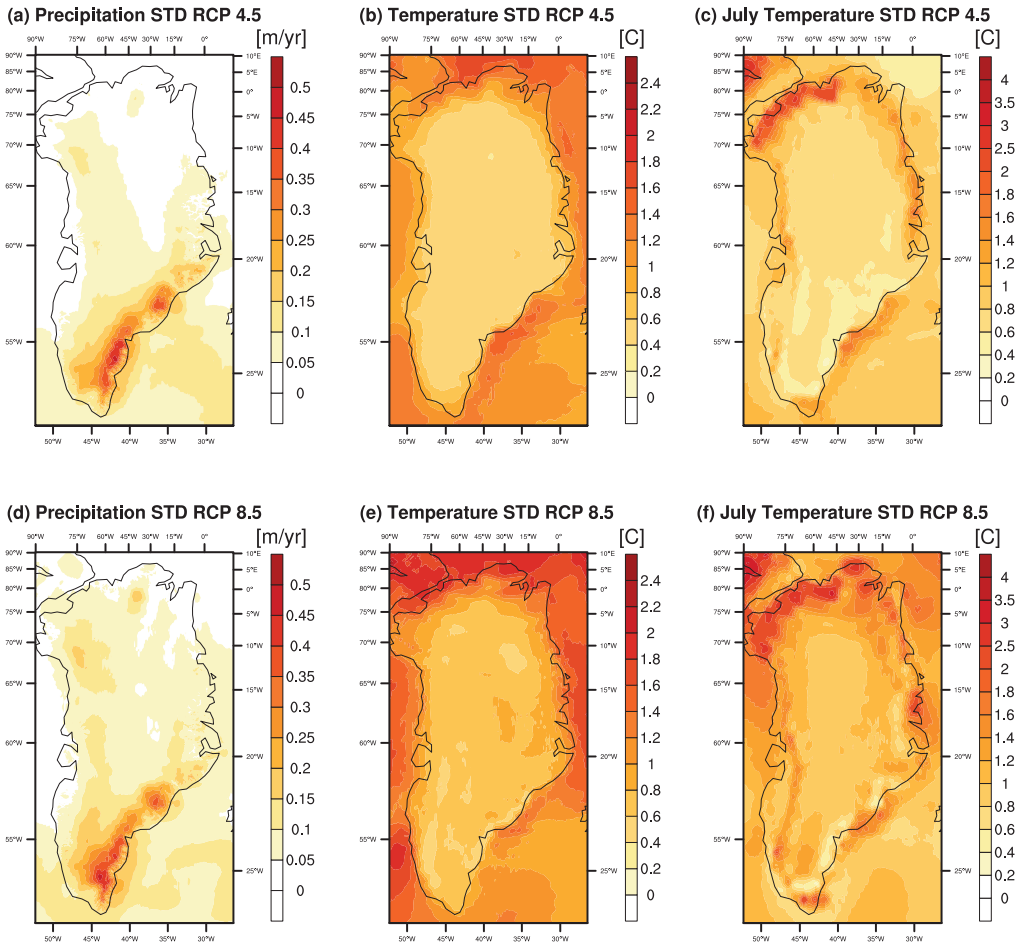

Figure 3.9: Spatial distribution of (a,d) annual precipitation standard deviation (m/yr), (b,e) annual air surface temperature standard deviation (°C) and (c,f) July air surface temperature standard deviation (°C) of the anomaly fields depicted in Figure 3.8. The standard deviation is computed accounting for the complete set of CMIP5-based simulations. The first row reports the anomaly fields obtained under a RCP 4.5 scenario, while the second row are obtained under a RCP 8.5 scenario.

To account for the uncertainties derived by the set of CMIP5 forcing, we evaluate the standard deviation of the anomaly fields (Figure 3.9). In particular, the precipitation field

exhibits the largest uncertainties in the southeastern region (up to 0.5 m/yr, Figures 3.9a and 3.9d), which corresponds to the region with the largest amount of precipitation (e.g. Ettema et al. 2009). The mean annual temperature field show the largest uncertainties along the northern margin of the studied domain (values up to 2.4 $°C$, Figures 3.9b and 3.9e), which is the region with the simulated largest increase in time (Figures 3.8b and 3.8e). Finally, the mean July temperature field displays high standard deviation values along the GIS margins, with the largest values along the northwestern margin of Greenland (up to 3.4 $°C$ under a RCP 4.5 scenario, Figure 3.9c, and up to 3.8 $°C$ under a RCP 8.5 scenario, Figure 3.9f).

Chapter 4

Greenland Surface Mass Balance

4.1 Introduction

Recent satellite observations show an increase in the amplitude of the Greenland ice sheet melting over the last decades evolving from near equilibrium conditions during the 1990s to more imbalanced conditions during the first decade of the 21st century and depict also an acceleration in mass loss during the last years (e.g. Shepherd et al. 2012; Velicogna et al. 2014, and more detail in Section 1.3.2). Motivated by the ability to provide projections of future evolution, the changes in Greenland surface mass balance, then, have been extensively studied by means of numerical models (e.g. Ettema et al. 2009; Greve et al. 2011; Rae et al. 2012; Seddik et al. 2012; Fettweis et al. 2013; Quiquet et al. 2013a; Edwards et al. 2014, and more detail in Sections 1.3.2 and 1.3.3).

The purpose of the present chapter, therefore, is to provide new surface mass balance projections for the Greenland ice sheet for the 20th and 21st centuries, by employing the most recent CMIP5 climate forcing fields in connection with the two numerical ice-sheet models presented in Section 2.3. In particular, in this chapter, I investigate the impact of resolution, ice-sheet models and climate forcing on the Greenland surface mass balance.

4.2 Methodology and Experiment Design

The experiments developed in this chapter are performed by means of the two thermo-mechanical ice sheet-ice shelves models described in Chapter 2: GRISLI (Section 2.3.3, Ritz et al. 2001) and SICOPOLIS (Section 2.3.4, Greve 1997a,b). The values of the main model parameters used in GRISLI and SICOPOLIS for the experiments analyzed in this chapter are reported in Table 4.1.

The ice-sheet models, due to the slow diffusivity of surface temperature through the ice sheet, require a spin-up. The spin-up simulations are developed following the initialization procedure used by Greve et al. (2011) in the framework of the SeaRISE experiment and described more in details in Section 2.4.

The simulations from pre-industrial (year 1850) to 21st century, using the climate fields of the selected CMIP5 AOGCMs (Table 3.1), are branched from the spin-up (Figure 4.1).

Due to the coarse horizontal resolution of AOGCMs compared with ISMs, the use of the absolute climate forcing can lead to misrepresentations of SMB (e.g. Quiquet et al. 2012). For this reason, we follow an anomaly method (e.g. Huybrechts et al. 2004; Yan

Table 4.1: Main model parameters of GRISLI and SICOPOLIS. Values taken from [1] Fausto et al. (2009), [2] Quiquet et al. (2012), [3] Tarasov and Peltier (2002), [4] Reeh (1991), and [5] Bales et al. (2009)

Parameter	**GRISLI values**	**SICOPOLIS values**
Gravitational acceleration (g)	9.81 $m\ s^{-2}$	9.81 $m\ s^{-2}$
Density of ice (ρ)	918 $kg\ m^{-3}$	918 $kg\ m^{-3}$
Atmospheric lapse rate (λ) [1]	6.309 $°C\ km^{-1}$	6.309 $°C\ km^{-1}$
Precipitation correction factor (γ) [2]	0.07	0.07
PDD standard deviation (σ_{pdd}) [3]	5.2 $°C$	5.2 $°C$
Cold temperature limit (T_C) [3]	-1 $°C$	-1 $°C$
Warm temperature limit (T_W) [3]	10 $°C$	10 $°C$
DDF for ice $T_{July} < T_C$ (β^C_{ice}) [3]	17.22 $mmw.e.\ d^{-1}\ °C^{-1}$	17.22 $mmw.e.\ d^{-1}\ °C^{-1}$
$T_{July} > T_W$ (β^W_{ice}) [3]	8.3 $mmw.e.\ d^{-1}\ °C^{-1}$	8.3 $mmw.e.\ d^{-1}\ °C^{-1}$
DDF for snow $T_{July} < T_C$ (β^C_{snow}) [3]	2.65 $mmw.e.\ d^{-1}\ °C^{-1}$	2.65 $mmw.e.\ d^{-1}\ °C^{-1}$
$T_{July} > T_W$ (β^W_{snow}) [3]	4.3 $mmw.e.\ d^{-1}\ °C^{-1}$	4.3 $mmw.e.\ d^{-1}\ °C^{-1}$
Saturation factor for formation of superimposed ice (csi) [4]	0.6	0.6
Marsiat temperature limits:		
only liquid precipitation (T_{liq}) [5]	7.2 $°C$	7.2 $°C$
only solid precipitation (T_{solid}) [5]	-11.6 $°C$	-11.6 $°C$
Flow law enhancement factor, Glen	3	3
linear	1	-

et al. 2014), that consists in adding climate anomalies from a coarser model on top of a high resolution climate data set. In the present work, ERA Interim and MAR climates averaged over the years 1980–1999 are considered as the high-resolution reference climates on top of which the coarse CMIP5 AOGCMs climate anomalies are added. For each year of the time series spanning the pre-industrial to the 21st century, the climate forcing fields are calculated as follow:

$$Forcing^{1850-2100}_{annual} = Reference^{1980-1999}_{mean} + \left(AOGCM^{1850-2100}_{annual} - AOGCM^{1980-1999}_{mean}\right) \tag{4.1}$$

where $Forcing^{1850-2100}_{annual}$ represents the final climate fields used to force the ISMs, $AOGCM^{1850-2100}_{annual}$ are the simulated climate from each of the seven CMIP5 AOGCMs, while $AOGCM^{1980-1999}_{mean}$ represents their respective 1980–1999 climatology. Finally, $Reference^{1980-1999}_{mean}$ correspond to the ERA Interim or MAR averaged climatology. In this way, we obtain two different sets of climate forcing (Figure 4.1), one based on ERA Interim climatology ($\text{AOGCM}_{\text{ERAI}}$ in Table 4.2) and one based on MAR climatology ($\text{AOGCM}_{\text{MAR}}$ in Table 4.2). In the present work, the years between 1980 and 1999 are chosen as the reference climatology period, as in the fourth assessment report of the IPCC (2007).

Finally, we define six sets of experiments, summarized in Table 4.2, differing in the horizontal resolution or in the choice of the ISM. Note that the simulations at 5 km horizontal resolution are performed only with GRISLI. The choice of GRISLI for resolution test is motivated by the use of SSA for ice stream areas. Those six sets of experiments are repeated for each realization of the 20th and 21st centuries from the seven CMIP5

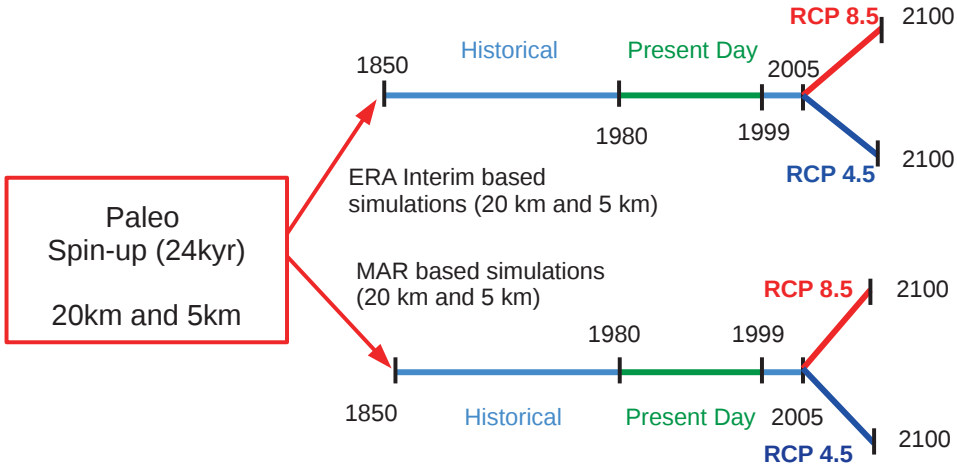

Figure 4.1: Numerical design of the simulations. GRISLI and SICOPOLIS are spun up with 24 kyr paleo-runs. The ISMs climate forcing for the pre-industrial, 20th and 21st centuries simulations are derived according to Eq. 4.1, leading to two subsets of simulations. The 21st century climate forcing follow two future emission scenarios: RCP 4.5 and RCP 8.5. The combinations of ISMs, horizontal resolutions and climate forcing lead to the six sets of experiments under investigation in this study, as reported in Table 4.2.

AOGCMs selected in Table 3.1.

4.3 Impact of climate forcing, resolution and dynamics: 20th century

4.3.1 Overall Greenland SMB analysis (20th century)

The SMBs obtained from the six sets of experiments reported in Table 4.2 are compared in Figure 4.2 and further compared to values reported previously in the literature (Table 4.3). The individual values of Figure 4.2 are reported in Tables 4.4 to 4.6.

Given the formulation in anomaly mode for the climate forcing (Eq. 4.1), we consider two aspects of climate forcing that can impact on SMB: (1) change in reference climatology and (2) use of different CMIP5 AOGCMs from which anomalies are taken.

The impact of changes in the reference climatology is studied by comparing the sets of experiments based on ERA Interim (G_{E20}, S_{E20}, G_{E5}) with the sets of MAR-based experiments (G_{M20}, S_{M20}, G_{M5}), respectively. In general, the computed SMB is generally lower in the sets of experiments based on MAR than in the sets of experiments based on ERA Interim (mean difference ~91 Gt/yr) since ablation is larger when using MAR as the reference climatology (mean difference ~114 Gt/yr, Figure 4.2b). This is because MAR tends to be warmer than ERA Interim along the GIS margins where most of the ablation occurs, as described in Section 3.2.4 (Figure 3.3). No substantial difference in accumulation is simulated between MAR and ERA Interim based experiments (mean

Table 4.2: Experiments developed in this chapter using GRISLI and SICOPOLIS. GRISLI simulations are performed using two different resolutions. Two subsets of forcing fields are derived from Eq. 4.1: one based on present-day (1980–1999) ERA Interim fields and one based on MAR climate fields. Note that the G_E and S_E correspond to the simulations carried out using GRISLI and SICOPOLIS respectively and forced with ERA Interim as reference climatology. G_M and S_M refer to the MAR-based experiments, and 20 and 5 correspond to the horizontal resolution of the simulations.

Name	**ISM**	**Resolution**	**Reference**	**Forcing**
G_{E20}	GRISLI	20 km	ERA Interim	$AOGCM_{ERAI}$
G_{M20}	GRISLI	20 km	MAR	$AOGCM_{MAR}$
S_{E20}	SICOPOLIS	20 km	ERA Interim	$AOGCM_{ERAI}$
S_{M20}	SICOPOLIS	20 km	MAR	$AOGCM_{MAR}$
G_{E5}	GRISLI	5 km	ERA Interim	$AOGCM_{ERAI}$
G_{M5}	GRISLI	5 km	MAR	$AOGCM_{MAR}$

Table 4.3: Reported estimate of accumulation (Acc), ablation (Abl) and surface mass balance (SMB) from literature. Values are given in Gt/yr.

Paper	*Model*	*Period*	*Acc*	*Abl*	*SMB*
Hanna et al. (2005)	ECMWF reanalysis	1958–2003	573 ± 70	280 ± 69	293 ± 104
Box et al. (2006)	Polar MM5	1988–2004	543 ± 131	373 ± 66	170 ± 152
Fettweis (2007)	MAR	1979–2005	612 ± 55	304 ± 96	308 ± 125
Ettema et al. (2009)	RACMO2/GR	1958–2007	743 ± 78	274 ± 67	469 ± 41
Fettweis et al. (2013)	MAR (ERA Interim)	1980–1999	662 ± 55	274 ± 66	388 ± 103

difference ∼23 Gt/yr, Figure 4.2a).

Further, especially the GRISLI simulations are highly sensitive to the use of different climate forcing, especially at 20 km resolution (G_{E20} and G_{M20} in Figure 4.2). For example, the simulations forced with CCSM4, CNRM and IPSL fields present SMB values 127 Gt/yr higher in average with respect to the other AOGCMs (Figure 4.2c). This difference is mostly driven by ablation, since the computed accumulation does not differ significantly among all the AOGCMs (about 28 Gt/yr). This difference in ablation is related to higher air surface temperature simulated by these AOGCMs along the northern GIS margins areas compared to ERA Interim (Figures 3.5 and 3.6 in Section 3.2.4).

SICOPOLIS, instead, is less sensitive than GRISLI to the different climate forcing, showing spreads two or three times smaller than spreads obtained with GRISLI (largest difference among AOGCMs: 14 Gt/yr in accumulation, 64 Gt/yr in ablation and 53 Gt/yr in SMB, Figure 4.2). The different behavior of SICOPOLIS and GRISLI derives from the simulated spin-up ice topographies and especially from the ice-sheet profile resulting from both ISMs (Figure 4.3). In SICOPOLIS, the ice-sheet slopes are steeper than in GRISLI. Therefore, a smaller ice-sheet surface area is exposed to the changes in climate occurring along the margins where most of the ablation occurs (Figure 4.3a). In fact, the largest difference between SICOPOLIS spin-up and observation occur in the region close to the coast (Figure 4.3b).

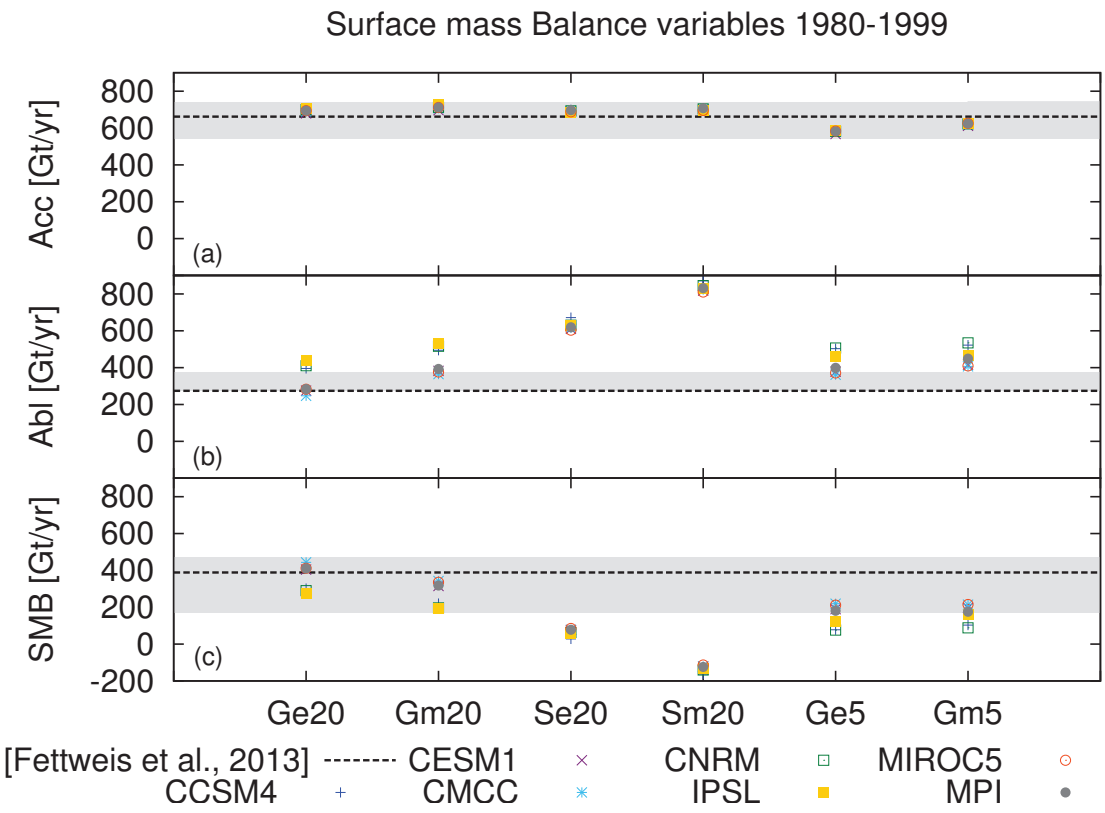

Figure 4.2: Mean annual simulated (a) accumulation (Acc, Gt/yr), (b) ablation (Abl, Gt/yr), and (c) surface mass balance (SMB, Gt/yr) averaged over 1980–1999 for each experiment described in Table 4.2 and for each of the considered AOGCMs climate forcing. These variables are computed in each ice-covered grid point, which evolve in time. Grey shaded regions give the range of values from previous studies reported in Table 4.3. The black dashed lines shows the simulated values by Fettweis et al. (2013), which are averaged over the same years (Table 4.3).

The impact of ISM dynamics on the SMB is tested by comparing runs G_{E20} and G_{M20} to S_{E20} and S_{M20}.

SICOPOLIS generates a lower initial topography, which induces higher ablation rates than using GRISLI during runtime by means of the elevation correction feedback (Eq. 2.53 and Eq. 2.54). This difference leads to simulated mean negative SMB values (S_{M20}, mean value of -131 Gt/yr), or close to zero (S_{E20}, mean value of 66 Gt/yr) when using SICOPOLIS (Figure 4.2c). On the contrary, when using GRISLI, the SMB remains positive over the whole 20th century and values are in the range of published estimates (G_{E20} mean SMB value $\sim$ 362 Gt/yr, G_{M20} mean SMB value $\sim$ 275 Gt/yr), even if the ablation values are slightly overestimated compared to estimates from previous studies (Table 4.3). Note that this differences are not attributable to the dynamical difference of the two ISMs (SICOPOLIS, SIA model, and GRISLI, SIA-SSA model). In fact, we run a SIA-version of GRISLI which presents lower ablation values ($\sim$36 Gt/yr) with respect to our G_{E20} simulations. This behavior can be ascribed to a faster flow simulated by the SSA accounted for in G_{E20} which leads to thinning at the lower parts of the ice sheet

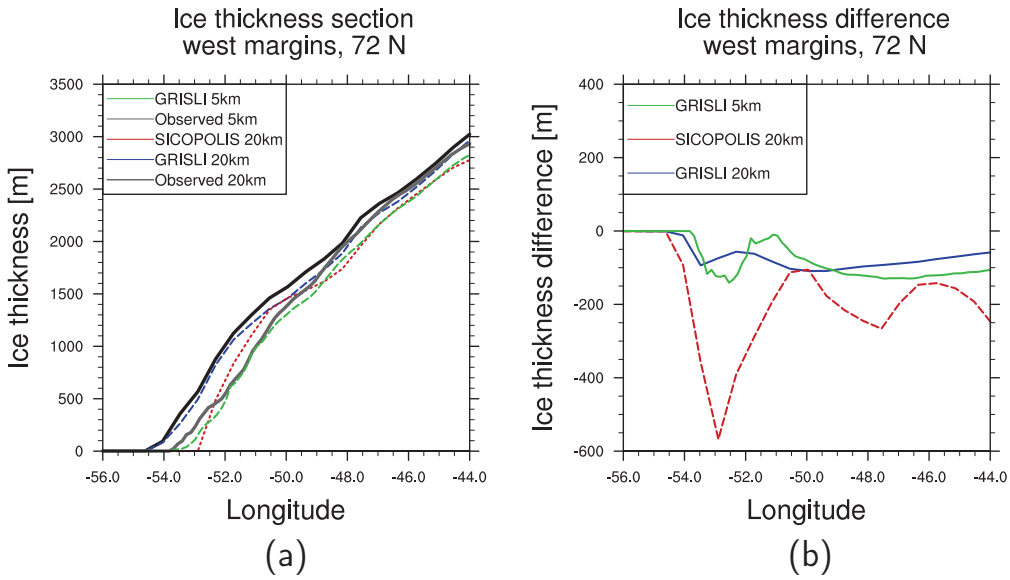

Figure 4.3: (a) Profiles of ice thickness along the western margin of Greenland at 72 °N from observations (black and gray curves, Bamber (2001) and Bamber et al. (2013), respectively) and from spin-up runs (blue, red and green curves, GRISLI at 20 km resolution, SICOPOLIS at 20 km resolution and GRISLI at 5 km resolution, respectively). (b) The difference in ice thickness along the same section between spin-up runs and observations.

surface supporting a larger ablation region with respect to the SIA-version of GRISLI.

To investigate the impact of resolution we compare the results obtained with GRISLI using the two different horizontal resolutions: 20-km resolution (G_{E20} and G_{M20}) and 5-km resolution (G_{E5} and G_{M5}). Increasing horizontal resolution leads to a SMB reduction of about 160 Gt/yr (Figure 4.2c). About two thirds of this difference is explained by a decrease in accumulation in the 5-km sets of experiments (100 Gt/yr on average, Figure 4.2a), while the remaining one third is due to differences in simulated ablation (60 Gt/yr on average, Figure 4.2b). The sets of experiments performed with GRISLI at 5-km resolution better resolve the ice-sheet topography, especially along the GIS margins, with respect to the sets of experiments based on GRISLI at 20 km. These differences in ice-sheet topography impact the downscaling and elevation correction techniques (Eq. 2.53 and Eq. 2.54), as well as the accumulation through the Marsiat (1994) relationship, leading to the simulated discrepancies in SMB values.

In summary, both ISMs at 20 km resolution show a similar sensitivity to the reference climate, i.e. MAR or ERA Interim. On the contrary, the simulations developed with GRISLI at 5 km resolution present small differences when the reference climatology is changed (Figure 4.2). Both ISMs are sensitive to the choice of the climate forcing, GRISLI exhibiting the most AOGCM-dependent SMB values. Over the whole six sets of experiments, the largest difference in ablation and SMB is given by the comparison of the two ISMs and not by the spread obtained out of the seven CMIP5 AOGCMs. The differences between the two ISMs mainly derives from the discrepancies in the initial spin-up ice-sheet topographies (Figure 2.14). The change in resolution have the smallest impact on the calculation of SMB, and mainly influences accumulation.

Table 4.4: Averaged values of accumulation (Acc, Gt/yr), ablation (Abl, Gt/yr) and surface mass balance (SMB, Gt/yr) over the period 1980-1999 for the whole Greenland Ice Sheet area obtained with the sets of experiments G_{E20} and G_{M20}. The values reported are the model realization averages, except for CMCC CM and IPSL which have only one realization. The bold values are in line with the previous literature works (Table 4.3).

Model	**Acc**		**Abl**		**SMB**	
	G_{E20}	G_{M20}	G_{E20}	G_{M20}	G_{E20}	G_{M20}
CCSM4	**696 ± 4**	**714 ± 4**	395 ± 35	494 ± 29	**301 ± 34**	**220 ± 26**
CESM1	**679 ± 5**	**697 ± 7**	**275 ± 13**	382 ± 27	**404 ± 12**	**315 ± 22**
CMCC CM	**690 ± 1**	**707 ± 1**	247 ± 1	**365 ± 1**	**443 ± 1**	**342 ± 1**
CNRM	**700 ± 1**	**712 ± 1**	410 ± 39	516 ± 37	**290 ± 39**	**196 ± 36**
IPSL	**708 ± 1**	**725 ± 1**	436 ± 1	530 ± 1	**272 ± 1**	**195 ± 1**
MIROC5	**694 ± 4**	**711 ± 3**	**283 ± 38**	376 ± 36	**411 ± 37**	**335 ± 36**
MPI	**694 ± 2**	**711 ± 1**	**284 ± 8**	393 ± 13	**410 ± 7**	**318 ± 12**

Table 4.5: As Table 4.4, but for the sets of experiments S_{E20} and S_{M20}. The values are given in Gt/yr and averaged over the period 1980–1999. The bold values are in line with the previous literature works (Table 4.3).

Model	**Acc**		**Abl**		**SMB**	
	S_{E20}	S_{M20}	S_{E20}	S_{M20}	S_{E20}	S_{M20}
CCSM4	**699 ± 4**	**707 ± 4**	671 ± 11	870 ± 10	28 ± 9	-163 ± 8
CESM1	**686 ± 5**	**696 ± 4**	610 ± 17	818 ± 15	77 ± 12	-122 ± 11
CMCC CM	**691 ± 1**	**702 ± 1**	615 ± 1	823 ± 1	77 ± 1	-121 ± 1
CNRM	**693 ± 5**	**704 ± 6**	630 ± 13	845 ± 10	63 ± 17	-141 ± 11
IPSL	**684 ± 1**	**695 ± 1**	627 ± 1	828 ± 1	57 ± 1	-133 ± 1
MIROC5	**688 ± 5**	**696 ± 4**	603 ± 9	810 ± 10	85 ± 5	-114 ± 7
MPI	**697 ± 1**	**707 ± 1**	619 ± 8	831 ± 6	78 ± 9	-124 ± 7

Finally, we compare the SMB estimates obtained with the six sets of experiments against previous values from literature work (Table 4.3). We consider five distinct studies: one based on reanalysis (Hanna et al. 2005), one based on the RCM Polar MM5 (Box et al. 2006), two studies using the RCM MAR (Fettweis 2007; Fettweis et al. 2013) and one study based on the RCM RACMO2/GR (Ettema et al. 2009). The SMB values derived from those studies present a large spread, with values ranging between 170 Gt/yr (Box et al. 2006) and 469 Gt/yr (Ettema et al. 2009). Accumulation present values in the range between 543 Gt/yr (Box et al. 2006) and 743 Gt/yr (Ettema et al. 2009), while ablation between 274 Gt/yr (Ettema et al. 2009; Fettweis et al. 2013) and 373 Gt/yr (Box et al. 2006). Note that the values provided in each of those studies were calculated on different time periods, as reported in Table 4.3. Only Fettweis et al. (2013) perform their estimates on the period 1980–1999, as done in this work. Therefore, in addition to the different methods used in those studies, the periods do not exactly match, which partly explains the large spread in SMB values. For example, the lower bound of 170 Gt/yr in SMB values is obtained over the period 1988–2004 with the RCM Polar MM5 (Box et al.

Table 4.6: As Table 4.4, but for the sets of experiments G_{E5} and G_{M5}. The values are given in Gt/yr and averaged over the period 1980–1999. The bold values are in line with the previous literature works (Table 4.3).

Model	**Acc**		**Abl**		**SMB**	
	G_{E5}	G_{M5}	G_{E5}	G_{M5}	G_{E5}	G_{M5}
CCSM4	**582 ± 3**	**625 ± 3**	503 ± 28	522 ± 16	78 ± 29	103 ± 16
CESM1	**567 ± 8**	**612 ± 6**	378 ± 18	416 ± 10	**189 ± 22**	**197 ± 9**
CMCC CM	**580 ± 1**	**621 ± 1**	**361 ± 1**	**407 ± 1**	**219 ± 1**	**214 ± 1**
CNRM	**582 ± 1**	**622 ± 2**	506 ± 59	534 ± 63	76 ± 58	88 ± 62
IPSL	**586 ± 1**	**627 ± 1**	463 ± 1	465 ± 1	123 ± 1	161 ± 1
MIROC5	**583 ± 4**	**625 ± 3**	**371 ± 29**	409 ± 27	**211 ± 30**	**215 ± 26**
MPI	**581 ± 1**	**624 ± 1**	399 ± 8	449 ± 3	**181 ± 8**	**175 ± 2**

2006), while the upper bound of 469 Gt/yr corresponds to the period 1958–2007 with the RCM RACMO2/GR (Ettema et al. 2009).

In general, the accumulation values simulated in the six sets of experiments are in line with the values of the previous studies (gray shaded region in Figure 4.2a). On the contrary, in general, the simulated ablation values overestimate the estimates from literature, especially in the sets of experiments based on SICOPOLIS (gray shaded region in Figure 4.2b). Finally, the SMBs computed with GRISLI, especially at 20 km resolution, fall in the range of the SMB values suggested in the set of previous studies reported in Table 4.3 (gray shaded region in Figure 4.2c).

4.3.2 Regional SMB analysis (20th century)

In the previous section, we presented the SMB values averaged over the entire Greenland ice sheet. Few studies perform a regional analysis at sub-basins scale (e.g. Tedesco and Fettweis 2012; Vernon et al. 2013), and only Fürst et al. (2015) evaluate their present-day CMIP5-based experiments at regional scale. Therefore, in the following, we investigate the impact of climate forcing, ISM dynamics and ISM horizontal resolution on the regional variations of accumulation, ablation and SMB for the seven main drainage basins of Greenland, as defined by Sasgen et al. (2012).

The simulated present-day SMB for half of the considered sub-regions can be either positive or negative depending on the sets of experiments considered. The other basins, instead, show a consistent behavior in SMB for all the sets of experiments (Figure 4.4). The northern basin has negative SMB values in all the cases ($\sim$ -66 Gt/yr, on average), due to low accumulation rates (25 Gt/yr, on average). Differences in ablation, on the contrary, drive the spread of the SMB values (from -27 Gt/yr, G_{E20}, to -95 Gt/yr, S_{M20}). The eastern, south-eastern and southern basins feature positive SMB values in all the sets of experiments (average SMB of 87 Gt/yr, 102 Gt/yr and 34 Gt/yr, respectively). These sub-regions get the highest amount of precipitation of all the GIS. In fact, the high simulated SMB mostly results from high accumulation values occurring in those basins (always above 54 Gt/yr).

On the contrary, the north-western, south-western and north-eastern basins exhibit model-dependent values. In fact, those regions presents SMB values either positive or

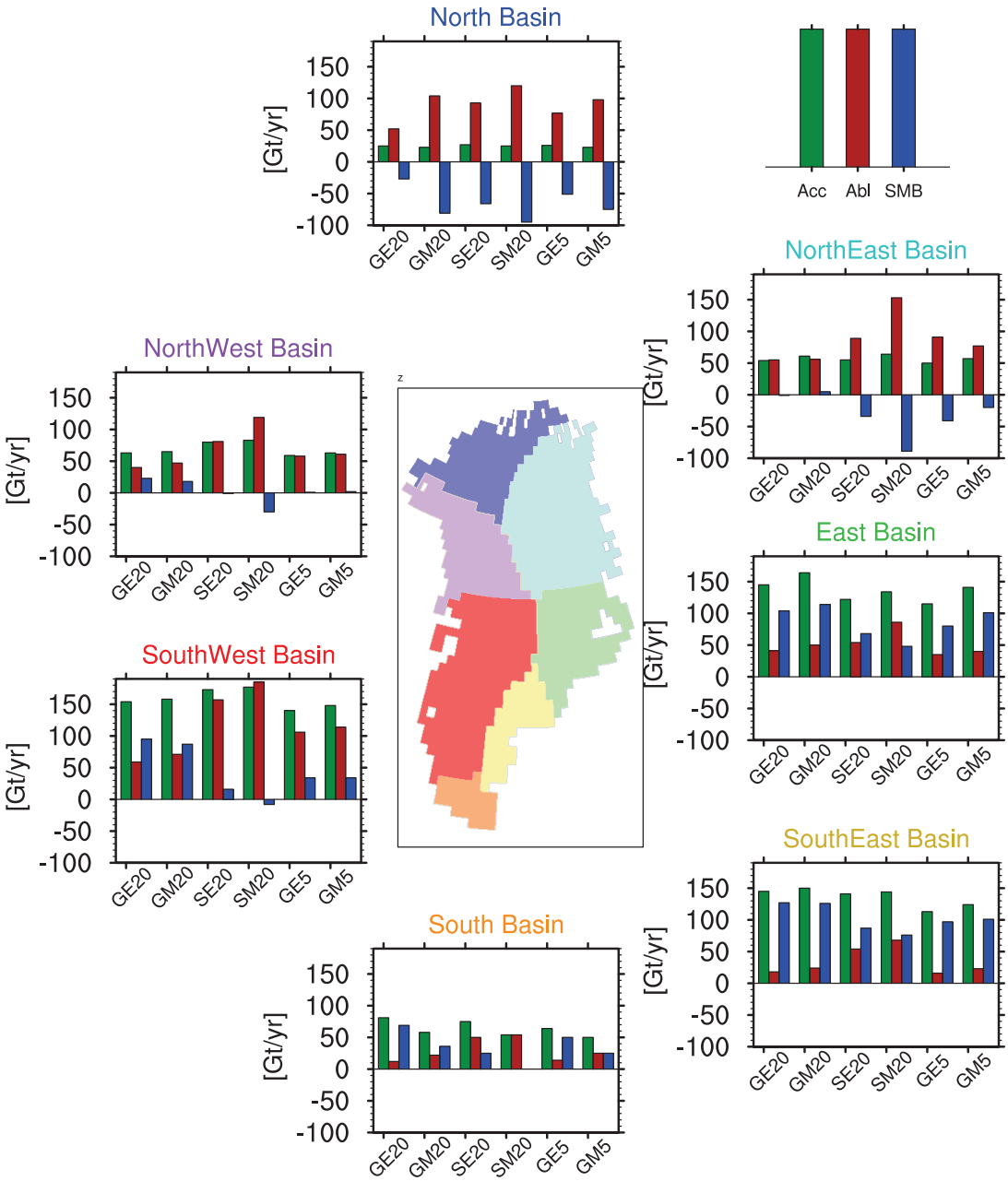

Figure 4.4: Regional mean values of accumulation (Acc, green), ablation (Abl, red), and surface mass balance (SMB, blue) obtained with the set of experiments reported in Table 4.2 over the period 1980–1999 in Gt/yr. The regional basin subdivision is from Sasgen et al. (2012). The black horizontal lines correspond to 0 Gt/yr.

negative depending on the considered set of experiments. For example, the SMB values computed in the north-western basin range between -30 Gt/yr (S_{M20}) and 23 Gt/yr (G_{E20}). The discrepancies among each set of experiments are mostly due to changes in ablation (Figure 4.4). However, on average, the north-western, south-western and north-eastern basins exhibit approximately balanced condition (6 Gt/yr), a positive SMB value (43 Gt/yr) and a negative SMB value (-30 Gt/yr), respectively.

In general, the lowest SMB estimates correspond to the MAR-based experiments carried out with SICOPOLIS, as previously found in the total GIS SMB values. The accumulation shows only small variations among the different cases, while the ablation changes impact on the SMB differences between the sets of experiments, as seen previously in Figure 4.2.

The regional SMB patterns obtained here are similar to those reported in Vernon et al. (2013). They obtain the lowest SMB in the northern part of GIS, however with positive values (∼16 Gt/yr), and the highest SMB along the southeastern coast (∼132 Gt/yr). These discrepancies result from the different methodology used in Vernon et al. (2013) (RCMs) and from the different reference period on which the averages are calculated, i.e. 1961–1990 in Vernon et al. (2013), 1980–1999 in the present study.

Finally, to assess the performance of our simulations at regional scale, we compare the spatial distribution of elevation changes to the average changes of the same variable on the period 2003–2009 derived from the satellite observations ICESat (Figure 4.5, Sørensen et al. 2011; Sasgen et al. 2012). Note that there are not many continuous spatial observations available and this comparison is performed over six years. Our analysis is performed considering the simulations carried out using the AOGCMs climate forcing leading to SMB values which are in better agreement with previous literature estimates (Figure 4.2, Fettweis et al. 2013). These six experiments exhibit a large reduction in ice thickness in the northern regions (Figure 4.5), while the eastern margin exhibits an increase in elevation in all the experiments except for G_{M5} and S_{M20} (Figure 4.5c and 4.5d). The western and southern margins ice elevation changes, instead, do not show the same behavior: an increase in elevation is simulated in the experiments G_{M20}, G_{E20}, and G_{E5} (Figures 4.5b, 4.5e, and 4.5f), while a decrease in elevation is computed in the experiments G_{M5}, S_{M20}, and S_{E20} (Figures 4.5c, 4.5d, and 4.5g).

ICESat data (Sasgen et al. 2012) over the same period (2003–2009) show a decrease in elevation along the southeastern and western margins (Figure 4.5a). On the contrary, the elevation changes in the northeastern and the northern margins, exhibit a local variability which is strongly influenced by the behavior of each outlet glaciers, as stated by Sørensen et al. (2011). The experiment G_{M5} (Figure 4.5c) exhibits a pattern of elevation changes similar to observations. This good match might result from the high grid resolution used in this experiment allowing for a better representation of the marginal processes, combined to the high resolution present-day reference climate MAR, which better resolves the climate along the GIS margins with respect to ERA Interim (Figure 3.3). Anyhow, even this case (G_{M5}) still show large discrepancies with respect to observation (Figure 4.5).

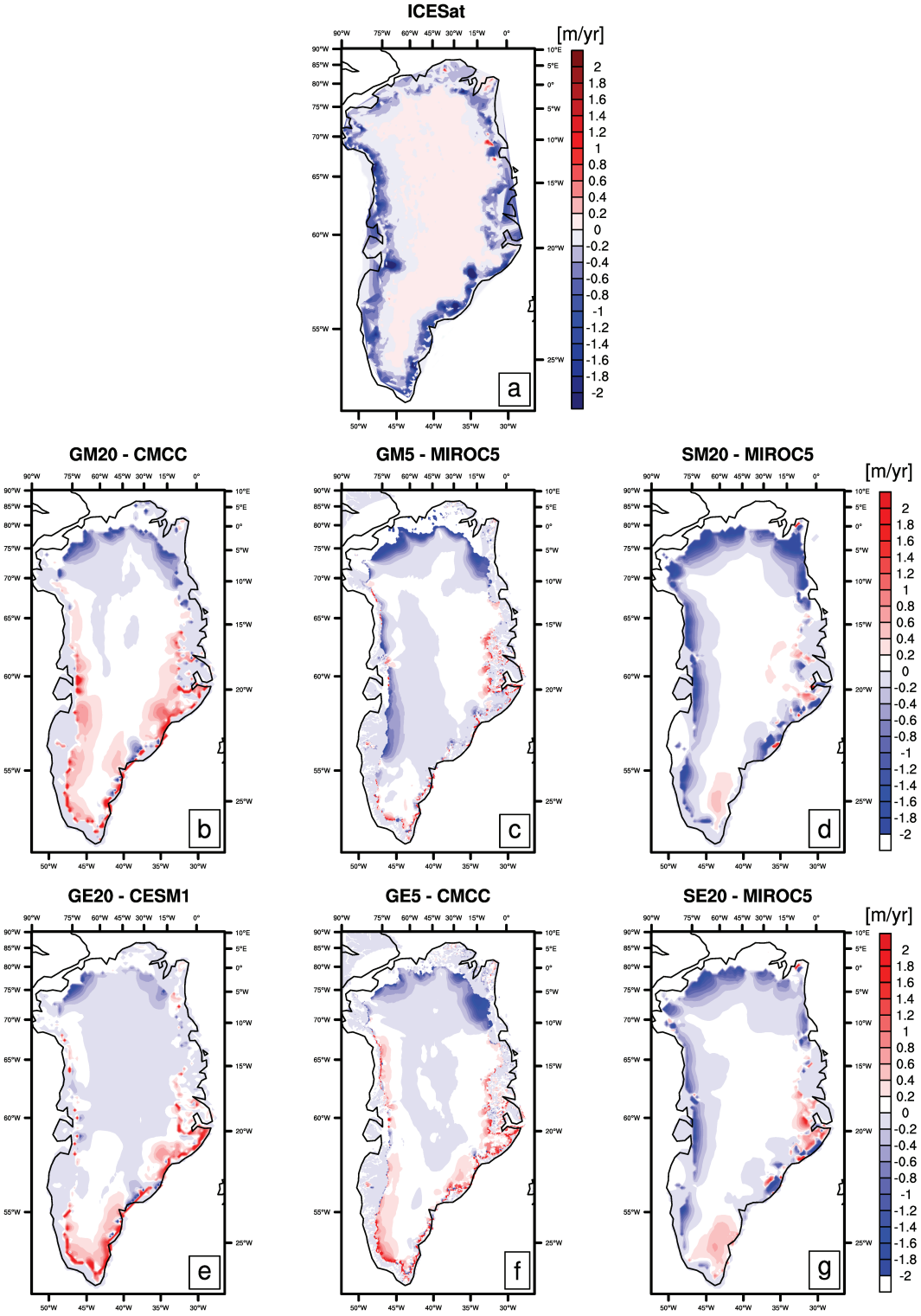

Figure 4.5: (a) Observed elevation changes (m/yr) by means of ICESat data on the period 2003–2009 (Sasgen et al. 2012). (b-g) Simulated spatial distribution of elevation changes (m/yr) averaged on the period 2003–2009 for each set of experiments.

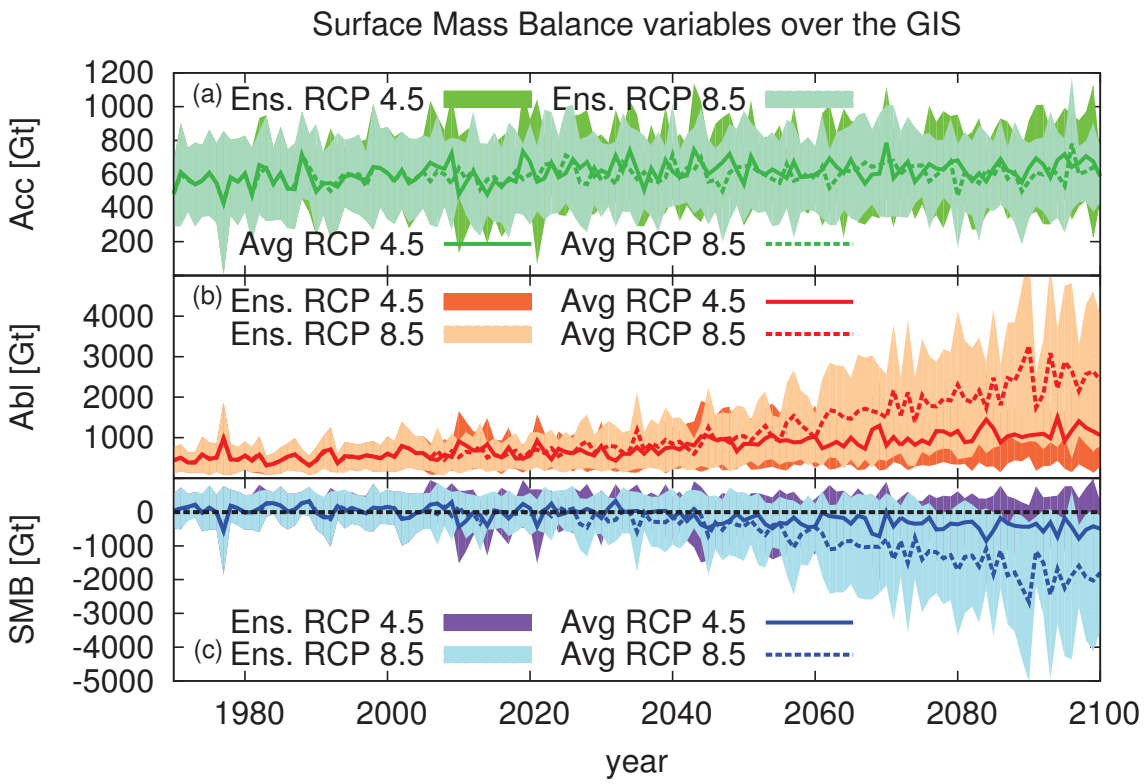

Figure 4.6: Time series of (a) accumulation (Acc), (b) ablation (Abl), and (c) surface mass balance (SMB) obtained with G_{E5} in Gt/yr. Shaded regions indicate the ensemble spread, while solid and dashed lines represent the multi-model ensemble means. Black dashed line correspond to SMB equals to zero.

4.4 Greenland surface mass balance evolution: 21st century

4.4.1 Overall Greenland SMB analysis (21st century)

The 21st century simulations are performed using the two future emission scenarios RCP 4.5 and RCP 8.5 (Figure 4.1). The climate fields come from the set of seven CMIP5 AOGCMs (Table 3.1). The number of realizations differ for each AOGCM and between future scenarios. In particular, we have 20 realizations with RCP 8.5 future scenario and 18 with RCP 4.5 one, as reported in Table 3.1. Given the large number of realizations, we start by analyzing their impact on the future evolution of the GIS SMB. As an example, we describe the results obtained with one of the high resolution ice-sheet model configuration, G_{E5} (Figure 4.6).

The set of CMIP5 AOGCMs leads to a large spread of 21st century GIS SMB future evolution (Figure 4.6c). The RCP 4.5 simulations show a slow decrease in SMB that becomes negative by the end of the 2040s, with values ranging between -1463 Gt/yr and 610 Gt/yr by the end of the 21st century. In the RCP 8.5 simulations, SMB becomes negative in the first half of the 21st century (end of 2020s), with a larger spread by 2100 (-3634 Gt/yr to -16 Gt/yr). Note that in the most extreme RCP 8.5 simulation SMB is

negative since 1970 and reaches -4000 Gt/yr by 2090s, while the most optimistic RCP 4.5 simulation show an almost steady SMB during the entire 21st century (Figure 4.6c). The trend in SMB over the 21st century results from time-increasing ablation (Figure 4.6b) because accumulation does not vary substantially between the two scenarios by the end of the 21st century (Figure 4.6a).

In the following, we apply a 10-year moving average with step of 5 years to the ensemble mean accumulation, ablation and SMB time series in order to increase readability. GRISLI is highly sensitive to the future scenario considered. In fact, the difference between the two SMB values in 2100 using RCP 4.5 and RCP 8.5 climate forcing is of about 1350 Gt/yr (Figures 4.7a and 4.7c). On the contrary, the difference in SMB between RCP 4.5 and RCP 8.5 simulated with SICOPOLIS at the end of the 21st century is about 600 Gt/yr (Figure 4.7b). This discrepancy derives from the differences in the behavior of accumulation and ablation computed by the two ISMs. In the GRISLI experiments at both resolutions, 20 km and 5 km, the accumulation stays constant during the entire 21st century (about 700 Gt/yr, in average) for both scenarios. The difference in computed SMB between the two RCP scenarios in GRISLI, then, results from ablation. In fact, the RCP 8.5 simulations exhibit a stronger increase in ablation with respect to RCP 4.5 simulations, which lead to a difference of $\sim$ 1390 Gt/yr by 2100, comparable to the difference in SMB. The SICOPOLIS experiments, instead, exhibit a large increase in accumulation during the 21st century with a different amplitude depending on the considered RCP scenario (up to 1100 Gt/yr for RCP 4.5, and 1410 Gt/yr for RCP 8.5). Note that SICOPOLIS maintains a SMB close to zero in the RCP 4.5 scenario during the entire 21st century.

The cumulative decreases in ice volume, that range from 10.8 to 12.9 $cm\,SLE$ (14.9 to 18.0 $cm\,SLE$) over the period 2006–2100 under a RCP 4.5 (RCP 8.5) scenario, are in line with the results obtained in similar works in which the same external climate forcing, i.e. CMIP5 with RCP 4.5 and RCP 8.5 scenarios, are used (e.g. Yan et al. 2014; Fürst et al. 2015). Differently from Yan et al. (2014) and Fürst et al. (2015), we highlight the changes and the impact of each the components of the SMB, i.e. accumulation and ablation, on the final variations in SMB. Furthermore, we use two different ISMs at two different resolutions with the aim to highlight the uncertainties of model dynamics and resolution together with the uncertainties coming from the use of many climate forcing.

Finally, the projections of SMB in the 21st century can be used in estimating a timing in which the mean GIS SMB reaches a long-term negative condition, as done, for example, by Fettweis et al. (2013). A long-term negative condition for GIS represents a tipping point for the climate system (Lenton et al. 2008). Therefore, we take the zero SMB value as a threshold. However, the choice of zero SMB as threshold, in our sets of experiments, could be questionable since a negative SMB will occur earlier for experiments that underestimate the current SMB, as highlighted by Fettweis et al. (2013). If we do not consider the lower bound case (S_{M20}), for which the threshold is passed already in the 20th century, the SMB values simulated by the sets of experiments reach and pass the zero SMB threshold between 2040 (G_{E5} and G_{M5}) and 2080 (G_{E20}) for the RCP 4.5 case and between 2010 (G_{E5} and G_{M5}) and 2050 (G_{E20}) for the RCP 8.5 case (Figure 4.7). Given the assumption on which our approach relies, one should be careful on the interpretation of those timings. In fact, the negative SMB condition occurs about two decades earlier than what expected, if we directly consider the temperature thresholds of Gregory and Huybrechts (2006) (4.5 °C increase in mean annual air surface

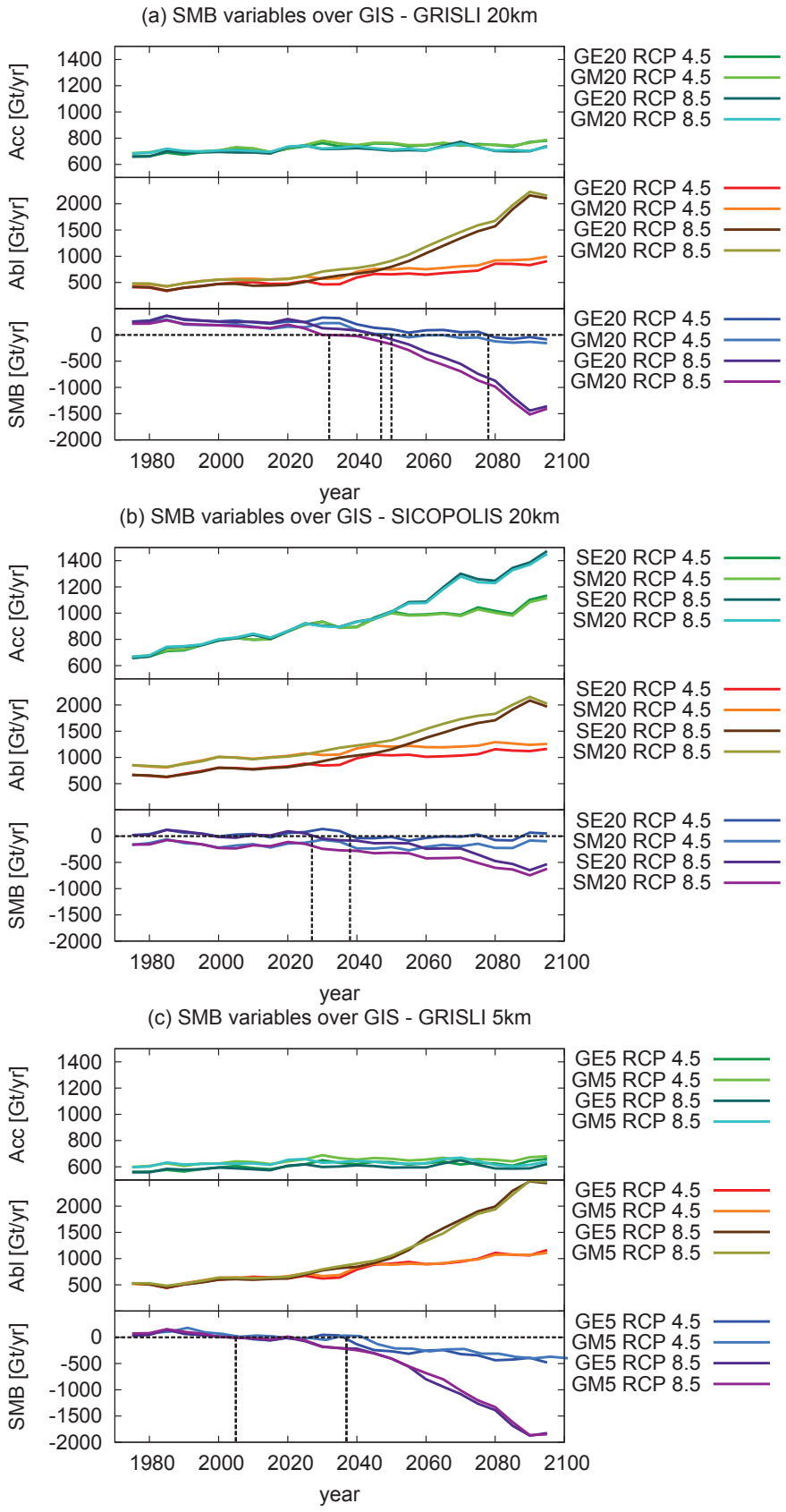

Figure 4.7: Time series of accumulation (Acc), ablation (Abl), and surface mass balance (SMB) obtained with (a) GRISLI at 20 km resolution, (b) SICOPOLIS at 20 km resolution and (c) GRISLI at 5 km resolution for both future scenarios in Gt/yr. The curves represent the multi-model ensemble mean on which a 10-year moving average with 5 years step is applied. The horizontal black line represent the zero SMB threshold, while the vertical ones help in locating the year when the zero SMB threshold is passed.

temperature with respect to pre-industrial) and Robinson et al. (2012) (1.6 °C increase in mean summer air surface temperature with respect to pre-industrial) on the simulated AOGCMs air surface temperature evolution.

4.4.2 Regional SMB analysis (21st century)

Differently from previous work in which CMIP5 climate forcing are employed (e.g. Yan et al. 2014; Fürst et al. 2015), we analyze the evolution of SMB in the seven Greenland sub-regions defined by Sasgen et al. (2012), as done in the 20th century analysis. The comparison between observation and simulations in Section 4.3.2 shows the limit of our simulations in computing a proper distribution of ice elevation changes at 20 km, if compared to satellite data (e.g., ICESat, Sasgen et al. 2012; Sørensen et al. 2011). The experiments developed at 5-km resolution with GRISLI, instead, show a better agreement with observations even if large discrepancies still persist (Figure 4.5). For this reason, in this section, we analyze only the simulated time evolution of SMB obtained with GRISLI on the 5-km resolution grid (G_{E5} and G_{M5}).

In general there is no large difference between the simulated SMB based on ERA Interim and based on MAR reference climates (25 Gt/yr in average), except in the southern basin and in the north-eastern basin (Figure 4.8). The largest simulated reduction in SMB by the end of the 21st century reaches 1.6 Gt/yr^2, in average, over the period 2010–2100 in the northern basin for RCP 4.5 simulations, and 3.9 Gt/yr^2, in average, over the same period in the north-western basin for RCP 8.5 simulations. Furthermore, the decrease in SMB accelerates after the decade 2031–2040 in the entire set of experiments for both scenarios. However, this acceleration is less important in RCP 4.5 than in RCP 8.5 simulations. For example, the RCP 4.5 experiments show an increase in acceleration from 0.7 Gt/yr^2 over the period 1970–2035 to 1.7 Gt/yr^2 over the period 2035–2100 in the northern basin, while the RCP 8.5 experiments go from 1 Gt/yr^2 to 4.3 Gt/yr^2 in the same basin and time frames. Note that in the southern regions, on the contrary, the reduction in SMB is smaller than in the other basins in both scenarios case. We relate it to larger precipitation rates projected in those areas by the end of the 21st century (Figure 3.8).

The trend of the RCP 4.5 SMB projection for the entire GIS mainly results from the SMB of the northern regions, since the southern regions SMB changes are smaller. On the other hand, in the case of the RCP 8.5 scenario, all the basins exhibit the same SMB time-evolution by the end of the 21st century. Therefore, the averaged SMB changes over the entire GIS reflect the regional changes through out the 21st century.

This regional analysis shows us that the northern part of Greenland seems to be the area that might influence the most the future trend of the Greenland ice sheet SMB, which is in agreement with previous works (e.g. Quiquet et al. 2012; Tedesco and Fettweis 2012). Moreover, the regional analysis exhibits that the western part of the ice sheet will be in imbalance sooner than the eastern part, as stated by Tedesco and Fettweis (2012). The large reduction in the northern Greenland ice volume could be explained by local reduction in albedo resulting from the projected melting of the Arctic sea-ice cover along the coast of Greenland, that causes a local warming (Fettweis et al. 2013). Since the projected precipitation remains low over this area in the CMIP5 AOGCMs, the melting of the northern GIS due to this local warming is not compensated for. As opposed to northern GIS evolution, the southern region shows balanced conditions over the 21st century resulting from the increase in precipitation simulated by the CMIP5 AOGCMs

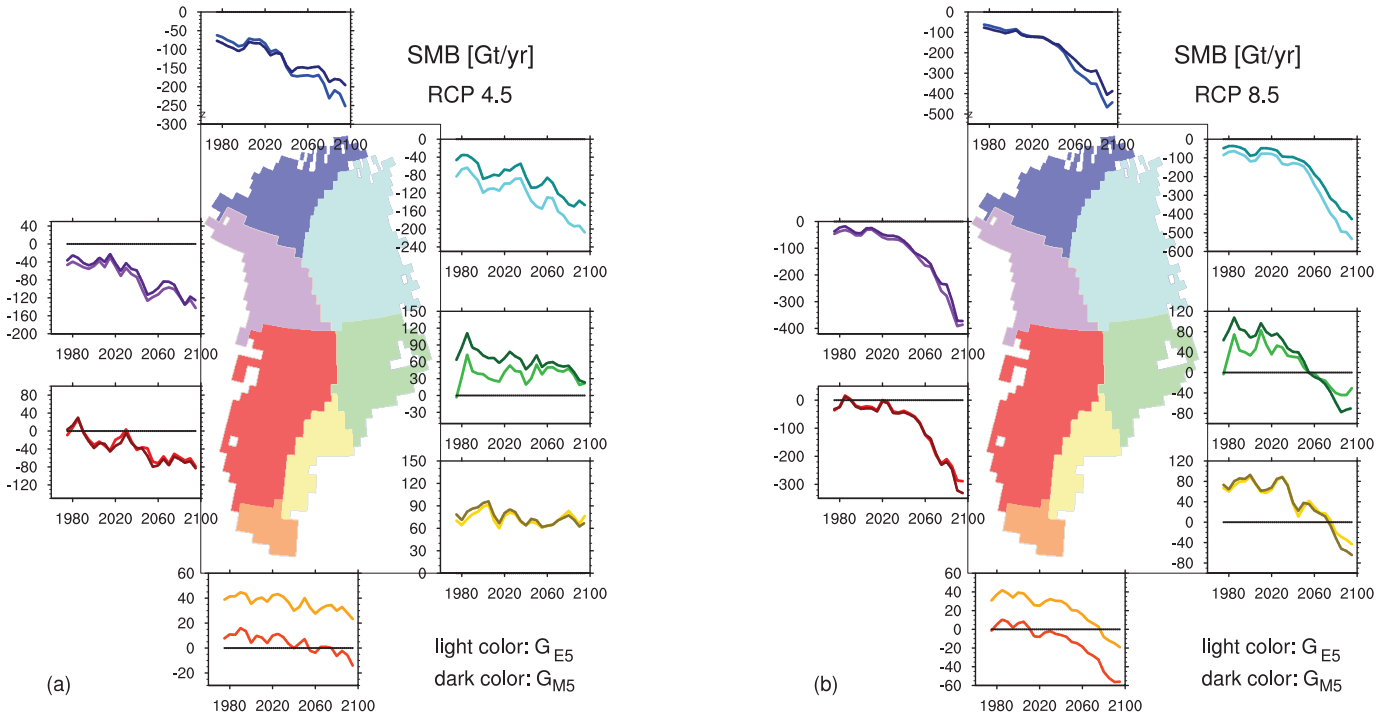

Figure 4.8: Regional SMB time series in Gt/yr simulated with G_{E5} and G_{M5} using (a) RCP 4.5 and (b) RCP 8.5 future scenarios. Black line corresponds to zero SMB. The curves represent the multi-model ensemble mean on which a 10-year moving average with 5 years step is applied. Note that the scale varies between the basins.

evolution in the RCP 4.5 scenario. Only an increase in temperature as large as in the RCP 8.5 scenario could overwhelm this balance between accumulation and ablation simulated for the RCP 4.5 scenario.

4.5 Summary

20th and 21st centuries simulations of the Greenland ice sheet SMB were carried out using two ISMs forced with the anomalies of a set of seven CMIP5 AOGCMs on top of reanalysis (ERA Interim) and regional climate model (MAR) fields. We provided and analyzed the evolution of the SMB components, namely accumulation and ablation, at both Greenland scale and sub-regional scale. Our results show that:

- the change of climate forcing, ISM dynamics and ISM horizontal resolution impact on the overall GIS SMB estimates during 20th and 21st centuries. In particular:
  - the increase in resolution leads to lower SMB value due to a lower accumulation;
  - the choice of ISM has a substantial impact on ablation, which mainly comes from differences in the initial ice sheet topography;
  - the ISMs are sensitive to the reference climate, i.e. MAR or ERA Interim, and both ISMs are sensitive to the changes in CMIP5 AOGCMs climate forcing, GRISLI being the most sensitive;
- on regional scale, the simulated present-day SMB of a set of basins (namely north-eastern, south-western and north-western) can be either positive or negative depending on the chosen ice-sheet model, resolution and climate forcing;
- the experiments developed at higher resolution, especially G_{M5}, show spatial pattern of elevation changes close to ICESat observations, even if large discrepancies still remain;
- during the 21st century, the regional SMB trends exhibit a common decreasing pattern characterized by an acceleration after the 2030s, which is more evident in the RCP 8.5 scenario;
- the northern regions exhibit negative values since the last decades of the 20th century, and the largest SMB variations by 2100 occur in those areas for both scenarios;
- the GIS SMB reaches a long-term negative condition (pass the zero SMB threshold) in the period 2040–2080 (2010–2050), when RCP 4.5 (RCP 8.5) simulations are considered.

Chapter 5

Greenland Runoff

5.1 Introduction

The freshwater input from Greenland is expected to increase in the next century and it can impact on the oceanic circulation, and, consequently on the climate system (more detail in Section 1.2). However, the amount of runoff from the melting of Greenland ice sheet into the nearby ocean and its evolution over the last decades are poorly constrained by observations and by models (Section 1.3.2). The following chapter is an attempt to simulate the evolution of Greenland runoff during the 20th and 21st centuries. In this work, the runoff corresponds to the fraction of meltwater and, in a set of experiments, the rainfall able to reach the Greenland margins. The meltwater is evaluated by means of a state-of-the-art ice sheet-ice shelves thermo-mechanical model and the runoff is computed by means of a routing scheme that I implemented for this study. As for the evolution of the surface mass balance in the previous chapter, the evolution during the 20th and 21st centuries is studied by performing sets of transient simulations forced with the climate simulated from seven CMIP5 models.

5.2 Methodology and Experiment Design

The experiments developed in this chapter are performed by means of the thermo-mechanical ice sheet-ice shelves models GRISLI (Section 2.3.3). Simulations are performed on the 5 km grid since high resolution allows to capture better the ablation process. The values of the main model parameters used in GRISLI for the experiments analyzed in this chapter are reported in Table 4.1.

After implementing the routine scheme into GRISLI, the 20th and 21st centuries simulations are branched on the spin-up described in Section 2.4. The simulations carried in Chapter 4 using the CMIP5 climate forcing are repeated along with the runoff module activated. Similarly to what has been done in Chapter 4, two reference climatologies averaged over the period 1980–1999, one based on ERA Interim reanalysis and one based on MAR climate model, are used to obtain two different sets of climate forcing (Figure 4.1).

Runoff is defined by the sum of the rainfall that does not freeze and the meltwater production. The runoff distribution is calculated by means of a routing scheme implemented inside GRISLI. The routing scheme is developed starting from the "multiple flow direction" scheme by Quinn et al. (1991), on which I add the possibility to store water

Table 5.1: Experiments carried out in this chapter. The two subsets of climate forcing fields are derived from Eq. 4.1: one based on present-day (1980–1999) ERA Interim reanalysis and one based on MAR climate model. For each of the climate forcing subset, two subsets of experiments are derived from the different sources of meltwater (with or without rainfall). The abbreviations in the second column refer to the used retention scheme (Section 2.3.1): RE stands for the method by Reeh (1991) (Eq. 2.46) and JH stands for the method by Janssens and Huybrechts (2000) (Eq. 2.47). In the third column the meltwater sources are abbreviated using: IM for ice melt, SM for snow melt and RA for rainfall.

Name	**Retention scheme**	**Sources of meltwater**	**Reference**
$\text{NoRain}_{\text{ERAI}}$	RE	IM, SM	ERA Interim
$\text{NoRain}_{\text{MAR}}$	RE	IM, SM	MAR
$\text{Rain}_{\text{ERAI}}$	JH	IM, SM, RA	ERA Interim
Rain_{MAR}	JH	IM, SM, RA	MAR

inside the topographic depression met along the water flow-path. More details on the routing scheme are given in Section 2.3.2. To separate the impact of the rainfall on the runoff production and distribution, two sets of simulations are defined: one accounting for rainfall and meltwater as source of runoff and one accounting for meltwater only. The combination of these two sets of simulations forced with the two sets of climate forcing leads to a total of four sets of transient simulations summarized in Table 5.1. Note that the set of simulations $\text{NoRain}_{\text{ERAI}}$ and $\text{NoRain}_{\text{MAR}}$ correspond to the set of simulations G_{E5} and G_{M5}, of Chapter 4 in which the runoff module is activated. We rename these set of simulations in order to point out the difference with respect to the other two sets of simulations performed in this chapter. In fact, these sets of simulations account for only meltwater as source of runoff. In particular, the refreezing scheme derived from Reeh (1991) (Eq. 2.46), which was developed specifically to describe the refreeze of meltwater alone, is applied in these simulations. On the contrary, the other two sets of simulations, namely $\text{Rain}_{\text{ERAI}}$ and Rain_{MAR}, account for rainfall and meltwater as source of runoff. For this reason, we apply the refreezing scheme derived from Janssens and Huybrechts (2000) (Eq. 2.47), which applies on both rainfall and meltwater. Finally, we perform also an extra set of simulations (named $\text{NoRain}_{\text{ERAI}}$ + $\text{Rainfall}_{\text{ERAI}}$) in which the computation of the runoff with both rainfall and meltwater as sources are developed by applying the retention scheme by Reeh (1991) on the meltwater and by accounting for the entire rainfall as runoff without considering any refreezing of this source (only rainfall part is named $\text{Rainfall}_{\text{ERAI}}$). Note that we will only investigate the difference in meltwater and runoff production under the different sets of simulations, in this chapter.

5.3 Overall Greenland runoff production

In the following, the runoff is defined as the amount of meltwater effectively able to reach the coasts of Greenland, after applying the routing scheme to the initial distribution of meltwater. Consequently, the runoff represents only a fraction of the total meltwater. In fact, the amount of meltwater and runoff differ from each other, since the routing scheme implemented in the ice sheet model also account for the possible storage of meltwater inside topographic depressions along the flow-path. The total averaged runoff produced

Table 5.2: Total multi-model ensemble mean amount of runoff ($mm\,SLE/yr$) for the whole Greenland ice sheet. The percentage of meltwater able to reach the coasts is also reported. The values are averaged over 1980–1999 and 2081–2100. The second part of the table report the amount of runoff produced by rainfall alone without accounting for refreezing ($Rainfall_{ERAI}$) and the amount of runoff when total rainfall and meltwater under the retention scheme by Reeh (1991) are accounted for as runoff sources ($NoRain_{ERAI}$ + $Rainfall_{ERAI}$).

Case	*Runoff [$mm\,SLE/yr$]*			*Coastal meltwater [%]*		
	Present-day 1980–1999	RCP 4.5 2081–2100	RCP 8.5 2081–2100	Present-day 1980–1999	RCP 4.5 2081–2100	RCP 8.5 2081–2100
$\text{NoRain}_{\text{ERAI}}$	0.78	1.34	2.53	70	55	55
$\text{NoRain}_{\text{MAR}}$	0.79	1.25	2.36	64	49	50
$\text{Rain}_{\text{ERAI}}$	0.85	1.51	2.94	69	55	55
Rain_{MAR}	0.86	1.41	2.80	64	49	51
$\text{Rainfall}_{\text{ERAI}}$	0.13	0.41	0.76	73	70	69
$\text{NoRain}_{\text{ERAI}}$ + $\text{Rainfall}_{\text{ERAI}}$	0.91	1.75	3.29			

in Greenland for the multi-model ensemble mean of each subset of experiments is reported in Table 5.2.

The four sets of experiments exhibit values of runoff ranging from 0.78 $mm\,SLE\,yr^{-1}$ ($\text{NoRain}_{\text{ERAI}}$) to 0.86 $mm\,SLE\,yr^{-1}$ (Rain_{MAR}) in the period 1980–1999. This spread of values can be attributed (1) to the reference climatology, in fact the MAR climate is warmer along the margins, where most of the melting occurs, with respect to ERA Interim (Figure 3.3); and (2) to the rainfall fraction, which increases the amount of runoff simulated, when it is taken into account. Furthermore, this values of runoff represent 64 to 70 % of the amount of meltwater produced over the overall Greenland ice sheet. The remaining percentage of meltwater that does not reach Greenland margins is trapped along the path in topographic depressions.

Many literature works present estimates of the amount of runoff flowing out of Greenland (e.g. Mote 2003; Hanna et al. 2005; Box et al. 2006; Fettweis 2007; Ettema et al. 2009; Mernild and Liston 2012; Rae et al. 2012). The values obtained in our simulations are in line with those literature values (Table 5.3). For example, Rae et al. (2012) obtain a runoff of about 0.75 $mm\,SLE\,yr^{-1}$ on the period 1980–1999. This value is the average of an ensemble of RCMs simulations. Similar values are obtained by Mernild and Liston (2012). They use SnowModel, which is a snow and ice evolution model, coupled with the runoff routing model HydroFlow. They obtain runoff values of 0.86 $mm\,SLE\,yr^{-1}$ for the decade 1980–1989, and 0.90 $mm\,SLE\,yr^{-1}$ for the period 1990–1999. In general, our lower bound value, i.e. 0.78 $mm\,SLE\,yr^{-1}$, is close to Rae et al. (2012) values, while the upper bound, i.e. 0.86 $mm\,SLE\,yr^{-1}$, is closer to the calculations by Mernild and Liston (2012).

However, the source of climate forcing has a strong impact on the runoff production (Figure 5.1). In particular, the simulations forced with the CCSM4 AOGCM exhibit the largest amount of runoff reaching values up to 1.0 $mm\,SLE/yr$ over the period 1980–1999 under the $\text{Rain}_{\text{ERAI}}$ set of experiments. On the contrary, the simulations based on the CMCC-CM AOGCM show the smallest runoff production with values low to 0.65

Table 5.3: Estimate of runoff from various literature sources. Note that the value of Rae et al. (2012) is the multi-model ensemble mean of the set of regional climate model considered in their work, while for the other references, only one model was used. Values are given both in $km^3\ yr^{-1}$ and $mm\,SLE\ yr^{-1}$. The latter unit is given in order to have a direct comparison with the values reported in the present work and to estimate the contribution to the ocean. The second part of the table report some estimate for the future increase in Greenland runoff. The two reference periods over which the runoff increase is computed are reported in the third and fourth columns. Note that the estimates from Yoshimori and Abe-Ouchi (2012) are based on a temperature index (TI) method applied on GCMs climate fields.

Paper	**Method**	**Period**	**Runoff** $[km^3\ yr^{-1}]$	**Runoff** $[mm\,SLE\ yr^{-1}]$
Mote (2003)	Observations	1988–1999	278	0.71
Hanna et al. (2005)	ECMWF rean.	1993–1998	324	0.82
Box et al. (2006)	Polar MM5	1988–2004	373	0.95
Fettweis (2007)	MAR	1979–2006	304	0.77
Ettema et al. (2009)	RACMO2/GR	1958–2007	270	0.69
Mernild and Liston (2012)	SnowModel +	1980–1989	337	0.86
Mernild and Liston (2012)	HydroFlow	1990–1999	355	0.90
Rae et al. (2012)	RCMs	1980–1999	293	0.75
Future	**Method**	**from period**	**up to**	**Runoff increase** $[mm\,SLE\ yr^{-1}]$
Rae et al. (2012)	RCMs	1980–1999	2080–2099	0.1–1.7
Yoshimori and Abe-Ouchi (2012)	TI	1980–1999	2090–2099	0.0–2.5
Meehl et al. (2007)	IPCC AR4	1980–1999	2090–2099	0.2–2.8
Church et al. (2013)	IPCC AR5	1986–2005	2090–2099	0.0–1.3

$mm\,SLE/yr$ over the same time frame, but under the $\text{NoRain}_{\text{ERAI}}$ set of experiments. This behavior can be linked to the general biases of these AOGCMs. In fact, the CCSM4 AOGCM present the largest overestimation in precipitation and the lowest cold bias in temperature (Figure 3.2). These conditions support a large production of meltwater. On the contrary, the CMCC AOGCM exhibits the smallest precipitation overestimation and the largest cold bias among the set of AOGCMs (Figure 3.2), favoring a small meltwater production.

In the two final decades of the 21st century (2081–2100), the simulated runoff reaches values two to four times larger than simulated over the last decade of the 20th century. In particular, the runoff reaches values from 1.25 $mm\,SLE\ yr^{-1}$ to 1.34 $mm\,SLE\ yr^{-1}$ under a RCP 4.5 scenario, when not accounting for rainfall as source of runoff. The runoff increase to values from 2.36 $mm\,SLE\ yr^{-1}$ to 2.53 $mm\,SLE\ yr^{-1}$ under a RCP 8.5 scenario. On the contrary, when the rainfall is accounted for in runoff calculation the amount of runoff reaches value from 1.41 $mm\,SLE\ yr^{-1}$ to 1.51 $mm\,SLE\ yr^{-1}$ under a RCP 4.5 scenario, and from 2.80 $mm\,SLE\ yr^{-1}$ to 2.94 $mm\,SLE\ yr^{-1}$ under a RCP 8.5 scenario (Table 5.2). However, the percentage of meltwater accounted as runoff reduces to 52% in average. This increase of meltwater trapped inside topographic depressions during the flow can be attributed (1) to an increase in melting area, which leads to longer path with a higher probability for the meltwater to be trapped during its routing, and (2) to a retreat of the Greenland ice sheet margins with respect to the Greenland coasts, leaving a larger part of the meltwater routing path to be performed on an irregular

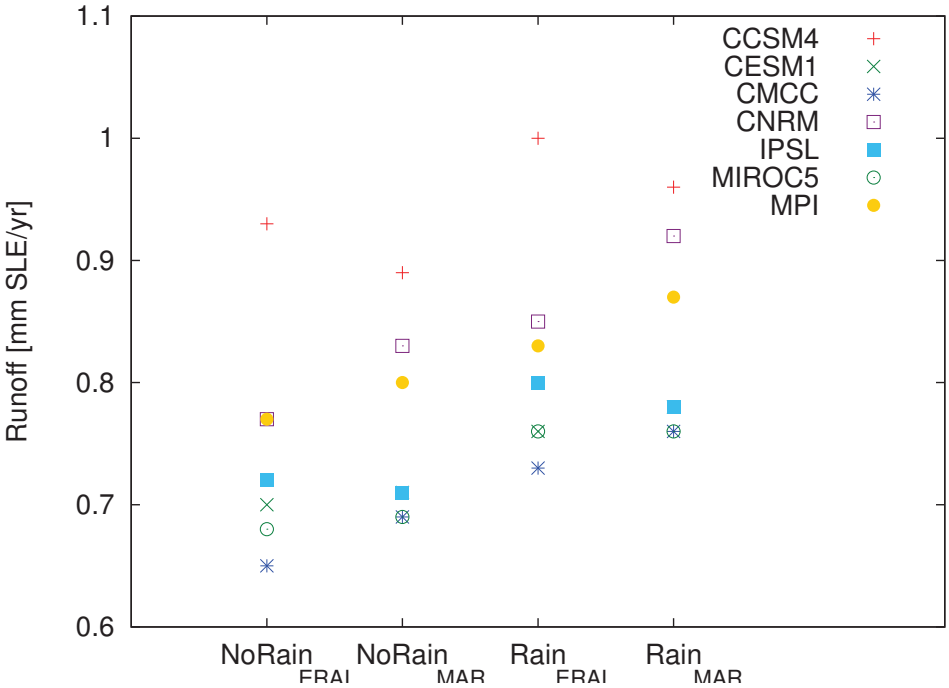

Figure 5.1: Mean annual runoff [mm SLE/yr] averaged over 1980–1999 for each experiment described in Table 5.1 and for each of the considered AOGCMs climate forcing. These values are computed in each ice-covered grid point.

unfrozen land with numerous topographic depressions.

The time evolution of the runoff production exhibits a scenario-dependent behavior, while small difference are simulated among each of the set of experiments (Figure 5.2). In general, similar trends are shown by the four sets of experiments (Figure 5.2), even if small differences in the amplitude of the increase in runoff are simulated (Table 5.2).

In particular, the simulations under a RCP 4.5 scenario show a small increase during the 21st century, showing an almost linear trend in the multi-model ensemble means (mean increase from 1980–1999 to 2081–2100 of about 0.56 $mm\,SLE/yr$). On the contrary, the simulations under a RCP 8.5 scenario exhibit an acceleration in the runoff production by the middle of the 21st century (period 2040–2060), reaching an increase in runoff about three times larger than the increase depicted by the RCP 4.5 simulations (mean increase from 1980–1999 to 2081–2100 of about 1.83 $mm\,SLE/yr$). Similarly, the ensemble spread has two different behavior. The RCP 4.5 simulations show an almost constant ensemble spread during the 21st century going from a spread of about 1.3 $mm\,SLE/yr$ over the period 1980–1999 to 2.0 $mm\,SLE/yr$ over the period 2081–2100. On the contrary, the RCP 8.5 simulations show an initial spread similar to the one simulated under a RCP 4.5 scenario ($\sim$ 1.3 $mm\,SLE/yr$) which, however, increases during the 21st century reaching a final spread of about $\sim$ 3.5 $mm\,SLE/yr$. As seen for the ablation in Chapter 4 (Figure 4.6b), the RCP 8.5 simulation with the largest change reaches runoff values up to 6 $mm\,SLE/yr$ during the last decades of the 21st century in all the sets of experiments except for $\text{NoRain}_{\text{MAR}}$, in which the largest runoff values

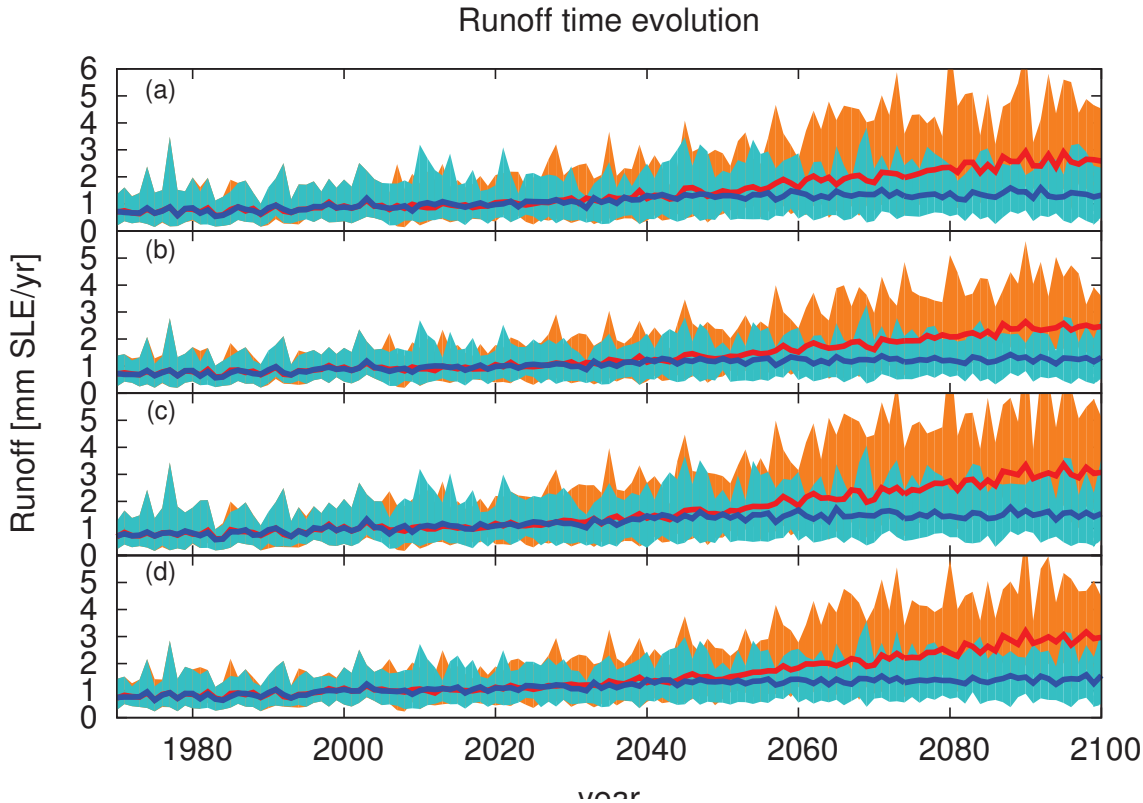

Figure 5.2: Time evolution of the runoff production [mm SLE/yr] for the four sets experiments reported in Table 5.1: (a) $NoRain_{ERAI}$, (b) $NoRain_{MAR}$, (c) $Rain_{ERAI}$, (d) $Rain_{MAR}$. The shaded regions represent the ensemble spread (orange for the RCP 8.5 scenario and cyan for the RCP 4.5 one), while the solid lines are the multi-model ensemble mean (red for the RCP 8.5 scenario and blue for the RCP 4.5 one).

reach about 5.6 $mm\,SLE/yr$. On the contrary, the most optimistic RCP 4.5 simulations show an almost steady runoff production during the entire 21st century (Figure 5.2). Note that, in all the simulations, a model drift should be accounted for, and its impact leads to a decrease of about 0.5% in the runoff values. This uncertainty is evaluated by means of a control run in which the present-day conditions are extended into the 21st century.

The simulated increase in runoff by the end of the 21st century is similar to previous estimate (e.g. Meehl et al. 2007; Rae et al. 2012; Yoshimori and Abe-Ouchi 2012; Church et al. 2013). In particular, the simulated increase in runoff are in line with the estimates of the fifth assessment report of the IPCC (from 0 to 1.3 $mm\,SLE\ yr^{-1}$, Church et al. 2013).

Finally, we compute the runoff with both rainfall and meltwater as sources in which the retention scheme by Reeh (1991) is applied on the meltwater and the entire rainfall, without considering any refreezing of this source, is regarded as runoff (Table 5.2). In general, the runoff produced in this computation exhibits larger values with respect to the previous experiments (Table 5.2). Furthermore, the impact of the rainfall on the runoff

production tends to increase in time ($\text{Rainfall}_{\text{ERAI}}$ in Table 5.2). In particular, during the period 1980–1999 only 0.13 $mm\,SLE\ yr^{-1}$ are retrieved directly from rainfall, while, at the end of the 21st century, the rainfall contributes with about 0.41 $mm\,SLE\ yr^{-1}$ (0.76 $mm\,SLE\ yr^{-1}$) under a RCP 4.5 (RCP 8.5) scenario. This increase in contribution from the rainfall can be attributed (1) to a general increase in precipitation during the 21st century (Figures 3.7a and 3.8a,d) and (2) to an increase in the rainfall fraction of the precipitation due to a warmer climate (Figures 3.7 and 3.8). Note that this computation is developed using only the ERA Interim reference climatology, as example.

5.4 Runoff at regional scale

Few studies analyze the runoff distribution at regional scale. Therefore we provide an analysis of the runoff distribution and its evolution during the 20th and 21st centuries on the same set of seven sub-basins regions as considered in Chapter 4 (Sasgen et al. 2012).

For the last decades of the 20th century, the four sets of experiments exhibit differences in runoff distribution, even if the main patterns tends to stay the same from one set to another (Figure 5.3). In particular, in all the experiments the largest amount of runoff is located in the northern and western basins, which correspond to the areas with the lowest surface mass balance (northern basins) and with the highest ablation values (western basins), as obtained from the analysis of Chapter 4 (Section 4.3.2 and Figure 4.4).

The results also show that the change in reference climatology impacts on the runoff distribution, as already shown in Chapter 4 for the surface mass balance calculations. In particular, the largest amount of runoff occurs in the north-eastern basin when using ERA Interim and in the northern basin in the MAR-based experiments (Figure 5.3). Further, the eastern and southern basins present a larger amount of runoff in the MAR-based experiments with respect to the ones based on ERA Interim (Figure 5.3). However, the total amount of runoff over Greenland remains almost the same (mean difference of 0.01 $mm\,SLE\ yr^{-1}$), as reported in Table 5.2. These small differences are also found in the ablation, when the multi-model ensemble mean is analyzed (difference in MME ablation between experiment G_{E5} and G_{M5}: $\sim 31\ Gt/yr$, Figure 4.2), and can be related to the differences in the reference climatologies.

When using a more complex refreezing scheme (Eq. 2.47, Janssens and Huybrechts 2000) and accounting for rainfall as source of meltwater we obtain an increase in the overall runoff (mean increase of about 0.07 $mm\,SLE\ yr^{-1}$, Table 5.2). This increase is also found at regional scale with the largest increase in the north-eastern basin (~ 0.014 $mm\,SLE\ yr^{-1}$) and the lowest increase in the north-western basin (~ 0.005 $mm\,SLE\ yr^{-1}$).

As stated before, only few studies focus on the freshwater fluxes from Greenland (e.g. Large and Yeager 2008; Bamber et al. 2012), and the few available runoff observations are recovered only in localized regions, for example in the Zackenberg basin (Mernild et al. 2008), or in the Kangerlussuaq region (West Greenland Hasholt et al. 2012), or for a set of glaciers (Rignot and Kanagaratnam 2006). Bamber et al. (2012) perform a regional analysis similar to what is discussed in this chapter. However, they use the regional climate model RACMO2 (Ettema et al. 2009), and calculate the total freshwater flux from Greenland, split in: (1) ice sheet runoff (0.70 $mm\,SLE\ yr^{-1}$ on average over the period 1961–1990) , (2) solid ice discharge (calving, 1.38 $mm\,SLE\ yr^{-1}$ on average

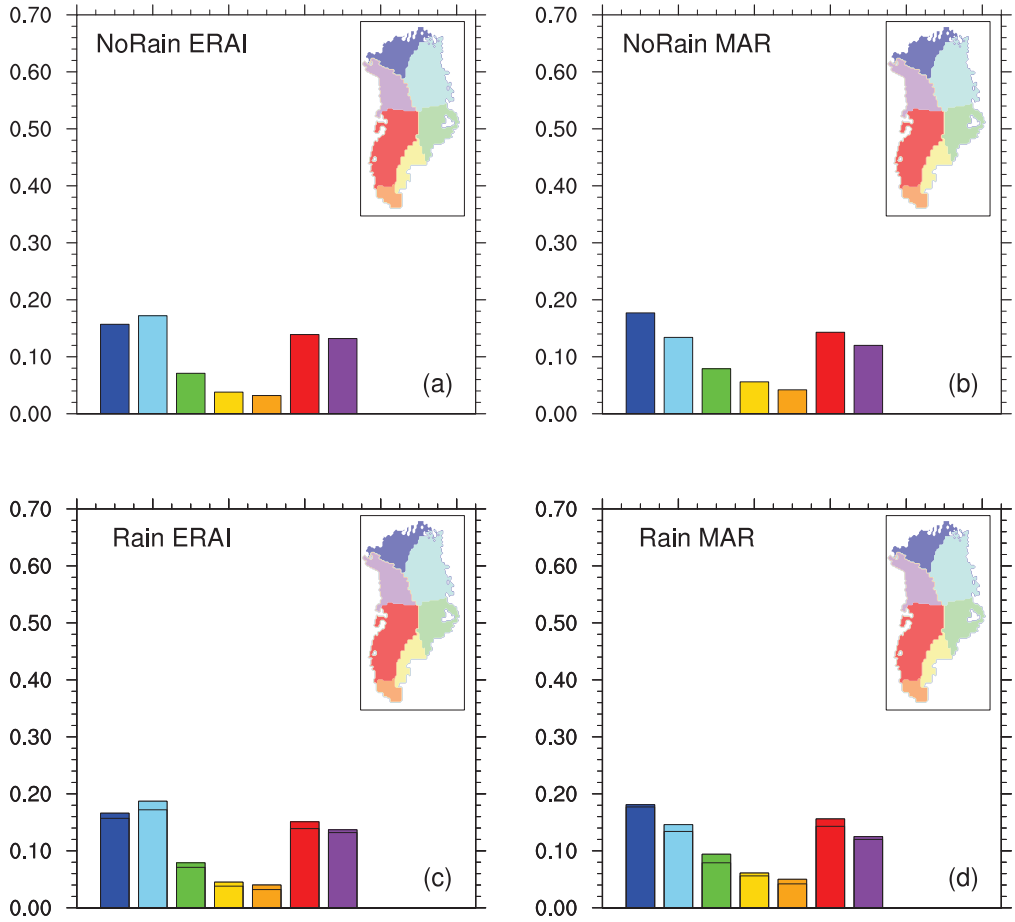

Figure 5.3: Regional multi-model ensemble mean runoff distribution (in mm SLE yr^{-1}) averaged over 1980–1999, for the sets of experiments (a) $NoRain_{ERAI}$, (b) $NoRain_{MAR}$, (c) $Rain_{ERAI}$, and (d) $Rain_{MAR}$. The panels (c) and (d) report also the values of panel (a) and (b), respectively, as black horizontal lines in order to facilitate the comparison.

over the period 1961–1990) and (3) tundra runoff (runoff from non glaciated areas, 0.46 $mm\,SLE\,yr^{-1}$ on average over the period 1961–1990). On regional scale, Bamber et al. (2012) found the largest amount of freshwater flowing out of Greenland in the southern basins ($\sim 0.62\ mm\,SLE\,yr^{-1}$ in their southwestern region and $\sim 0.74\ mm\,SLE\,yr^{-1}$ in their southeastern region), which is opposite to our findings. However, our calculation corresponds to the ice sheet runoff which represents only a fraction of the total freshwater flux values proposed by Bamber et al. (2012), which could explain the difference in regional distribution. Note that in Chapter 6, we also provide with an estimate for calving.

Differently from previous works (e.g. Bamber et al. 2012), we analyze the runoff distribution evolution during the 21st century, as well. At the end of the 21st century (2081–2100), the largest amount of runoff comes from the north-western basins for both emission scenarios, RCP 4.5 (Figure 5.4) and RCP 8.5 (Figure 5.5). In this area indeed we simulated a large reduction in surface mass balance by the end of the 21st century (see

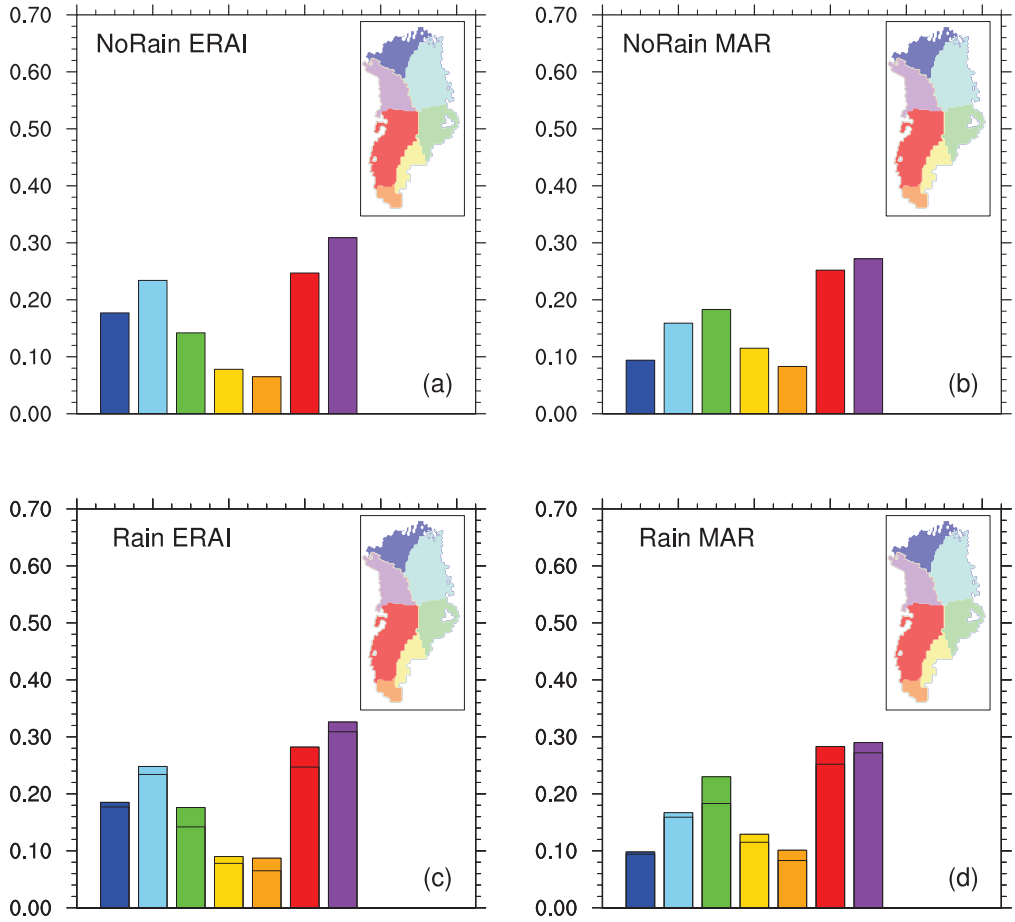

Figure 5.4: Regional multi-model ensemble mean runoff distribution (in mm SLE yr^{-1}) averaged over 2081–2100 under RCP 4.5, for the sets of experiments (a) $NoRain_{ERAI}$, (b) $NoRain_{MAR}$, (c) $Rain_{ERAI}$, and (d) $Rain_{MAR}$. The panels (c) and (d) report also the values of panel (a) and (b), respectively, as black horizontal lines in order to facilitate the comparison.

Section 4.4.2 and Figure 4.8). In Chapter 4, the analysis showed that the northern basin would also experienced a large reduction in surface mass balance. However, the runoff exhibits values similar or lower than the present-day values, in all the sets of experiments. This behavior derives from the large reduction in the percentage of meltwater accounted for as runoff (Table 5.2). The percentage of meltwater reaching the coast in the northern basin for the set of experiments $NoRain_{ERAI}$ in a RCP 4.5 scenario is about 37% which is about half the percentage obtained in the same region during the period 1980–1999. This reduction could be related to the increased length of the flow path to the coasts and to the retreat of the Greenland ice sheet margins, as stated before (Section 5.3).

Moreover, projected 21st century global warming enhances the differences among experiments in simulating runoff distribution. The sets of MAR-based experiments exhibit lower values of runoff in the northern basins and increased runoff in the eastern basins with respect to ERA Interim-based experiments (Figures 5.4 and 5.5). These discrepancies can be explained once again by the differences between the reference cli-

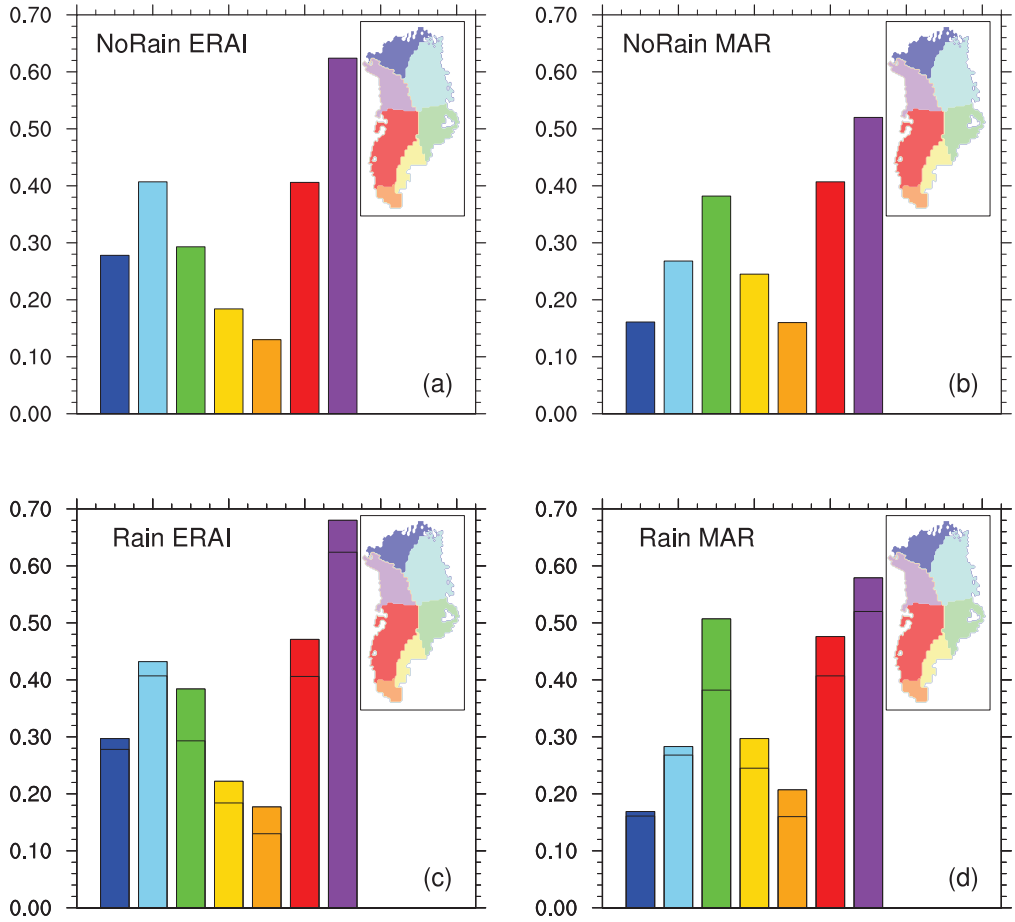

Figure 5.5: Regional multi-model ensemble mean runoff distribution (in mm SLE yr^{-1}) averaged over 2081–2100 under a RCP 8.5 emission scenario, for the sets of experiments (a) $NoRain_{ERAI}$, (b) $NoRain_{MAR}$, (c) $Rain_{ERAI}$, and (d) $Rain_{MAR}$. The panels (c) and (d) report also the values of panel (a) and (b), respectively, as black horizontal lines in order to facilitate the comparison.

matologies. For example, the MAR climatology shows higher air mean annual surface temperature values along the eastern coast (Figure 3.3), which could explain the larger amount of runoff along that coast in the MAR-based experiments with respect to the ERA Interim-based ones.

Since the climate forcing have more precipitation along the eastern and southern coasts, especially in the RCP 8.5 scenario (Figure 3.8), the amount of runoff increases more in those areas when accounting for rainfall routing (Figures 5.4 and 5.5). In addition, since MAR climate enhances the amount of precipitation compared with ERA Interim, the amount of runoff in those area result even larger in the MAR-based experiments.

5.5 High resolution runoff distribution

The experiments developed in this chapter allow to obtain a runoff distribution along the Greenland coasts at a high horizontal resolution (5x5 km). This runoff distribution could be used as freshwater forcing for ocean models at multiple scales.

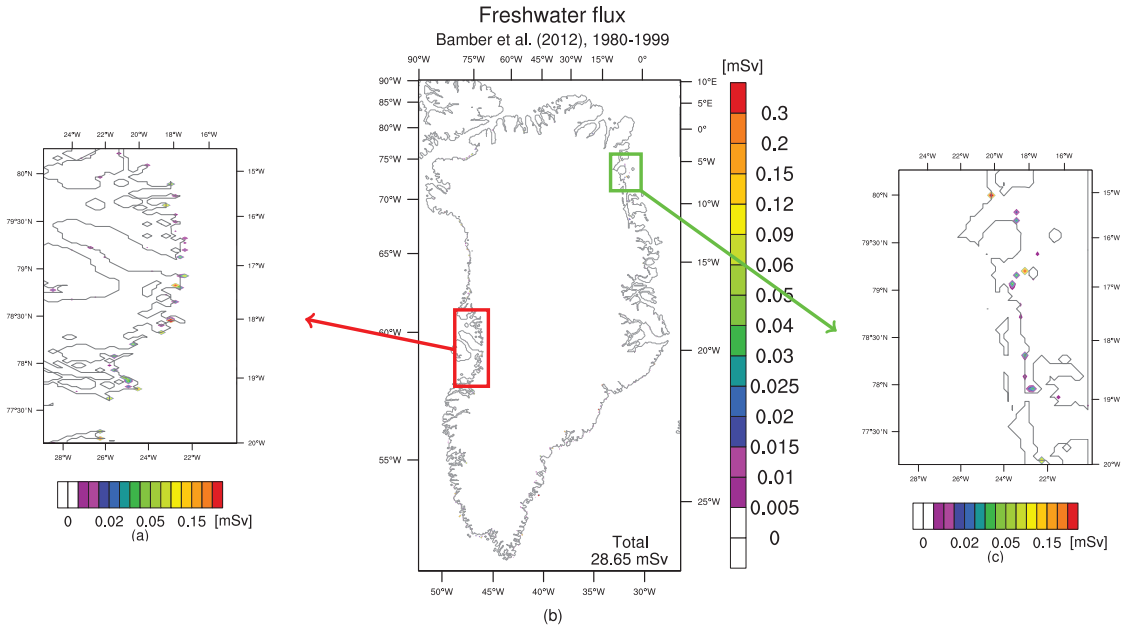

Figure 5.6: Freshwater fluxes distribution along Greenland coasts over the period 1980–1999 from the work by Bamber et al. (2012). (a) Close-up of the western Greenland coasts, (b) the GIS freshwater fluxes, and (c) close-up of the north-eastern part of Greenland. The values are reported in mSv and are obtained on a 25 km horizontal grid. The values obtained by our experiments in the red and green boxes regions are reported in Figures 5.7 and 5.8.

Only few studies present a freshwater distribution along the Greenland coasts (e.g. Large and Yeager 2008; Bamber et al. 2012) and all of them focus their analysis on the present-day freshwater distribution. For example, Bamber et al. (2012) use the regional climate model RACMO2 to evaluate the total freshwater fluxes flowing out of Greenland on a 25x25 km grid. In general, they obtain the largest amount of freshwater fluxes at the main rivers and fjords locations, as obtained in our simulations (Figure 5.6). However, their analysis takes into account three components: (1) ice sheet runoff, (2) calving and (3) tundra runoff. Our experiments, instead, account only for the ice sheet runoff, which is only a fraction of their estimates. For this reason, their total amount of freshwater fluxes flowing out of Greenland are about three times larger than our values (Figure 5.6 and Tables 5.4 and 5.5) at present-day time. However, the future mass loss of the GIS will be mainly dominated by the increase in surface melting since the contribution from ice discharge and calving will be self-limited by thinning and retreat of the marine margins of the GIS (e.g. Fürst et al. 2015). Consequently, our simulations represent a first attempt to simulate the evolution of the coastal distribution of the majority of the freshwater runoff flowing out of the GIS during the 21st century.

Hereafter, the analysis of the runoff during the 20th and 21st century focus on two regions in order to simplify the visualization of the results. One region is located in

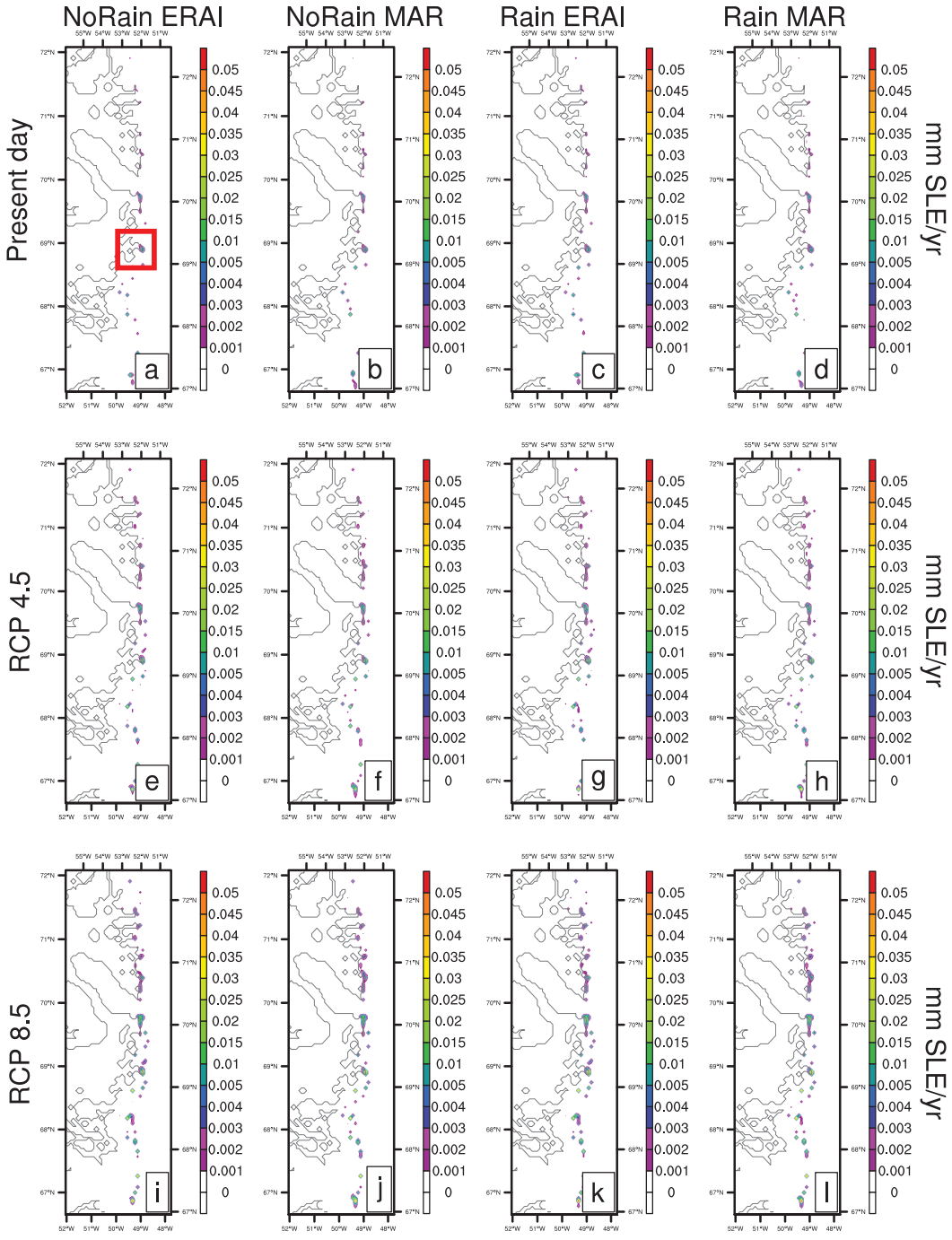

Figure 5.7: Runoff distribution along the western Greenland coasts (red box in Figure 5.6). The first row (panels a–d) shows the values averaged over the period 1980–1999, the second row (panels e–h) exhibits the values averaged over the period 2081–2100 in a RCP 4.5 scenario, and the last row (panels i–l) displays the values averaged over the period 2081–2100 in a RCP 8.5 scenario. Similarly, each column shows a specific set of experiments, from left to right: $NoRain_{ERAI}$ (panels a, e, i), $NoRain_{MAR}$ (panels b, f, j), $Rain_{ERAI}$ (panels c, g, k), and $Rain_{MAR}$ (panels d, h, l). The values are reported in mm SLE yr^{-1}.

the Greenland western coast (red box in Figure 5.6) and one in the north-eastern part of Greenland (green box in Figure 5.6). Along the western Greenland coast, Bamber et al. (2012) simulate the largest amount of freshwater flux at the end of the main fjords (Figure 5.6a). In the north-eastern region, they simulate the largest amount of freshwater flux at the front of the main NEGIS outlet glaciers (Figure 5.6c).

The first region, which is taken along the Greenland western coast (red box in Figure 5.6), is characterized by many outlet glaciers situated in the main fjords, where the meltwater is expected to flow out of Greenland. As expected, in the central and northern part of the analyzed area, the runoff accumulate at the fjords areas (Figure 5.7). On the contrary, in the southern part of the considered area, the runoff is trapped in the interior part of Greenland (Figure 5.7). More specifically, the meltwater stop at the boundary between iced region and unfrozen area, where topographic depressions could be formed by the land deformation due to the ice sheet burden. The runoff produced in this region increases in time. For example, the runoff flowing out of the Jakobshavn glacier area (red box in Figure 5.7a) exhibits values passing from 0.008 $mm\,SLE\ yr^{-1}$ in the present-day (1980–1999) to 0.013 $mm\,SLE\ yr^{-1}$ under a RCP 4.5 scenario by the end of the 21st century (2081–2100) or to 0.020 $mm\,SLE\ yr^{-1}$ under a RCP 8.5 scenario.

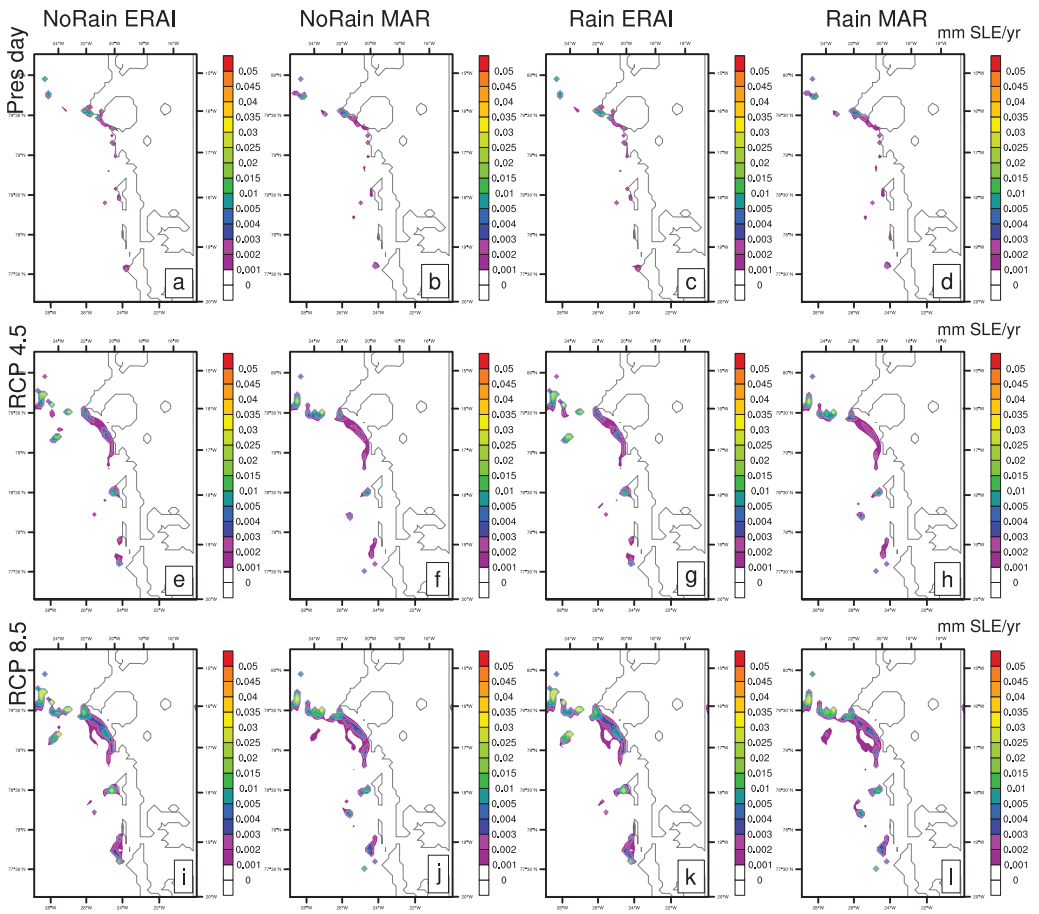

Figure 5.8: As for Figure 5.7, but for the runoff distribution in the north-eastern part of Greenland (green box in Figure 5.6). The values are reported in $mm\,SLE\ yr^{-1}$.

The second region is taken in the north-eastern part of Greenland (green box in Figure 5.6). This area is located at the end of the North East Greenland Ice Stream. In this region, the runoff tends to cover a broader region along the Greenland coasts, instead of accumulate in few specific fjords (Figure 5.8). This behavior is due to the multiple flow direction feature of the routing scheme used in performing the analysis. As a consequence, in this region, the amount of runoff increase in magnitude in time, but also the extent of coastal areas in which runoff occurs tends to grow during the 21st century (Figure 5.8). Also in this region, it is possible to see that part of the meltwater is trapped in some topographic depressions in the interior part of Greenland.

In general, the results at high resolution give information on both the evolution in runoff magnitude and the evolution of runoff locations and extent.

5.6 Outlook: Impact on ocean

The runoff is an important variable especially in studying the ice sheet-ocean interactions. In fact, the impact of a large freshwater flux flowing out of Greenland on the ocean circulation and, consequently, on the climate system has been largely studied by the so-called hosing experiments (e.g. Rahmstorf et al. 2005; Stouffer et al. 2006; Driesschaert et al. 2007; Stammer et al. 2011; Swingedouw et al. 2013).

Table 5.4: Estimate of freshwater fluxes from Greenland from various literature sources, and runoff estimates from the present work in Sv (1 Sv = 10^6 m^3 s^{-1}).

Paper	**Method**	**Period**	**Runoff [Sv]**
Gregory and Lowe (2000)	HadCM3	1990–2000	0.017
Luthcke et al. (2006)	GRACE	2003–2005	0.005
Dickson et al. (2007)	Review	-	0.018
Bamber et al. (2012)	RACMO2	1961–1990	0.029
Rae et al. (2012)	RCMs	1980–1999	0.009
Experiment			
$\text{NoRain}_{\text{ERAI}}$	GRISLI	1980–1999	0.010
$\text{NoRain}_{\text{MAR}}$	GRISLI	1980–1999	0.010
$\text{Rain}_{\text{ERAI}}$	GRISLI	1980–1999	0.011
Rain_{MAR}	GRISLI	1980–1999	0.011

Only few work analyze and provide estimates of the runoff distribution along the Greenland coasts (Large and Yeager 2008; Bamber et al. 2012). However, various literature works report estimates of runoff production (Table 5.4). These estimates exhibit a large range of values going from 0.005 Sv to 0.029 Sv (1 $Sv = 10^6$ m^3 s^{-1}). These discrepancies can be related to the methodology and sources accounted for in the computation, and to the reference period on which the values are averaged on. For example, the lower bound, i.e. 0.005 Sv (Luthcke et al. 2006) is obtained from satellite gravimeter data, while the upper bound, i.e. 0.029 Sv (Bamber et al. 2012), is obtained applying a mass budget method on the fields simulated with the regional climate model RACMO2, and three sources of freshwater fluxes are accounted for: (1) ice sheet runoff, (2) calving and (3) tundra runoff.

Nevertheless, the values simulated by our experiments for the present-day (1980–1999) runoff flowing from Greenland are in line with the previous estimate (Table 5.4).

Table 5.5: Estimate of Greenland runoff from the set of experiments developed in this chapter in mSv (1 mSv = 10^3 m^3 s^{-1}).

Experiment	**Present-day** 1980–1999	**RCP 4.5** 2081–2100	**RCP 8.5** 2081–2100
$\text{NoRain}_{\text{ERAI}}$	9.8	16.8	31.6
$\text{NoRain}_{\text{MAR}}$	9.9	15.6	29.5
$\text{Rain}_{\text{ERAI}}$	10.6	18.9	36.8
Rain_{MAR}	10.8	17.6	35.0

These small values of runoff are not able to impact on the ocean circulation simulated by the ocean models, since this values are smaller than the decadal variability described by an unforced control simulation (internal variability of the model). For this reason, the hosing experiments developed with the aim to evaluate the ocean response to the freshwater input from Greenland are performed using large freshwater fluxes (from 0.1 to 1 Sv Stouffer et al. 2006; Driesschaert et al. 2007; Swingedouw et al. 2013). However, Stammer et al. (2011) performed their simulations applying a freshwater input of about 0.0275 Sv (=27.5 mSv) which is large enough to obtain a response with a magnitude larger than the internal variability of the coupled ocean-atmosphere general circulation model used in their experiment. This value, then, can be used as a possible estimate of the threshold above which the freshwater flux flowing out of Greenland is able to impact on the ocean circulation on a global scale. Given this threshold, the runoff simulated by our experiments are able to become visible in ocean models only at the end of the 21st century under a RCP 8.5 scenario (Table 5.5). Agarwal et al. (2015) evaluate the impact of the simulated freshwater fluxes from Greenland on the global sea level until 2100. In their simulation, the freshwater fluxes from Greenland exhibit an impact of about 1 $cm\,SLE$ on the mean global sea level change by the end of the 21st century. However, only in few regions the impact of the freshwater from Greenland give a signal beyond the system internal variability.

Finally, the experiments performed in this chapter aims to provide an high resolution data set of Greenland runoff production for the 20th and 21st centuries to be used as freshwater forcing in ocean models at multiple scales (Figure 5.9).

5.7 Summary

In this chapter, I evaluate the amount of runoff flowing out of Greenland, where the runoff is defined by the sum of the rainfall that does not freeze and the meltwater production. This analysis is developed by performing four sets of experiments with the ice sheet-ice shelves thermo-mechanical model GRISLI, in which a multiple flow direction routing scheme is implemented. GRISLI is forced with the anomalies of a set of seven CMIP5 AOGCMs on top of reanalysis (ERA Interim) and regional climate model (MAR) fields. The results of this analysis show that:

- the runoff at overall Greenland scale will increase during the 21st century reaching

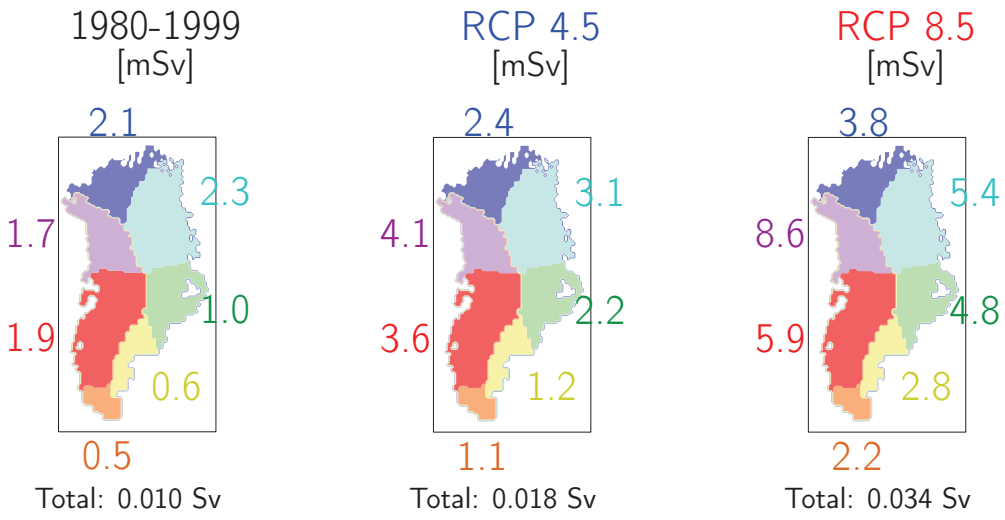

Figure 5.9: Example of runoff distribution on regional scale obtained with the set of experiments $Rain_{ERAI}$. Values are in mSv.

values about two (three) times larger than present-day values in a RCP 4.5 (RCP 8.5) scenario;

- the amount of runoff is influence by the sources considered. In fact, when rainfall is considered as source of runoff, the final runoff is higher with respect to the experiments in which this source is not accounted for. Furthermore, on regional scale, the eastern coast is more influenced by the rainfall as source of runoff with respect to the rest of Greenland, due to the high precipitation in those areas;

- the MAR-based experiments at overall Greenland scale exhibit runoff values slightly higher than in the experiments based on ERA Interim. On regional scale, the MAR-based experiments present lower amount of runoff in the northern basins and higher amount in the eastern ones with respect to the experiments based on ERA Interim. These discrepancies in distribution are linked to the differences in air surface temperature and precipitation of the two climatologies;

- in general, on regional scale, the highest amount of runoff is found in the northern and western basins, and the north-western one presents the largest increase during the 21st century;

- the runoff distribution at 5 km resolution allows to evaluate the evolution in both runoff magnitude and runoff extent during the 21st century, showing the impact of regional features;

- the runoff simulated in our experiments is large enough to impact on the ocean circulation simulated by the ocean model only at the end of the 21st century under a RCP 8.5 scenario.

Chapter 6

Greenland mass loss

6.1 Introduction

The surface runoff flowing out of Greenland, which is analyzed in the previous chapter, is only one mechanism that constitutes the overall Greenland mass loss. In this chapter, I briefly analyze two more mechanisms that contribute to the total Greenland mass loss: (1) the basal melting and its routing to the coasts, and (2) the solid ice discharge given by calving at the ice shelves and outlet glaciers front.

The ice flow results from a combination of internal deformation of ice due to its weight, sliding at the ice bed and deformation of underlying sediments. Moreover, basal sliding over a lubricated bed is often source of fast ice motion (e.g. greater than 100 m/yr, Paterson 1994; Joughin et al. 2008a, and Figure 6.1).

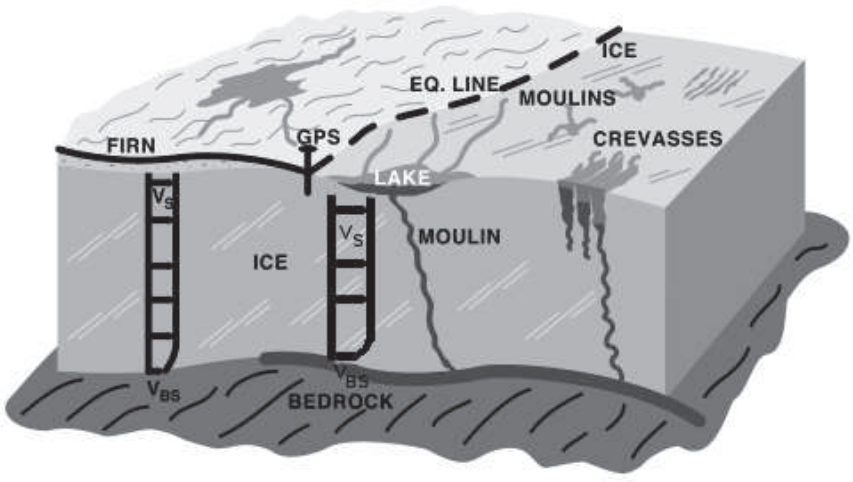

Figure 6.1: Ice flow for basal ice at the pressure melting point is partly from basal sliding and partly from ice deformation. The lubricate bed is source of fast ice motion. Figure after Zwally et al. (2002).

For this reason, the meltwater at the ice base exerts a strong influence on ice flow, but the knowledge on basal melt processes is strongly limited by the lack of observations of ice-sheet bed properties (e.g. Fahnestock et al. 2001). For example, some information

for the ice base could be retrieved from the boreholes locations (e.g. Hulbe and MacAyeal 1999), but those observations are only punctual. Changes in sub-glacial hydrology and the increase of melting due to a warmer climate are expected in the near-future and their impact on the ice flow is analyzed in many works through changes in their enhancing effect on the basal sliding (e.g. Nowicki et al. 2013).

The calving occurring at the front of ice shelves has been extensively observed and studied (e.g. Ritz et al. 2001; Stearns and Hamilton 2007; Nick et al. 2010, 2013; Khan et al. 2014; Calov et al. 2015, and more detail in Section 1.3.2). Many of the simulated values are based on parameterizations embedded in ice sheet models: thickness criterion, which is used in GRISLI and in the present analysis (Section 2.2.5), calving criteria based on penetration of surface and basal crevasses (e.g. Nick et al. 2010, 2013; Pollard et al. 2015), or by dealing with the non-resolved fast ice discharge in each grid point by means of an heuristic statistical approach via the local thickness of ice and the distance from the nearest ocean point (Calov et al. 2015).

This chapter aims to evaluate the ability of the GRISLI ice sheet model in simulate the calving along Greenland coasts. Moreover, the basal meltwater and the calving are analyzed as components of the mass loss flowing out of Greenland.

6.2 Methodology and experiment design

In this chapter, I investigate two different mechanisms. For this reason, I present two different sets of simulations: one developed in order to investigate the changes in basal melting and one performed to analyze the sensitivity of the parameterization used in calculating the calving of the Greenland ice shelves. More details of these two sets of experiments are given in the following sections.

6.2.1 Basal melting experiments

The basal melting occurs at the base of the ice sheet and the meltwater forms in areas where the basal ice temperature reaches the pressure melting point, which depends on the height of the above column of ice (Eq. 2.13). Given the slow diffusivity (10^4 years) of temperature from the surface to the base the present-day ice sheet vertical temperature structure and especially the basal temperature is mainly influenced by the spin-up method. For this reason, we carried out two paleo spin-up simulations: one covering the last 24 kyrs, similarly to Chapters 4 and 5 and here named $\text{Paleo}_{\text{G24}}$ and $\text{Paleo}_{\text{S24}}$ for GRISLI and SICOPOLIS respectively, and one covering the entire last glacial cycle (125 kyrs, Figure 6.2). Those paleo-runs are developed following the method by Greve et al. (2011), as described in section 2.4.

The present-day and near-future evolution of the basal melting is calculated by using two different ice sheet models: GRISLI and SICOPOLIS (Figure 6.2). The two ice sheet models are used in order to evaluate the impact of the different vertical temperature structure described by GRISLI and SICOPOLIS. In fact, GRISLI presents a vertical structure in which only cold ice is accounted for, while SICOPOLIS is characterized by a polythermal structure. More details on these ice-sheet models and on their differences are given in sections 2.3.3 and 2.3.4.

The simulations are performed using one specific reference climate, i.e. MAR, and

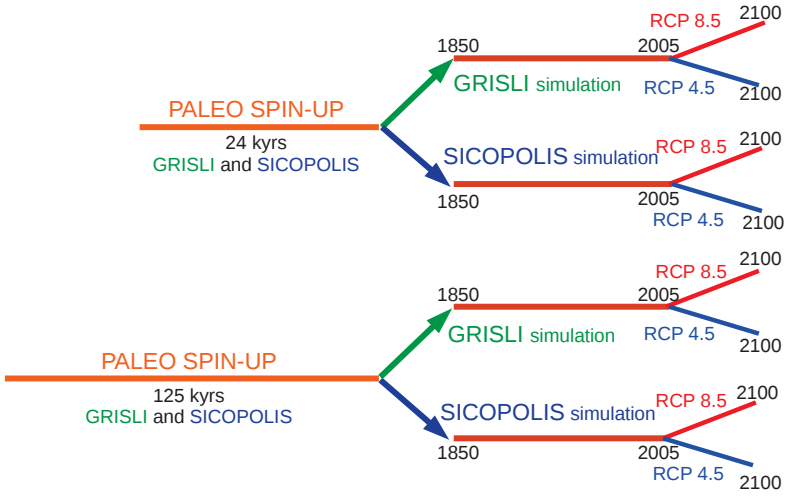

Figure 6.2: Numerical design of the simulations. GRISLI and SICOPOLIS are spun up with a 24 kyrs and a 125 kyrs paleo-runs, respectively. The present-day and near-future simulations are developed using one specific climate forcing (Eq. 6.1) and the 21st century is described by two emission scenarios: RCP 4.5 and RCP 8.5. See Section 2.4 for more details.

one AOGCM climate forcing, i.e. CMCC-CM, defined by:

$$Forcing_{annual}^{1850-2100} = MAR_{mean}^{1980-1999} + \left(CMCC_{annual}^{1850-2100} - CMCC_{mean}^{1980-1999}\right) \qquad (6.1)$$

where the $MAR_{mean}^{1980-1999}$ represent the high resolution present day climatology, which is retrieved from the regional climate model MAR (Fettweis et al. 2013). The anomaly fields instead are given by the CMIP5 simulations carried out with the CMCC-CM AOGCM (Scoccimarro et al. 2011). As described in Chapter 4, the 21st century simulations follow the two future emission scenarios RCP 4.5 and RCP 8.5.

Differently from the two previous chapters, the simulations are performed using one reference climatology and one AOGCM only. The choice of using MAR and CMCC-CM climates is determined by their intermediate to high horizontal resolution. In fact, the CMCC-CM simulations have been performed with the highest resolution among the set of seven CMIP5 AOGCMs considered in this work (0.75° x 0.75° Table 3.1). Similarly, MAR presents a higher horizontal resolution with respect to ERA Interim (25x25 km, Table 3.1). Furthermore, the CMCC AOGCM has been chosen since it simulates a climate with a cold bias in temperature, which can compensate the overestimated melting obtained with the PDD scheme, but, at the same time, it simulates precipitation close to the observation, as shown in Figure 3.2.

Finally, the simulations performed with GRISLI and SICOPOLIS to investigate the basal melting are developed at a horizontal resolution of 20x20 km. The use of this resolution allows to perform the long-term paleo spin-up used in this chapter in reasonable computational time and also to use SICOPOLIS avoiding too many numerical instabilities. In both ISMs, we apply the routing scheme described in Section 2.3.2 to the basal meltwater in order to evaluate the amount of it that is able to reach the coasts and form

Table 6.1: Summary of the basal melting experiments carried out in this chapter. The first part of the table provides the main features of the spin-up, which differs in the length of the simulations and in the ice sheet model used. The second part of the table reports the main characteristics of the set of eight simulations over the period 1850–2100.

Paleoruns		
Name	**Length**	**Model**
$\text{Paleo}_{\text{G24}}$	24 kyrs	GRISLI
$\text{Paleo}_{\text{S24}}$	24 kyrs	SICOPOLIS
$\text{Paleo}_{\text{G125}}$	125 kyrs	GRISLI
$\text{Paleo}_{\text{S125}}$	125 kyrs	SICOPOLIS

1850–2100 runs			
Name	**Paleorun**	**Model**	**Scenario**
G45_{24}	$\text{Paleo}_{\text{G24}}$	GRISLI	RCP 4.5
S45_{24}	$\text{Paleo}_{\text{S24}}$	SICOPOLIS	RCP 4.5
G45_{125}	$\text{Paleo}_{\text{G125}}$	GRISLI	RCP 4.5
S45_{125}	$\text{Paleo}_{\text{S125}}$	SICOPOLIS	RCP 4.5
G85_{24}	$\text{Paleo}_{\text{G24}}$	GRISLI	RCP 8.5
S85_{24}	$\text{Paleo}_{\text{S24}}$	SICOPOLIS	RCP 8.5
G85_{125}	$\text{Paleo}_{\text{G125}}$	GRISLI	RCP 8.5
S85_{125}	$\text{Paleo}_{\text{S125}}$	SICOPOLIS	RCP 8.5

runoff to be added to the superficial one.

The combinations of the different spin-ups, ice sheet models and future emission scenarios lead to a set of eight experiments, summarized in Table 6.1.

6.2.2 Calving experiments

Calving occurs at the front of the ice shelves and outlet glaciers. In Greenland, the few ice shelves and outlet glaciers are usually located at the end of fjords. However, most of those fjords are about or less than 5 km wide. For this reason, the set of experiments carried out to analyze the calving are performed by means of the GRISLI ice sheet model at the horizontal resolution of 5x5 km, differently from the basal melting experiments.

The calving process in GRISLI is described by means of a simple parameterization based on a thickness criterion (Section 2.2.5). This parameterization calculates the evolution of an ice shelf by accounting for (1) the amount of ice coming from the upstream points, (2) the melting at the surface (surface mass balance), and (3) the melting at the ice shelf base (b_{melt}), which is parameterized using two prescribed uniform values: one at the grounding line ($\text{b}_{\text{melt,grz}}$), and one for the floating part of the ice shelf ($\text{b}_{\text{melt,shelf}}$). Finally, (4) the calving occurs when the ice thickness is lower than a thickness threshold (H_{calv}). Note that these terms are summarized in Figure 2.7. Here, we investigate the sensitivity of the calving production to changes in the basal melting values ($b_{\text{melt,grz}}$ and $b_{\text{melt,shelf}}$) and in the ice thickness threshold at the front (H_{calv}).

First of all, the experiments start with a paleo spin-up that covers the period from 24 kyrs BP to 1.5 kyrs BP (Figure 6.3). For this part, the spin-up is identical to that described in the Section 2.4 and used in the previous chapters. The calving parameters

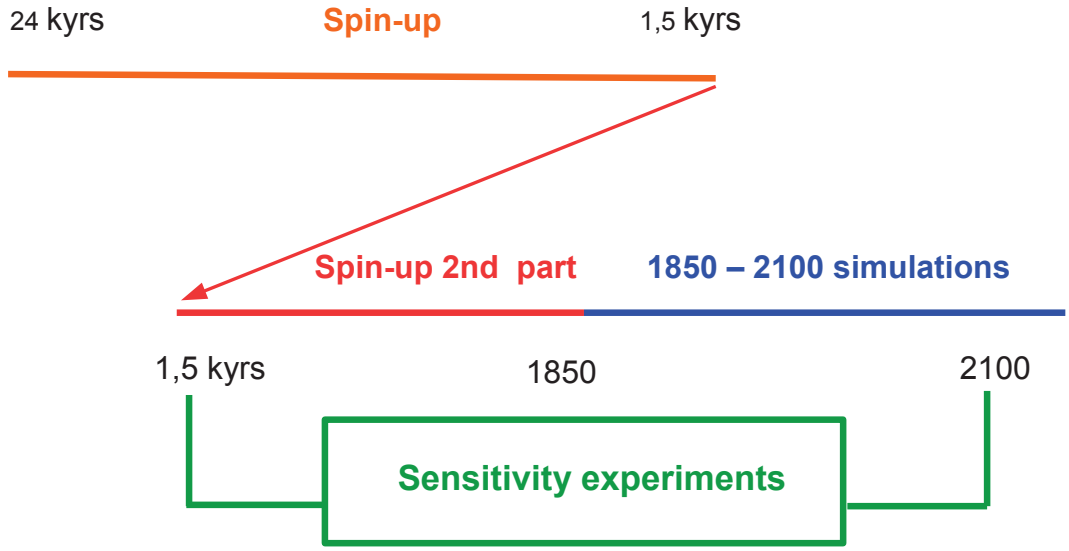

Figure 6.3: Numerical design of simulations. GRISLI is spun up with a simulations from 24 kyrs before 1850 to 1.5 kyrs before 1850. The last 1500 years of the spin-up are already part of the sensitivity studies (summarized in Table 6.2). The forcing used for the simulations in the period 1850–2100 are calculated using Eq. 6.1.

Table 6.2: Calving experiments settings. Values of ice shelf front thickness threshold (H_{calv}) and ocean basal melting fluxes at the grounding line ($b_{melt,grz}$) and under the shelf ($b_{melt,shelf}$) used for the set of nine sensitivity tests. These values are applied on the last 1500 years of the spin-up until 2100.

Name	$\mathbf{b_{melt,grz}}$ $[m\ yr^{-1}]$	$\mathbf{b_{melt,shelf}}$ $[m\ yr^{-1}]$	$\mathbf{H_{calv}}$ $[m]$
$\text{Paleo}_{\text{G24}}$	0.5	0.1	250
Hcalv_{250}	3.4	0.1	250
Hcalv_{150}	3.4	0.1	150
Hcalv_{125}	3.4	0.1	125
Hcalv_{100}	3.4	0.1	100
Hcalv_{75}	3.4	0.1	75
Hcalv_{50}	3.4	0.1	50
Bshelf_0	3.4	0.0	100
Bgrz_0	0.0	0.1	100
Bmelt_0	0.0	0.0	100

H_{calv} and b_{melt} are set to the standard values reported in Table 6.2 ($\text{Paleo}_{\text{G24}}$). The last 1500 years of the spin-up, i.e. 1.5 kyrs BP to 1850 AD (Figure 6.3), and the simulations in the period 1850–2100 are performed using a set of nine combinations of H_{calv} and b_{melt} listed in Table 6.2. Six experiment deal with the impact of H_{calv} on the simulated calving. This value is set to 250 m as reference value and, subsequently, it varies from 150 m to 50 m with step of 25 m. The last three experiments study the impact of the basal melting terms (b_{melt}) on the calving production. Note that the value of melting at grounding line is defined as the mean ice shelf melting observed in the Antarctic ice shelves characterized by an area comparable to the area of the floating part of NEGIS ($\sim$ 2750 km^2). The observed values come from the work by Rignot et al. (2013), and the final $b_{\text{melt,grz}}$ values is set to 3.4 $m\ yr^{-1}$. The use of Antarctic values is due to the absence of observed values on annual scale in Greenland. On the contrary the melting at the ice shelves front is kept low (0.1 $m\ yr^{-1}$). The last 1500 years of the spin-up are included in the sensitivity experiments, in order to evaluate the impact of the calving parameters on the ice shelves and outlet glaciers expansion along the Greenland coasts. In fact, the calving can occur only if some ice shelves and outlet glaciers subsist along the Greenland oceanic margins at the end of the spin-up.

Finally, the simulations for the period 1850–2100 are carried out using the climate forcing calculated by Eq. 6.1 based on MAR reference climatology and simulated CMCC-CM AOGCM climate anomalies following the two future emission scenario RCP 4.5 and RCP 8.5.

6.3 Basal melting

6.3.1 Spin-up simulations

The basal melting can be found in the areas where the basal temperature reaches the pressure melting point. At the end of the spin-up simulations carried out with GRISLI, namely $\text{Paleo}_{\text{G24}}$ and $\text{Paleo}_{\text{G125}}$, the basal temperature reaches the pressure melting point all along the Greenland ice sheet margins (Figures 6.4a and 6.4b). The areas affected by basal melting are larger, especially in the North of Greenland ice sheet in the longer spin-up $\text{Paleo}_{\text{G125}}$ with respect to $\text{Paleo}_{\text{G24}}$ (Figures 6.4a and 6.4b). In particular, the two experiments differ in the NEGIS area. The higher basal temperature in the longer spin-up ($\text{Paleo}_{\text{G125}}$) can be explained (1) by a larger ice thickness and (2) by a larger impact of the basal friction heat production in that area. This latter effect can be related to the use of a constant in time basal drag, retrieved with an inverse method (Section 2.2.4 and Figure 2.5), that promotes fast flow in the observed present-day fast flowing region, such as NEGIS.

The spin-up carried out with SICOPOLIS, namely $\text{Paleo}_{\text{S24}}$ and $\text{Paleo}_{\text{S125}}$, are highly different from GRISLI ones (Figures 6.4d and 6.4e). While in $\text{Paleo}_{\text{S24}}$ basal temperature reaches the pressure melting point over most of the glaciated area, this is less the case in $\text{Paleo}_{\text{S125}}$ (Figure 6.4d). This is because in SICOPOLIS, a temperate layer is accounted for at the base of the ice sheet (polythermal mode, Section 2.3.4), then, it requires longer simulations to adjust the vertical temperature. In fact, the basal temperature distribution gets close to $\text{Paleo}_{\text{G125}}$ on the longer spin-up simulation ($\text{Paleo}_{\text{S125}}$), where the southern half of the ice sheet has the basal temperature at the pressure melting point, while the northern part exhibits a cold base in the central parts. Compared with the shorter

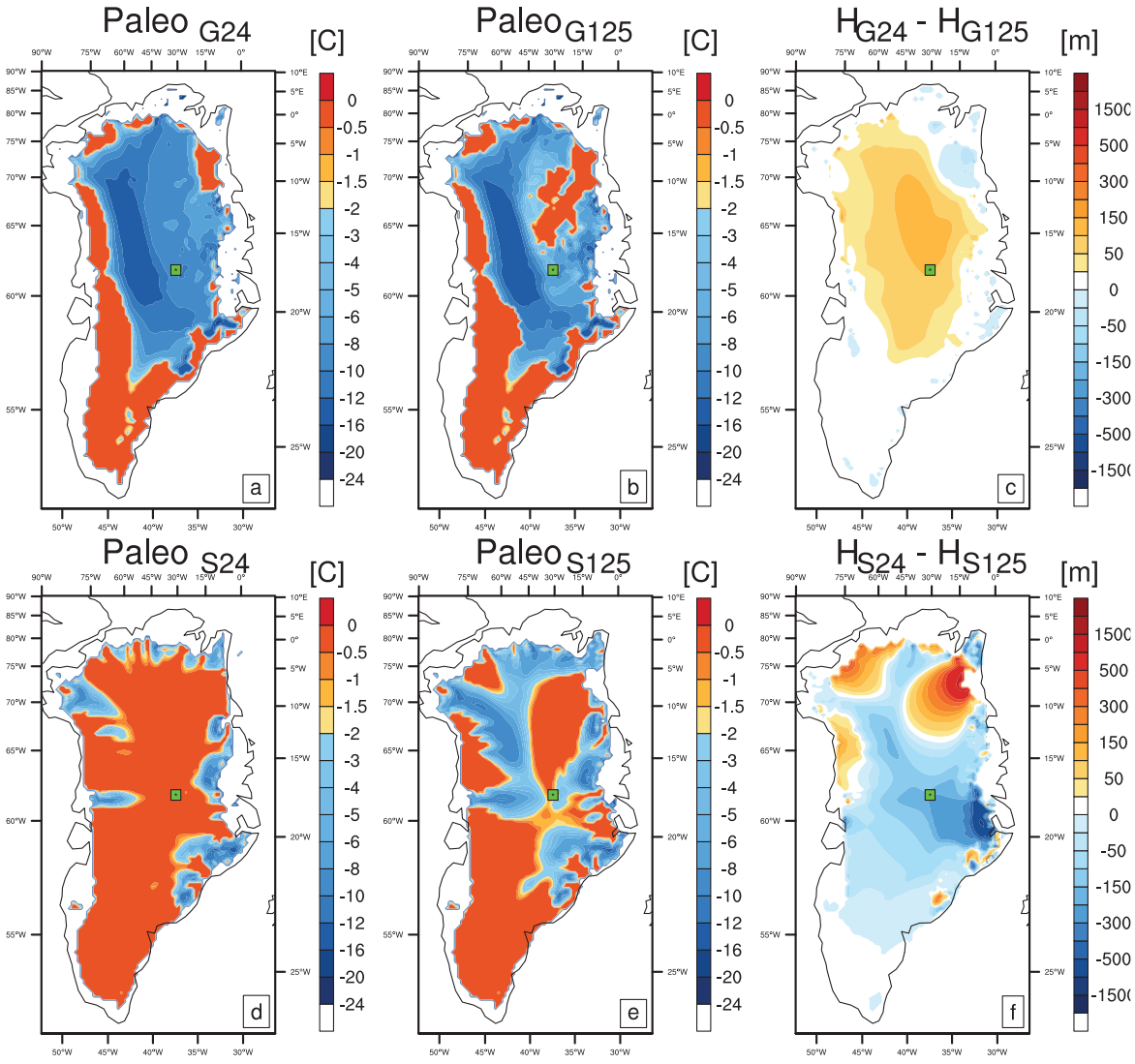

Figure 6.4: Basal temperature (°C) at the end of the spin-up simulations: (a) $Paleo_{G24}$, (b) $Paleo_{G125}$, (d) $Paleo_{S24}$, and (e) $Paleo_{S125}$ (Table 6.1). The orange regions represent the areas with the base at the pressure melting point. Ice thickness difference (m) at the end of the paleo-runs: (c) difference between $Paleo_{G24}$ and $Paleo_{G125}$, (f) difference between $Paleo_{S24}$ and $Paleo_{S125}$. The green rectangle indicate the GRIP site location.

spin-up, Paleo$_{S125}$ tends to have thinner ice (Figure 6.4e), however the amplitude of this difference is not large enough to explain the cold base areas. The diffusion of temperature through the ice-sheet explains that after a longer spin-up under cold climate conditions, the base tends to get colder than in a shorter run. Moreover, the polythermal mode of SICOPOLIS could also explain part of the difference with GRISLI.

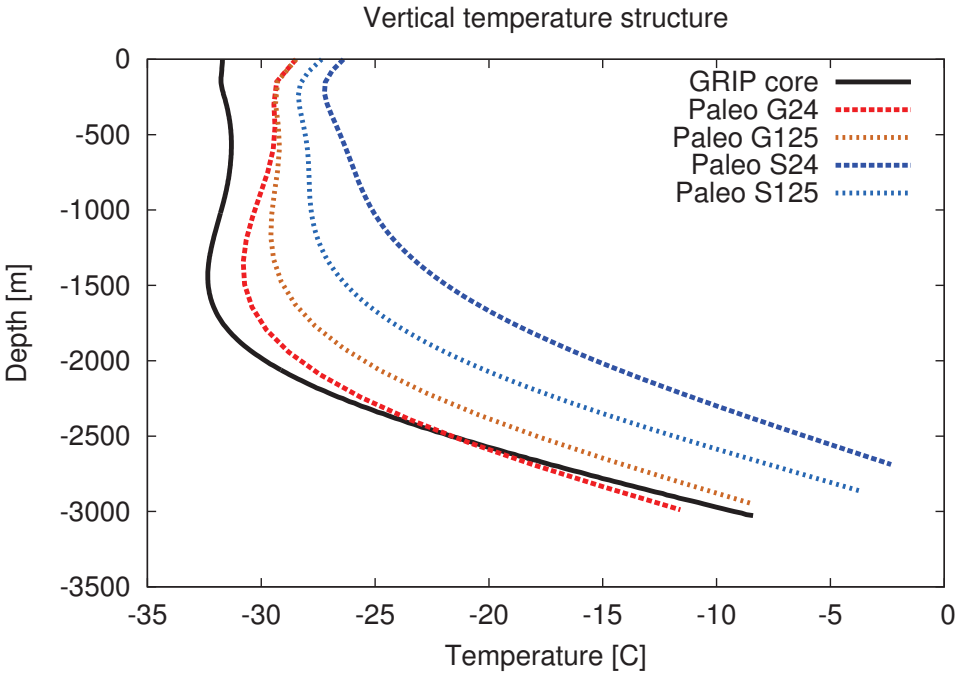

Figure 6.5: Vertical temperature profiles at the GRIP bore hole location (72.58 °N, 37.63 °W Johnsen et al. 1995). The black solid line represents the values from the GRIP ice core, the dashed curves stand for the simulated temperature: red line for Paleo$_{G24}$, orange line for Paleo$_{G125}$, dark blue line for Paleo$_{S24}$, and cyan line for Paleo$_{S125}$. Values are in °C. Note that the simulated values are taken from the grid point closer to the observed point, and this grid point represents not the precise location but an area of 20x20 km.

The temperature at the base of the ice sheet derives from the diffusion of the surface temperature through the ice, from the geothermal heat flux, from the heat generated by friction during the sliding and from the weight of the column of ice. As shown in Figures 6.4c and 6.4f, the differences in ice thickness between the short and long spin-up can only be partially linked to difference in the ice elevation for both ice sheet models. In fact only few marginal regions present large differences between the simulated ice thicknesses (Figure 6.4c and 6.4f). Thus, the differences in basal temperature could be linked to the length of the paleo-runs and its impact on the temperature diffusion through the ice. To check this hypothesis the simulated vertical temperature structure through the ice sheet at the GRIP site (72.58 °N, 37.63 °W) is compared to the vertical temperature measurements retrieved from the GRIP ice core (Johnsen et al. 1995). The simulations performed with GRISLI exhibit a vertical profile highly similar to the measured temperature at the GRIP site (Figure 6.5), even if the temperature in the central and upper part of the pro-

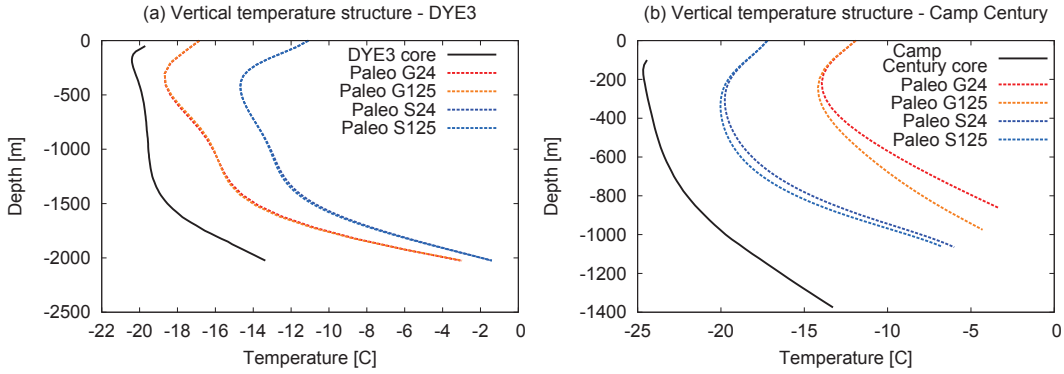

Figure 6.6: Vertical temperature profiles at the (a) DYE3 bore hole location (65.11 °N, 43.49 °W, Gunderstrup and Hansen 1984; Dahl-Jensen and Johnsen 1986) and (b) Camp Century bore hole location (77.10 °N, 61.08 °W, Robin 1976). The black solid line represents the values from the ice cores, the dashed curves stand for the simulated temperature: red line for $Paleo_{G24}$, orange line for $Paleo_{G125}$, dark blue line for $Paleo_{S24}$, and cyan line for $Paleo_{S125}$. Values are in °C. Note that the simulated values are taken from the grid point closer to the observed point, and this grid point represents not the precise location but an area of 20x20 km.

files are warmer than the observed values (black solid line in Figure 6.5). Nevertheless, both spin-ups reach temperatures in high agreement with the GRIP measurements.

On the contrary, the spin-ups carried out with SICOPOLIS present a temperature profile highly different from GRIP. While the increased length of the spin-up simulations from $Paleo_{S24}$ to $Paleo_{S125}$ improve the temperature at its upper and lower part, the vertical profile is still far from GRIP. The warmer profile in SICOPOLIS simulations can be explained (1) by the thinner ice thickness in the GRIP grid point with respect to GRISLI simulations ($\sim 200\ m$ difference), and (2) by the different temperature structure considered in the two ice sheet models, in fact SICOPOLIS account for the more complex polythermal structure.

To test these hypothesis, we compare the vertical profile of GRISLI and SICOPOLIS at two more ice core sites: DYE3 and Camp Century (Figure 6.6, ice core sites locations reported in Figure 1.10). In general, GRISLI perform better than SICOPOLIS at DYE3, while SICOPOLIS is closer to observation at Camp Century. However, in both cases the ISM that performs better is also the ISM that simulates the ice thickness closer to the observed value. In fact, SICOPOLIS simulates a thinner ice with respect to GRISLI (difference of about 94 m) at DYE3. On the contrary, GRISLI simulates a thinner ice with respect to SICOPOLIS (difference of about 143 m) at Camp Century. Consequently, the ability of an ISM in simulating the GIS ice thickness is a key factor in determining its ability in simulating the vertical temperature profile, as well.

The largest amount of basal melting occurs along the southeastern coast in all simulations (Figure 6.7). This area presents fjords with fast flowing ice, which release heat from basal friction, and high values of geothermal heat flux (Figure 1.9). As seen for the basal temperature, basal melting occurs also in correspondence of the NEGIS region, and in the longer GRISLI spin-up simulation ($Paleo_{G125}$) the basal melting in this area occurs further inland with respect to $Paleo_{G24}$. SICOPOLIS simulations show basal melting further inland than in GRISLI simulations, as seen for the basal temperature

(Figure 6.4), even if most of the internal part of the GIS shows basal melting values of the order of 0.001 $m\ yr^{-1}$ (Figure 6.7). For example, only the Paleo_{S24} simulation presents values of basal melting different from zero at the GRIP location, with basal melting values of about 0.0006 $m\ yr^{-1}$. Finally, the total basal melting is higher in SICOPOLIS experiments with respect to GRISLI ones. This discrepancy can be linked to the warmer temperature structure of SICOPOLIS with respect to GRISLI one (Figures 6.4, 6.5 and 6.6).

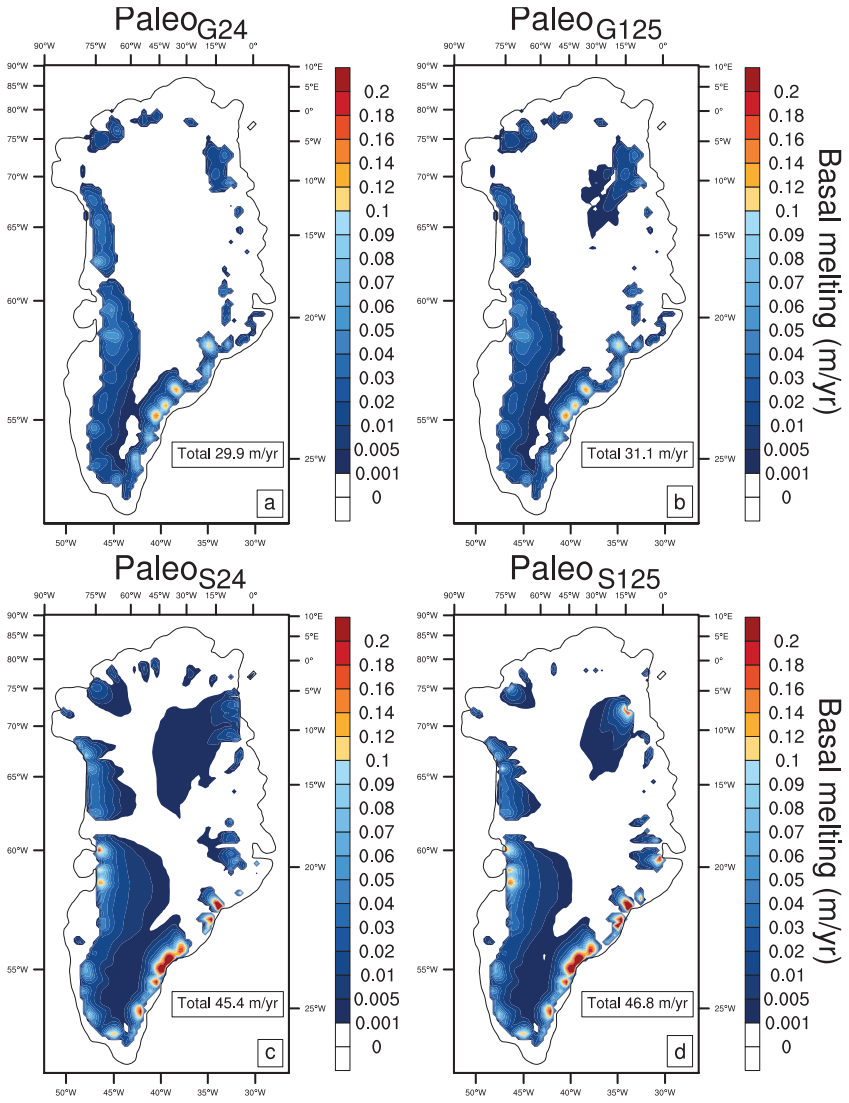

Figure 6.7: Basal melting ($m\ yr^{-1}$) at the end of the spin-up simulations: (a) Paleo_{G24}, (b) Paleo_{G125}, (c) Paleo_{S24}, and (d) Paleo_{S125} (Table 6.1).

6.3.2 1850–2100 simulations

Due to the slow diffusivity of surface temperature within the ice sheet, the evolution of basal melting is slow and the period 1850–2100 represents a too short time-window to

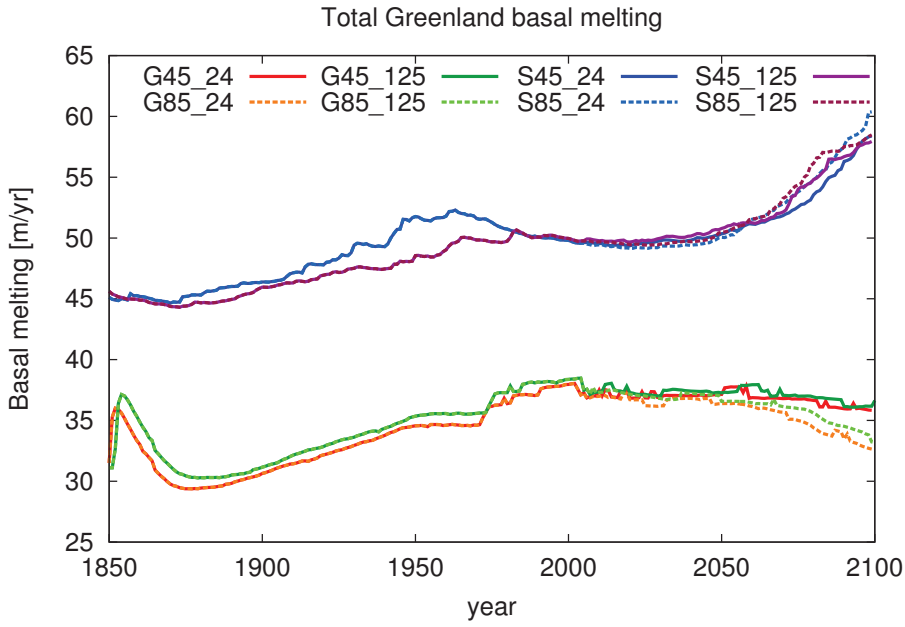

Figure 6.8: Total Greenland ice sheet basal melting production until 2100 ($m\ yr^{-1}$). The solid lines correspond to the simulations conducted under a RCP 4.5 future emission scenario, while the dashed lines correspond to a RCP 8.5 scenario. Red curves are for the simulations performed with GRISLI and branched from the 24 kyrs spin-up, green curves are simulations branched from the 125 kyrs spin-up. Similarly, blue lines are for the simulations performed with SICOPOLIS and branched from the 24 kyrs spin-up, and purple lines correspond to simulations branched from the 125 kyrs spin-up. Note that GRISLI simulations exhibit an initial step due to the restart from the spin-up simulations, which is less visible in SICOPOLIS simulations.

really simulate large changes. However, between 1850 and 2100 some differences emerge from the simulations (Figure 6.8).

In general, the length of the spin-up exhibits a small impact on the averaged basal melting production at century timescale until 2100. In particular, the difference in SICOPOLIS simulations is of about 0.88 $m\,yr^{-1}$, and, in GRISLI case, the difference stay around 0.73 $m\,yr^{-1}$. On the contrary, the difference between GRISLI-based simulations and SICOPOLIS-based simulations is of about 14.6 $m\,yr^{-1}$. A similar difference was found already in the spin-up simulations (Figure 6.7), and it can be related (1) to difference in simulated ice thickness and melting area and (2) to difference in simulated ice velocity at the ice sheet base.

The difference between future scenarios is also characterized by differences between GRISLI-based simulations and SICOPOLIS ones (Figure 6.8). The GRISLI simulations based on a RCP 8.5 emission scenario exhibit values of basal melting lower than the simulations based on a RCP 4.5 scenario (0.93 $m\,yr^{-1}$, on average). On the contrary, the simulations performed with SICOPOLIS show small differences between RCP 8.5 scenario and RCP 4.5 one during the 21st century, and an increasing trend in basal melting production during the second half of the 21st century is simulated (Figure 6.8). These differences can be ascribed to variations (1) in basal melting extent and (2) in ice

sheet velocity at the ice base. The different behavior between $G45_{125}$ and $G85_{125}$ can be related to a difference in basal melting area of about 3360 km^2 on average over the period 2050–2100. Furthermore, the simulation $G45_{125}$ exhibits an increase in vertical averaged velocity of about 0.47 m/yr on average over the entire ice sheet during the period 2005–2095. On the contrary, the simulation $G85_{125}$ shows a reduction in vertical averaged velocity of about 0.21 m/yr on average over the same period. The large increase in basal melting production during the 21st century depicted by the SICOPOLIS simulations $S45_{125}$ and $S85_{125}$ can be explained by a large increase in basal ice sheet velocity. The simulation $S45_{125}$ exhibits an increase of about 7.62 m/yr on average over the entire ice sheet during the period 2005–2095, while the simulation $S85_{125}$ shows an increase of about 9.51 m/yr on average over the same period. Note that the basal drag coefficient in GRISLI is inferred with an iterative inverse method based on the present-day observed velocity (Figure 2.5, Edwards et al. 2014), while SICOPOLIS describes the basal sliding by means of a Weertman-type sliding law (Eq. 2.31) in which the basal drag is derived from the basal pressure and the surface slope (Eq. 2.33). More detailed description is given in Sections 2.2.4 and 2.3.

However, the basal melting represents a small percentage with respect to the surface melting considered in the previous chapter (Chapter 5). For example, the meltwater produced at the base in the simulations $G45_{24}$ is equivalent to the 4% of the meltwater produced on the surface, on average in the period 1850–2100. This percentage is lower during the 21st century (about 2.7%), since the surface has a faster response to the increase in air surface temperature with respect to the ice sheet base.

6.3.3 Basal meltwater routing

Finally, we evaluate the amount of basal meltwater able to reach the coasts and form runoff. The routing scheme described in Section 2.3.2 is applied to the basal meltwater and the routing is computed over the bedrock topography. As example, the results are reported for the two simulations $G45_{24}$ and $G85_{24}$.

The basal meltwater is located in the areas where the basal temperature is at the pressure melting point (see Figures 6.4 and 6.9), and, as seen in the previous section (Section 6.3.2), the basal meltwater has very small changes in time. In fact, the panels of Figure 6.9 do not show visible changes between present-day (1980–1999, Figure 6.9a) and near-future (2081–2100, Figures 6.9c and 6.9e) simulations.

The distribution of the basal meltwater after applying the routing scheme exhibits a peculiar behavior (Figures 6.9b, 6.9d and 6.9f). Differently from the surface routing, the basal meltwater is trapped in the numerous bedrock topographic depressions, while, on the GIS surface, topography is smoother (Figure 1.12). Furthermore, the bedrock exhibits also slopes directed inland due to the isostatic depression which can also affect the flow of the basal meltwater (Figure 1.12a). In fact, only the 42% of the total basal meltwater is able to reach the coasts. Note that the total basal meltwater is conserved before and after applying the routing scheme, but only a small fraction, i.e. 42% in our simulations on average, can be accounted as runoff.

In general, this analysis shows that the basal meltwater production is smaller than the surface meltwater production, and it highlights the difficulty of the basal meltwater in reaching the Greenland coastal areas in order to become runoff. Further improvements of the sub-glacial hydrology knowledge is crucial to better constrain those aspect.

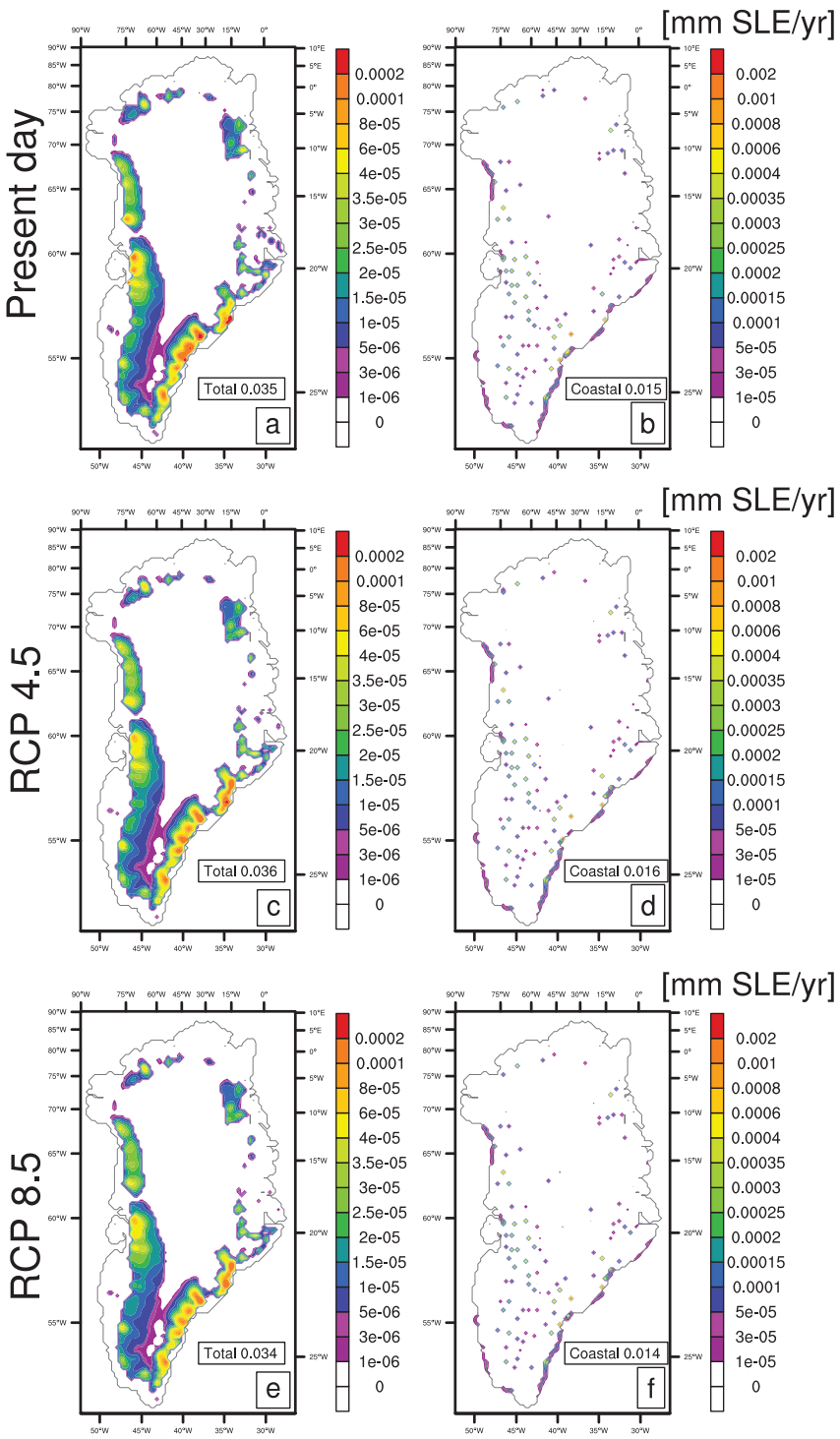

Figure 6.9: Spatial distribution of basal meltwater (panels a,c,e) and its distribution after applying the routing scheme (panels b,d,f). The values are in mm SLE yr^{-1}. Note that the coastal values in panels b,d,f represent the fraction of basal meltwater reaching the coast, even if the total amount of basal meltwater remain the same (values in panels a,c,e).

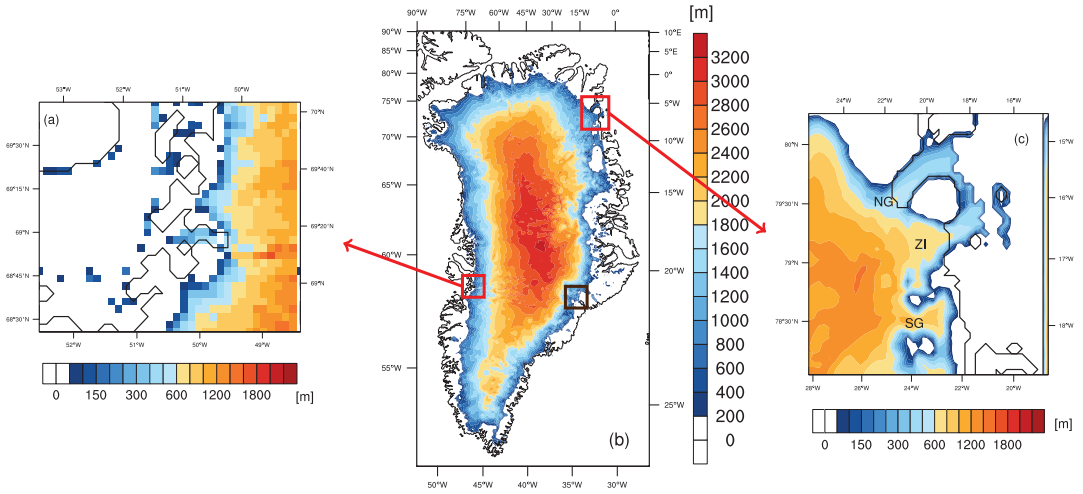

Figure 6.10: Present-day observed ice thickness (in m, Bamber et al. 2013). (a) Close-up of the Jakobshavn outlet glacier ice thickness (note that the outlet glacier tongue in GRISLI is represented by two grid point in width and seven in length), (b) the GIS ice thickness, and (c) close-up of the NEGIS ice streams outlets, namely the Nioghalvfjerdsfjorden Glacier (NG), the Zachariae Isstrøm (ZI), and the Storstrømmen Glacier (SG). The black line is the observed coastline. The brown box exhibit the Kangerdlugssuaq glacier region location.

6.4 Calving

6.4.1 Simulated spin-up floating ice along GIS coasts

About half of the recent mass loss is attributed to an increase in surface melting, with the remain due to increased ice discharge (e.g. van den Broeke et al. 2009; Bamber et al. 2012). The calving of the Greenland ice sheet occurs at the front of the main outlet glaciers which are located on small fjords. Thus, the grid resolution usually applied in ice sheet model is too coarse to simulate the fjords scale and to account properly for the processes at the marine ice front with sufficient detail (e.g. Goelzer et al. 2013).

For this reason, our analysis focuses on two regions (Figure 6.10): the Jakobshavn Glacier area in the western coast of Greenland, and the NEGIS area in the northeastern part of Greenland. The Jakobshavn Glacier drains about the 5.4% of the Greenland ice sheet (e.g. Rignot and Kanagaratnam 2006) and it is one of the largest GIS outlet glacier (Motyka et al. 2011). However, its mean width is of about 6 km (e.g. Sohn et al. 1998), which is at the limit of our ice sheet model horizontal resolution. On the contrary, the NEGIS floating area has an extent of about 2750 km^2 (e.g. Bamber et al. 2013) and it is characterized by three main outlets: the Nioghalvfjerdsfjorden Glacier, the Zachariae Isstrøm and the Storstrømmen Glacier (NG, ZI and SG in Figure 6.10c, respectively). The Nioghalvfjerdsfjorden Glacier exhibits a calving front 20-km wide (e.g. Khan et al. 2014), which can be better resolved in our simulations at 5-km horizontal resolution, with respect to Jakobshavn Glacier.

Calving depends on whether or not the ice sheet reaches the coasts at the end of our spin-up. In order to investigate the ability of GRISLI to simulate calving along the coasts, the presence of ice along the coasts is checked at the end of the spin-up, i.e. at pre-industrial period (Figure 6.3).

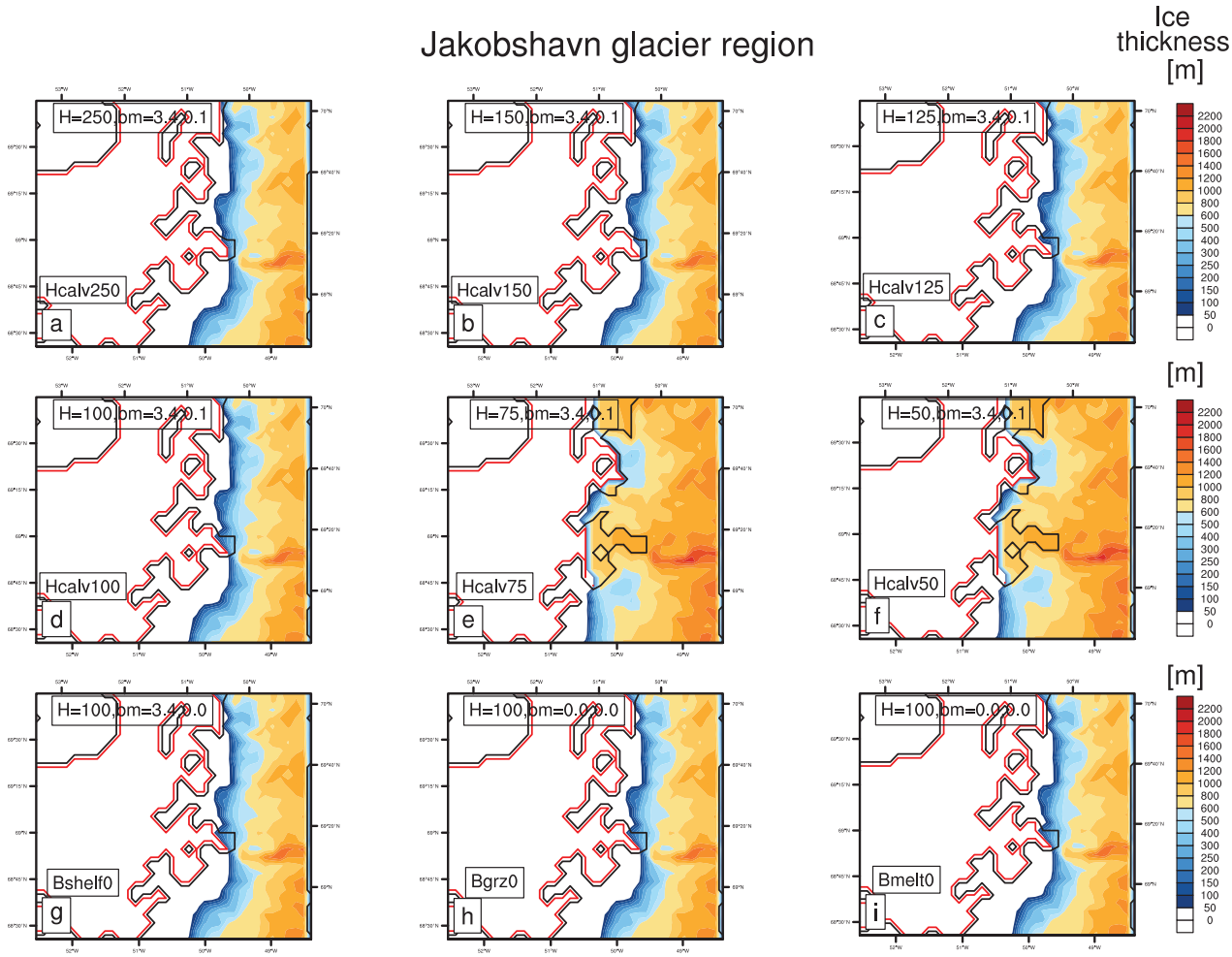

Figure 6.11: Ice thickness at the end of the spin-up simulations (year 1850) in the Jakobshavn glacier region. A set of nine simulations are obtained using the values in Table 6.2, which are applied to the last 1500 years of the paleo-run. Values are in m. The black line represents the observed coast line and the red line the simulated one.

For most of Greenland, the horizontal resolution of 5 km is not enough to capture the outlet glaciers evolution in the narrow fjords, whose width goes well below 1 km. For example, the ice thicknesses obtained in the year 1850 in the set of experiments for the Jakobshavn show that GRISLI is not able to reproduce the floating glacier tongue as visible in observations (Figures 6.10a and 6.11). Because of resolution, calving and SMB in our spin-up, the glacier retreats at the beginning of the spin-up and never float again, whatever the H_{calv} and b_{melt} is used. The reduction in H_{calv} give some difference when the values goes below 75 m, in fact the experiments Hcalv_{75} and Hcalv_{50} show a larger ice sheet able to go beyond the present-day coast line, but the ice thickness reach the bedrock giving no floating ice even in this simulations (Figures 6.11e and 6.11f). On the contrary, the changes in b_{melt} values seem not to affect the ice thickness at the margins of the Jakobshavn glacier region (Figures 6.11g, 6.11h and 6.11i). The difficulty in reproduce the Jakobshavn glacier can be linked to the too coarse resolution of the ice

sheet model which is not able to properly resolve the fjord scale (Figure 6.10a).

In the case of NEGIS, the ice shelf does not retire completely with respect to observations (Figures 6.10c and 6.12). The experiments carried out with high values of H_{calv}, namely Hcalv_{250} and Hcalv_{150} (Figures 6.12a and 6.12b), exhibit only few floating grid points. On the contrary, the $b_{melt,grz}$ parameter has a strong impact on the Zachariae Isstrøm (ZI in Figure 6.10c) growth. In fact, the two experiments performed with $b_{melt,grz}$ set equal to zero, namely Bgrz_0 and Bmelt_0 (Figures 6.12h and 6.12i), exhibit a larger expansion of that outlet glacier. Note that the largest expansion of the outlet glacier is obtained in the experiments with values of H_{calv} equal or lower than 100 m. This is in agreement with the few calving studies that indicate a front thickness of about 80 m in this region (Reeh et al. 2001). In general, the NEGIS area shows some floating point, even if GRISLI is not able to fully expand the outlet glaciers as much as it should be.

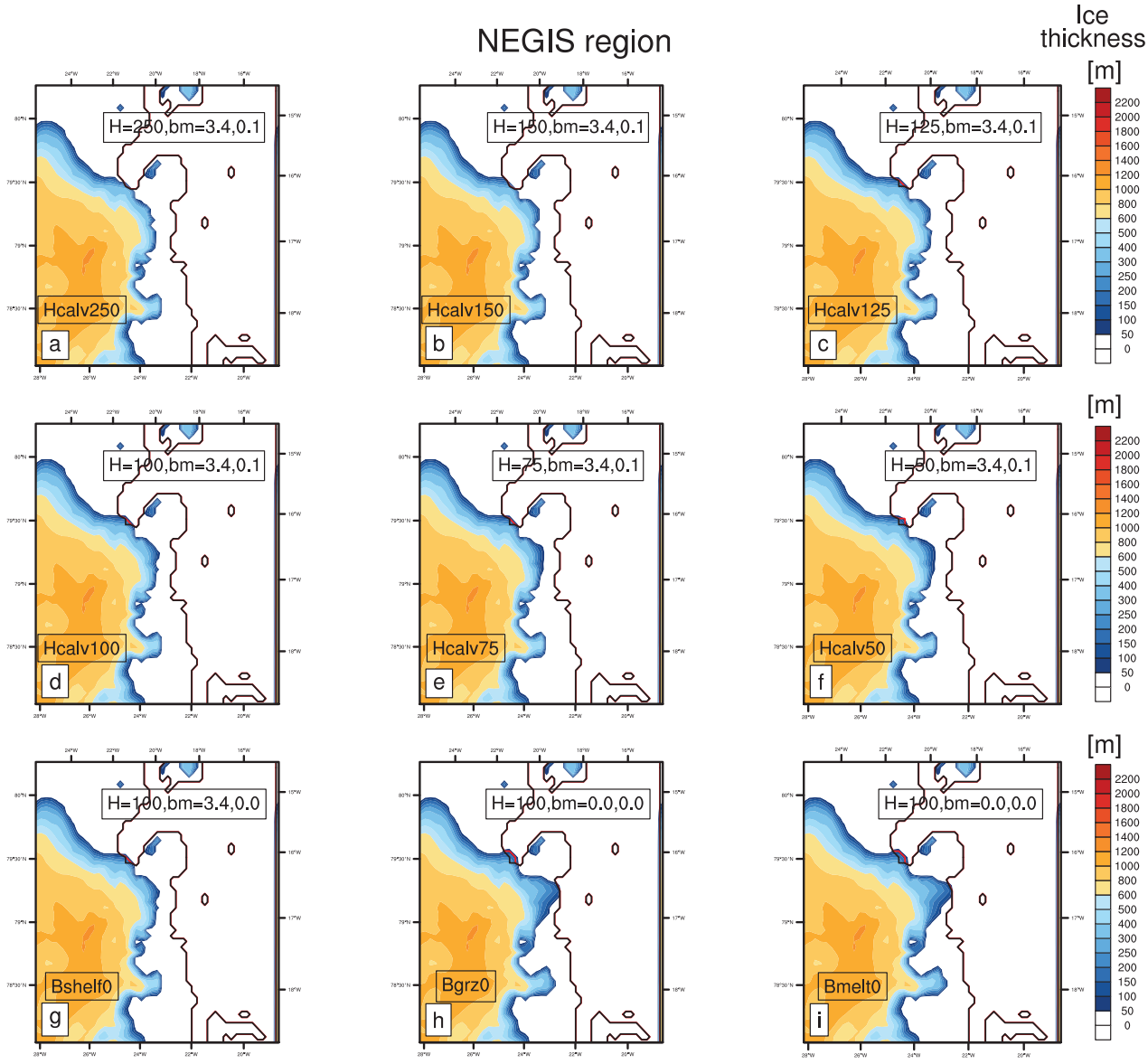

Figure 6.12: As Figure 6.11, but in the NEGIS region. Values are in m.

6.4.2 Calving in time (1850–2100)

GRISLI proved to be able to produce some floating ice in the NEGIS area, while the Jakobshavn outlet glacier is too narrow to be properly simulated in GRISLI simulations. For this reason, in this section, only the NEGIS area is considered. Note that the time evolution of calving is simulated under both future emission scenarios, i.e RCP 4.5 and RCP 8.5 (Figure 6.13).

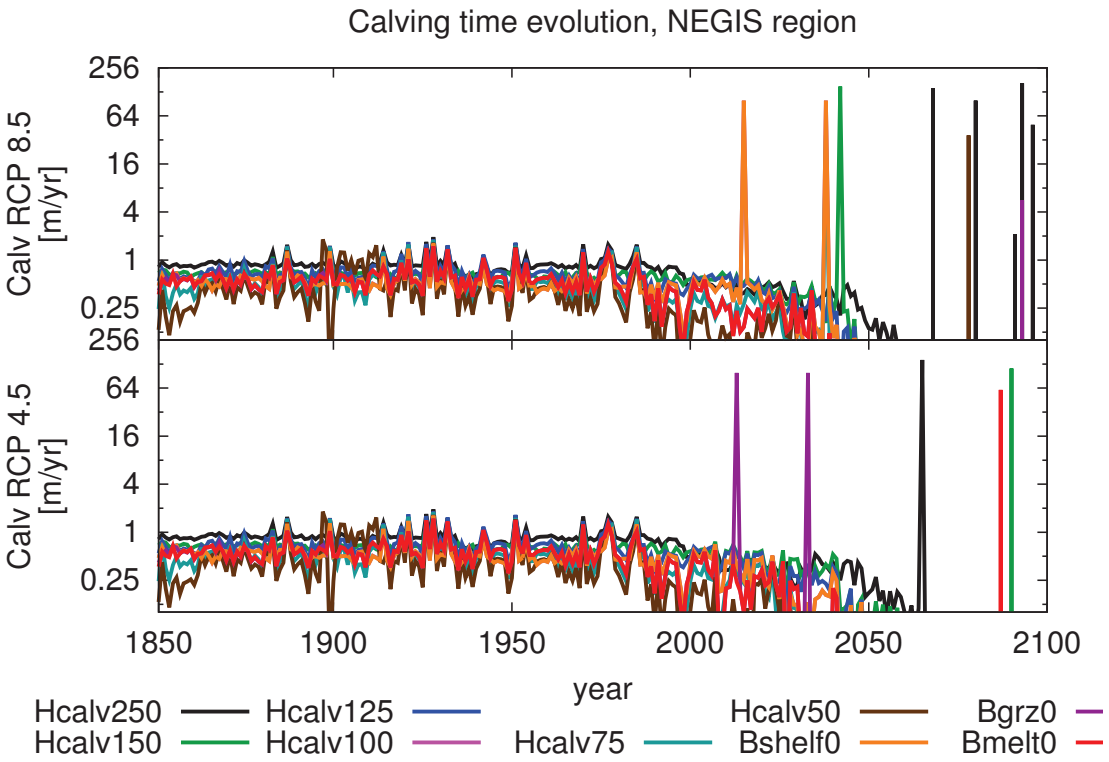

Figure 6.13: The time evolution of simulated calving in the NEGIS region under (a) a RCP 4.5 scenario and (b) a RCP 8.5 scenario. The simulations come from the set of nine experiments summarized in Table 6.2. Values are in $m\,yr^{-1}$.

The calving during the 20th century exhibits an almost constant behavior with values around 0.6 $m\ yr^{-1}$, on average, in all the experiments. However, some years present larger calving values, which reach values up to 2 $m\ yr^{-1}$. This small amount of calving represents the calve of the small amount of ice transported at the outlet glaciers front. Note that the different behavior of each experiments partially derives from the differences in the outlet glaciers extent simulated at the end of the spin-up runs (Figure 6.12). On the contrary, during the 21st century some of the experiments show years with high values of calving that can be attributed to the lowering of a floating point below the thickness threshold H_{calv}, due to the long-term impact of melting at the surface and at the base of the floating point. The climate forcing is influencing the calving behavior as well. For example, the experiment Bgrz_0 (purple lines in Figure 6.13) exhibits an unique case of high calving ($\sim$ 6 $m\ yr^{-1}$ in the year 2092) in the RCP 8.5 simulation. The

RCP 4.5 experiment, instead, shows two events with calving at $\sim 100\ m\ yr^{-1}$ (in the years 2012 and 2032), that corresponds to the value of H_{calv}, and represent the calve of two frontal floating points. This different behavior highlights the influence of the surface mass balance component on the retreat of the marginal areas and on the calving parameterization.

The marginal retreat, then, is driven by two mechanisms: (1) calving and (2) surface melting. However, the ice sheet models are not able to properly simulate the calving along the Greenland margins. This limitation could be related to the low model resolution compared to the scales of the fjords, as seen in the Jakobshaven glacier region, and to the approximations for the dynamical part of the model, as already stated by Graversen et al. (2010). To overcome this limitations, many works, developed with the aim of studying the overall Greenland mass loss, describe the dynamical ice discharge part by means of observations (e.g. Rignot et al. 2011; Shepherd et al. 2012) or by means of specific outlet glacier models (e.g. Goelzer et al. 2013). More recent work embedded more complex calving parameterization in ice sheet models in order to improve their ability in simulating this process. For example, Calov et al. (2015) introduce in SICOPOLIS an heuristic statistical approach to account for the non-resolved fast ice discharge in each grid point, using ice thickness and distance from the ocean as driving variables. Nick et al. (2010) and Pollard et al. (2015), instead, simulate the calving process as response to the propagation of surface and basal crevasses.

6.4.3 Outlook: ice fluxes changes

As stated before, the ice sheet models used in this work are not able to simulate the dynamical discharge of the GIS by means of calving. One of the main limitations is given by the model resolution. Unfortunately, we cannot use higher resolutions with these ISMs, since their physics is based on the assumption of a shallow ice. Consequently, this approximation will not hold for horizontal resolutions too close to the typical vertical dimension of the GIS ($\sim$ 1 km to 3 km). However, the dynamical discharge can be investigated through the study of the changes in ice fluxes at the main fast-flowing coastal location.

Table 6.3: The set of multi-model ensemble mean experiments analyzed in Section 6.4.3. The simulations are performed with GRISLI at 5-km resolution and are based on the MME climate forcing combined with two reference climatology: one based on ERA Interim and one based on MAR climate. The 21st century climate are described by two future emission scenarios: RCP 4.5 and RCP 8.5. The set of calving values are the same used in the experiment $Hcalv_{100}$.

Name	**Reference climate**	**Future sccenario**
$\text{MME45}_{\text{ERAI}}$	ERA Interim	RCP 4.5
$\text{MME45}_{\text{MAR}}$	MAR	RCP 4.5
$\text{MME85}_{\text{ERAI}}$	ERA Interim	RCP 8.5
$\text{MME85}_{\text{MAR}}$	MAR	RCP 8.5

Here, we present a preliminary study of changes in ice thickness linked to variations of surface mass balance and ice velocity at three fast-flowing coastal locations: NEGIS area, Jakobshavn glacier region and Kangerdlugssuaq glacier region (Figure 6.10). In partic-

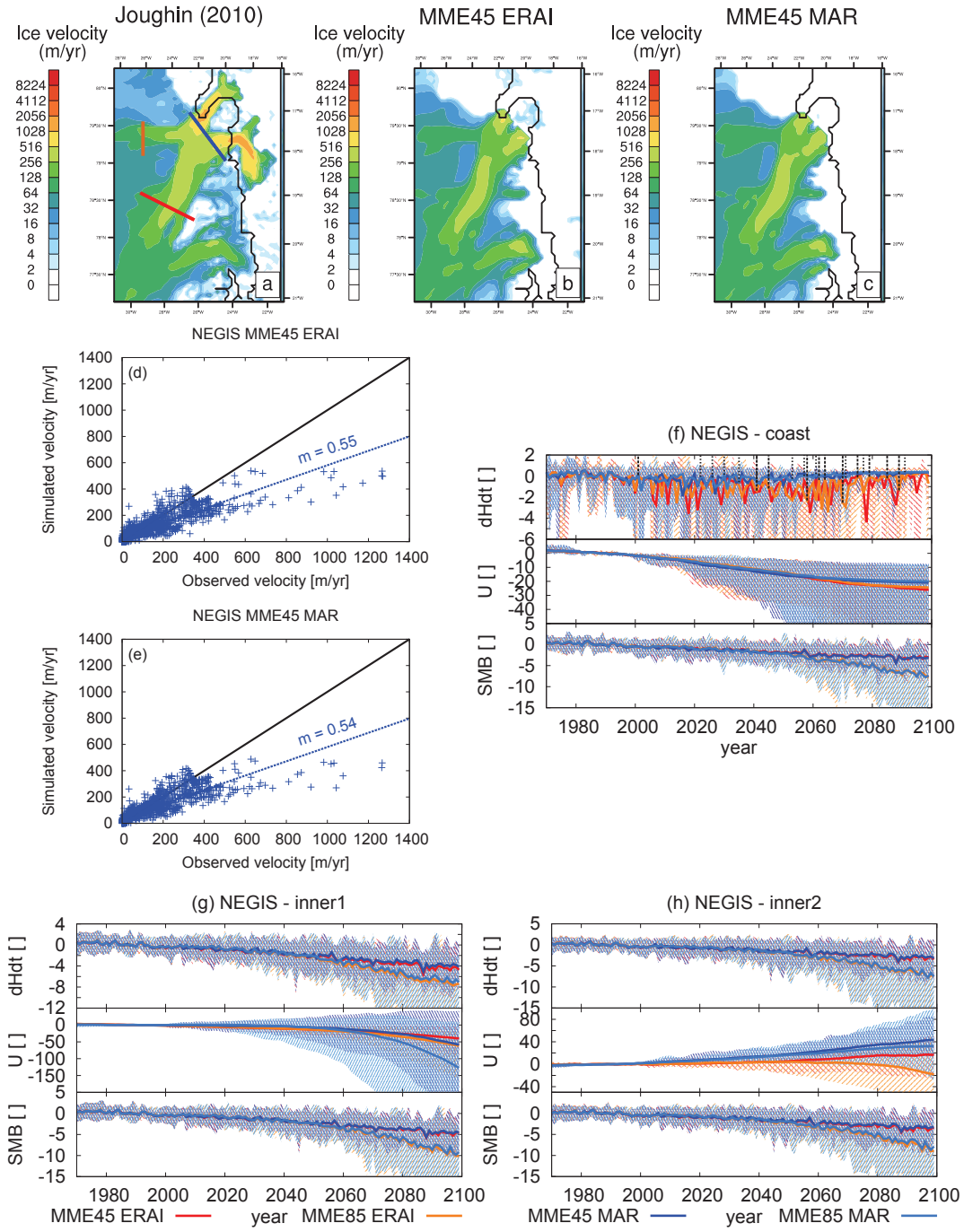

Figure 6.14: Focus on the NEGIS area. (a) Observed present-day surface velocities (Joughin et al. 2010). Simulated surface velocities with the experiments: (b) $MME45_{ERAI}$, and (c) $MME45_{MAR}$. (d-e) Scatter plot of simulated versus observed velocities in the studied area. Time evolution of ice elevation differences (dHdt), velocity (U) and surface mass balance (SMB) (f) at the coastal gate (blue line in panel (a)), (g) at the first inner gate (orange line in panel (a)) and (h) at the second inner gate (red line in panel (a)). Note that the values are standardized with respect to the period 1980–1999. The shaded areas represent the range of values simulated with the complete set of CMIP5 models, while the black lines highlight year in which the coastal gate reduce due to the ice retreat.

ular, we developed a set of four 5-km GRISLI simulations based on the MME climate forcing, which differ in the reference climatology and future emission scenario (summarized in Table 6.3). Note that the calving parameters are set equal to the intermediate case Hcalv_{100}. Moreover, the values of ice elevation differences (dHdt), velocity (U) and surface mass balance (SMB), used in the analysis, are standardized with respect to the present-day conditions.

NEGIS

The NEGIS region presents three main outlet glaciers, two of them characterized by a floating terminus (Figure 6.14a, e.g. Khan et al. 2014; Mouginot et al. 2015). GRISLI model is not able to reproduce completely the floating part of these outlet glaciers (Figures 6.14b and 6.14c). However, GRISLI is able to properly simulate the surface ice velocity in the inner part of the NEGIS region. In fact, the direct comparison between observed and simulated velocities (Figures 6.14d and 6.14e) shows a good match in the areas with velocities between 0 and 200 m/yr, while the fast part of the domain (from 400 to 1400 m/yr) is always underestimated in our simulations. The analysis at the coastal gate shows an initial decrease in dHdt, mainly driven by changes in SMB, which are mitigated in the last decades of the 21st century by the decrease in velocity (Figure 6.14f). The coastal gate at the NEGIS area is also influenced by the retreat of the ice sheet in that area. In fact, by the end of the 21st century, almost the entire ice sheet retreats behind the coastal gate. The two inner gates show a similar decrease in SMB, while the velocity fields exhibit a different behavior (Figures 6.14g and 6.14h). At the first inner gate (Figure 6.14g, orange line in Figure 6.14a) the velocity exhibits an initial stable condition followed by a decrease in velocity starting from the second half of the 21st century. On the contrary, the velocity at the second inner gate (Figure 6.14h, red line in Figure 6.14a) shows an initial stable conditions followed by an increase in velocity, except for the $\text{MME85}_{\text{ERAI}}$ simulation which presents a small decrease in velocity in the last decades of the 21st century. The dHdt variations follow the changes in SMB. Only at the first inner gate, the reduction in velocity is able to mitigate the impact of SMB.

Jakobshaven

The Jakobshavn glacier region is located along the western coast of Greenland (Figure 6.10). This glacier is characterized by a fast flowing ice which flows in a narrow fjord (Figure 6.15a, e.g. Joughin et al. 2008c, 2010; Nick et al. 2013). This geometrical characteristics are only partially captured by GRISLI (Figures 6.15b and 6.15c), since the maximum width of the terminating glacier is of about 6 km, which is not far from the model resolution. The direct comparison between observed velocities and simulated ones highlight the limits of our simulations in reproducing the fast-flowing ice in this region (Figures 6.15d and 6.15e). In particular, the grid point with velocities higher than 2000 m/yr are always highly underestimated in our simulations.

During the 21st century, the dHdt presents small variations under a RCP 4.5 scenario at the inner gate, due to a reduction in ice velocity and to small variations in SMB (Figure 6.15f). On the contrary, the reduction in SMB under a RCP 8.5 scenario leads to a reduction of dHdt at the inner gate. A similar behavior can be found at the coastal gate, where the simulations $\text{MME45}_{\text{ERAI}}$ and $\text{MME45}_{\text{MAR}}$ exhibit a stable behavior for the ice thickness (Figure 6.15g). On the contrary, the SMB decreases simulated by

$MME85_{ERAI}$ and $MME85_{MAR}$ are large enough to lead to a reduction in the dHdt value with respect to present-day conditions (Figure 6.15g). Note that the GRISLI limitations in simulating the fast-flowing ice at the mouth of the Jakobshavn glacier can lead to an underestimation of the impact of the ice sheet dynamics in this region.

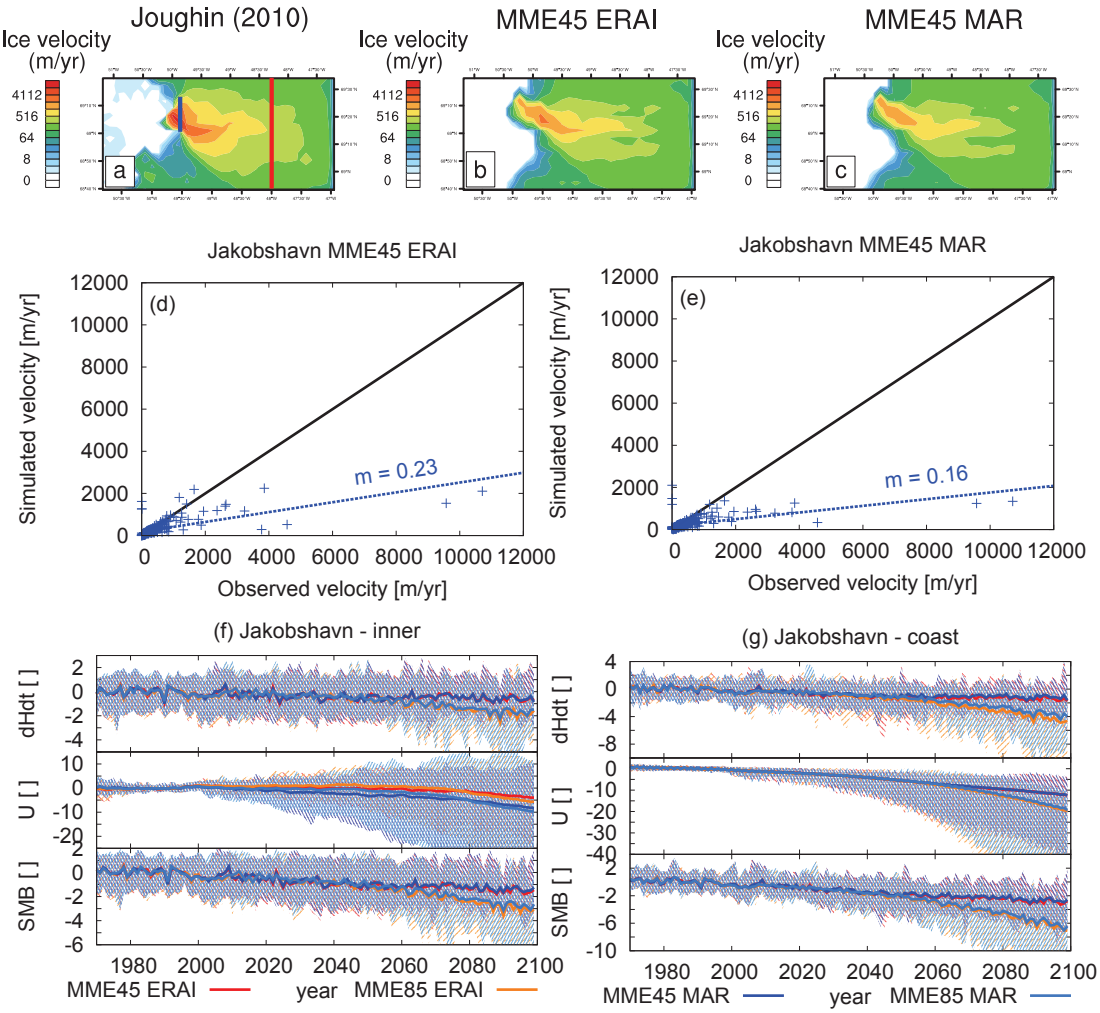

Figure 6.15: As Figure 6.14, but for the Jakobshaven glacier region.

Kangerdlugssuaq

The Kangerdlugssuaq glacier region is located along the eastern coast of Greenland (Figure 6.10), and it is characterized by a multiple-tributary structure (Figure 6.16a, e.g. Joughin et al. 2008b; Greve and Herzfeld 2013; Nick et al. 2013). Unfortunately, some gaps in the observations are located along the boundaries of our studied area (Figure 6.16a, Joughin et al. 2010). Our simulations are able to capture properly the surface velocity and the multiple-tributary structure characteristic of this area (Figures 6.16b and 6.16c). Furthermore, the direct comparison between observed and simulated velocities (Figures 6.16d and 6.16e) highlights a good match between the two fields. In particular,

the simulated velocities slightly overestimate the observed ones, especially at the fastest grid point. This good results can be ascribed to the ISM resolution and, mainly, to the use of an inverse method in defining the basal drag values (Figure 2.5 Edwards et al. 2014). Similarly to NEGIS region, we define three gates, a coastal one and two inner gates, where we develop our ice sheet evolution analysis. The differences in ice thickness at the coastal gate exhibit a large interannual variability which follows the similar changes in the velocity fields, while the decreasing trends in dHdt follow the variations in SMB (Figure 6.16f). However, the large reduction in ice velocity during the last decades of the 21st century, especially in the RCP 8.5 simulations, leads to a stabilization of dHdt. On the contrary, in both inner gates (Figures 6.16g and 6.16h), the dHdt decreases in time following the oscillations in surface mass balance, even if the increase in ice velocity affects the dHdt variations, as well. In general, then, at the fast-flowing coastal gate the impact of dynamics and surface mass balance are similar, while in the interior areas both dynamics and surface mass balance act in reducing the ice thickness, with a larger influence of SMB with respect to ice dynamics.

6.5 Closing Greenland ice sheet mass balance

This chapter dealt with the last two component of the Greenland mass balance: basal melting and calving. Both processes are not well simulated in ice sheet model due (1) to lack of observation of basal hydrology and basal processes to be used in constraining the ISMs parameterizations and (2) to the coarse resolution of the ice sheet model compared to the fjords scale.

The complete set of values is obtained for the simulation developed with GRISLI at 5 km forced by the anomaly climate fields coming from the CMCC-CM AOGCM and from the MAR reference climatology. In general, the surface mass balance account for about the 99% of the mass loss in our simulations. The remaining ∼1% is divided between calving and basal melting, with the basal melting values being two times larger than calving values. In our simulations, then, the surface mass balance is the main driver of the Greenland evolution. However, further improvements in describing basal melting and especially calving are required, since observations (e.g. Velicogna et al. 2014) and model results (e.g. Bamber et al. 2012) show that Greenland mass loss variations are coming half from surface melting and half from the outlet glacier discharge increase.

6.6 Summary

In this chapter, I analyze the ability of the ice sheet models in simulating the Greenland mass loss from two more mechanisms: basal melting and calving.

These processes are both influenced by the ice sheet conditions obtained at the end of the paleo-runs simulations. In particular, the vertical temperature structure and, especially, the temperature at the ice sheet base determine the regions where basal melting could occur. However, the temperature inside the ice sheet is strongly influenced by the spin-up, due to the slow diffusivity of the temperature along the ice sheet. For this reason, the length of the spin-up is important in evaluating the basal melting. Similarly, the ice topography, especially along the Greenland margins, at the end of the spin-up simulation is important for calving. In fact, in order to have any calving, some ice shelves are required to form and survive until the end of the spin-up simulation.

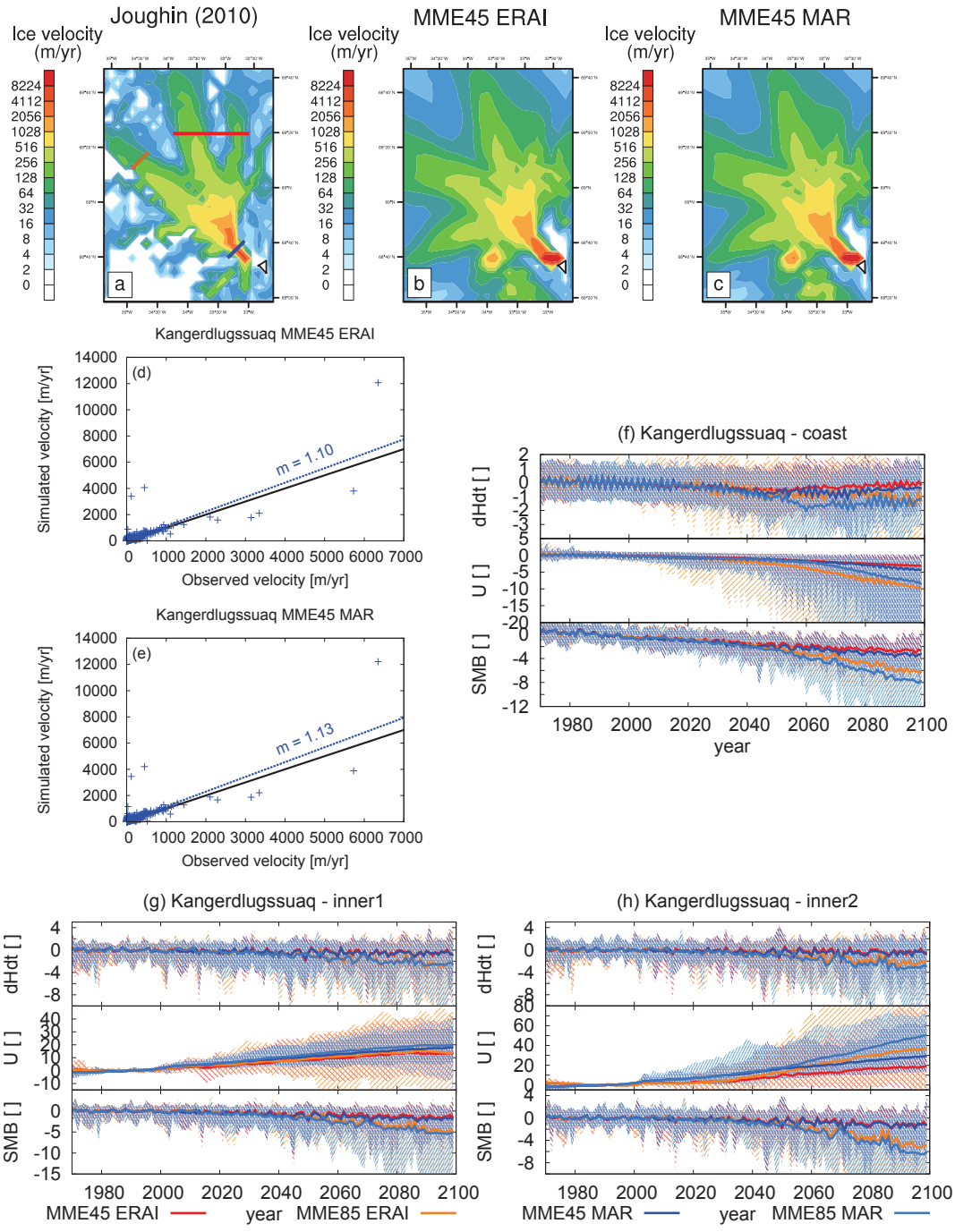

Figure 6.16: As Figure 6.14, but for the Kangerdlugssuaq glacier region.

The ability of the GRISLI calving parameterization in simulating the dynamical discharge along the Greenland coasts is strongly limited by the model resolution and by the approximations used in simulating the ice-sheet dynamics. In fact, GRISLI is able to simulate some calving in large ice shelf regions, such as the NEGIS region, while the calving occurring in the small coastal fjords is not well reproduced by the model, as in the Jakobshavn glacier region.

In general, the basal melting represents only a small fraction of the surface meltwater, and, in particular, only a small fraction of the meltwater produced at the base of the ice sheet is able to reach the coastal areas becoming runoff. On the contrary, calving and dynamical discharge from the GIS represent about half of the present-day mass loss from Greenland. However, calving occurs in small areas along the Greenland margins which are not properly reproduced in our ice sheet models due to a too low resolution, unable to properly resolve the fjords scale, and to the approximations used in simulating the ice sheet dynamics. For this reason, the dynamical discharge in these models might be retrieved from estimates of ice fluxes changes, as suggested here, or from ice discharge observations or from specific outlet glacier models, as done in many literature works.

Chapter 7

Discussion

7.1 Introduction

In this chapter, I discuss the limits of the methodology used to investigate Greenland ice sheet evolution through the experiments described in the previous chapters. Subsequently, I discuss the main implications in the global climate framework of the results obtained in the present work.

7.2 Initialization of ice sheet models

In the present work, the spin-up of both ice sheet models has been performed using an index method, following the techniques described by Greve et al. (2011). In particular, our spin-up method uses the $\delta^{18}O$ retrieved from the GRIP ice core (Dansgaard et al. 1993; Johnsen et al. 1997) to reconstruct the past time evolution of air surface temperature and precipitation departing from present-day climate conditions (more details in Section 2.4). However, different spin-up techniques can be found in literature (e.g. Payne and Baldwin 1999; Charbit et al. 2002; Born and Nisancioglu 2012; Edwards et al. 2014; Fyke et al. 2014). For example, Edwards et al. (2014) uses the present-day observation of ice thickness (Bamber et al. 2013), combined with geothermal heat flux (Shapiro and Ritzwoller 2004) and ice velocities (Joughin et al. 2010), to better constrain the ice-sheet geometry and shorten the time of spin up. However, in this case the resulting temperature profile does not contain the effect of the last glacial cycle.

The initialization of the ice sheet model is fundamental to obtain proper initial temperature conditions to simulate the present day and future ice-sheet dynamics. The importance of the ice sheet spin-up in simulating Greenland surface mass balance has been already shown by Rogozhina et al. (2011) and Yan et al. (2013). For example, the simulated surface mass balance values obtained in Chapter 4 are strongly influenced by the initial conditions of our system simulated by the two different ice sheet models. Aside from the impact of the differences in initial ice thickness, the comparison between GRISLI and SICOPOLIS results highlights also the importance of the ice sheet surface slopes along the margins, especially when different climate forcing are considered. Furthermore, in Chapter 6, the importance of the Greenland ice sheet spin-up has been shown for two more variables: the basal melting and the calving. Therefore, the use of a different initialization technique or a different set of parameters, as shown in Chapter 6

for calving, could affect the ice sheet geometry especially along the margins, where the studied variables (such as ablation, basal melting and runoff) occur.

7.3 Parameterizations

Many works show the influence of parameters on the ice-sheet dynamics (e.g. Ritz et al. 2001; Stone et al. 2010; Robinson et al. 2011; Applegate et al. 2012; Quiquet et al. 2013a). For example, Robinson et al. (2011) performed a large ensemble of Eemian GIS simulations using SICOPOLIS and concluded that the geometry of the GIS is highly sensitive to the choice of the model parameters, such as geothermal heat flux, sliding law coefficient, and SMB parameters. Applegate et al. (2012) performed an ensemble of 100 simulations in which five model parameters are varied (namely ice flow enhancement factor, basal sliding factor, geothermal heat flux, and ice and snow melting factors). In general, they found many combinations of these five parameters able to reproduce the observed present-day ice volume within a 10% error (blue cross in Figure 7.1). In the present work the experiments are carried out using fixed set of parameters values (summarized in Table 4.1) coming from literature. Only few sensitivity experiments are performed to analyze the calving process in GRISLI (Chapter 6). However, many mechanisms in the ice sheet models are based on parameterizations which values can influence the results obtained in the present work. For example, the PDD method is based on a set of parameters, i.e. the melting factors C_{ice} and C_{snow}, and the standard deviation of the temperature distribution σ_{pdd}, which are used in literature with different values (e.g. Tarasov and Peltier 2002; Greve 2005; Fausto et al. 2009). In the previous chapters, we used the values introduced by Tarasov and Peltier (2002) (Table 4.1). Here, we test, as example, the impact of a different value of σ_{pdd} on the ablation simulated with GRISLI at 5 km forced with MME climate. In particular, we use the value of 2.53 $^{\circ}C$ indicated by Fausto et al. (2009). In this case the ablation reduce from 285 Gt/yr to 117 Gt/yr. Consequently, a reduction in the σ_{pdd} lead to an almost equivalent reduction in the final ablation values. Moreover, other parameters are accounted for in our simulations. For example, the atmospheric lapse rate (λ) in Eq. 2.53 regulates the impact of changes in elevation on the air surface temperature. A similar effect is done by the precipitation correction factor (γ) in Eq. 2.54 (e.g. Quiquet et al. 2013a). Consequently, larger values of λ and γ would enlarge the impact of the elevation corrections on the air surface temperature and precipitation leading, for example, to larger differences between experiments in the simulated accumulation and ablation values due to elevation differences compared to the values reported in Chapter 4. The melting factor used in Eq. 2.51 are derived from observation following Tarasov and Peltier (2002), however, larger values of these parameters can lead to an enhanced surface melting (e.g. Applegate et al. 2012). For this reason, the parameter sensitivity study could be the aim of further studies.

7.3.1 Downscaling and Elevation feedback

The ice sheet models require air surface temperature and precipitation from AOGCMs that generally have a coarser horizontal resolution with respect to the ISM grids. There are two types of corrections applied to the climate fields in our ice sheet simulations: (1) a pre-run downscaling from AOGCMs grids to ISM grids; (2) a runtime correction of the climate fields with changes in ice elevation since our ISM are not coupled to

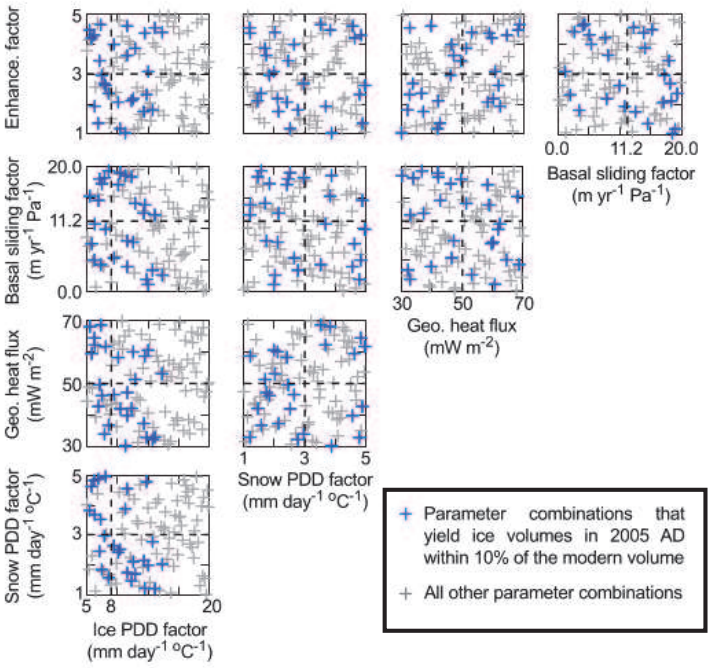

Figure 7.1: Figure 1 in Applegate et al. (2012). Ensemble of sensitivity experiments.

a climate model. For this reason a downscaling of the climate fields is necessary and many methodology could be found in literature, each of them with their own limitations. Here, I use a simple downscaling technique based on an atmospheric lapse rate and a precipitation factor (respectively λ and γ in Eq. 3.1). More complex downscaling methods can be found in literature, such as the SMHiL (surface mass balance high-resolution downscaling) method by Agosta et al. (2013), which was developed to compute the surface mass balance over Antarctica using a high-resolution topography, which allows to keep into account both orographic and non-orographic precipitation; or techniques based on dynamical approach, where a higher-resolution climate model is embedded within the low resolution one, or statistical method, where empirical relationship between coarse resolution and high-resolution climate variables are established (e.g. Fowler et al. 2007). The use of such techniques would improve the downscaled geographical pattern of air surface temperature and precipitation, especially in regions with complex topography, i.e. the southeastern mountainous area of Greenland.

In the climate system, surface temperature and precipitation evolve with the changes in surface topography. As elevation increases, temperature decrease and sometimes also precipitation. This mechanism is known as the elevation feedback. Our ISM does not account for this effect, therefore, we use a runtime climate correction using an atmospheric lapse rate values and a precipitation factor (Eq. 3.1). To understand how much of our SMB variations are due to this elevation feedback, the ISM is run inhibiting the elevation corrections. This test is performed using one specific configuration as an example: GRISLI at 20 km resolution forced by the CMCC-CM AOGCM on top of the MAR reference climatology (Table 3.1). In this case, the simulated surface mass balance presents a variations of 3.8 Gt/yr^2 (14.6 Gt/yr^2) during the 21st century (2000–2090), when the scenario RCP 4.5 (RCP 8.5) is used. This trend increases to 6.2 Gt/yr^2 (21.5

Gt/yr^2), when the elevation feedback is taken into account. This simple analysis shows that the elevation feedback has an impact of about 40 % on our simulated surface mass balance values. The work by Vizcaíno et al. (2015) retrieve an impact of the elevation feedback in the range 8% to 11% during the 21st century. The discrepancy between the work by Vizcaíno et al. (2015) likely comes from the difference in SMB scheme, lack of coupling with a climate model and horizontal resolution. Furthermore, the present analysis is developed starting from initial present-day spun-up ice-sheet topography not perfectly matching observations, leading to a thinner ice-sheet, which may enhances the impact of the elevation feedback.

7.3.2 Positive Degree Day

The calculations of surface mass balance and surface meltwater rely on the computation of ablation performed by the ice sheet models. The ablation simulated in the experiments presented in Chapter 4 exhibits values larger than the values simulated in previous studies that use a different ablation method (Figure 4.2). This discrepancy is mainly due to the methods used to calculate the surface mass balance. In this work, both GRISLI and SICOPOLIS use the positive degree day semi-empirical and semi-analytical methods. Previous studies, in fact, showed that the PDD method is more sensitive to temperature variations with respect to more physically based methods, such as energy balance models. For example, van de Wal (1996) shows that the sensitivity of a PDD model for a 1 °C perturbation in air surface temperature is about 20% higher than the sensitivity of an energy-balance model. Furthermore, Bougamont et al. (2007), in their 300 years simulations under a $4xCO_2$ condition, found that the PDD model generates annual runoff rates almost twice as large as runoff rates simulated by the energy balance model, and roughly half of this difference results from the snowpack thermo-dynamics. Thus, the lack of a proper description for the snowpack above the ice is one of the major drawback of the PDD method. Therefore, the use of a more complex ablation scheme would lead to higher SMB values than obtained in this work, especially under the warm RCP scenarios.

7.4 Physical approximations

The ice sheet models presented in this work belong to the hybrid category, and are based on shallow ice and shallow shelf approximations (Section 2.2.2). This class of ice-sheet models have some limitations, imposed by the considered approximations, that restrict their ability in resolve the dynamic in areas with complex topography. A Full-Stokes model, i.e. solving the main equations with no hydrostatic approximation, could overcome these limitations. However, Full-Stokes models cannot be run on long-term, such as for paleo-climate spin-up simulations (e.g. Gillet-Chaulet et al. 2012; Seddik et al. 2012), due to their high-demanding computational resources. To compensate for the limitations of the two previous categories of ISMs, the scientific community is focusing on multi-flow ice dynamics models which include both SIA and Full-Stokes physics and represent an intermediate solution to high computational resources (e.g. Thoma et al. 2014). The use of these category of ice sheet models would improve the simulation of ice dynamics in regions with complex topography, such as the outlet glaciers along Greenland margins.

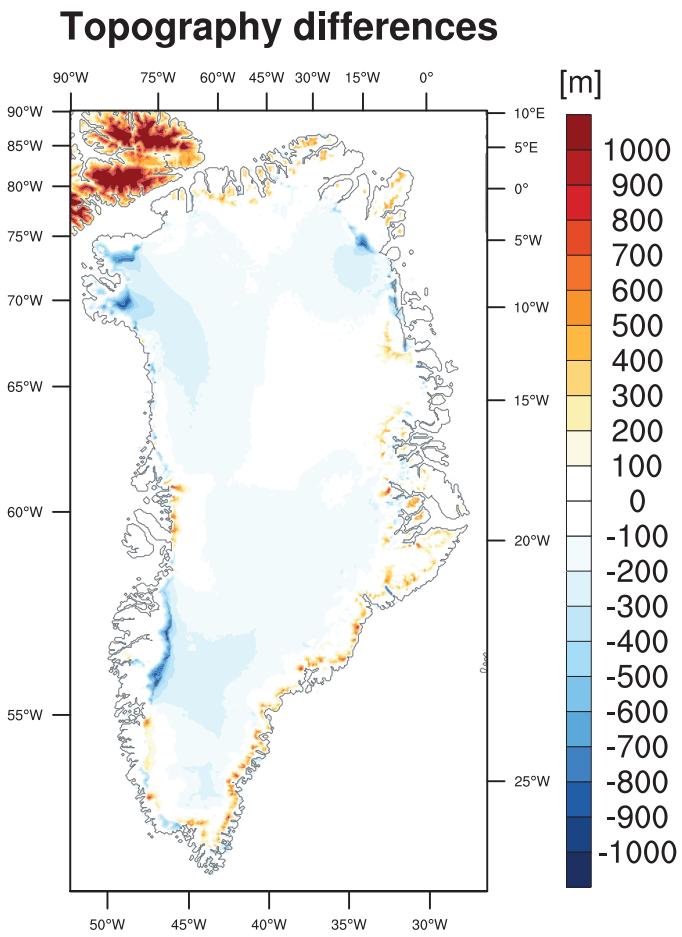

Figure 7.2: The differences between Obs (Bamber et al. 2013) and Sim initial topographies. Values are in m. The simulated topography is averaged over the period 1980–1999.

7.5 Impact of surface ice topography on the runoff distribution

The routing scheme used in Chapter 5 requires few input fields: the initial meltwater distribution and the surface topography. However, the Greenland topography obtained at the end of the spin-up simulations presented in Section 2.4 (Figure 2.14e) exhibits some discrepancies with respect to the present-day observed surface topography (Bamber et al. 2013). These differences in surface topography, then, could change the final runoff distribution along the Greenland coasts. For this reason, the routing scheme is run offline, using the same initial meltwater distribution, and (1) the surface topography from one 20th century experiment (hereafter Sim experiment); (2) the observed present-day topography (hereafter Obs experiment, Bamber et al. 2013). Note that the surface meltwater initial distribution and the topography used in the Sim experiment are taken from the simulation performed using GRISLI at 5 km resolution forced by the CMCC-CM AOGCM on top of the ERA Interim reference climatology, for example. Both variables,

surface meltwater and topography, are averaged over the period 1980–1999.

The topographies obtained in the two simulations exhibit discrepancies mainly along the marginal areas of the Greenland ice sheet (Figure 7.2). In particular, the simulated topography exhibits higher amount of ice in the southeastern and northern part of Greenland with respect to observations. On the contrary, the western and northeastern coasts present a lower topography (less ice) in the simulated topography with respect to the observed one.

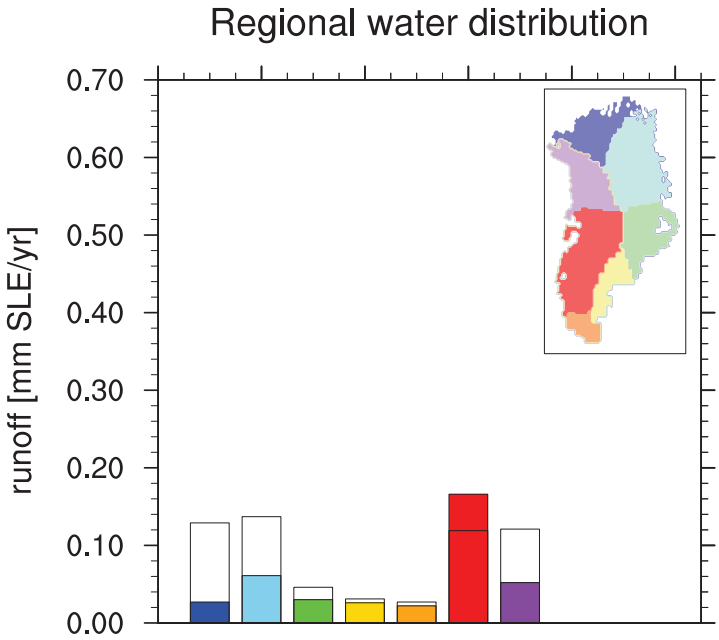

Figure 7.3: Runoff distribution for the seven basins considered in Chapter 5 (Sasgen et al. 2012). Colored column are the values obtained when the routing scheme is applied on the observed topography (Bamber et al. 2013). The white part of the columns represents the extra runoff in each region with the simulated topography Sim. Values are in $mm\,SLE\ yr^{-1}$.

These discrepancies in topographies impact on the amount of meltwater that reaches the coast, becoming runoff. When the routing scheme is applied on the Obs topography, the total meltwater able to reach the Greenland coasts amounts to 0.41 $mm\,SLE\ yr^{-1}$. On the contrary, the total runoff amounts to 0.65 $mm\,SLE\ yr^{-1}$ in the Sim experiment. The discrepancy is explained by the retention of meltwater in topographic depressions, that are more numerous on Obs surface topography. In fact, the percentage of meltwater able to reach the coasts varies from 69%, when the routing scheme is applied to the simulated topography, to 44%, when the Obs topography is used. The differences in runoff between the two simulations are not equally distributed along the Greenland coastal areas. In fact, the runoff simulated by the Sim experiment exhibits higher values in all the basins, except in the southwestern one, with respect to the Obs experiment. The largest difference between the two simulations lie in the northern basin (difference $\sim 0.102\ mm\,SLE\ yr^{-1}$), while the smallest differences are located in the southern and southeastern basins (difference $\sim 0.005\ mm\,SLE\ yr^{-1}$).

The routing scheme, then, is strongly sensitive to the topography used, and conse-

quently, the final runoff distribution is topography-dependent.

7.6 Meltwater infiltration

The runoff distribution obtained in Chapter 5 is based on the strong assumption that all the surface meltwater flows on the ice surface. However, observations show that the meltwater produced on the ice sheet surface only partially drains over the ice sheet surface via supraglacial streams. In fact, part of the surface meltwater flows through the ice sheet via moulins or crevasses which can deliver surface meltwater to the base of the ice sheet, where it can influence the ice sliding and the calving of outlet glaciers through velocity acceleration as well (e.g. Figures 2.6 and 6.1, Das et al. 2008; Catania and Neumann 2010; Andrews et al. 2014).

The flow of the meltwater from the surface to the base has, then, large implications both on the ice sheet dynamics and on the routing of the surface meltwater. However, only few works focus on the implementation of this process in the ISMs. So far, these few existing infiltration models usually focus on small specific regions where observations are available (e.g. Clason et al. 2012; Banwell et al. 2013; Clason et al. 2015). For example, Clason et al. (2015) found that about 80% of meltwater transfers from surface to bed during the 2009 and 2010 summer seasons at the Leverett Glacier (Southwest Greenland).

The implementation of simple models of meltwater infiltration from surface to ice base is important to calculate more precisely the runoff from the GIS to the nearby ocean, as well as to better constraint basal velocities.

7.7 Projected impact on global sea level

The runoff simulated by the set of experiments performed in Chapter 5 exhibits a cumulative change in sea level ranging from 10.8 to 12.9 $cm\,SLE$ over the period 2006-2100 under a RCP 4.5 scenario. The cumulative values increase to 14.9 to 18.0 $cm\,SLE$, when a RCP 8.5 scenario is accounted for.

The SeaRISE project (Bindschadler et al. 2013) simulates a range of possible projected GIS contribution to the mean global sea level in the next 100 years amounting to 0.9 to 6.6 $cm\,SLE$ under the SRES A1B climate scenario. Similarly, the ICE2SEA project (Edwards et al. 2014) obtains a mean Greenland ice sheet sea level contribution spanning from 5.7 $cm\,SLE$ to 6.4 $cm\,SLE$ by the end of the 21st century under the same future scenario.

The discrepancies between our simulations and the values obtained in the SeaRISE and ICE2SEA projects can be related (1) to the different future scenarios considered in the experiments, (2) to the larger sensitivity of the PDD method used in our simulations with respect to the energy balance model used, for example, to calculate the SMB values in Edwards et al. (2014) experiments, (3) to the lack of a proper snowpack in our experiments which impact on the storage of runoff and (4) to the difference in the spin-up of the ice sheet models. Furthermore, our simulations keep into account the elevation feedback which impact on the surface mass balance computation. In fact, when this feedback is considered in Edwards et al. (2014) simulations, their values increase of about 5%, reaching sea level contribution by 2100 from 5.9 to 6.7 $cm\,SLE$. However, the values presented here are in line with the results obtained by Yan et al. (2014) (0 to 27 $cm\,SLE$), and Fürst et al. (2015) (1.4 to 16.6 $cm\,SLE$), that developed their experiments

using the same external forcing applied here, i.e. CMIP5 with RCP 4.5 and RCP 8.5 scenarios.

7.8 Outreach of the study

The Greenland ice sheet has an important impact on both regional and global climate. For this reason, it has been largely studied and analyzed by means of observations (e.g. Dansgaard et al. 1993; Oerlemans and Vugts 1993; Johnsen et al. 1995, 1997; Bamber 2001; Hanna et al. 2005; Joughin et al. 2010; Rignot et al. 2011; Sasgen et al. 2012; Bamber et al. 2013; Velicogna et al. 2014) and models (e.g. Fettweis 2007; Ettema et al. 2009; Bamber et al. 2012; Franco et al. 2012; Quiquet et al. 2012; Rae et al. 2012; Fettweis et al. 2013; Vernon et al. 2013; Edwards et al. 2014). These information are used to develop and validate the parameterization used in describing the present-day Greenland ice sheet conditions (e.g. Marsiat 1994; Tarasov and Peltier 2002; Bales et al. 2009; Fausto et al. 2009). Consequently, the parameterizations used in Greenland ice sheet models are properly set to reproduce the present-day conditions. For this reason, for example, both the present-day surface mass balance and runoff values simulated in Chapters 4 and 5 are in line with observations and previous modeling studies.

Large efforts have been developed in studying the near-future conditions of Greenland, as well. This can explain also the likeness of the results presented here (Chapters 4 and 5) in comparison to previous literature works. However, some discrepancies in simulating present-day and near-future Greenland ice sheet exist. Many studies analyze some of the sources of these discrepancies (e.g. van de Wal 1996; Rogozhina et al. 2011; Franco et al. 2012; Rae et al. 2012; Vernon et al. 2013; Yan et al. 2013). In general, from the results presented here, I can state that the main differences derives from:

1. the long term spin-up simulations. The spin-up simulation has a direct impact on the initial Greenland ice sheet topography, which impacts on many processes. For example, the shape of the Greenland ice sheet influences the response of the ice sheet to different climate forcing. Similarly, the differences in topography impact on the surface mass balance of the ice sheet by means of the elevation feedback. Furthermore, the discrepancies between spin-up simulations can also influence directly other processes such as basal melting and calving, as described in Chapter 6. Note that the importance of the initial condition of the Greenland ice sheet obtained at the end of the spin-up simulations it has been largely studied (e.g. Rogozhina et al. 2011; Yan et al. 2013);

2. the dynamics described from the models. The differences between GRISLI and SICOPOLIS ice sheet models come from discrepancies in the initial conditions of the ice sheet as well as from differences in the dynamics described by the two models. SICOPOLIS approximates the ice sheet dynamics by means of the shallow ice approximation. On the contrary, GRISLI uses both the shallow ice and shallow shelf approximations. This difference has an impact on the simulated ice sheet thickness and basal condition, especially, in regions characterized by a fast flowing regime, such as the NEGIS region. For this reason, the scientific community is aiming to these issue by developing ice sheet models able to take into account both approximations (shallow ice and shallow shelf approximations) and full-Stokes

physics (multi-flow ice dynamics models, e.g. RIMBAY, Thoma et al. 2014). This category of models allow to apply the suitable physics in each part of the ice sheet;

3. the processes occurring in the interior and basal part of the ice sheet. These areas have few and localized observations, which reduce the knowledge of the present-day conditions in these regions. This lack of knowledge limits the possibility to test and validate the modeled values in those areas. For example, the thermodynamics through the ice sheet and at the base of the ice sheet has a large impact on the ice flow, but no validation could be developed at the entire ice scale. Similarly, the penetration and motion of the meltwater from the surface to the base of the ice sheet is unknown at the ice-sheet scale. However, many efforts have been done with the aim to improve the observations and knowledge on this areas (e.g. Andrews et al. 2014; van de Wal et al. 2015).

Another important point, not directly assessed in the present work, are the surface processes. Here, both ice sheet models calculate the ablation using a PDD method. This method presents many limitations, as presented before (Section 7.3.2). In particular, the PDD method lacks of a proper description of the snowpack above the ice sheet, which has been proven to influence the amount of ablation (Bougamont et al. 2007), and to exert a storage effect on the meltwater (Harper et al. 2012; Forster et al. 2014). For these reasons, further studies on modeling these surface mechanisms can be developed in order to evaluate their impact on the present-day, and, especially, near-future ablation and runoff production in Greenland.

Many efforts have been addressed to improve the ice sheet model resolution, in order to better simulate the ice sheet processes. However, in the present work, the resolution shows smaller impact on surface mass balance with respect to other features, such as the ice sheet model formulation. Furthermore, the work by Franco et al. (2012) investigate the impact of spatial resolution on the Greenland ice sheet surface mass balance by means of the regional climate model MAR. In their analysis, the horizontal resolution required to simulate the observed surface mass balance need to be high enough to resolve the marginal slopes, while further increase in resolution will lead to smaller improvements. However, high resolutions are required to simulate processes occurring in small coastal areas, such as the outlet glacier calving. Consequently, the need for high resolution ice sheet models depends on the analyzed process. The use of anisotropic mesh grid (e.g. Elmer/Ice model grid, Gillet-Chaulet et al. 2012; Seddik et al. 2012) represent a good tool to be used in studying processes at both local and ice sheet scales, since it allows to refine the mesh along the marginal areas where higher resolution is needed.

In general, the state-of-the-art ice sheet models are able to capture the main and the majority of the processes occurring in Greenland. However, large uncertainties especially in future projections still exists. For example, the Greenland ice sheet is expected to reach a tipping point by the end of the 21st century. The Greenland ice sheet passing the tipping point is important from the scientific point of view as well as for socio-economical reasons. However, no precise estimate of this timing has been found due to the models uncertainties and to a non-unique definition for the tipping point itself. In fact, the tipping point has been studied from a temperature increase point of view (e.g. Ridley et al. 2010; Robinson et al. 2012) and from a surface mass balance point of view (e.g. Fettweis et al. 2013, and present work). For example, the present work place the tipping point (= mean negative SMB over the GIS) in the period 2010–2080 depending

on (1) the ice sheet model, (2) the resolution, (3) the climate forcing and (4) the future emission scenario considered. This large spread of values highlights the need of more precise studies to better assess the timing at which the Greenland tipping point is going to be passed. Similar uncertainties are found also in the simulated values of many other variables and processes.

Part of this uncertainties can be reduced by dealing with the technical limitations presented previously in this chapter. However, part of this uncertainties lie in the complexity of the Earth climate system. Consequently, only the development of a coupled model which take into account all the climate system component (atmosphere, land-ice, sea-ice, ocean, vegetation, etc.) would be able to simulate and account for almost all the mechanisms and feedbacks that occur in the system, leading to a reduction of the uncertainties and a better understanding of the whole Earth climate system.

Chapter 8

Conclusions

The Greenland ice sheet has an important impact on both regional and global climate. For this reason, in the previous chapters, I investigated the Greenland ice sheet evolution up to 2100 by means of two different ice sheet models forced by a set of CMIP5 climate forcing. Furthermore, the analysis are performed at both overall ice sheet and basins scales.

First of all, the ice sheet models require climate forcing fields (precipitation and air surface temperature) coming from reanalysis, regional climate model or global climate models. The source of these forcing, then, can impact on the simulations of the ice sheet dynamics. For this reason, in the present work I use a set of climate forcing sources: (1) one reanalysis (ERA Interim), (2) one regional climate model (MAR) and (3) a set of seven atmosphere-ocean general coupled model coming from the CMIP5 project.

Based on this set of forcing, I evaluated the ability of the ISMs in simulating the 20th century surface mass balance, and, then, I simulated the projected changes in SMB during the 21st century under two emission scenarios (RCP 4.5 and RCP 8.5). The GIS SMB is projected to decrease during the 21st century reaching negative SMB values in the period 2010–2080, depending on the considered scenario. On regional scale, the northern basins exhibit negative SMB values since the last decades of the 20th century and the largest SMB variations by 2100 occurs in those areas for both scenarios.

Subsequently, I simulated the runoff distribution from meltwater and rainfall over the Greenland ice sheet during the 20th and 21st century. The meltwater is evaluated by means of the ISM GRISLI and the runoff is computed by means of a routing scheme that I implemented for this study. The aim was to produce a detailed runoff distribution along Greenland coasts to force oceanic models.

Finally, I evaluated and computed the calving and basal meltwater productions in order to close the GIS mass balance.

- In general, in our simulations the surface mass balance is projected to decrease during the 21st century reaching values ranging from 59 Gt/yr to -436 Gt/yr for the RCP 4.5 simulations, and from -591 Gt/yr to -1857 Gt/yr for the RCP 8.5 simulations by 2100. Furthermore, the decreasing trend exhibits an acceleration after the 2030s in both scenarios.

- On regional scale, the largest reduction are located in the northern basins of the Greenland ice sheet. In particular, the largest changes are simulated in the northern basin under a RCP 4.5 scenario with an average reduction of about 1.6 $Gt\ yr^{-2}$

in the period 2010–2100. Under a RCP 8.5 scenario, the largest variations are simulated in the north-western basin with an average reduction of about 3.9 $Gt\ yr^{-2}$ over the 21st century.

- The increase in resolution impacts on accumulation, which leads to a reduction of about 100 $Gt\ yr^{-1}$ in surface mass balance values. The use of different ice sheet models impacts on ablation, especially, due to differences in the initial ice sheet elevation obtained in the long-term spin-ups. In particular, GRISLI shows to be more sensitive to climate forcing with respect to SICOPOLIS, because the GRISLI ice sheet margins are slightly flatter than in SICOPOLIS.

- The simulated runoff increases during the entire 21st century reaching values about two (three) times larger than present-day values under a RCP 4.5 (RCP 8.5) scenario. In addition, the amount of meltwater trapped during its flow towards the Greenland coastal areas increases during the 21st century, going from 33% over the period 1980–1999 to 48% over the period 2081–2100, on average.

- On regional scale, the runoff simulated increases mainly in the northern and western basins of Greenland, corresponding to the regions where the SMB projects the largest reduction. In particular, the largest runoff values are simulated in the north-western basin with values going from 0.120–0.137 $mm\,SLE\ yr^{-1}$ over the period 1980–1999 to 0.272–0.326 $mm\,SLE\ yr^{-1}$ (0.520–680 $mm\,SLE\ yr^{-1}$) over the period 2081–2100 under a RCP 4.5 (RCP 8.5) scenario.

- The total freshwater flux from Greenland ice sheet requires also to account for the mass loss from calving and basal melting, along with the surface runoff. However, both mechanisms can be neglected in our simulations: the basal melting represent only a small fraction of meltwater with respect to the surface one since most of it is trapped in topographic depressions; calving occurs in small embayments along the Greenland margins which are not properly captured in the ice sheet models due to a too coarse resolution, unable to properly resolve the narrow fjords. In addition, the inland retreat of the GIS margins during the spin-up is also a major drawback for future calving simulations.

- The Greenland ice sheet SMB reaches a long-term negative conditions (passes the zero surface mass balance threshold, that is considered as the tipping point for Greenland) in the period 2040–2080 (2010–2050), when RCP 4.5 (RCP 8.5) simulations are considered.

The state-of-the-art ice sheet models are able to simulate the main processes and the evolution of the Greenland ice sheet. However, many physical and technical uncertainties and limits remain. Further work is required in order to improve the ice sheet models and their parameterizations. Many of the required improvements deal with the processes occurring within the ice sheet or at the ice sheet base. More observations of those areas are needed, since, nowadays, the amount of observations for those processes is small or missing. Other improvements deal with the runoff simulations. For example, it is possible to improve the runoff estimates by accounting for some processes occurring to the meltwater during its flow towards the ocean, such as storage in the snowpack layer or penetration of meltwater to the ice sheet base. Finally, the simulated runoff distribution

can be used as source of freshwater forcing in ocean models to investigate the impact of freshwater distribution on the regional oceanic circulation, sea water properties and sea-ice formation.

Appendix A

Main variables

Table A.1: Main variables used in this work with their symbols and units.

Symbol	Variable	Unit
Geometric and physical variables		
$\mathbf{u}$(x,y,z,t)	Ice velocity	$m\ yr^{-1}$
$\mathbf{u}_b$	Ice velocity at the ice base	$m\ yr^{-1}$
T(x,y,z,t)	Ice temperature	$^{\circ}C$
T*(x,y,z,t)	Temp. relative to pressure melting point	$^{\circ}C$
T_0(x,y)	Initial surface air temperature	$^{\circ}C$
T_{cor}(x,y,t)	Corrected air surface temperature field	$^{\circ}C$
T_{ism}(x,y,t)	Air surface temperature at ISM resolution	$^{\circ}C$
T_{model}(x,y,t)	Air surface temperature at AOGCM or RCM resolution	$^{\circ}C$
p(x,y,z,t)	Hydrostatic pressure	Pa
H(x,y,t)	Ice thickness	m
S(x,y,t)	Surface elevation	m
S_0(x,y)	Initial topography	m
B(x,y,t)	Bedrock elevation	m
Sl	Sea level	m
G(x,y)	Geothermal heat flux	$W\ m^{-2}$
P(x,y,t)	Precipitation	$m\ yr^{-1}$
P_0(x,y)	Initial precipitation	$m\ yr^{-1}$
P_{cor}	Corrected precipitation field	$m\ yr^{-1}$
P_{ism}(x,y,t)	Precipitation at ISM resolution	$m\ yr^{-1}$
P_{model}(x,y,t)	Precipitation at AOGCM or RCM resolution	$m\ yr^{-1}$
Runoff	Runoff	$mm\,SLE\ yr^{-1}$ mSv
Calv	Calving	$m\ yr^{-1}$

Table A.2: Main variables used in this work with their symbols and units.

Symbol	Variable	Unit
Mass balance and climate		
SMB(x,y,t)	Surface mass balance	$m\ yr^{-1}$ or $Gt\ yr^{-1}$
Abl(x,y,t)	Ablation	$m\ yr^{-1}$ or $Gt\ yr^{-1}$
Acc(x,y,t)	Accumulation	$m\ yr^{-1}$ or $Gt\ yr^{-1}$
F(x,y,t)	Melting rate at the ice base	$m\ yr^{-1}$
b_{melt}	Melting at the base of the ice shelf	$m\ yr^{-1}$
S_m(x,y,t)	Monthly solid precipitation	$m\ yr^{-1}$
P_m(x,y,t)	Monthly total precipitation	$m\ yr^{-1}$
T_m(x,y,t)	Monthly temperature	$^{\circ}C$
T_{ann}(x,y,t)	Mean annual surface air temperature	$^{\circ}C$
T_{july}(x,y,t)	Mean July surface air temperature	$^{\circ}C$
p_r	Retention fraction	-
csi	Percentage of ice that refreezes	%
d	Thickness of active layer	m
ρ_0	Dry snow density	$kg\ m^{-3}$
ρ_e	Wet snow density	$kg\ m^{-3}$
PDD	Number of positive degree day	-
σ_{pdd}	Standard deviation of daily air temp.	$^{\circ}C$
C_{ice}	Melting factor of ice	$mmw.e.\ d^{-1}\ ^{\circ}C^{-1}$
C_{snow}	Melting factor of snow	$mmw.e.\ d^{-1}\ ^{\circ}C^{-1}$
C_{ice}^{cor}	Corrected melting factor of ice	$mmw.e.\ d^{-1}\ ^{\circ}C^{-1}$
C_{snow}^{cor}	Corrected melting factor of snow	$mmw.e.\ d^{-1}\ ^{\circ}C^{-1}$
Ice deformation and sliding		
σ	Stress tensor	Pa
τ	Deviatoric stress tensor	Pa
η	Ice viscosity	$Pa\ yr^{-1}$
$\dot{\epsilon}$	Strain rate	s^{-1}
n	Exponent in the Glen flow law	-
A(T^*)	Coefficient of the Glen flow law	Pa
τ_*	Effective shear stress	Pa
N	Effective pressure at the base of the ice	Pa
p_w	Sub-glacial water pressure	Pa
p and q	Weertman sliding law coefficient	-
C_b	Sliding coefficient	$m\ yr^{-1}\ Pa^{-1}$
τ_b	Basal drag	Pa
c_f	Basal drag coefficient	-
B_{sl}	Sliding parameter	$m\ s^{-1}\ Pa^{-1}$
k_{sl}	Sliding law coefficient	$m\ yr^{-1}\ Pa^{-2}$

Table A.3: Main variables used in this work with their symbols and units.

Symbol	Variable	Unit
Basal hydrology		
K	Hydraulic conductivity	$m\ s^{-1}$
V_e	Sub-glacial flow velocity	$m\ yr^{-1}$
p_w	Sub-glacial water pressure	Pa
Polythermal structure		
W	Water content of the mixture	-
W_s	Surface water content	-
ρ_m	Density of the mixture	$kg\ m^{-3}$
$\mathbf{u}_m$	Barycentric velocity of the mixture	$m\ yr^{-1}$
$\mathbf{j}$	Diffusive water mass flux	$kg\ m^{-2}\ s^{-1}$
ν	Water diffusivity in ice	$kg\ m^{-2}\ s^{-1}$
Physical constant		
ρ	Density of ice	918 $kg\ m^{-3}$
ρ_w	Density of water	1000 $kg\ m^{-3}$
g	Gravitational acceleration	9.81 $m\ s^{-2}$
R	Ideal gas constant	8.3145 $J\ mol^{-1}\ {}^{\circ}C^{-1}$
β	Clausius-Clapeyron constant	9.76 $10^{-8}\ K\ Pa^{-1}$
L	Latent heat of ice	335 $kJ\ kg^{-1}$
Thermal properties		
c	Heat capacity of ice	$J\ mol^{-1}\ kg^{-1}$
$c(T)$	Specific heat capacity function of T in K	146.3 + 7.253 $T[K]$ $[J\ kg^{-1}\ K^{-1}]$
κ	Thermal conductivity of ice	$W\ {}^{\circ}C^{-1}\ m^{-1}$
Q_i	Deformational heat	$W\ m^{-2}$

Erratum

The anomaly method applied to the forcing field of our simulations is based on adding the anomaly to a reference climate (Eq. 4.1). However, the use of a difference to determine the precipitation anomalies could lead to areas with negative precipitation when these anomalies are added to the reference climatology. To avoid this problem, usually the precipitation anomalies are attained using a multiplicative factor:

$$Precip_{annual} = P_{ref} * \left(\frac{AOGCM_{annual}}{AOGCM_{ref}} \right)$$

We tested the difference between the two methods using GRISLI at 5-km resolution forced by the MME climate forcing. The use of the multiplicative method leads to a reduction in accumulation, especially in the south-western basin of the GIS. This influence increases in time reaching a maximum difference of about 122 Gt/yr (169 Gt/yr) by the end of the 21st century under a RCP 4.5 (RCP 8.5) scenario. Note that these differences fall in the range of simulated uncertainties.

Consequently, these differences do not impact on the main PhD conclusions.

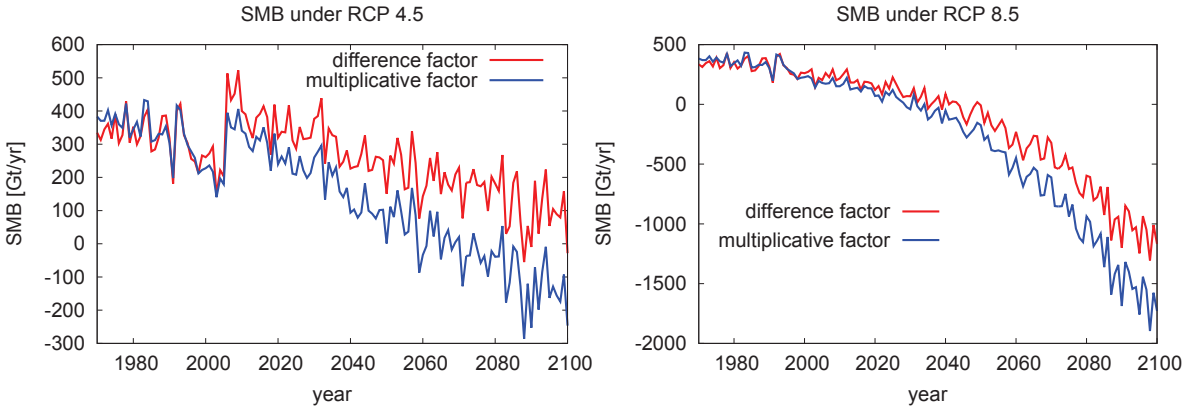

Figure: changes in SMB obtained using the difference factor (Eq. 4.1) and the multiplicative factor described here in a GRISLI simulation at 5 km resolution under the MME climate forcing.

Bibliography

Agarwal, N., Jungclaus, J. H., Köhl, A., Mechoso, C. R., and Stammer, D. Additional contributions to CMIP5 regional sea level projections resulting from Greenland and Antarctic ice mass loss. *Environ. Res. Lett.*, 10:074008, 2015. doi: 10.1088/1748-9326/10/7/074008.

Agosta, C., Favier, V., Krinner, G., Gallée, H., Fettweis, X., and Genthon, C. High-resolution modeling of the Antarctic surface mass balance, application for the twentieth, twenty first and twenty second centuries. *Clim. Dyn.*, 41:3247–3260, 2013. doi: 10.1007/s00382-013-1903-9.

Alley, R. B., Clark, P. U., Huybrechts, P., and Joughin, I. Ice-sheet and sea-level changes. *Science*, 310:456–460, 2005.

Alley, R. B., Horgan, H. J., Joughin, I., Cuffey, K. M., Dupont, T. K., Parizek, B. R., Anandakrishnan, S., and Bassis, J. A simple law fro ice-shelf calving. *Science*, 322: 1344, 2008.

Alley, R. B., Andrews, J. T., Brigham-Grette, J., Clarke, G. K. G., Cuffey, K. M., Fitzpatrick, J. J., Funder, S., Marshall, S. J., Miller, G. H., Mitrovica, J. X., Muhs, D. R., Otto-Bliesner, B. L., Polyak, L., and White, J. W. C. History of the Greenland ice sheet: paleoclimatic insights. *Quaternary Sci. Rev.*, pages 1–29, 2010. doi: 10.1016/j.quascirev.2010.02.007.

AMAP. *Snow, Water, Ice and Permafrost in the Arctic (SWIPA): climate change and the cryosphere*. Arctic Monitoring and Assessment Programme (AMAP), Oslo, Norway, 2011.

Andrews, L. C., Catania, G. A., Hoffman, M. J., Gulley, J. D., Lüthi, M. P., Ryser, C., Hawley, R. L., and Neumann, T. A. Direct observations of evolving subglacial drainage beneath the Greenland Ice Sheet. *Nature*, 514:80–83, 2014. doi: 10.1038/nature13796.

Applegate, P. J., Kirchner, N., Stone, E. J., Keller, K., and Greve, R. An assessment of key model parametric uncertainties in projections of Greenland Ice Sheet behavior. *The Cryosphere*, 6:589–606, 2012.

Arguez, A., O'Brien, J. J., and Smith, S. R. Air temperature impacts over Eastern North America and Europe associated with low-frequency North Atlantic SST variability. *Int. J. Climatol.*, 29:1–10, 2009. doi: 10.1002/joc.1700.

Argus, D. F., Peltier, W. R., Drummond, R., and Moore, A. W. The Antarctica component of postglacial rebound model ICE-6G-C (VM5a) based upon GPS positioning,

exposure age dating of ice thicknesses, and relative sea level histories. *Geophys. J. Int.*, 198(1):537–563, 2014. doi: 10.1093/gji/ggu140.

Bales, R. C., Guo, Q., Shen, D., McConnell, J. R., Du, G., Burkhart, J. F., Spikes, V. B., Hanna, E., and Cappelen, J. Annual accumulation for Greenland updated using ice core data developed during 2000–2006 and analysis of daily coastal meteorological data. *J. Geophys. Res.*, 114:D06116, 2009.

Bamber, J. Greenland 5 km DEM, Ice Thickness, and Bedrock Elevation Grids. (Greenland 5km dev1.2). Technical report, Boulder, Colorado USA: National Snow and Ice Data Center., 2001.

Bamber, J., van den Broeke, M., Ettema, J., Lenaerts, J., and Rignot, E. Recent large increase in freshwater fluxes from Greenland into the North Atlantic. *Geophys. Res. Lett.*, 39:L19501, 2012.

Bamber, J. L., Griggs, J. A., R. T. W. L. Hurkmans, J. A. D., Gogineni, S. P., Howat, I., Mouginot, J., Paden, J., Palmer, S., Rignot, E., and Steinhage, D. A new bed elevation dataset for Greeland. *The Cryosphere*, 7:499–510, 2013.

Banwell, A. F., Willis, I. C., and Arnold, N. S. Modeling subglacial water routing at Paakitsoq, W Greenland. *J. Geophys. Res. Earth*, 118:1–14, 2013. doi: 10.1002/jgrf.20093.

Bassett, S. E., Milne, G. A., Mitrovica, J. X., and Clark, P. U. Ice sheet and solid Earth influences on far-field sea-level histories. *Science*, 309:925–928, 2005. doi: 10.1126/science.1111575.

Bekryaev, R. V., Polyakov, I. V., and Alexeev, V. A. Role of polar amplification in long-term surface air temperature variations and modern Arctic warming. *J. Climate*, 23:3888–3906, 2010. doi: 10.1175/2010JCLI3297.1.

Belleflamme, A., Fettweis, X., Lang, C., and Erpicum, M. Current and future atmospheric circulation at 500 hPa over Greenland simulated by the CMIP3 and CMIP5 global models. *Clim. Dyn.*, 41:2061–2080, 2013. doi: 10.1007/s00382-012-1538-2.

Benn, D. I., Warren, C. R., and Mottram, R. H. Calving processes and the dynamics of calving glaciers. *Earth Science Reviews*, 82:143–179, 2007. doi: 10.1016/j.earscirev.2007.02.002.

Bindoff, N. L., Stott, P. A., AchutaRao, K. M., Allen, M. R., Gillett, N., Gutzler, D., Hansingo, K., Hegerl, G., Hu, Y., Jain, S., Mokhov, I. I., Overland, J., Perlwitz, J., Sebbari, R., and Zhang, X. Detection and attribution of climate change: from global to regional. In Stocker, T. F., Qin, D., Plattner, G.-K., Tignor, M., Allen, S. K., Boschung, J., Nauels, A., Xia, Y., Bex, V., and Midgley, P. M., editors, *Climate Change 2013: the Physical Science Basis. Contribution of Working Group I to the Fifth Assessment Report of the Intergovernmental Panel on Climate Change*. Cambridge University Press, Cambridge, United Kingdom and New York, NY, USA, 2013.

Bindschadler, R. A., Nowicki, S., Abe-Ouchi, A., Aschwanden, A., Choi, H., Fastook, J., Granzow, G., Greve, R., Gutowski, G., Herzfeld, U., Jackson, C., Johnson, J.,

Khroulev, C., Levermann, A., Lipscomb, W. H., Martin, M. A., Morlighem, M., Parizek, B. R., Pollard, D., Price, S. F., Ren, D., Saito, F., Sato, T., Seddik, H., Seroussi, H., Takahashi, K., Walker, R., and Wang, W. L. Ice-sheet sensitivities to environmental forcing and their use in projecting future sea level (the SeaRISE project). *J. Glaciol.*, 59:195–224, 2013. doi: 10.3189/2013JoG12J125.

Bonelli, S., Charbit, S., Kageyama, M., Woillez, M., Ramstein, G., Dumas, C., and Quiquet, A. Investigating the evolution of major northern hemisphere ice sheets during the last glacial–interglacial cycle. *Clim. Past*, 5:329–345, 2009.

Born, A. and Nisancioglu, K. H. Melting of Northern Greenland during the last interglacial. *The Cryosphere*, 6:1239–1250, 2012.

Bougamont, M., Bamber, J. L., and Greuell, W. A surface mass balance model for the Greenland ice sheet. *J. Geophys. Res.*, 110:F04018, 2005. doi: 10.1029/2005JF000348.

Bougamont, M., Bamber, J. L., Ridley, J. K., Gladstone, R. M., Greuell, W., Hanna, E., Payne, A. J., and Rutt, I. Impact of model physics on estimating the surface mass balance of the Greenland ice sheet. *Geophys. Res. Lett.*, 34:L17501, 2007. doi: 10.1029/2007GL030700.

Box, J. E., Bromwich, D. H., Veenhuis, B. A., Bai, L.-S., Stroeve, J. C., Rogers, J. C., Steffen, K., Haran, T., and Wang, S.-H. Greenland ice sheet surface mass balance variability (1988–2004) from calibrated Polar MM5 output. *J. Climate*, 19:2783–2800, 2006.

Bromwich, D. H., Fogt, R. L., Hodges, K. I., and Walsh, J. E. A troposhperic assessment of the ERA–40, NCEP and JRA–25 global reanalyses in the polar regions. *J. Geophys. Res.*, 112:D10111, 2007. doi: 10.1029/2006JD007859.

Brun, E., David, P., Sudul, M., and Brunot, G. A numerical model to simulate snow-cover stratigraphy for operational avalanche forecasting. *J. Glaciol.*, 38:13–22, 1992.

Calov, R. and Greve, R. A semi-analytical solution for the positive degree-day model with stochastic temperature variations. *J. Glaciol.*, 51(172):173–175, 2005.

Calov, R., Robinson, A., Perrette, M., and Ganopolski, A. Simulating the Greenland ice sheet under present-day and paleo constraints including a new discharge parameterization. *The Cryosphere*, 9:179–196, 2015. doi: 10.5194/tc-9-179-2015.

Catania, G. A. and Neumann, T. A. Persistent englacial drainage features in the Greenland Ice Sheet. *Geophys. Res. Lett.*, 37:L02501, 2010. doi: 10.1029/2009GL041108.

Cazenave, A. and Llovel, W. Contemporary sea level rise. *Annu. Rev. Marine Sci.*, 2: 145–173, 2010.

Charbit, S., Ritz, C., and Ramstein, G. Simulations of Northern Hemisphere ice-sheet retreat: sensitivity to physical mechanisms involved during the Last Deglaciation. *Quatern. Sci. Rev.*, 21:243–265, 2002.

Chen, L., Johannessen, O. M., Wang, H., and Ohmura, A. Accumulation over the Greenland ice sheet as represented in reanalysis data. *Adv. Atmos. Sci.*, 28(5):1030–1038, 2011. doi: 10.1007/s00376-010-0150-9.

Church, J. A., Clark, P. U., Cazenave, A., Gregory, J. M., Jevrejeva, S., Levermann, A., Merrifield, M. A., Milne, G. A., Nerem, R. S., Nunn, P. D., Payne, A. J., Pfeffer, W. T., Stammer, D., and Unnikrishnan., A. S. Sea level change. In Stocker, T. F., Qin, D., Plattner, G.-K., Tignor, M., Allen, S. K., Boschung, J., Nauels, A., Xia, Y., Bex, V., and Midgley, P. M., editors, *Climate Change 2013: the Physical Science Basis. Contribution of Working Group I to the Fifth Assessment Report of the Intergovernmental Panel on Climate Change*. Cambridge University Press, Cambridge, United Kingdom and New York, NY, USA, 2013.

Chylek, P., Box, J. E., and Lesins, G. Global warming and the Greenland ice sheet. *Climatic Change*, 63:201–221, 2004.

Clason, C., Mair, D. W. F., Burgess, D. O., and Nienow, P. W. Modelling the delivery of supraglacial meltwater to the ice/bed interface: application to the southwest Devon Ice Cap, Nunavut, Canada. *J. Glaciol.*, 58:361–374, 2012. doi: 10.3189/2012JoG11J129.

Clason, C. C., Mair, D. W. F., Nienow, P. W., Bartholomew, I. D., Sole, A., Palmer, S., and Schwanghart, W. Modelling the transfer of supraglacial meltwater to the bed of Leverett Glacier, Southwest Greenland. *The Cryosphere*, 9:123–138, 2015. doi: 10.5194/tc-9-123-2015.

Comiso, J. *Polar Oceans from Space*. Springer New York Dordrecht Heidelberg London, 2010.

Comiso, J. C. Large decadal decline of the Arctic multiyear ice cover. *J. Climate*, 25: 1176–1193, 2012. doi: 10.1175/JCLI-D-11-00113.1.

Comiso, J. C., Parkinson, C. L., Gersten, R., and Stock, L. Accelerated decline in the Arctic sea ice cover. *Geophys. Res. Lett.*, 35:L01703, 2008. doi: 10.1029/2007GL031972.

Cuffey, K. M. and Marshall, S. J. Substantial contribution to sea-level rise during the last interglacial from the Greenland ice sheet. *Nature*, 404:591–594, 2000.

Dahl-Jensen, D. and Johnsen, S. J. Paleotemperatures still exist in the Greenland ice sheet. *Nature*, 320:250–252, 1986.

Dansgaard, W., Johnsen, S. J., Clausen, H. B., Dahl-Jensen, D., Gundestrup, N. S., Hammer, C. U., Hvidberg, C. S., Steffensen, J. P., Sveinbjörnsdottir, A. E., Jouzel, J., and Bond, G. Evidence for general instability of past climate from a 250-kyr ice-core record. *Nature*, 364:218–220, 1993.

Das, S. B., Joughin, I., Behn, M. A., Howat, I. M., King, M. A., Lizarralde, D., and Bhatia, M. P. Fracture propagation to the base of the Greenland Ice Sheet during supraglacial lake drainage. *Science*, 320:778–781, 2008.

Davini, P., von Hardenberg, J., Filippi, L., and Provenzale, A. Impact of Greenland orography on the Atlantic Meridional Overturning Circulation. *Geophys. Res. Lett.*, 42, 2015. doi: 10.1002/2014GL062668.

Day, J. J., Bamber, J. L., and Valdes, P. J. The Greenland Ice Sheat's surface mass balance in a seasonally sea ice-free Arctic. *J. Geophys. Res. Earth Surf.*, 118:1533–1544, 2013. doi: 10.1002/jgrf.20112.

Dee, D. P., Uppala, S. M., Simmons, A. J., Berrisford, P., Poli, P., Kobayashi, S., Andrae, U., Balmaseda, M. A., Balsamo, G., Bauer, P., Bechtold, P., Beljaars, A. C. M., van de Berg, L., Bidlot, J., Bormann, N., Delsol, C., Dragani, R., Fuentes, M., Geer, A. J., Haimberger, L., Healy, S. B., Hersbach, H., Hólm, E. V., Isaksen, L., Kållberg, P., Köhler, M., Matricardi, M., McNally, A. P., Monge-Sanz, B. M., Morcrette, J.-J., Park, B.-K., Peubey, C., de Rosnay, P., Tavolato, C., Thépaut, J.-N., and Vitart, F. The ERA-Iinterim reanalysis: configuration and performance of the data assimilation system. *Q. J. R. Meteorol. Soc.*, 137:553–597, 2011.

Dickson, R., Rudels, B., Dye, S., Karcher, M., Meincke, J., and Yashayaev, I. Current estimates of freshwater flux through Arctic and subarctic seas. *Prog. Oceanogr.*, 73: 210–230, 2007. doi: 10.1016/j.pocean.2006.12.003.

Doake, C. S. M., Corr, H. F. J., Rott, H., Skvarca, P., and Young, N. W. Breakup and conditions fro stability of the northern Larsen Ice Shelf, Antarctica. *Nature*, 391: 778–780, 1998.

Driesschaert, E., Fichefet, T., Goosse, H., Huybrechts, P., Janssens, I., Mouchet, A., Munhoven, G., Brovkin, V., and Weber, S. L. Modeling the influence of Greenland ice sheet melting on the Atlantic meridional overturning circulation during the next millennia. *Geophys. Res. Lett.*, 34:L10707, 2007. doi: 10.1029/2007GL029516.

Edwards, T. L., Fettweis, X., Gagliardini, O., Gillet-Chaulet, F., Goelzer, H., Gregory, J. M., Hoffman, M., Huybrechts, P., Payne, A. J., Perego, M., Price, S., Quiquet, A., and Ritz, C. Effect of uncertainty in surface mass balance-elevation feedback on projections of the future sea level contribution of the Greenland ice sheet. *The Cryosphere*, 8:195–208, 2014. doi: 10.5194/tc-8-195-2014.

Ettema, J., van den Broeke, M. R., van Meijgaard, E., van de Berg, W. J., Bamber, J. L., Box, J. E., and Bales, R. C. Higher surface mass balance of the Greenland ice sheet revealed by high-resolution climate modeling. *Geophys. Res. Lett.*, 36:L12501, 2009. doi: 10.1029/2009GL038110.

Fahnestock, M., Abdalati, W., Joughin, I., Brozena, J., and Gogineni, P. High geothermal heat flow, basal melt, and the origin of rapid ice flow in central Greenland. *Science*, 294:2338–2342, 2001.

Fausto, R. S., Ahlstrøm, A. P., Van As, D., Bøggild, C. E., and Johnsen, S. J. A new present-day temperature parameterization for Greenland. *J. Glaciol.*, 55:95–105, 2009.

Fettweis, X. Reconstruction of the 1979-2006 Greenland ice sheet surface mass balance using the regional climate model MAR. *The Cryosphere*, 1:21–40, 2007.

Fettweis, X., Tedesco, M., van den Broeke, M., and Ettema, J. Melting trends over the Greenland ice sheet (1958–2009) from spaceborne microwave data and regional climate models. *The Cryosphere*, 5:359–375, 2011. doi: 10.5194/tc-5-359-2011.

Fettweis, X., Franco, B., Tedesco, M., van Angelen, J. H., Lenaerts, J. T. M., van den Broeke, M. R., and Gallée, H. Estimating the Greenland ice sheet surface mass balance contribution to future sea level rise using the regional atmospheric climate model MAR. *The Cryosphere*, 7:469–489, 2013. doi: 10.5194/tc-7-469-2013.

Fichefet, T., Poncin, C., Goosse, H., Huybrechts, P., Janssens, I., and Le Treut, H. Implications of changes in freshwater flux from the Greenland ice sheet for the climate of the 21st century. *Geophys. Res. Lett.*, 30:1911, 2003. doi: 10.1029/2003GL017826.

Flückiger, J., Knutti, R., and White, J. W. C. Oceanic processes as potential trigger and amplifying mechanisms for Heinrich events. *Paleoceanography*, 21:PA2014, 2006. doi: 10.1029/2005PA001204.

Forster, R. R., Box, J. E., van den Broeke, M. R., Burgess, C. M. E. W., van Angelen, J. H., Lenaerts, J. T. M., Koenig, L. S., Paden, J., Lewis, C., Gogineni, S. P., Leuschen, C., and McConnell, J. R. Extensive liquid meltwater storage in firn within the Greenland ice sheet. *Nature Geosci.*, 7:95–98, 2014. doi: 10.1038/NGEO2043.

Fowler, H. J., Blenkinsop, S., and Tebaldi, C. Linking climate change modelling to impacts studies: recent advances in downscaling techniques for hydrological modelling. *Int. J. Climatol.*, 27:1547–1578, 2007. doi: 10.1002/joc.1556.

Francis, J. A. and Vavrus, S. J. Evidence linking Arctic amplification to extreme weather in mid-latitudes. *Geophys. Res. Lett.*, 39:L06801, 2012. doi: 10.1029/2012GL051000.

Franco, B., Fettweis, X., Erpicum, M., and Nicolay, S. Present and future climates of the Greenland ice sheet according to IPCC AR4 models. *Clim. Dyn.*, 36:1897–1918, 2011. doi: 10.1007/s00382-010-0779-1.

Franco, B., Fettweis, X., Lang, C., and Erpicum, M. Impact of spatial resolution on the modeling of the Greenland ice sheet surface mass balance between 1990-2010, using the regional climate model MAR. *The Cryosphere*, 6:695–711, 2012. doi: 10.5194/tc-6-695-2012.

Fu, L. and Cazenave, A. *Satellite Altimetry and Earth Sciences. A Handbook of Techniques and Applications.* Academic Press, 2001.

Fürst, J. J., Goelzer, H., and Huybrechts, P. Ice-dynamic projections of the Greenland ice sheet in response to atmospheric and oceanic warming. *The Cryosphere*, 9:1039–1062, 2015. doi: 10.5194/tc-9-1039-2015.

Fyke, J. G., Sacks, W. J., and Lipscomb, W. H. A technique for generating consistent ice sheet initial conditions for coupled ice sheet/climate models. *Geosci. Model Dev.*, 7:1183–1195, 2014. doi: 10.5194/gmd-7-1183-2014.

Gallée, H. and Duynkerke, P. G. Air-snow interactions and the surface energy and mass balance over the melting zone of west Greenland during the Greenland Ice Margin Experiment. *J. Geophys. Res.*, 102:13813–13824, 1997.

Gallée, H. and Schayes, G. Development of a three-dimensional meso-γ primitive equation model: katabatic winds simulation in the area of Terra Nova Bay, Antarctica. *Mon. Weather Rev.*, 122:671–685, 1994.

Gallée, H., Guyomarc'h, G., and Brun, E. Impact of snow drive on the Antarctic ice sheet surface mass balance: possible sensitivity to snow-surface properties. *Bound.-Lay. Meteorol.*, 99:1–19, 2001.

Gillet-Chaulet, F., Gagliardini, O., Seddik, H., Nodet, M., Durand, G., Ritz, C., Zwinger, T., Greve, R., and Vaughan, D. G. Greenland ice sheet contribution to sea-level rise from a new-generation ice-sheet model. *The Cryosphere*, 6:1561–1576, 2012. doi: 10.5194/tc-6-1561-2012.

Glen, J. W. The creep of polycristalline ice. *Proceedings of the Royal Society London A*, 228:519–538, 1955.

Goelzer, H., Janssens, I., Nemec, J., and Huybrechts, P. A dynamic continental runoff routing model applied to the last Northern Hemisphere deglaciation. *Geosci. Model Dev.*, 5, 2012. doi: 10.5194/gmd-5-599-2012.

Goelzer, H., Huybrechts, P., Fürst, J., Nick, F. M., Andersen, M. L., Edwards, T. L., Payne, X. F. A. J., and Shannon, S. Sensitivity of greenland ice sheet projections to model formulations. *J. Glaciol.*, 59, 2013. doi: 10.3189/2013JoG12J182.

Graversen, R. G., Drijfhout, S., Hazeleger, W., van de Wal, R., Bintanja, R., and Helsen, M. Greenland's contribution to global sea-level rise by the end of the 21st century. *Clim. Dyn.*, 2010. doi: 10.1007/s00382-010-0918-8.

Gregory, J. M. and Huybrechts, P. Ice-sheet contributions to future sea-level change. *Phil. Trans. R. Soc. A*, 364, 2006. doi: 10.1098/rsta.2006.1796.

Gregory, J. M. and Lowe, J. A. Predictions of global and regional sea-level rise using AOGCMs with and without flux adjustment. *Geophys. Res. Lett.*, 27:3069–3072, 2000.

Gregory, J. M., Huybrechts, P., and Raper, S. C. B. Threatened loss of the Greenland ice-sheet. *Nature*, 428:616, 2004. doi: 10.1038/428616a.

Greve, R. Application of a polythermal three-dimensional ice sheet model to the Greenland ice sheet: response to steady-state and transient climate scenarios. *J. Climate*, 10(5):901–918, 1997a.

Greve, R. A continuum-mechanical formulation for shallow polytherma ice sheets. *Phil. Trans. R. Soc. Lond. A*, 355:921–974, 1997b.

Greve, R. Relation of measured basal temperatures and the spatial distribution of the geothermal heat flux for the greenland ice sheet. *Ann. Glaciol.*, 42:424–432, 2005.

Greve, R. and Blatter, H. *Dynamics of ice sheets and glaciers*. Springer-Verlag Berlin Heidelberg, 2009.

Greve, R. and Herzfeld, U. C. Resolution of ice streams and outlet glaciers in large-scale simulations of the Greenland ice sheet. *Ann. Glaciol.*, 54(63):209–220, 2013.

Greve, R., Saito, F., and Abe-Ouchi, A. Initial results of the SeaRISE numerical experiments with the models SICOPOLIS and IcIES for the Greenland ice sheet. *Ann. Glaciol.*, 52(58):23–30, 2011.

Gunderstrup, N. S. and Hansen, B. L. Bore-hole survey at DYE3, South Greenland. *J. Glaciol.*, 30:282–288, 1984.

Hanna, E., Huybrechts, P., Janssens, I., Cappelen, J., Steffen, K., and Stephens, A. Runoff and mass balance of the Greenland ice sheet: 1958–2003. *J. Geophys. Res.*, 110:D13108, 2005.

Hanna, E., McConnell, J., Das, S., Cappelen, J., and Stephens, A. Observed and modeled Greenland ice sheet snow accumulation, 1958–2003, and links with regional climate forcing. *J. Climate*, 19:344–358, 2006.

Hanna, E., Huybrechts, P., Steffen, K., Cappelen, J., Huff, R., Shuman, C., Irvine-Fynn, T., Wise, S., and Griffiths, M. Increased runoff from melt from the Greenland Ice Sheet: A response to global warming. *J. Climate*, 21:331–341, 2008.

Hanna, E., Jones, J. M., Cappelen, J., Mernild, S. H., Wood, L., Steffen, K., and Huybrechts, P. The influence of North Atlantic atmospheric and oceanic forcing effects on 1900-2010 Greenland summer climate and ice melt/runoff. *Int. J. Climatol.*, 33: 862–880, 2013.

Hansen, J. and Lebedeff, S. Global trends of measured surface air temperature. *J. Geophys. Res.*, 92:13345–13372, 1987.

Harper, J., Humphrey, N., Pfeffer, W. T., Brown, J., and Fettweis, X. Greenland ice-sheet contribution to sea-level rise buffered by meltwater storage in firn. *Nature*, 491: 240–243, 2012. doi: 10.1038/nature11566.

Hasholt, B., Mikkelsen, A. B., Nielsen, M. H., and Larsen, M. A. D. Observations of runoff and sediment and dissolved loads from the Greenland ice sheet at Kangerlussuaq, West Greenland, 2007 to 2010. *Z. Geomorphol.*, 2012. doi: 10.1127/0372-8854/2012/S-00121.

Haug, G. H. and Tiedemann, R. Effect of the formation of the isthmus of Panama on Atlantic ocean thermohaline circulation. *Nature*, 393:673–676, 1998.

Helsen, M. M., van de Wal, R. S. W., van den Broeke, M. R., van de Berg, W. J., and Oerlemans, J. Coupling of climate models and ice sheet models by surface mass balance gradients: application to the Greenland Ice Sheet. *The Cryosphere*, 6:255–272, 2012. doi: 10.5194/tc-6-255-2012.

Herzfeld, U. C., Fastook, J., Greve, R., McDonald, B., Wallin, B. F., and Chen, P. A. On the influence of greenland outlet glacier bed topography on results from dynamic ice-sheet models. *Ann. Glaciol.*, 53(60):281–293, 2012. doi: 10.3189/2012AoG60A061.

Hindmarsh, R. C. A. and Le Meur, E. Dynamical processes involved in the retreat of marine ice sheets. *J. Glaciol.*, 47(157):271–280, 2001.

Holgate, S. J., Matthews, A., Woodworth, P. L., Rickards, L. J., Tamisiea, M. E., Bradshaw, E., Foden, P. R., Gordon, K. M., Jevrejeva, S., and Pugh, J. New data systems and products at the Permanent Service for Mean Sea Level. *J. Coast. Res.*, 29(3): 493–504, 2013.

Holland, D. M., Thomas, R. H., Young, B. D., Ribergaard, M. H., and Lyberth, B. Acceleration of Jakobshavn Isbræ triggered by warm subsurface ocean waters. *Nature Geosci.*, 1:659–664, 2008. doi: 10.1038/ngeo316.

Howat, I. M., Joughin, I., and Scambos, T. A. Rapid changes in ice discharge from Greenland outlet glaciers. *Science*, 315:1559–1561, 2007.

Howat, I. M., Joughin, I., Fahnestock, M., Smith, B. E., and Scambos, T. A. Synchronous retreat and acceleration of southeast Greenland outlet glaciers 2000-06: ice dynamics and coupling to climate. *J. Glaciol.*, 54:646–660, 2008.

Hulbe, C. L. and MacAyeal, D. R. A new numerical model of coupled inland ice sheet, ice stream, and ice shelf flow and its application to the West Antarctica Ice Sheet. *J. Geophys. Res.*, 104:25349–25366, 1999.

Hurrell, J. W. Influence of variations in extratropical wintertime teleconnections on Northern Hemisphere temperature. *Geophys. Res. Lett.*, 23:665–668, 1996.

Hutter, K. *Theroretical glaciology: material science of ice and the mechanics of glaciers and ice sheets*. Springer, Reidel Publishing Company, Dordrecht, The Netherlands, 1983.

Huybrechts, P. Sea-level changes at the LGM from ice-dynamic reconstructions of the Greenland and Antarctic ice sheets during the glacial cycles. *Quat. Sci. Rev.*, 21: 203–231, 2002.

Huybrechts, P. and De Wolde, J. The dynamic response of the Greenland and Antarctic ice sheets to multiple-century climatic warming. *J. Climate*, 12:2169–2188, 1999.

Huybrechts, P., Gregory, J., Janssens, I., and Wild, M. Modelling Antarctic and Greenland volume changes during the 20th and 21st centuries forced by GCM time slice integrations. *Glob. Planet. Change*, 42:83–105, 2004. doi: 10.1016/j.gloplacha.2003.11.011.

IPCC. *Climate Change 2007: the physical science basis, contribution of working group I to the fourth assessment report of the Intergovernmental Panel on Climate Change*. Cambridge University Press, UK and New York, NY, USA, 2007.

Jansen, E., Fronval, T., Rack, F., and Channell, J. E. T. Pliocene-pleistocene ice rafting history and cyclicity in the Nordic seas during the last 3.5 Myr. *Paleoceanography*, 15: 709–721, 2000.

Janssens, I. and Huybrechts, P. The treatment of meltwater retention in mass-balance parameterizations of the Greenland ice sheet. *Ann. Glaciol.*, 31:133–140, 2000.

Johnsen, S. J., Dahl-Jensen, D., Dansgaard, W., and Gundestrup, N. S. Greenland paleotemperatures derived from GRIP bore hole temperature and ice core isotope profiles. *Tellus*, 47(5):624–629, 1995. doi: 10.1034/j.1600-0889.47.issue5.9.x.

Johnsen, S. J., Clausen, H. B., Dansgaard, W., Gundestrup, N. S., Hammer, C. U., Andersen, U., Andersen, K. K., Hvidberg, C. S., Dahl-Jensen, D., Steffensen, J. P., Shoji, H., Sveinbjörnsdottir, A. E., White, J., Jouzel, J., and Fisher, D. The δ^{18}O record along the Greenland Ice Core Project deep ice core and the problem of possible Eemian climatic instability. *J. Geophys. Res.*, 102(C12):26397–26410, 1997.

Joughin, I., Das, S. B., King, M. A., Smith, B. E., Howat, I. M., and Moon, T. Seasonal speedup along the western flank of the Greenland ice sheet. *Science*, 320:781–783, 2008a. doi: 10.1126/science.1153288.

Joughin, I., Howat, I., Alley, R. B., Ekstrom, G., Fahnestock, M., Moon, T., Nettles, M., Truffer, M., and Tsai, V. C. Ice-front variation and tidewater behavior on Helheim and Kangerdlugssuaq Glaciers, Greenland. *J. Geophys. Res.*, 113:F01004, 2008b. doi: 10.1029/2007JF000837.

Joughin, I., Howat, I., Fahnestock, M., Smith, B., Krabill, W., Alley, R. B., Stern, H., and Truffer, M. Continued evolution of Jakobshavn Isbræ following its rapid speedup. *J. Geophys. Res.*, 113:F04006, 2008c. doi: 10.1029/2008JF001023.

Joughin, I., Smith, B. E., Howat, I. M., Scambos, T., and Moon, T. Greenland flow variability from ice-sheet-wide velocity mapping. *J. Glaciol.*, 56(197):415–430, 2010.

Khan, S. A., Kjær, K. H., Bevis, M., Bamber, J. L., Wahr, J., Kjeldsen, K. K., Bjørk, A. A., Korsgaard, N. J., Stearns, L. A., van den Broeke, M. R., Liu, L., Larsen, N. K., and Muresan, I. S. Sustained mass loss of the northeast Greenland ice sheet triggered by regional warming. *Nat. Clim. Change*, 4:292–299, 2014. doi: 10.1038/NCLIMATE2161.

Kirchner, N., Hutter, K., Jakobsson, M., and Gyllencreutz, R. Capabilities and limitations of numerical ice sheet models: a discussion for Earth-scientists and modelers. *Quaternary Sci. Rev.*, 30:3691–3704, 2011. doi: 10.1016/j.quascirev.2011.09.012.

Kuipers Munneke, P., van den Broeke, M. R., Lenaerts, J. T. M., Flanner, M. G., Gardner, A. S., and van de Berg, W. J. A new albedo parameterization for use in climate models over the Antarctic ice sheet. *J. Geophys. Res.*, 116:D05114, 2011. doi: 10.1029/2010JD015113.

Lambeck, K. and Chappell, J. Sea level change through the last glacial cycle. *Science*, 292:679 – 686, 2001.

Large, W. G. and Yeager, S. G. The global climatology of an interannually varying air-sea flux data set. 2008. doi: 10.1007/s00382-008-0441-3.

Lefebre, F., Gallée, H., van Ypersele, J., and Greuell, W. Modeling of snow and ice melt at ETH Camp (West Greenland): a study of surface albedo. *J. Geophys. Res.*, 108(D8):4231, 2003. doi: 10.1029/2001JD001160.

Lenton, T. M., Held, H., Kriegler, E., Hall, J. W., Lucht, W., Rahmstorf, S., and Schellnhuber, H. J. Tipping elements in the Earth's climate system. *Proc. Natl. Acad. Sci. USA*, 105:1786–1793, 2008.

Lhomme, N., Clarke, G. K., and Marshall, S. J. Tracer transport in the Greenland Ice Sheet: constraints on ice cores and glacial history. *Quaternary Sci. Rev.*, 24:173–194, 2005.

Lucas-Picher, P., Wulff-Nielsen, M., Christensen, J. H., Aðalgeirsdóttir, G., Mottram, R., and Simonsen, S. B. Very high resolution regional climate model simulations over Greenland: identifying added values. *J. Geophys. Res.*, 117:D02108, 2012. doi: 10.1029/2011JD016267.

Lunt, D. J., Foster, G. L., Haywood, A. M., and Stone, E. J. Late Pliocene Greenland glaciation controlled by a decline in atmospheric CO_2 levels. *Nature*, 454:1102–1105, 2008. doi: 10.1038/nature07223.

Luthcke, S. B., Zwally, H. J., Abdalati, W., Rowlands, D. D., Ray, R. D., Nerem, R. S., Lemoine, F. G., McCarthy, J. J., and Chinn, D. S. Recent Greenland Ice Mass Loss by Drainage System from Satellite Gravity Observations. *Science*, 314:1286–1289, 2006. doi: 10.1126/science.1130776.

MacAyeal, D. R. Large-scale ice flow over a viscous basal sediment: theory and application to ice stream B, Antarctica. *J. Geophys. Res.*, 94:4071–4087, 1989.

Marsiat, I. Simulation of the northern hemisphere continental ice sheets over the last glacial-interglacial cycle: experiments with a latitude-longitude vertically integrated ice sheet model coupled to zonally averaged climate model. *Paleoclimates*, 1:59–98, 1994.

Meehl, G. A., Stocker, T. F., Collins, W. D., Friedlingstein, P., Gaye, A. T., Gregory, J. M., Kitoh, A., Knutti, R., Murphy, J. M., Noda, A., Raper, S. C. B., Watterson, I. G., Weaver, A. J., and Zhao, Z. C. Global climate projections. In Solomon, S., Qin, D., Manning, M., Chen, Z., Marquis, M., Averyt, K. B., Tignor, M., and Miller, H. L., editors, *Climate Change 2007: the Physical Science Basis. Contribution of Working Group I to the Fourth Assessment Report of the Intergovernmental Panel on Climate Change*. Cambridge University Press, Cambridge, United Kingdom and New York, NY, USA, 2007.

Mernild, S. H. and Liston, G. E. Greenland freshwater runoff. part II: distribution and trends, 1960-2010. *J. Clim.*, 25:6015–6035, 2012. doi: 10.1175/JCLI-D-11-00592.1.

Mernild, S. H., Hasholt, B., and Liston, G. E. Climatic control on river discharge simulations, Zackenberg River drainage basin, northeast Greenland. *Hydrol. Process.*, 22: 1932–1948, 2008. doi: 10.1002/hyp.6777.

Milne, G. A., Gehrels, W. R., Hughes, C. W., and Tamisiea, M. E. Identifying the causes of sea-level change. *Nat. Geosci.*, 2:471–478, 2009. doi: 10.1038/ngeo544.

Mitrovica, J. X. and Milne, G. A. On post-glacial sea level: I. general theory. *Geophys. J. Int.*, 154:253–267, 2003.

Morlighem, M., Rignot, E., Seroussi, H., Larour, E., Dhia, H. B., and Aubry, D. Spatial patterns of basal drag inferred using control methods from a full-Stokes and simpler models for Pine Island Glacier, West Antarctica. *Geophys. Res. Lett.*, 37:L14502, 2010. doi: 10.1029/2010GL043853.

Moss, R. H., Edmonds, J. A., Hibbard, K. A., Manning, M. R., Rose, S. K., van Vuuren, D. P., Carter, T. R., Emori, S., Kainuma, M., Kram, T., Meehl, G. A., Mitchell, J. F. B., Nakicenovic, N., Riahi, K., Smith, S. J., Stouffer, R. J., Thomson, A. M., Weyant, J. P., and Wilbanks, T. J. The next generation of scenarios for climate change research and assessment. *Nature*, 463:747–756, 2010. doi: 10.1038/nature08823.

Mote, T. L. Estimation of runoff rates, mass balance, and elevation changes on the Greenland ice sheet from passive microwave observations. *J. Geophys. Res.*, 108(D2): 4056, 2003. doi: 10.1029/2001JD002032.

Motyka, R. J., Truffer, M., Fahnestock, M., Mortensen, J., Rysgaard, S., and Howat, I. Submarine melting of the 1985 jakobshavn isbræ floating tongue and the triggering of the current retreat. *J. Geophys. Res.*, 116:F01007, 2011. doi: 10.1029/2009JF001632.

Mouginot, J., Rignot, E., Scheuchl, B., Fenty, I., Khazendar, A., Morlighem, M., Buzzi, A., and Paden, J. Fast retreat of Zachariæ Isstrøm, northeast Greenland. *Science*, 2015. doi: 10.1126/science.aac7111.

Nakićenović, N., Alcamo, J., Davis, G., and de Vries, B. *Special report on emissions scenarios: a special report of Working Group III of the Intergovernmental Panel on Climate Change*. Intergovernmental Panel on Climate Change, 2000.

Nerem, R. S., Leuliette, E., and Cazenave, A. Present−day sea−level change: A review. *C. R. Geoscience*, 338:1077–1083, 2006.

Nick, F. M., van der Veen, C. J., Vieli, A., and Benn, D. I. A physically based calving model applied to marine outlet glaciers and implications for the glacier dynamics. *J. Glaciol.*, 56:781–794, 2010.

Nick, F. M., Vieli, A., Andersen, M. L., Joughin, I., Payne, A., Edwards, T. L., Pattyn, F., and van de Wal, R. S. W. Future sea-level rise from Greenland's main outlet glaciers in a warming climate. *Nature*, 497:235–238, 2013. doi: 10.1038/nature12068.

North Greenland Ice Core Project members. High-resolution record of Northern Hemisphere climate extending into the last interglacial period. *Nature*, 431:147–151, 2004.

Nowicki, S., Bindschadler, R. A., Abe-Ouchi, A., Aschwanden, A., Bueler, E., Choi, H., Fastook, J., Granzow, G., Greve, R., Gutowski, G., Herzfeld, U., Jackson, C., Johnson, J., Khroulev, C., Larour, E., Levermann, A., Lipscomb, W. H., Martin, M. A., Morlighem, M., Parizek, B. R., Pollard, D., Price, S. F., Ren, D., Rignot, E., Saito, F., Sato, T., Seddik, H., Seroussi, H., Takahashi, K., Walker, R., and Wang, W. L. Insights into spatial sensitivities of ice mass response to environmental change from the SeaRISE ice sheet modeling project II: Greenland. *J. Geophys. Res. Earth Surf.*, 118:1025–1044, 2013. doi: 10.1002/jgrf.20076.

Oerlemans, J. and Vugts, H. F. A meteorological experiment in the melting zone of the greenland ice sheet. *Bull. Amer. Meteor. Soc.*, 74:355–365, 1993.

Onogi, K., Tsutsui, J., Koide, H., Sakamoto, M., Kobayashi, S., Hatsushika, H., Matsumoto, T., Yamazaki, N., Kamahori, H., Takahashi, K., Kadokura, S., Wada, K., Kato, K., Oyama, R., Ose, T., Mannoji, N., and Taira, R. The JRA-25 reanalysis. *J. Meteor. Soc. Japan*, 85:369–432, 2007.

Otto-Bliesner, B. L., Marshall, S. J., Overpeck, J. T., Miller, G. H., Hu, A., and CAPE Last Interglacial Project members. Simulating Arctic climate warmth and icefield retreat in the last interglaciation. *Science*, 311:1751–1753, 2006.

Overland, J. E., Francis, J. A., Hanna, E., and Wang, M. The recent shift in early summer Arctic atmospheric circulation. *Geophis. Res. Lett.*, 39:L19804, 2012. doi: 10.1029/2012GL053268.

Pagani, M., Liu, Z., LaRiviere, J., and Ravelo, A. C. High Earth-system climate sensitivity determined from Pliocene carbon dioxide concentrations. *Nat. Geosci.*, 3:27–30, 2010.

Paterson, W. S. B. *The Physics of Glaciers*. Butterworth Heinemann, Oxford, 3rd edition, 1994.

Pattyn, F. Antarctic subglacial conditions inferred from a hybrid ice sheet/ice stream model. *Earth Planet. Sc. Lett.*, 295:451–461, 2010.

Payne, A. J. and Baldwin, D. J. Thermomechanical modeling of the Scandinavian ice sheet: implications for ice-stream formation. *Ann. Glaciol.*, 28:83–89, 1999.

Peltier, W. R. Postglacial variations in the level of the sea: implications for climate dynamics and solid-Earth geophysics. *Rev. Geophys.*, 36:603–689, 1998.

Peltier, W. R. Global glacial isostasy and the surface of the ice-age earth: the ICE-5G (VM2) model and GRACE. *Ann. Rev. Earth Planet. Sci.*, 32:111 – 149, 2004.

Peltier, W. R., Argus, D. F., and Drummond, R. Space geodesy constrains ice-age terminal deglaciation: The global ICE-6G-C (VM5a) model. *J. Geophys. Res. Solid Earth*, 120:450–487, 2015. doi: 10.1002/2014JB011176.

Peyaud, V. *Rôle de la dynamique des calottes glaciaires dans les grands changements climatiques des périodes glaciaires-interglaciaires*. PhD thesis, Université Joseph Fourier, Grenoble, France, 2006.

Peyaud, V., Ritz, C., and Krinner, G. Modelling the Early Weichselian Eurasian Ice Sheets: role of ice shelves and influence of ice-dammed lakes. *Clim. Past*, 3:375–386, 2007.

Pollard, D., DeConto, R. M., and Alley, R. B. Potential Antarctic Ice Sheet retreat driven by hydrofracturing and ice cliff failure. *Earth Planet. Sci. Lett.*, 412:112–121, 2015. doi: 10.1016/j.epsl.2014.12.035.

Quinn, P., Beven, K., Chevallier, P., and Planchon, O. The prediction of hillslope flow paths for distributed hydrological modeling using digital terrain models. *Hydrol. Process.*, 5:59–79, 1991.

Quiquet, A., Punge, H. J., Ritz, C., Fettweis, X., Gallée, H., Kageyama, M., Krinner, G., Salas y Mélia, D., and Sjolte, J. Sensitivity of a Greenland ice sheet model to atmospheric forcing fields. *The Cryosphere*, 6:999–1018, 2012. doi: 10.5194/tc-6-999-2012.

Quiquet, A., Ritz, C., Punge, H. J., and Salas y Mélia, D. Greenland ice sheet contribution to sea level rise during the last interglacial period: a modelling study driven and constrained by ice core data. *Clim. Past.*, 9:353–366, 2013a.

Quiquet, A., Ritz, C., Punge, H. J., and Salas y Mélia, D. Greenland ice sheet contribution to sea level rise during the last interglacial period: a modelling study driven and constrained by ice core data. *Clim. Past.*, 9:353–366, 2013b. doi: 10.5194/cp-9-353-2013.

Rabineau, M., Berné, S., Olivet, J. L., Aslanian, D., Guillocheau, F., and Joseph, P. Pales sea levels reconsidered from direct observation of paleoshoreline position during glacia maxima (for the last 500,000 yr). *Earth Planet. Sci. Lett.*, 252:119 – 137, 2006.

Rae, J. G. L., Aðalgeirsdóttir, G., Edwards, T. L., Fettweis, X., Gregory, J. M., Hewitt, H. T., Lowe, J. A., Lucas-Picher, P., Mottram, R. H., Payne, A. J., Ridley, J. K., Shannon, S. R., van de Berg, W. J., van de Wal, R. S. W., and van den Broeke, M. R. Greenland ice sheet surface mass balance: evaluating simulations and making projections with regional climate models. *The Cryosphere*, 6:1275–1294, 2012. doi: 10.5194/tc-6-1275-2012.

Rahmstorf, S., Crucifix, M., Ganopolski, A., Goosse, H., Kamenkovich, I., Knutti, R., Lohmann, G., Marsh, R., Mysak, L. A., Wang, Z., and Weaver, A. J. Thermohaline circulation hysteresis: A model intercomparison. *Geophys. Res. Lett.*, 32:L23605, 2005. doi: 10.1029/2005GL023655.

Rapp, D. *Ice Ages and Intergalcials. Measurements, Interpretation, and Models.* Springer Heidelberg New York Dordrecht London, 2012.

Reeh, N. Parameterization of melt rate and surface temperature on the Greenland Ice Sheet. *Polarforschung*, 5913:113–128, 1991.

Reeh, N., Thomsen, H. H., Higgins, A. K., and Weidick, A. Sea ice and the stability of the north and northeast Greenland floating glacier. *Ann. Glaciol.*, 33:474–480, 2001.

Renssen, H. and Knoop, J. M. A global river routing network for use in hydrological modeling. *J. Hydrol.*, 230:230–243, 2000.

Ridley, J. K., Gregory, J. M., Huybrechts, P., and Lowe, J. A. Threshold for irreversible decline of the Greenland ice sheet. *Clim. Dyn.*, 35:1049–1057, 2010. doi: 10.1007/s00382-009-0646-0.

Rienecker, M. M., Suarez, M. J., Gelaro, R., Todling, R., Bacmeister, J., Liu, E., Bosilovich, M. G., Schubert, S. D., Takacs, L., Kim, G., Bloom, S., Chen, J., Collins, D., Conaty, A., da Silva, A., Gu, W., Joiner, J., Koster, R. D., Lucchesi, R., Molod, A., Owens, T., Pawson, S., Pegion, P., Redder, C. R., Reichle, R., Robertson, F. R., Ruddick, A. G., Sienkiewicz, M., and Woollen, J. MERRA: NASA's modern-era retrospective analysis for research and applications. *J. Climate*, 24:3624–3648, 2011. doi: 10.1175/JCLI-D-11-00015.1.

Rignot, E. and Kanagaratnam, P. Changes in the velocity structure of the Greenland ice sheet. *Science*, 311:986–990, 2006. doi: 10.1126/science.1121381.

Rignot, E., Koppes, M., and Velicogna, I. Rapid submarine melting of the calving faces of West Greenland glaciers. *Nat. Geosci.*, 3:187–191, 2010. doi: 10.1038/NGEO765.

Rignot, E., Velicogna, I., van den Broeke, M. R., Monaghan, A., and Lenaerts, J. T. M. Acceleration of the contribution of the Greenland and Antarctic ice sheets to sea level rise. *Geophys. Res. Lett.*, 38:L05503, 2011. doi: 10.1029/2011GL046583.

Rignot, E., Jacobs, S., Mouginot, J., and Scheuchl, B. Ice-shelf melting around Antarctica. *Science*, 341:266–270, 2013. doi: 10.1126/science.1235798.

Ritz, C., Rommelaere, V., and Dumas, C. Modeling the evolution of antarctic ice sheet over the last 420,000 years: Implications for altitude changes in the vostok region. *Journal of Geophysical Research*, 106:31943–31964, 2001.

Robin, G. D. Q. Reconciliation of temperature-depth profiles in polar ice sheets with past surface temperatures deduced from oxygen-isotope profiles. *J. Glaciol.*, 16:9–22, 1976.

Robinson, A., Calov, R., and Ganopolski, A. Greenland ice sheet model parameters constrained using simulations of the Eemian Interglacial. *Clim. Past.*, 7:381–396, 2011. doi: 10.5194/cp-7-381-2011.

Robinson, A., Calov, R., and Ganopolski, A. Multistability and critical thresholds of the Greenland ice sheet. *Nature Clim. Change*, 2:429–432, 2012. doi: 10.1038/NCLIMATE1449.

Rogozhina, I., Martinec, Z., Hagedoorn, J. M., Thomas, M., and Fleming, K. On the long-term memory of the Greenland Ice Sheet. *J. Geophys. Res.*, 116:F01011, 2011. doi: 10.1029/2010JF001787.

Rohling, E. J., Fenton, M., Jorissen, F. J., Bertrand, P., Ganssen, G., and Caulet, J. P. Magnitudes of sea-level lowstands of the past 500,000 years. *Nature*, 394:162–165, 1998.

Ruddiman, W. F. and Kutzbach, J. E. Forcing of late Cenozoic Northern Hemisphere climate by plateau uplift in southern Asia and the American West. *J. Geophys. Res.*, 94:18409–18427, 1989. doi: 10.1029/JD094iD15p18409.

Rutt, I. C., Hagdorn, M., Hulton, N. R. J., and Payne, A. J. The Glimmer comunity ice sheet model. *J. Geophys. Res.*, 114:F02004, 2009. doi: 10.1029/2008JF001015.

Saha, S., Moorthi, S., Pan, H., Wu, X., Wang, J., Nadiga, S., Tripp, P., Kistler, R., Woollen, J., Behringer, D., Liu, H., Stokes, D., Grumbine, R., Gayno, G., Wang, J., Hou, Y., H. Chuang, H. H. J., Sela, J., Iredell, M., Treadon, R., Kleist, D., van Delst, P., Keyser, D., Derber, J., Ek, M., Meng, J., Wei, H., Yang, R., Lord, S., van den Dool, H., Kumar, A., Wang, W., Long, C., Chelliah, M., Xue, Y., Huang, B., Schemm, J., Ebisuzaki, W., Lin, R., Xie, P., Chen, M., Zhou, S., Higgins, W., Zou, C., Liu, Q., Chen, Y., Han, Y., Cucurull, L., Reynolds, R. W., Rutledge, G., and Goldberg, M. The NCEP climate forecast system reanalysis. *Bull. Amer. Meteorol. Soc.*, 91:1015–1057, 2010.

Sasgen, I., van den Broeke, M., Bamber, J. L., Rignot, E., Sørensen, L. S., Wouters, B., Martinec, Z., Velicogna, I., and Simonsen, S. B. Timing and origin of recent regional ice-mass in Greenland. *Earth Planet. Sci. Lett.*, 333–334:293–303, 2012.

Scoccimarro, E., Gualdi, S., Bellucci, A., Sanna, A., Fogli, P., Manzini, E., Vichi, M., Oddo, P., and Navarra, A. Effects of tropical cyclones on ocean heat transport in a high-resolution coupled general circulation model. *J. Climate*, 24:4368–4384, 2011. doi: 10.1175/2011JCLI4104.1.

Seddik, H., Greve, R., Zwinger, T., Gillet-Chaulet, F., and Gagliardini, O. Simulations of the Greenland ice sheet 100 years into the future with the full Stokes model Elmer/Ice. *J. Glaciol.*, 58(209):427–440, 2012.

Shapiro, N. M. and Ritzwoller, M. H. Inferring surface heat flux distributions guided by a global seismic model: particular application to Antarctica. *Earth Planet. Sci. Lett.*, 223:213–224, 2004.

Shepherd, A., Ivins, E. R., A, G., Barletta, V. R., Bentley, M. J., Bettadpur, S., Briggs, K. H., Bromwich, D. H., Forsberg, R., Galin, N., Horwath, M., Jacobs, S., Joughin, I., King, M. A., Lenaerts, J. T. M., Li, J., Ligtenberg, S. R. M., Luckman, A., Luthcke, S. B., McMillan, M., Meister, R., Milne, G., Mouginot, J., Muir, A., Nicolas, J. P., Paden, J., Payne, A. J., Pritchard, H., Rignot, E., Rott, H., Sørensen, L. S., Scambos, T. A., Scheuchl, B., Schrama, E. J. O., Smith, B., Sundal, A. V., van Angelen, J. H., van de Berg, W. J., van den Broeke, M. R., Vaughan, D. G., Velicogna, I., Wahr, J., Whitehouse, P. L., Wingham, D. J., Yi, D., Young, D., and Zwally, H. J. A reconciled estimate of ice-sheet mass balance. *Science*, 338:1183–1189, 2012. doi: 10.1126/science.1228102.

Siddall, M., Rohling, E. J., Almogi-Labin, A., Hemleben, C., Meischner, D., Schmelzer, I., and Smeed, D. A. Sea-level fluctuations during the last glacial cycle. *Nature*, 423: 853–858, 2003.

Sillmann, J., Kharin, V. V., Zhang, X., Zwiers, F. W., and Bronaugh, D. Climate extremes indices in the CMIP5 multimode ensemble: Part 1. model evaluation in the present climate. *J. Geophys. Res. Atmos.*, 118:1716–1733, 2013. doi: 10.1002/jgrd.50203.

Sohn, H.-G., Jezek, K. C., and van der Veen, C. J. Jakobshavn Glacier, West Greenland: 30 years of spaceborne observations. *Geophys. Res. Lett.*, 25:2699–2702, 1998.

Sørensen, L. S., Simonsen, S. B., Nielsen, K., Lucas-Picher, P., Spada, G., Adalgeirsdottir, G., Forsberg, R., and Hvidberg, C. S. Mass balance of the Greenland ice sheet (2003-2008) from ICESat data - the impact of interpolation, sampling and firn density. *The Cryosphere*, 5:173–186, 2011.

Stammer, D., Agarwal, N., Hermann, P., Köhl, A., and Mechoso, C. R. Response of a coupled ocean-atmosphere model to Greenland ice melting. *Surv. Geophys.*, 32: 621–642, 2011. doi: 10.1007/s10712-011-9142-2.

Stearns, L. A. and Hamilton, G. S. Rapid volume loss from two East Greenland outlet glaciers quantified using repeat stereo satellite imagery. *Geophys. Res. Lett.*, 34:L05503, 2007. doi: 10.1029/2006GL028982.

Steffensen, J. P., Andersen, K. K., Bigler, M., Clausen, H. B., Dahl-Jensen, D., Fischer, H., Goto-Azuma, K., Hansson, M., Johnsen, S. J., Jouzel, J., Masson-Delmotte, V., Popp, T., Rasmussen, S. O., Röthlisberger, R., Ruth, U., Stauffer, B., Siggaard-Andersen, M.-L., Sveinbjörnsdóttir, A. E., Svensson, A., and White, J. W. C. High-resolution Greenland ice core data show abrupt climate change happens in few years. *Science*, 321:680–684, 2008. doi: 10.1126/science.1157707.

Stone, E. J., Lunt, D. J., Rutt, I. C., and Hanna, E. Investigating the sensitivity of numerical model simulations of the modern state of the Greenland ice-sheet and its future response to climate change. *The Cryosphere*, 4:397–417, 2010. doi: 10.5194/tc-4-397-2010.

Stouffer, R. J., Yin, J., Gregory, J. M., Dixon, K. W., Spelman, M. J., Hurling, W., Weaver, A. J., Eby, M., Flato, G. M., Hasumi, H., Hu, A., Jungclaus, J. H., Kamenkovich, I. V., Levermann, A., Montoya, M., Murakami, S., Nawrath, S., Oka, A., Peltier, W. R., Robitaille, D. Y., Sokolov, A., Vettoretti, G., and Weber, S. L. Investigating the causes of the response of the thermohaline circulation to past and future climate changes. *J. Climate*, 19:1365–1387, 2006.

Straneo, F., Hamilton, G. S., Sutherland, D. A., Stearns, L. A., Davidson, F., Hammill, M. O., Stenson, G. B., and Rosin-Asvid, A. Rapid circulation of warm subtropical waters in a major glacial fjord in East Greenland. *Nature Geosci.*, 3:182–186, 2010. doi: 10.1038/NGEO764.

Stroeve, J. C., Kattsov, V., Barrett, A., Serreze, M., Pavlova, T., Holland, M., and Meier, W. N. Trends in Arctic sea ice extent from CMIP5, CMIP3 and observation. *Geophys. Res. Lett.*, 39:L16502, 2012. doi: 10.1029/ 2012GL052676.

Svendsen, P. L., Andersen, O. B., and Nielsen, A. A. Acceleration of the Greenland ice sheet mass loss as observed by GRACE: confidence and sensitivity. *Earth Planet. Sci. Lett.*, 364:24–29, 2013. doi: 10.1016/j.epsl.2012.12.010.

Swingedouw, D., Rodehacke, C. B., Behrens, E., Menary, M., Olsen, S. M., Gao, Y., Mikolajewicz, W., Mignot, J., and Biastoch, A. Decadal fingerprints of freshwater discharge around Greenland in a multi-model ensemble. *Clim. Dyn.*, 41:695–720, 2013. doi: 10.1007/s00382-012-1479-9.

Tarasov, L. and Peltier, W. R. Greenland glacial history and local geodynamic consequences. *Geophys. J. Int.*, 150:198–229, 2002.

Tarasov, L. and Peltier, W. R. Arctic freshwater forcing of the Younger Dryas cold reversal. *Nature*, 435:662–665, 2005. doi: 10.1038/nature03617.

Taylor, K. E., Stouffer, R. J., and Meehl, G. A. An overview of CMIP5 and the experiment design. *Bull. Amer. Meteor. Soc.*, 93:485–498, 2012.

Tedesco, M. and Fettweis, X. 21st century projections of surface mass balance changes for major drainage systems of the Greenland ice sheet. *Environ. Res. Lett.*, 7:045405, 2012. doi: 10.1088/1748-9326/7/4/045405.

Thoma, M., Grosfeld, K., Barbi, D., Determann, J., Goeller, S., Mayer, C., and Pattyn, F. RIMBAY - a multi-approximation 3D ice-dynamics model for comprehensive applications: model description and examples. *Geosci. Model Dev.*, 7:1–21, 2014. doi: 10.5194/gmd-7-1-2014.

Tushingham, A. M. and Peltier, W. R. Ice-3g: A new global model of late pleistocene deglaciation based upon geophysical predictions of post-glacial relative sea level change. *J. Geophys. Res.*, 96:4497 – 4523, 1991.

van de Wal, R. S. W. Mass-balance modeling of the Greenland ice sheet: a comparison of an energy-balance and a degree-day model. *Ann. Glaciol.*, 23:36–45, 1996.

van de Wal, R. S. W., Smeets, C. J. P. P., Boot, W., Stoffelen, M., van Kampen, R., Doyle, S. H., Wilhelms, F., van den Broeke, M. R., Reijmer, C. H., Oerlemans, J., and Hubbard, A. Self-regulation of ice flow varies across the ablation area in south-west Greenland. *The Cryosphere*, 9:603–611, 2015. doi: 10.5194/tc-9-603-2015.

van den Broeke, M., Bamber, J., Ettema, J., Rignot, E., Schrama, E., van de Berg, W. J., van Meijgaard, E., Velicogna, I., and Wouters, B. Partitioning recent Greenland mass loss. *Science*, 326:984–986, 2009. doi: 10.1126/science.1178176.

Vaughan, D. G., Comiso, J. C., Allison, I., Carrasco, J., Kaser, G., Kwok, R., Mote, P., Murray, T., Paul, F., Ren, J., Rignot, E., Solomina, O., Steffen, K., and Zhang, T. Observations: Cryosphere. In Stocker, T. F., Qin, D., Plattner, G.-K., Tignor, M., Allen, S. K., Boschung, J., Nauels, A., Xia, Y., Bex, V., and Midgley, P. M., editors, *Climate Change 2013: the Physical Science Basis. Contribution of Working Group I to the Fifth Assessment Report of the Intergovernmental Panel on Climate Change.* Cambridge University Press, Cambridge, United Kingdom and New York, NY, USA, 2013.

Velicogna, I., Sutterley, T. C., and van den Broeke, M. R. Regional acceleration in ice mass loss from Greenland and Antarctica using GRACE time-variable gravity data. *J. Geophys. Res. Space Physics*, 41:8130–8137, 2014. doi: 10.1002/2014GL061052.

Vernon, C. L., Bamber, J. L., Box, J. E., van den Broeke, M. R., Fettweis, X., Hanna, E., and Huybrechts, P. Surface mass balance model inter comparison for the Greenland ice sheet. *The Cryosphere*, 7:599–614, 2013. doi: 10.5194/tc-7-599-2013.

Vizcaíno, M., Mikolajewicz, U., Jungclaus, J., and Schurgers, G. Climate modification by future ice sheet changes and consequences for ice sheet mass balance. *Clim. Dyn.*, 34:301–324, 2010. doi: 10.1007/s00382-009-0591-y.

Vizcaíno, M., Lipscomb, W. H., Sacks, W. J., van Angelen, J. H., Wouters, B., and van den Broeke, M. R. Greenland surface mass balance as simulated by the Community Earth System Model. part I: Model evaluation and 1850–2005 results. *J. Climate*, 26: 7793–7812, 2013. doi: 10.1175/JCLI-D-12-00615.1.

Vizcaíno, M., Lipscomb, W. H., Sacks, W. J., and van den Broeke, M. R. Greenland surface mass balance as simulated by the Community Earth System Model. part II: twenty-first-century changes. *J. Climate*, 27:215–226, 2014. doi: 10.1175/JCLI-D-12-00588.1.

Vizcaíno, M., Mikolajewicz, U., Ziemen, F., Rodehacke, C. B., Greve, R., and van den Broeke, M. Coupled simulations of Greenland Ice Sheet and climate up to A.D. 2300. *Geophys. Res. Lett.*, 42:3927–3935, 2015. doi: 10.1002/2014GL061142.

Walsh, J. E., Chapman, W. L., Romanovsky, V., Christensen, J. H., and Stendel, M. Global climate model performance over Alaska and Greenland. *J. Climate*, 21:6156–6174, 2008.

Wara, M. W., Ravelo, A. C., and Delaney, M. L. Permanent El Niño -like conditions during the Pliocene warm period. *Science*, 309:758–761, 2005.

Weertman, J. On the sliding of glaciers. *J. Glaciol.*, 3:33–38, 1957.

WGMS. *Global glacier changes: fact and figures*. UNEP and World Glacier Monitoring Service, Zurich, Switzerland, 2008.

Winkelmann, R., Martin, M. A., Haseloff, M., Albrecht, T., Bueler, E., Khroulev, C., and Levermann, A. The Potsdam Parallel Ice Sheet Model (PISM-PIK)-part 1: model description. *The Cryosphere*, 5:715–726, 2011. doi: 10.5194/tc-5-715-2011.

Winkelmann, R., Levermann, A., Martin, M. A., and Frieler, K. Increased future ice discharge from Antarctica owing to higher snowfall. *Nature*, 492:239–242, 2012. doi: 10.1038/nature11616.

Woollings, T., Hannachi, A., Hoskins, B., and Turner, A. A regime view of the North Atlantic Oscillation and its response to anthropogenic forcing. *J. Climate*, 23:1291–1307, 2010. doi: 10.1175/2009JCLI3087.1.

Yan, Q., Zhang, Z., Gao, Y., Wang, H., and Johannessen, O. M. Sensitivity of the modeled present-day Greenland Ice Sheet to climatic forcing and spin-up methods and its influence on future sea level projections. *J. Geophys. Res. Earth Surf.*, 118: 2174–2189, 2013. doi: 10.1002/jgrf.20156.

Yan, Q., Wang, H., Johannessen, O. M., and Zhang, Z. Greenland ice sheet contribution to future global sea level rise based on CMIP5 models. *Adv. Atmos. Sci.*, 31:8–16, 2014. doi: 10.1007/s00376-013-3002-6.

Yoshimori, M. and Abe-Ouchi, A. Sources of spread in multimodel projections of the Greenland ice sheet surface mass balance. *J. Clim.*, 25:1157–1175, 2012. doi: 10.1175/2011JCLI4011.1.

Zwally, H. J., Abdalati, W., Herring, T., Larson, K., Saba, J., and Steffen, K. Surface melt-induced acceleration of Greenland ice-sheet flow. *Science*, 297:218–222, 2002. doi: 10.1126/science.1072708.

Zwally, H. J., Li, J., Brenner, A. C., Beckley, M., Cornejo, H. G., Marzio, J. D., Giovinetto, M. B., Neumann, T. A., Robbins, J., Saba, J. L., Yi, D., and Wang, W. Greenland ice sheet mass balance: distribution of increased mass loss with climate warming; 2003-07 versus 1992-2002. *J. Glaciol.*, 57:88–102, 2011.